POLYPUBLIE
Polytechnique Montréal

POLYTECHNIQUE MONTRÉAL
UNIVERSITÉ D'INGÉNIERIE

Titre: Title:	Development of a Spherical Indentation Inverse Methodology to Estimate Bulk Tensile Properties of Metals for Applications to Welds
Auteur: Author:	Gabrielle Turcot
Date:	2022
Type:	Mémoire ou thèse / Dissertation or Thesis
Référence: Citation:	Turcot, G. (2022). Development of a Spherical Indentation Inverse Methodology to Estimate Bulk Tensile Properties of Metals for Applications to Welds [Thèse de doctorat, Polytechnique Montréal]. PolyPublie. https://publications.polymtl.ca/10251/

Document en libre accès dans PolyPublie
Open Access document in PolyPublie

URL de PolyPublie: PolyPublie URL:	https://publications.polymtl.ca/10251/
Directeurs de recherche: Advisors:	Sylvain Turenne, Daniel Paquet, & Martin Lévesque
Programme: Program:	PhD.

Ce fichier a été téléchargé à partir de PolyPublie, le dépôt institutionnel de Polytechnique Montréal
This file has been downloaded from PolyPublie, the institutional repository of Polytechnique Montréal

https://publications.polymtl.ca

POLYTECHNIQUE MONTRÉAL
affiliée à l'Université de Montréal

Development of a spherical indentation inverse methodology to estimate bulk tensile properties of metals for applications to welds

GABRIELLE TURCOT
Département de génie mécanique

Thèse présentée en vue de l'obtention du diplôme de *Philosophiæ Doctor*
Génie mécanique

Mars 2022

© Gabrielle Turcot, 2022.

POLYTECHNIQUE MONTRÉAL
affiliée à l'Université de Montréal

Cette thèse intitulée :

Development of a spherical indentation inverse methodology to estimate bulk tensile properties of metals for applications to welds

présentée par **Gabrielle TURCOT**
en vue de l'obtention du diplôme de *Philosophiæ Doctor*
a été dûment acceptée par le jury d'examen constitué de :

Charles AUDET, président
Sylvain TURENNE, membre et directeur de recherche
Daniel PAQUET, membre et codirecteur de recherche
Martin LÉVESQUE, membre et codirecteur de recherche
Henri CHAMPLIAUD, membre
Denis THIBAULT, membre externe

DEDICATION

To my friends, my family, and my better half.

"Soak it in the sun and make a groovy lemon pie."

ACKNOWLEDGEMENTS

This research would not have been possible without the help and support of the many people surrounding me. This applies for technical aspects of the work, but also to the encouragement and comforting received from friends, colleagues and loved ones.

I first want to thank my supervisors, Prof. Sylvain Turenne and Prof. Martin Lévesque from École Polytechnique de Montréal, as well as Daniel Paquet, Ph.D., from the Hydro-Quebec research institute. I am incredibly grateful that they believed in me enough to accept me as a student and gave me the opportunity to work in collaboration between a university and the industry. I have learned tremendously from their various areas of expertise. On top of the technical guidance received from my supervisors, Prof. Lévesque and Dr Paquet have shown me the importance of rigour while Prof. Turenne showed me the importance of taking a step back (and drinking a cup of chamomile tea) to calm down when things don't go as planned. All three of them have helped me grow as a person and I will carry their teachings through my whole career.

I then want to thank colleagues from the Hydro-Quebec Research Institute that greatly helped in the completion of this work. Particularly, Carlo Baillargeon was an indispensable resource for technical advice, troubleshooting and training on several laboratory equipment. He has also helped immensely with specimen preparation and tensile tests. I am also grateful to researcher Jean-Benoît Lévesque, M.Sc., whom has helped me in many spheres of this research, particularly for finite element simulations using ANSYS as well as aspects linked to welded joints and EDM. I thank my colleague Pierre-Antony Deschênes, with whom I shared an office for a couple of years. I greatly appreciate his overflowing ideas which are incredibly useful in brainstorming sessions. I also thank him for his help with EBSD observations. Of course, I want to thank Jacques Lanteigne, Ph.D., whom is in charge of the CoReTHY project for which I was hired as a student. I admire his passion for science and am grateful for his immense metallurgical knowledge which has helped me through this work. Finally, I want to give a different thanks to Pierre-Antony Deschênes, Jean-Benoît Lévesque and Daniel Paquet, a trio I affectionately call the "pep-talk squad", for believing in me and getting me back up on my feet whenever I wanted to quit. Their words and all the laughs we shared made a real difference.

I want to thank Prof. Mohammad Jahazi, from École de Technologie Supérieure (ÉTS), who granted us access to a LEXT LS4100 laser scanning 3D microscope, which was essential in this work for characterizing the indentation residual imprints, and his student Ali Vedaei

for his help in using this equipment. I also want to express my gratitude to researcher Gilles Rousseau from the Hydro-Quebec Research Institute for his assistance in the ultrasonic measurements of elastic properties.

I want to acknowledge the financial support received from a research and development co-operative, led by Prof. Henri Champliaud, including the Hydro-Quebec Research Institute, Finkl Steel, the CRITM, the NSERC, ÉTS and École Polytechnique de Montréal.

Finally, I want to thank my friends, my family and my boyfriend for all the emotional support they have provided over the last few years.

RÉSUMÉ

Le comportement des joints soudés en service est difficile à prédire en raison des propriétés élasto-plastiques inhomogènes à travers les différentes régions du joint. À travers le métal de base, la zone affectée thermiquement (ZAT) et le métal d'apport, la microstructure évolue en raison des vitesses de refroidissement variables pendant le processus de soudage. Des contraintes résiduelles apparaissent également lors du refroidissement du joint et du métal environnant.

Ce travail a été mené dans le cadre d'un projet coopératif de recherche et développement visant à étudier la fabrication et la réparation de turbines hydrauliques par soudage par le biais d'analyses expérimentales et numériques. En particulier, un besoin a été identifié par l'Institut de Recherche d'Hydro-Québec pour la caractérisation des courbes de traction locales dans les régions soudées des turbines hydrauliques. Ces propriétés locales pourraient ensuite être utilisées dans des simulations pour évaluer l'intégrité du joint ou la qualité de la réparation de la soudure. Ce besoin du partenaire industriel a été la motivation première des travaux présentés dans cette thèse.

L'indentation instrumentée est une méthode expérimentale de choix pour la caractérisation locale des joints soudés. En effet, il s'agit d'une technique pouvant être utilisée de manière non destructive, et qui engendre moins de difficultés expérimentales que les tests de millitraction. Cependant, plusieurs défis existent lors de l'analyse des résultats d'indentation, car les champs de contrainte et de déformation générés lors d'un test d'indentation ne sont pas uniformes et évoluent au cours du processus d'indentation. L'objectif général de cette thèse est le développement d'une méthodologie inverse polyvalente et fiable permettant l'estimation des courbes macroscopiques de contrainte vraie-déformation vraie des métaux par indentation sphérique qui pourrait être utilisée pour effectuer la caractérisation locale d'un joint soudé.

Une revue de la littérature concernant l'indentation instrumentée démontre que plusieurs facteurs expérimentaux peuvent influencer les résultats d'indentation. Comme premier objectif spécifique, une étude expérimentale est jugée nécessaire pour s'assurer que les résultats d'indentation obtenus sont aussi fiables que possible pour la validation et les applications futures de la méthodologie inverse développée. Quatre aciers sont soumis à plusieurs tests concernant le processus de fabrication des échantillons, les méthodes de préparation de surface et l'installation des échantillons sur la machine d'indentation. La complaisance de la machine a été calculée à $C_f = 0,0229$ µm par une méthode directe développée pour le montage expérimental utilisé. La correction des données expérimentales pour tenir compte de

cette complaisance mène à une diminution de l'erreur sur le module d'élasticité estimé par la méthode d'Oliver et Pharr. Par exemple, dans le cas de l'acier SAE 1080, la norme de l'erreur diminue de 22,6% à 3,5% en appliquant la correction pour la complaisance.

Une analyse de la littérature existante concernant l'estimation des propriétés élasto-plastiques par indentation démontre que la meilleure approche pour la réalisation de l'objectif principal est le développement d'une méthode inverse basée sur l'optimisation, qui nécessite des simulations par éléments finis. Une amélioration potentielle identifiée en étudiant les méthodes répertoriées de ce type est d'éviter d'utiliser un modèle d'écrouissage pré-défini pour estimer le comportement en traction du matériau étudié. Il est démontré dans cette thèse qu'aucun des modèles d'écrouissage les plus utilisés ne peut représenter avec précision la véritable courbe de contrainte vraie-déformation vraie de tous les matériaux. Cette approche est particulièrement intéressante pour l'application aux soudures, car la microstructure de celles-ci évolue et la forme globale de la courbe de traction peut changer d'une position à l'autre. La supposition d'un modèle d'écrouissage spécifique, constant pour toutes les positions locales testées, peut mener à des erreurs importantes. Les deuxième et troisième objectifs spécifiques de recherche sont définis comme le développement du modèle d'éléments finis d'indentation nécessaire à la méthode inverse, et le développement de la méthode inverse elle-même. Le défi majeur lié à ces objectifs est d'élaborer une approche pour l'estimation de la courbe contrainte vraie-déformation vraie des métaux sans la supposition d'un modèle d'écrouissage. Ceci constitue la principale nouveauté de ce travail de recherche.

L'approche développée dans cette thèse repose sur une procédure d'optimisation qui extrait un groupe de six points sur la courbe contrainte vraie-déformation vraie distribués selon une progression géométrique dans l'espace des déformations, ainsi que le module d'élasticité. Un algorithme d'optimisation de recherche directe en boîte noire est utilisé et s'avère capable d'éluder les minima locaux. Une approche d'optimisation par fonction substitut est introduite comme étape préliminaire dans la méthodologie, qui permet de trouver un point de départ approprié pour l'étape finale d'optimisation de la fonction objectif.

La performance de la méthodologie inverse développée est étudiée à travers des études numériques et expérimentales, en utilisant quatre aciers avec des comportements d'écrouissage différents. En utilisant des données numériques d'indentation, les courbes de contrainte vraie-déformation vraie estimées se situent à une différence maximale de 5,7% par rapport aux courbes de traction cibles correspondantes. Les erreurs maximales sur le module élastique extrait et la limite d'élasticité sont respectivement de 0,5% et 11,1%. À titre de comparaison, des applications de la méthode, mais en utilisant des modèles d'écrouissage populaires, sont également menées à l'aide de données d'indentation numériques. Il a été observé que l'uti-

lisation d'un modèle d'écrouissage pré-défini mène toujours à une augmentation de l'erreur moyenne sur la zone d'écrouissage pour tous les modèles et matériaux étudiés. Cependant, le temps de calcul requis pour atteindre la convergence est jusqu'à dix fois plus court que lors de l'utilisation de l'approche développée sans modèle d'écrouissage.

L'application expérimentale de la méthode aux quatre aciers étudiés effectuée dans ce travail de recherche fait également partie de ce qui se démarque de la littérature, dans laquelle les validations expérimentales sont rares. La méthodologie inverse proposée utilisant des données expérimentales d'indentation mène à des estimations précises des courbes de contrainte vraie-déformation vraie pour les aciers ASTM A516 et SAE 1080. Ces courbes présentent des erreurs moyennes sur les régions d'écrouissage de 0,89% et 3,9%, respectivement. Cependant, les courbes de traction estimées pour les aciers AISI 415 et AISI 304L ne sont pas précises, présentant des erreurs de 75,7% sur la limite d'élasticité pour AISI 415 et une erreur moyenne sur la zone d'écrouissage de 29% pour l'acier AISI 304L. La diminution des performances de la méthode pour ces deux aciers pourrait s'expliquer par des transformations de phase induites par les déformations qui ne sont pas incluses dans les modèles de comportement des matériaux utilisés dans les modèles par éléments finis. Cela pourrait aussi résulter de la différence d'échelle entre les essais de traction et les essais d'indentation, puisque le nombre moyen de grains échantillonnés pour l'AISI 304L et de blocs de martensite échantillonnés pour l'AISI 415 sont estimés à 4 et 8, respectivement. En comparaison, pour les aciers ASTM A516 et SAE 1080, cette estimation du nombre de grains échantillonnés s'éleve plutôt à 80 et 12, respectivement.

Puisque le but global de ce travail de recherche est l'obtention d'une méthode inverse permettant de caractériser les propriétés locales d'une soudure, le dernier objectif spécifique est d'appliquer la méthode développée à une soudure. La méthode a ainsi été testée sur un cordon de soudure d'acier AWS ER70s-6 déposé sur une plaque d'acier ASTM A516. Ces métaux ont des comportements mécahniques similaires. La soudure a été étudiée à l'état brut de soudure et à l'état traité thermiquement pour relaxer les contraintes résiduelles. Des mesures de diffraction des rayons-X ont été réalisées par un laboratoire externe pour permettre leur inclusion dans la méthode développée et d'étudier leur effet sur les résultats obtenus. Il a été déterminé que de négliger les contraintes résiduelles présentes peut induire des erreurs significatives dans la méthodologie. Par exemple, pour une mesure dans une certaine position dans la ZAT d'une éprouvette à l'état brut de soudage, négliger la valeur mesurée de -78,8 MPa mène à une différence de 20,1% sur la limite d'élasticité estimée.

Les essais d'indentation ont été réalisés sur des surfaces découpées sur les éprouvettes soudées, dans la direction parallèle à la soudure. Cette application a donc utilisé l'indentation

instrumentée de manière destructive. Pour appliquer la méthode aux turbines hydrauliques, il faudrait réaliser les indentations sur la surface visible de la soudure, sans couper de matière, pour que les essais soient alors non-destructifs. Des équipements d'indentation portables existent et pourraient être utilisés directement sur les régions soudées des turbines.

En observant les courbes contrainte vraie-déformation vraie estimées à travers les échantillons de soudure, on constate que la méthode est capable de capturer l'évolution des propriétés du matériau à travers le métal d'apport, la ZAT et le métal de base. De plus, ces variations sont telles qu'attendues en fonction de l'effet du procédé de soudage sur la microstructure du matériau dans les différentes zones de soudure.

Les tendances observées dans les résultats obtenus à travers les soudures ainsi que la validation expérimentale de la méthode dans l'acier ASTM A516 soutiennent que cette méthodologie inverse proposée pourrait être appliquée pour caractériser les soudures faites d'aciers à faible teneur en carbone par le partenaire industriel, ou d'autres instituts de recherches et entreprises, avec confiance dans les résultats obtenus. De la recherche et du développement supplémentaires seront nécessaires pour étendre la méthode aux aciers austénitiques et martensitiques utilisés pour la fabrication et la réparation des turbines.

ABSTRACT

The behaviour of welded joints in service is difficult to predict due to the in-homogeneous elasto-plastic properties through the different regions of the joint. Through the base metal, the heat affected zone (HAZ) and the weld metal, the microstructure evolves due to varying cooling rates during the welding process. Residual stresses also appear during the cooling of the joint and its surroundings.

This work was conducted within a research and development cooperative project aiming to study the fabrication and repair of hydraulic turbines by welding through experimental and numerical analyses. Particularly, a need was identified by the Hydro-Quebec Research Institute for the characterization of local tensile properties in welded regions of hydraulic turbines. These local properties could then be used in simulations to evaluate the integrity of the joint, or the quality of the weld repair. This requirement by the industrial partner was the prime motivation for the work presented in this thesis.

Instrumented indentation is a prime candidate as an experimental method for the local characterization of welded joints. Indeed, it can be used in a non-destructive manner and it is not as experimentally challenging as milli-tensile tests. However, several challenges exist for the analysis of indentation results as the stress and strain fields induced during an indentation test are non-uniform and evolve during the indentation process. The general objective of this work is the development of a versatile and reliable inverse methodology for the estimation of local macroscopic true stress-true strain curves in metals by spherical indentation which can be applied to a weld.

A literature review on instrumented indentation shows that several experimental factors can influence indentation results. As a first specific objective, an experimental study is deemed necessary to ensure that the indentation results obtained are as reliable as possible for the validation and future applications of the developed inverse methodology. Four steels are subjected to several tests regarding the fabrication process, surface preparation methods and installation of specimen on the indentation machine. The machine compliance was calculated to be $C_f = 0.0229$ µm through a direct method developed for the experimental setup used in this work. Correcting the experimental data for this value leads to an important decrease in the error on the estimated elastic modulus using Oliver and Pharr's method. For example, in the case of SAE 1080 steel, the magnitude of the error decreases from 22.6% to 3.5% when a correction for the compliance is included in the analysis.

An analysis of the literature existing for the estimation of elasto-plastic properties by inden-

tation demonstrates that the best approach for the completion of the general objective is the development of an optimization-based inverse method, which requires finite element simulations. A potential improvement to common methods of this type is identified as avoiding the use of a specific hardening model to estimate the tensile behaviour. It is demonstrated in this work that none of the most commonly used hardening models can accurately represent the true stress-true strain curve of all materials. This approach is particularly interesting for the application to welds, as their microstructures evolve, and the overall shape of the tensile curve could change from one position to the next. Pre-defining a hardening model, constant to all tested local positions, might lead to significant errors. The second and third specific objectives are set as the development of the indentation finite element model needed for the inverse method, and the development of the inverse method itself. The major challenge for these objectives is to find an approach for the estimation of the true stress-true strain curve of metals without the supposition of a pre-defined hardening model. This constitutes the main novelty of this work.

The approach developed in this thesis relies on an optimization procedure which extracts a group of six points on the true stress-true strain curve distributed as per a geometric progression in the strain space, as well as the elastic modulus. A direct search black-box optimization algorithm is used and is shown to be capable of eluding local minima. A surrogate step is introduced in the methodology, which is a simplified version of the inverse problem, to find a suitable starting point.

The performance of the developed inverse methodology is investigated through numerical and experimental studies, using four steels with different hardening behaviours. When using numerical indentation data, the estimated true stress-true strain curves lie within a maximum error of 5.7% from the corresponding target tensile curves. The maximum errors on the extracted elastic modulus and yield stress are 0.5% and 11.1%, respectively. For comparison, applications of the method by using popular hardening models were conducted using numerical indentation data. It was observed that using a hardening model always leads to an increase in the average error over the hardening region for all models and materials studied. However, the computational time required for reaching convergence is up to ten times shorter than when using the developed approach without a pre-specified hardening model.

The experimental application of the method to the four studied steels is also a part of this work which stands out from the literature, in which experimental validations are rare. The proposed inverse methodology using experimental indentation data leads to accurate estimations of the true stress-true strain curves for ASTM A516 and SAE 1080 steels, with average errors over the hardening regions of 0.89% and 3.9%, respectively. However, the

estimated tensile curves for AISI 415 and AISI 304L steels are not accurate, presenting errors of 75.7% on the yield stress for AISI 415 and an average error over the hardening region of 29% for AISI 304L. The decrease in the performance of the method for these two steels could be explained by strain induced phase transformations which are not included in the material behaviour models used in the finite element models. It could also result from the difference in scale between the tensile tests and the indentation tests, as the average number of grains sampled for AISI 304L and of martensite blocks sampled for AISI 415 were approximately 4 and 8, respectively. Comparatively, the number of grains sampled for ASTM A516 and SAE 1080 steels was around 80 and 12, respectively.

Since the culmination of this work is to obtain an inverse method which can characterize the local properties in a weld, the last specific objective was to apply the developed method to a weld. The method was thus tested on an AWS ER70s-6 steel weld deposited on an ASTM A516 steel plate. The mechanical behaviour of these weld and base metals are similar. The weld was studied in the as welded state and in the heat treated state to relieve residual stresses. X-ray diffraction measurements were performed by an outside laboratory to enable their inclusion in the developed method and to study their effect on the extracted results. It was determined that neglecting residual stresses which are present can induce significant errors into the methodology. For example, in one position in the HAZ of a specimen in the as welded state, neglecting the measured value of -78.8 MPa leads to a difference of 20.1% in the estimated yield stress.

The indentation tests were conducted on surfaces cut from the welded specimens, in the direction parallel to the weld. This application thus used instrumented indentation in a destructive way. To apply the method to hydraulic turbines, the indentation tests would need to be non-destructive. The indentations then need to be conducted on the visible surface of the weld, without cutting any material. Portable indentation equipment exists and could be used directly on the welded regions of the turbines.

When observing the true stress-true strain curves estimated through the weld specimens, it is found that the method is able to capture the evolution of material properties through the weld metal, HAZ and base metal. Furthermore, these variations are as expected based on the welding process effect on the microstructure of the material within the weld zone.

The approach developed in this work, which avoids the assumption of a specific hardening model, is shown to be beneficial in the application to a weld since the estimated tensile curves vary in shape through the weld zones. Particularly, some estimated true stress-true strain curves appear to have a linear hardening behaviour, while others resemble a power-law. Furthermore, a plastic plateau appears in certain positions. This variability in shape could

not have been captured by an inverse method which assumes a hardening model.

The observed trends in the results obtained in the welds as well as the experimental validation of the method in ASTM A516 support that the proposed inverse method could be applied to characterize welds made of low-carbon steels by the industrial partner, or other research institutes and companies involving research and development, with confidence in the obtained results. Further research and development will be required for an extension of the method to austenitic and martensitic steels used for the fabrication and repair of the turbines.

TABLE OF CONTENTS

DEDICATION iii

ACKNOWLEDGEMENTS iv

RÉSUMÉ vi

ABSTRACT x

TABLE OF CONTENTS xiv

LIST OF TABLES xvii

LIST OF FIGURES xxi

LIST OF SYMBOLS AND ACRONYMS xxvii

CHAPTER 1 INTRODUCTION 1

CHAPTER 2 LITERATURE REVIEW 3

2.1 Instrumented indentation 3

2.2 Important courses of error in indentation analysis 6

2.2.1 Machine compliance and indenter geometry 6

2.2.2 Effect of scale of indentation 8

2.3 Extraction of elastic properties by instrumented indentation 8

2.4 Extraction of elasto-plastic properties by instrumented indentation 10

2.4.1 Empirical methods 10

2.4.2 Dimensional analysis 14

2.4.3 Inverse method by numerical optimization 23

2.4.4 Comparison of the three approaches with regard to potential applications to welds 27

2.5 Finite elements modeling of instrumented indentation 30

2.5.1 Geometry 30

2.5.2 Boundary conditions 31

2.5.3 Meshing 31

2.5.4 Material behaviour and yield criteria 32

2.5.5 Contact and friction 33

2.6 Numerical optimization . . . 34
2.6.1 Optimization algorithm . . . 35
2.6.2 Handling of constraints . . . 36
2.6.3 Optimization using quadratic models . . . 36
2.6.4 Surrogate function strategy . . . 37
2.6.5 Performance analysis tool: identifiability index . . . 37
2.7 Instrumented indentation and residual stresses . . . 39
2.7.1 Effect of existing residual stresses on instrumented indentation results 39
2.7.2 Measurement of residual stresses by indentation . . . 41
2.8 Application of instrumented indentation to welded joints . . . 42
2.9 Literature review synthesis and relevance to the research project . . . 44

CHAPTER 3 RESEARCH OBJECTIVES AND ORIGINALITY . . . 46
3.1 General objective . . . 46
3.2 Specific objectives . . . 46
3.3 Originality . . . 46

CHAPTER 4 EXPERIMENTAL INDENTATION STUDY AND DIRECT MEASUREMENT OF THE MACHINE COMPLIANCE . . . 47
4.1 Materials and methods . . . 47
4.1.1 Materials . . . 47
4.1.2 Instrumented indentation . . . 53
4.1.3 Study of the effect of experimental parameters on indentation results 58
4.1.4 Direct measurement of the machine compliance . . . 65
4.2 Results and discussion . . . 70
4.2.1 Study of the effect of experimental parameters on indentation results 70
4.2.2 Direct measurement of the machine compliance and its effect on indentation curves . . . 76
4.3 Conclusions . . . 80

CHAPTER 5 DEVELOPMENT OF INDENTATION FINITE ELEMENT MODELS 82
5.1 Spherical indentation: Detailed model . . . 82
5.2 Spherical indentation: Surrogate model . . . 86
5.3 Flat punch indentation for direct calibration of machine compliance . . . 87
5.4 Performance of the indentation finite element models . . . 88
5.4.1 Detailed model . . . 88
5.4.2 Surrogate model . . . 93

5.4.3 Flat punch indentation model 94
5.5 Conclusions 94

CHAPTER 6 INVERSE METHODOLOGY FOR THE ESTIMATION OF TRUE STRESS-TRUE STRAIN CURVES BY INDENTATION WITHOUT THE ASSUMPTION OF A PRE-DEFINED HARDENING MODEL 96
6.1 Description of the method 96
6.1.1 Surrogate step: determination of suitable starting point for subsequent optimization step 97
6.1.2 Optimization step: final estimation of true stress-true strain curves . 103
6.2 Methods used for the performance study of the developed inverse method . . 110
6.3 Tensile properties and power law curve fitting 113
6.4 Results of the performance study of the developed inverse methodology . . . 115
6.4.1 Numerical application 115
6.4.2 Experimental application 122
6.4.3 Analysis using the identifiability-index 129
6.5 Conclusions 139

CHAPTER 7 APPLICATION OF THE PROPOSED INVERSE METHODOLOGY TO A WELD 141
7.1 Approach used for the application of the proposed methodology to a weld . . 141
7.1.1 Materials and welding 141
7.1.2 Specimen preparation 142
7.1.3 Residual stress measurements 143
7.1.4 Instrumented indentation 144
7.1.5 Inclusion of residual stresses in the finite element models 144
7.1.6 Extraction of local true stress-true strain curves in the weld through the application of the developed inverse methodology 145
7.2 Results and discussion 147
7.2.1 Residual stress measurements 147
7.2.2 Microstructure analysis 149
7.2.3 Estimated true stress-true strain curves 156
7.3 Conclusions 164

CHAPTER 8 CONCLUSION 166

REFERENCES 171

LIST OF TABLES

Table 2.1 Summary of five empirical methods for the extraction of elasto-plastic properties. 13

Table 2.2 Comparison of the accuracy of several dimensional analysis methods assuming a power law presented in the literature and validated with numerical indentation data. 22

Table 2.3 Comparison of the accuracy of several dimensional analysis methods assuming a power law presented in the literature and validated with experimental indentation data. 22

Table 2.4 Comparison of the accuracy of several numerical optimization methods presented in the literature assuming a power law and validated with numerical indentation data. 26

Table 2.5 Comparison of the accuracy of several numerical optimization methods presented in the literature assuming a power law and validated with experimental indentation data. 27

Table 2.6 Principal advantages, disadvantages and limitations of methods to extract elasto-plastic properties by instrumented indentation based on dimensional analysis, numerical optimization and spherical or sharp indentation empirical methods. 29

Table 4.1 General characteristics of the four steels studied in this work. . 48

Table 4.2 Measurements of hardness variations across plates of AISI 415 and ASTM A516 steels. 49

Table 4.3 Chemical composition (% wt.) of SAE 1080. 50

Table 4.4 Chemical composition (% wt.) of ASTM A516. 51

Table 4.5 Chemical composition (% wt.) of AISI 415. 51

Table 4.6 Chemical composition (% wt.) of AISI 304L. 51

Table 4.7 Average of the elastic modulus, $\overline{E}$, and the yield stress, $\overline{\sigma_y}$, calculated from the experimental tensile curves, as well as the standard deviation of these values, s_E and s_{σ_y}, respectively. The average standard deviation over the hardening region of the curve, $\overline{s}_{[\varepsilon_y,\ \varepsilon_{max}]}$, is also shown. 54

Table 4.8 Summary of the characteristics of the specimens used for the studies of different experimental effects on indentation results. 62

Table 4.9 Geometrical characteristics associated with the original specimen holder, the new specimen holder and the mortar. 70

Table 4.10 Differences in important indentation parameters obtained when comparing results from specimens with surface preparation procedures ending with a polishing step using 1 µm and 0.05 µm particles. 75

Table 4.11 Elastic moduli, E_0, computed with the Oliver and Pharr method and a machine compliance of 0 µm/N when using an experimentally measured contact area; and the error on the estimation of the moduli compared to the expected values calculated from tensile experiments, ΔE_0. 77

Table 4.12 Elastic moduli, $E_{0.0299}$, computed with the Oliver and Pharr method and the measured machine compliance of 0.0299 µm/N when using an experimentally measured contact area; error on the estimation of the elastic moduli compared to the expected values calculated from tensile experiments, $\Delta E_{0.0299}$, and improvement on the absolute value of the error, when compared to when using a null machine compliance. 80

Table 5.1 Differences between indentation maximum load, P_{max}, contact stiffness, S, residual depth, h_r, and maximum pile-up height, u_{max}, obtained from experiments and those obtained by the detailed finite element model. 90

Table 5.2 Average number of grains (SAE 1080, ASTM A516, AISI 304L) or martensite blocks (AISI 415) contained within a plastic zone, as approximated from the residual imprint topography, on the undeformed surface prior to indentation. 92

Table 5.3 Differences between important indentation parameters obtained from the surrogate model and those obtained by the detailed finite element model. 94

Table 6.1 Finite element study for the obtention of the contact radius, a, from which Tabor's indentation strain, ε_{ind}, is computed, and the maximum equivalent plastic strain after unloading, ε_{max}. 104

Table 6.2 Summary of the parameters defining the optimization problems to be solved in the surrogate and optimization steps of the proposed methodology. 110

Table 6.3 Ramberg-Osgood parameters obtained by the surrogate step of the optimization procedure. 116

Table 6.4 Errors on the estimated elastic modulus, ΔE, and yield stress, $\Delta\sigma_y$, and the average of the absolute value of the error over the hardening region of the true stress-true strain curve derived from the extracted material parameters, $|\overline{\Delta\sigma_p}|$, obtained by the optimization step when using the proposed methodology and when assuming either the Ramberg-Osgood, Hollomon or hybrid hardening model. 118

Table 6.5 Optimization starting points defined by elasto-plastic parameters of a Ramberg-Osgood hardening model obtained by the surrogate step of the optimization procedure for the experimental application of the method. 126

Table 6.6 Values of the extracted elastic moduli, E, and yield stresses, σ_y, as well as their relative errors with respect to the experimental tensile curves, ΔE and $\Delta\sigma_y$, and the average of the absolute value of the error over the hardening region of the estimated true stress-true strain curve, $|\overline{\Delta\sigma_p}|$, obtained by the material parameters identified in the optimization step of the method. 126

Table 6.7 Standard deviations of E and σ_y as well as the average of the standard deviation in the hardening regions of the curves. Also ives the variability around the average tensile curves which represents the 95th percentile, calculated by taking the standard deviation multiplied by a factor of 1.96. 127

Table 6.8 Differences between indentation maximum load, P_{max}, contact stiffness, S, residual depth, h_r, and maximum pile-up height, u_{max}, obtained from experiments and those obtained by the detailed finite element model. 127

Table 6.9 I-index, I, quantifying the identifiability of sets containing between 5 and 9 parameters leading to estimated true stress-true strain curves comprising of 4 to 8 points. 130

Table 6.10 I-indices obtained for the identification of $\mathbf{X}$ using different indentation data in the objective function: the indentation curve only, the residual imprint only, or a combination of both. 131

Table 6.11 I-indices obtained for the identification of $\mathbf{X}$ using the indentation curve and either the full residual imprint topography in a single sub-function or the residual imprint separated into two sub-functions accounting for the contact and free surface regions of the imprint. . . 132

Table 6.12 I-indices obtained for the identification of $\mathbf{X}$ using weight values which were optimized to obtain the smallest I-index for each material, when compared to using weights of 1. 133

Table 6.13 I-index values, I, found through a numerical study varying indentation maximum load of 2.5 N, 5 N, and 7.5 N, as well as the corresponding h_{max}/R ratios for all materials. 134

Table 6.14 Errors on the estimated elastic modulus, ΔE, and yield stress, $\Delta\sigma_y$, and the average of the absolute value of the error over the hardening region of the true stress-true strain, $|\overline{\Delta\sigma_p}|$, obtained by the optimization step when using the proposed methodology with maximum loads of 2.5, 5 or 7.5 N generating different h_{max}/R ratios. 137

Table 7.1 Chemical composition (% wt.) of the ASTM A516 steel used as the base metal for the application to a weld and the weld metal, AWS ER70s-6 steel. 142

Table 7.2 Errors induced by neglecting the presence of residual stresses on the estimated yield stress, $\Delta\sigma_y$, and plastic region of the tensile curve, $|\overline{\Delta\sigma_p}|$, for all positions studied in the as-welded specimens. 162

LIST OF FIGURES

Figure 2.1 Illustration of typical indentation data: (a) Indentation curve; (b) and (c) example of specimen surface and indenter geometry at maximum load and after the removal of the load for a pyramidal indenter. 5

Figure 2.2 Sinking-in/piling-up of the surface in residual indentation imprints and the effects on contact area. 5

Figure 2.3 Comparison between a similar and non-similar indenter geometry: (a) a sharp indenter; and (b) a spherical indenter. 6

Figure 2.4 Illustration of spherical indentation parameters for empirical methods: the indenter radius, R, the indentation depth, h, and the contact radius, a. 12

Figure 2.5 Flowchart displaying an example of application of a dimensional analysis method for elasto-plastic properties extraction by instrumented indentation. 16

Figure 2.6 Dimensionless function Π_1 constructed using three different values of ε_r. 17

Figure 2.7 Example of the influence of the ratio of maximum indentation depth to indenter diameter, h_{max}/D, on the indentation data of mystical materials. 19

Figure 2.8 Flow-chart describing the inverse method by numerical optimization for the extraction of elasto-plastic properties by instrumented indentation. 23

Figure 2.9 Effect of ratio h_{max}/R on the distinguishability of simulated indentation residual imprints. 26

Figure 2.10 Effect of the presence of compressive or tensile equi-biaxial residual stresses on the experimental Vickers indentation results on 2024 aluminum alloy. 40

Figure 2.11 Indentation curves normalized by their respective maximum load, P_{max}, and maximum depth, h_{max}, obtained by conical indentation finite elements simulations on specimens containing different states of residual stress. 40

Figure 2.12 Effect of equi-biaxial compressive or tensile residual stresses on the residual imprint profiles obtained by conical indentation finite elements simulations for a material with $\sigma_y = 400$ MPa. 42

Figure 2.13 Comparison of the tensile curve obtained from an experiment on a SM490 steel welded joint to the tensile curves simulated from finite element models using the extracted tensile curves by instrumented indentation and using only the base metal properties. 44
Figure 4.1 Geometry of specimens for homogeneity and isotropy study as well as approximate position of hardness tests. 49
Figure 4.2 Microstructure of SAE 1080 steel in the L direction. 51
Figure 4.3 Microstructure of ASTM A516 steel in the: (a) T; and (b) L directions. 52
Figure 4.4 Microstructure of AISI 415 steel in the: (a) T; and (b) L directions. 52
Figure 4.5 Microstructure of AISI 304L steel in the: (a) T; and (b) L directions. 53
Figure 4.6 Experimental true stress-true strain curves obtained for the four studied steels. 54
Figure 4.7 Geometry of the indenter used in this work. 56
Figure 4.8 Position matrix of indentations (10 × 2 indents) with reference coordinate system. 56
Figure 4.9 Indentation load and depth as a function of time for ASTM A516 steel. 57
Figure 4.10 Example of the residual imprint of an indentation performed with a sphero-conical indenter of radius $R = 50$ µm and a maximum load of 5 N in an ASTM A516 steel specimen. 59
Figure 4.11 Comparison between the residual imprint of an indentation in ASTM A516 steel and the geometry of the indenter, positioned at the maximum indentation depth achieved during the test. 60
Figure 4.12 Installation setup of a baseline specimen, A516-B. 60
Figure 4.13 Installation setup as proposed by the manufacturer of the micro indentation machine, Anton-Paar, for specimen A516-G. 62
Figure 4.14 Installation setup for conventionally machined specimen, A516-CM. 64
Figure 4.15 Illustration of the specimen installation conceived to overcome alignment issues in the method for direct measurement of the machine compliance. 67
Figure 4.16 Final setup for direct calibration of the machine compliance with specimen AO-2 after the ageing of the mortar. 69

Figure 4.17 Comparison of indentation results from the ASTM A516 steel baseline specimen and the specimen installed with an aluminum support and a layer of glue. 72
Figure 4.18 Comparison of indentation curves obtained on the ASTM A516 steel baseline specimen, with those obtained on a conventionally machined specimen. 73
Figure 4.19 Comparison of experimental indentation data obtained on the baseline specimens, when compared to those obtained on specimens which were polished further with 0.05 µm particles. 74
Figure 4.20 Flat punch indentation results obtained on specimen AO-2. . . 78
Figure 4.21 Average contact stiffness measured at the onset of unloading as a function of applied load, for specimens: (a) AO-1; and (b) AO-2. . . 78
Figure 4.22 Effect of machine compliance correction on indentation curves for the four studied steels using the calculated C_f of 0.0299 µm/N. . . 81
Figure 5.1 Finite element meshes for spherical indentation tests with $R =$ 50 µm, used in the: (a) detailed model; and (b) surrogate model. . . . 84
Figure 5.2 Finite element mesh of the flat punch indentation model. . . . 88
Figure 5.3 Comparison of numerical and experimental indentation data obtained with a sphero-conical indenter with $R = 50$ µm, by applying a maximum load of 5 N. 89
Figure 5.4 Simulated equivalent plastic strain distributions obtained with a sphero-conical indenter with $R = 50$ µm, by applying a maximum load of 5 N using the detailed finite element model. 91
Figure 5.5 Simulated flat punch indentation curve and calculated slope of 809.7 N/µm. 95
Figure 6.1 Flowchart describing the inverse methodology proposed in this thesis: (a) the surrogate step; and (b) the optimization step. 98
Figure 6.2 Typical indentation data: (a) indentation curve comprised of loading and unloading parts and (b) indentation residual imprint profile separated in contact and free surface regions. 100
Figure 6.3 Illustration of the variables for the optimization step. 105
Figure 6.4 Examples of true stress-true strain curves which do not respect each of the constraints, when compared to a true stress-true strain curve which respects all constraints of the optimization step. 106

Figure 6.5 Examples of tensile curves obtained with different $\mathbf{X}$ in which ε_{pl} lies within the intervals $[\varepsilon_y, \varepsilon_1]$, $]\varepsilon_1, \varepsilon_2]$ and $]\varepsilon_2, \varepsilon_3]$ and extrapolations to estimate the actual position of ε_{pl}. 109

Figure 6.6 Experimental true stress-true strain behaviour of four steels compared to the tensile curves obtained by fitting the models developed by Hollomon, Ramberg-Osgood and the hybrid model, to the experimental tensile curves. 114

Figure 6.7 Comparison of the target true stress-true strain curves to the starting points obtained from the surrogate step, and those estimated with the optimization step when using the proposed methodology and when assuming either the Ramberg-Osgood, Hollomon or hybrid hardening model. 117

Figure 6.8 Estimation of the actual yield point elongation by extrapolation of the σ_2 to σ_3 segment of the true stress-true strain curve obtained for SAE 1080 steel. 118

Figure 6.9 Indentation data obtained by finite element simulation using the target curve, and the estimated true stress-true strain curves using the proposed methodology, and when assuming either the Ramberg-Osgood, Hollomon or hybrid hardening model for ASTM A516 steel. 119

Figure 6.10 Convergence plots of the proposed method for four materials using numerically obtained target indentation data for: (a) the surrogate step; (b) the optimization step; and (c) the optimization step without the surrogate step. 121

Figure 6.11 Comparison of the convergence plots of the optimization step when using the proposed methodology and when assuming either the Ramberg-Osgood, Hollomon or hybrid hardening model. 123

Figure 6.12 Comparison of the experimental true stress-true strain curves to those estimated by the surrogate step and upon full completion of the proposed methodology using experimentally obtained target indentation data. 125

Figure 6.13 Comparison of the experimental true stress-true strain curves to those estimated with the proposed methodology using unity weights or optimized weights to minimize the I-index value for ASTM A516 and SAE 1080 steels. 134

Figure 6.14 Comparison of the target true stress-true strain curves to those estimated with the optimization step when using maximum indentation loads of 2.5 N, 5 N and 7.5 N. 136
Figure 6.15 Convergence plots of the optimization step of the proposed method for four materials using numerically obtained target indentation data and maximum indentation loads of 2.5 N, 5 N and 7.5 N to vary the ratio h_{max}/R. 138
Figure 7.1 Illustration of the specimens' geometry, locations and states (as-welded, AW, or heat treated, HT) within the welded plate. 143
Figure 7.2 Residual stresses measurements characteristics. 145
Figure 7.3 Finite element meshes for spherical indentation tests, including the radial displacement used to generate the residual stresses. 146
Figure 7.4 Residual stresses measured by XRD in the heat treated (HT1 and HT2) and as-welded (AW1 and AW2) specimens in the positions and directions previously illustrated in Figure 7.2. 148
Figure 7.5 Principal stresses computed in all positions in the as-welded specimens AW1 and AW2, as well as the average of these principal stresses to be inputted into the finite element models when residual stresses are considered. 150
Figure 7.6 Micrograph image of half of as-welded specimen AW1 and heat treated specimen HT1 taken after indentation tests. 150
Figure 7.7 Micrograph image of indents located in positions 0 and 1 in as-welded specimen AW1 and heat treated specimen HT1 taken after indentation tests. 151
Figure 7.8 Micrograph image of indents located in positions 2 and 3 in as-welded specimen AW1 and heat treated specimen HT1 taken after indentation tests. 152
Figure 7.9 Micrograph image of indents located in positions 4 and 5 in as-welded specimen AW1 and heat treated specimen HT1 taken after indentation tests. 153
Figure 7.10 Micrograph image of indents located in positions 6 and 7 in as-welded specimen AW1 and heat treated specimen HT1 taken after indentation tests. 154
Figure 7.11 Apparent Brinell hardness as a function of position in the weld for specimens AW1 and HT1, when compared to expected values for fresh martensite, tempered martensite (371°C) and fine pearlite. . . . 156

Figure 7.12 True stress-true strain curves obtained with the proposed methodology for indentations conducted in the weld metal (positions 0 and 1). 158
Figure 7.13 True stress-true strain curves obtained with the proposed methodology for indentations conducted in the HAZ (positions 2 to 6). . . . 159
Figure 7.14 True stress-true strain curves obtained with the proposed methodology for indentations conducted in the base metal (position 7). . . . 160
Figure 7.15 Estimated yield stress values and stress values at a strain of $\varepsilon = 0.28$ obtained with the proposed methodology for indentations spanning the weld metal (positions 0 and 1), the HAZ (positions 2 to 6) and the base metal (position 7). 160
Figure 7.16 Variability between extracted true stress-true strain curves obtained with the proposed methodology for indentations spanning the weld metal (positions 0 and 1), the HAZ (positions 2 to 6) and the base metal (position 7). 161

LIST OF SYMBOLS AND ACRONYMS

Latin

a	Real contact radius
a_{id}	Ideal contact radius
A_c	Contact area
A_p	Projected contact area
BHN	Brinell hardness number
C	Curvature of the indentation loading curve
C_f	Machine compliance
C_f^*	Measured machine compliance
C_M	Mortar compliance
C_N	New specimen holder compliance
C_O	Original specimen holder compliance
C_{AO}	Aluminum oxyde specimen compliance
c_k	Optimization constraint
d_d	Radial displacement used to generate a residual stress state in the detailed finite element model
d_s	Radial displacement used to generate a residual stress state in the surrogate finite element model
E	Elastic modulus
E_T	Tangent modulus
E_r	Reduced modulus
E^*	Alternate symbol used in the literature for the reduced modulus
EDM	Electric discharge machining
$\tilde{f}(\mathbf{Y})$	Surrogate function
$\tilde{f}_{IC}(\mathbf{Y})$	Surrogate sub-function accounting for the contact region of the residual imprint
$\tilde{f}_{IF}(\mathbf{Y})$	Surrogate sub-function accounting for the free surface region of the residual imprint
$\tilde{f}_L(\mathbf{Y})$	Surrogate sub-function accounting for indentation loading curve
$\tilde{f}_S(\mathbf{Y})$	Surrogate sub-function accounting for the contact stiffness
$f(\mathbf{X})$	Objective function
$f_{IC}(\mathbf{X})$	Objective sub-function accounting for the contact region of the residual imprint

$f_{IF}(\mathbf{X})$	Objective sub-function accounting for the free surface region of the residual imprint
$f_I(\mathbf{X})$	Objective sub-function accounting for the full residual imprint
$f_L(\mathbf{X})$	Objective sub-function accounting for indentation loading curve
$f_S(\mathbf{X})$	Objective sub-function accounting for the contact stiffness
$\mathbf{H}$	Sensitivity dimensionless matrix
h	Measured indentation depth
h_a	Sink-in depth (> 0) or pile-up height (< 0)
h_c	Contact depth
h_d	Specimen height in the detailed model
h_e	Elastic depth
h_{max}	Maximum depth
h_r	Residual depth
h_s	Specimen height in the surrogate model
H	Hardness
H_{IT}	Indentation hardness
HAZ	Heat affected zone
I	Identifiability index
K	Hardening constant
M_C	Position of the node marking the separation of the contact and free surface regions of the residual imprint
M_{max}	Position of the node at which the pile-up height is the largest
n	strain hardening coefficient
P	Measured indentation load
P_{max}	Maximum indentation load
p_m	Indentation averaged pressure
R	Indenter radius
r_d	Specimen radius in the detailed model
r_s	Specimen radius in the surrogate model
$S = \frac{dP}{dh}$	Contact stiffness
s_d	Smallest element size in the specimen of the detailed model
$s_{d,i}$	Smallest element size in the indenter of the detailed model
s_s	Smallest element size in the specimen of the surrogate model
$s_{s,i}$	Smallest element size in the indenter of the surrogate model
$\mathbf{S}^{IC}$	Sensitivity vector for the objective sub-function accounting for the contact region of the residual imprint

$\mathbf{S}^{IF}$	Sensitivity vector for the objective sub-function accounting for the free surface region of the residual imprint
$\mathbf{S}^{L}$	Sensitivity vector for the objective sub-function accounting for the indentation loading curve
$\mathbf{S}^{S}$	Sensitivity vector for the objective sub-function accounting for the contact stiffness
u	Height of the residual imprint profile
u_{max}	Maximum pile-up height
v_{IC}	Weight associated with the objective sub-function accounting for the contact region of the residual imprint
v_{IF}	Weight of the objective sub-function accounting for the free surface region of the residual imprint
v_L	Weight of the objective sub-function accounting for indentation loading curve
v_S	Weight of the objective sub-function accounting for the contact stiffness
W_e	Indentation elastic work
w_{IC}	Weight associated with the surrogate sub-function accounting for the contact region of the residual imprint
w_{IF}	Weight of the surrogate sub-function accounting for the free surface region of the residual imprint
w_L	Weight of the surrogate sub-function accounting for indentation loading curve
w_S	Weight of the surrogate sub-function accounting for the contact stiffness
W_p	Indentation plastic work
W_t	Total indentation work
$\mathbf{Y}$	Surrogate step variable vector
$\mathbf{Y}_l$	Lower bounds of surrogate step variable vector
$\mathbf{Y}_u$	Upper bounds of surrogate step variable vector
$\mathbf{Y}_u$	Starting point of surrogate step variable vector
$\mathbf{X}$	Optimization step variable vector
$\mathbf{X}_l$	Lower bounds of optimization step variable vector
$\mathbf{X}_u$	Upper bounds of optimization step variable vector
$\mathbf{X}_u$	Starting point of optimization step variable vector

Greek

δ_i	Mesh size parameter in the OrthoMADS optimization algorithm
δ_{min}	Minimum mesh size parameter
Δ_i	Mesh size parameter in the OrthoMADS optimization algorithm
ϵ_S	Surrogate step tolerance stopping criteria
ϵ_O	Optimization step tolerance stopping criteria
ε_{ind}	Indentation strain
ε_{max}	Strain value of the last point estimated on the true stress-true strain curve
ε_p	Plastic strain
ε_{pl}	Plastic strain value at the end of Lüders plateau
ε_r	Representative strain
ε_y	Yield strain
θ	Pyramidal and conical indenter half-angle
μ	Friction coefficient
ν	Poisson's ratio
σ_r	Representative stress
σ_y	Yield stress
σ_{ind}	Indentation stress
Ψ	Indentation constraint factor

CHAPTER 1 INTRODUCTION

The knowledge of local true stress-true strain curves in components featuring microstructure gradients is essential to the prediction of their macroscopic plasticity response in service. For instance, the heat affected zone of a welded joint is characterized by spatial variations of the yield stress and hardening behaviours. These variations are due to an evolving microstructure which appears with the different cooling rates involved, as well as position dependent strain hardening taking place during the welding process. When studying fatigue behaviour, the knowledge of local true stress-true strain curves is required to understand, model, and predict the plastic response of the material through the applied load cycles.

Hydro-electric turbines feature welded joints that are subjected to fatigue loading. Fatigue failure in these turbines greatly impacts electricity production and unexpected service interruptions generate significant costs and profit loss during the necessary repairs. A reliable method capable of estimating local tensile behaviour would offer an evaluation of the mechanical state of the welded joints and contribute to avoid such unexpected service interruptions. It would also be a tool to evaluate the effectiveness of performed repairs and guide the development of new repairs, leading to increased weld lifetimes.

Methods such as milli-tension tests and instrumented indentation can be used to obtain bulk local true stress-true strain curves. The former method directly provides measurements of the true stress-true strain response of the material since it measures the applied load and elongation of a uni-axial specimen. It however requires very precise machining of specimens at the millimetre scale and it is destructive. On the other hand, instrumented indentation tests are comparatively simpler to implement since the specimen preparation is standardized and they can be conducted in a non-destructive manner. The challenge with instrumented indentation rests upon the analysis of the results since the stress and strain fields induced during an indentation test are non-uniform and evolve during the indentation process. Hence, there is no direct correlation between indentation data and the material true stress-true strain curve. The development of a robust methodology for estimating tensile curves from instrumented indentation data has received a considerable amount of research interest in the past two decades [15, 51, 106].

A supplemental challenge arises when characterizing the tensile properties in welded joints, as residual stresses appear during the cooling of the joint and its surroundings. Residual stresses have significant effects on indentation data and can thus impact the estimated tensile properties [86, 131, 136]. Various studies used indentation-based methods to extract local

tensile curves in welded joints [107,117,135]. However, in many of these studies, the presence of residual stresses is completely ignored. The estimated tensile properties must then be interpreted with caution because of the sensitivity of the indentation data to the presence of residual stresses.

This Ph.D. project is part of a cooperative research and development project, focused on experimental and simulation studies of the fabrication and repair of hydraulic turbines by welding. It regroups two universities, École Polytechnique de Montréal and École de Technologie Supérieure, as well as industrial partners Hydro-Quebec and Finkl Steel. The general objective of the work presented in this thesis is to develop a novel method for estimating the local true stress-true strain curves of metals by instrumented indentation, which could then be used to characterize welded joints in hydraulic turbines. To reach this objective, an experimental study was conducted to understand the effect of several parameters on indentation results and ensure that the experiments led to the most reliable indentation data possible. A literature review was also performed to make the appropriate choices with regards to the development of the method and the finite element models. Finally, to demonstrate that this method is suitable for the sought application, the novel method is used to characterize a welded joint, including residual stresses in the analysis by measuring them by X-ray diffraction.

This thesis is organized as follows: Chapter 2 presents a detailed review of the literature relevant to this research project, which leads to the definition of the research objectives in Chapter 3. The four following chapters present the methods, results and discussion relevant to each specific objective defined in Chapter 3. First, Chapter 4 presents the experimental study and a novel method which was developed to characterize the machine compliance. Then, Chapter 5 describes the developed finite element models and presents an analysis of their performance. The developed inverse method is presented and analyzed in Chapter 6, including applications to numerical and experimental data. The application of the proposed methodology to a weld is presented in Chapter 7. Finally, the main conclusions of the work are highlighted in Chapter 8 along with some recommendations for future works.

CHAPTER 2 LITERATURE REVIEW

The present chapter gives a detailed literature review of indentation research works relevant to the present thesis. First, a general introduction to instrumented indentation is given in Section 2.1, followed by a description of important sources of error in this field, in Section 2.2.1. Next, the existing methods for the extraction of elastic and elasto-plastic properties by instrumented indentation are described in Sections 2.3 and 2.4, respectively. A comparison between the different approaches used is then made in Section 2.4.4, and it is concluded that an optimization-based method is most suitable for applications to welds.

To understand of the building blocks of optimization-based inverse methods and provide guidance for the development of such a methodology, the different approaches used in finite element modeling of instrumented indentation are detailed in Section 2.5 and a background on numerical optimization is provided in Section 2.6.

Since the developed inverse methodology must be capable of characterizing welds, the coupling of indentation with residual stresses is then addressed in Section 2.7. Different applications of indentation testing to welded joints are then presented in Section 2.8.

Finally, a synthesis of the literature review is given in Section 2.9, which creates the basis upon which the research objectives are elaborated in Chapter 3.

2.1 Instrumented indentation

An indentation test consists in the application of a force between the rigid tip of an indenter with known elastic properties and the flat surface of a specimen to characterize. The resulting penetration depth of the indenter into the specimen surface as a function of the applied load is progressively acquired during the test. Depending on the applied load and the resulting indentation depth, the stress and strain fields generated in the material vary in dimensions. This experimental technique therefore permits the study of material behaviour at different scales. Macro-indentation is classified by loads between 2 N and 30 kN and samples a sufficiently large material volume to characterize bulk material behaviour in a local region of interest [56]. Micro-indentation is classified by loads smaller than 2 N while maintaining depths larger than 200 nm, and nano-indentation is characterized by indentation depths lower than 200 nm. At these scales, very localized material behaviour and microstructural features can be studied.

The possibility of extracting local material parameters enabling the estimation of the tensile

curves of metallic materials has received considerable research interest in the past decades. This field of study is complex due to the triaxiality of the generated stress and strain fields as well as geometric and material non-linearities. Finite element simulations are therefore often used to analyze indentation data.

Figure 2.1(a) shows a typical indentation curve as well as its characterizing parameters. The geometrical equivalent of these parameters on the surface of a specimen are illustrated in Figure 2.1(b) at maximum load, P_{max}, and in Figure 2.1(c), after unloading. The contact depth, h_c, enables the calculation of the projected contact area, A_p, which corresponds to the projected area of the indenter, at a distance h_c from its tip. $S = \frac{dP}{dh}$ is the contact stiffness and h_{max}, h_r and h_e are respectively the maximum, residual and elastic depths. Finally, parameter h_a corresponds to the difference between h_{max} and h_c.

The indentation curve is separated into two parts, loading and unloading. During loading, the applied load, P, can be expressed as a function of the indentation depth, h, through:

$$P = Ch^2, \tag{2.1}$$

where C is the curvature of the loading curve computed by fitting the experimental data [58].

The contact depth, h_c, does not directly correspond to a depth on the indentation curve. When observing the residual imprint left after an indentation test, one of two phenomena can be distinguished: the sinking-in or the piling-up of the surface. The extent of these phenomena depends strongly upon the plasticity response of the studied material. A material exhibiting high strain hardening will sink-in, while a material exhibiting weak strain hardening will pile-up [58]. Figure 2.2 illustrates both possibilities and exposes their respective influence on the value of h_c. The parameter α quantifies the intensity of the sinking-in or the piling-up. It is obtained by taking the ratio of the projected area at the contact depth, $A_p(h_c)$, to the projected area at the maximum depth, $A_p(h_{max})$. Thus, $\alpha < 1$ when sinking-in occurs and $\alpha > 1$ when piling-up occurs.

Indenters are classified into three categories: sharp, spherical and flat punch indenters. Sharp indenters have a geometrically similar shape, *i.e.*, the ratio of the projected area to depth is constant with depth. Spherical indenters do not display this property. Figure 2.3 illustrates the difference of geometrical similarity between sharp and spherical indenters. Geometrical similarity plays a primary role in the definition of the representative strain, ε_r, which will be defined in Section 2.4.1. Sharp indenters are described by their half-angles, θ. The most commonly used are the three-sided Berkovich ($\theta = 65.35°$) and cube-corner ($\theta = 35.3°$) pyramids, the four-sided Vickers pyramid ($\theta = 68°$) and cones (varying θ). Spherical indenters

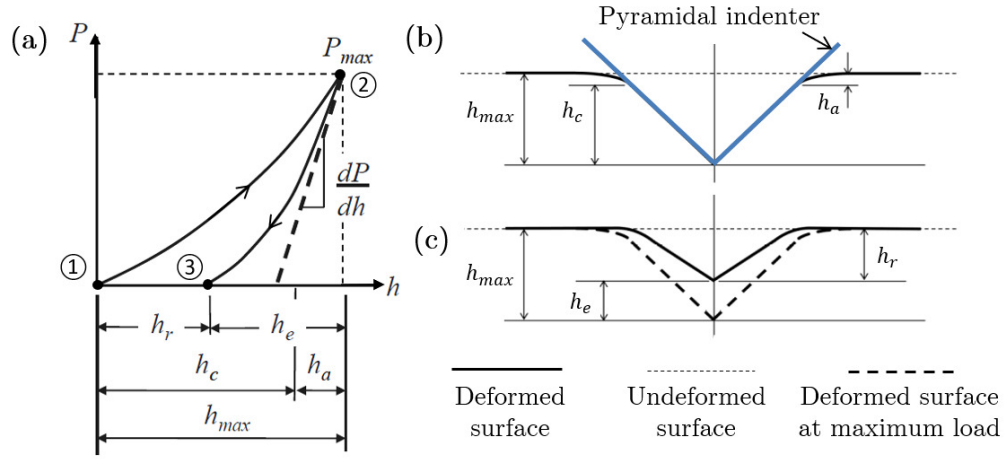

Figure 2.1 Illustration of typical indentation data: (a) Indentation curve where segment 1-2 corresponds to loading and segment 2-3 corresponds to unloading; (b) and (c) examples of specimen surface and indenter geometry at maximum load (equivalent to point 2 on the curve) and after the removal of the load (equivalent to point 3 on the curve) for a pyramidal indenter. P_{max} is the maximum load; h_{max}, h_c, h_r and h_e are the maximum, contact, residual and elastic depths, respectively; h_a is the difference between h_{max} and h_c; and $S = \frac{dP}{dh}$ is the contact stiffness (adapted from [58]).

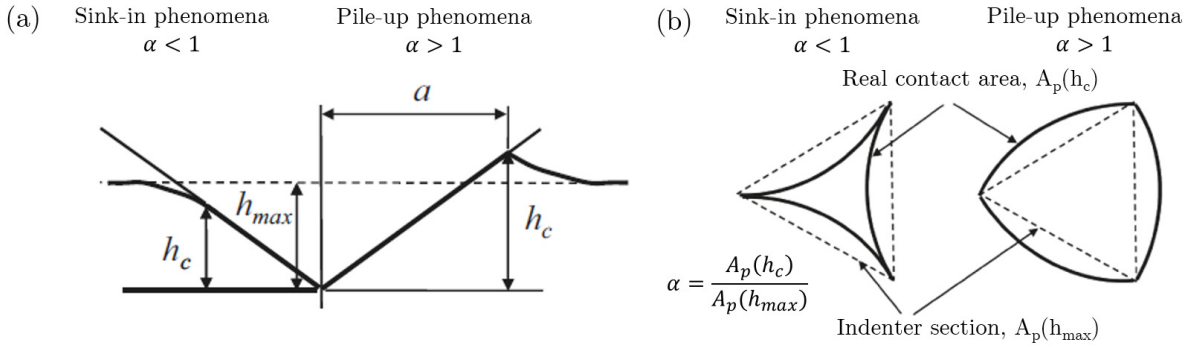

Figure 2.2 Sinking-in/piling-up phenomena observed in the topography of an indentation residual imprint and their effect on the contact area, A_p: (a) side view; and (b) top view. α is the ratio between the projected area at the contact depth, $A_p(h_c)$, and the projected area at the maximum depth, $A_p(h_{max})$ (adapted from [58]).

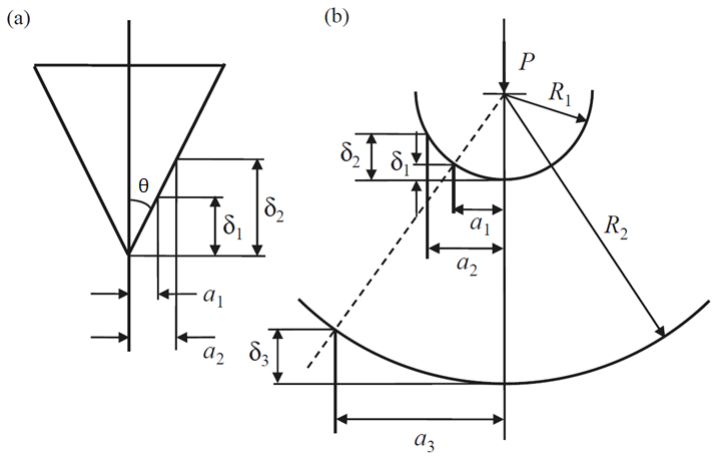

Figure 2.3 Comparison between a similar and non-similar indenter geometry: (a) a geometrically similar sharp indenter, for which $a_1/\delta_1 = a_2/\delta_2$; and (b) a geometrically non-similar spherical indenter, for which $a_1/\delta_1 \neq a_2/\delta_2$, but $a_1/\delta_1 = a_3/\delta_3$ if $a_1/R_1 = a_3/R_2$. Taken from [58].

are characterized by their tip radius, R, and flat punch indenters, by their diameter, D.

2.2 Important courses of error in indentation analysis

Three important sources of experimental error exist in indentation tests: the machine compliance, the indenter geometry and the scale of indentation.

2.2.1 Machine compliance and indenter geometry

During the test, the total displacement of the indenter is measured as opposed to uniquely the depth into the surface of the specimen. There is thus a portion of the measured displacement that is caused by the deformation of the experimental setup. The total measured displacement, h_d, can be written as:

$$h_d = h + C_f P, \tag{2.2}$$

where h is the portion of the displacement truly accountable for the indentation process and the second term is the portion resulting from machine deformation. C_f is the machine compliance and P is the applied load. To correct the measured displacement to obtain the indentation depth, the value of C_f associated with the experimental setup in use must be known.

The indenter geometry is defined through the projected area as a function of the contact depth $A_p(h_c)$. It is imperative to obtain $A_p(h_c)$ with the highest possible accuracy to ensure that the properties identified from indentation data are accurate.

Several techniques have been developed to obtain C_f and $A_p(h_c)$. The most commonly used calibrates both unknowns by indenting two reference specimens until the certified elastic properties are found with the Oliver and Pharr method [57, 97] (Section 2.3). This method is indirect and several assumptions are present in the Oliver and Pharr method. Also, it is assumed that C_f and the elastic properties are constant with the applied load. Many variants of this approach exist [77, 90, 96, 125]), but all are indirect and are based on similar hypotheses.

To obtain more reliable values for these parameters, direct measurement methods must be used to avoid the assumptions necessary in indirect methods. The direct measurement of the indenter area function is simple to implement, since the geometry of the indenter can be measured by an atomic force microscope, or a profilometer, depending on the studied indentation scale. With $A_p(h_c)$ known, the ISO-14577 standard proposes a calibration procedure for C_f in which it is now the single unknown [57]. However, the procedure remains indirect.

Van Vliet et al. [126] proposed a direct measurement method of C_f. They replaced the indenter by a platen which was several millimeters in diameter, which permitted the dispersion of the load on a much larger surface. This in turn minimized the stress applied to the specimen and led to its minimal deformation. Another way to minimize specimen deformation is the use of a highly rigid material, like a ceramic as the specimen for such tests. The penetration depth into the specimen is then negligible and the measured displacement can be solely attributed to the deformation of the experimental setup. In these conditions, C_f can directly be deduced.

The authors first observed poor repeatability of the directly measured C_f values. They attributed this variability to setup misalignment, which is in line with observations made by Pelletier et al. [103] that flat punch indenters are the indenters for which misalignment, even when very small, has the largest effect on indentation curves. These effects appear as contact detection difficulties as well as non-linear indentation curves, contrary to expectations for a flat punch indenter.

To solve the misalignment problem, Van Vliet et al. [126] inserted a thin layer of low viscosity cyanoacrylate glue between the platen and the specimen. The polymerization of the glue took place while a 10 N load was applied, as if an indentation test was conducted, but it was maintained for a period of 90 minutes to enable the complete hardening of the adhesive. The polymer then became a geometrical shim perfectly adapted to create proper alignment

between the platen and the specimen.

A complication of this technique was the necessity to modify the indenter holder to permit the removal of the indenter and specimen once they were glued together. This meant that the setup for the measurement of C_f was slightly different than when typical indentation tests are conducted. The measured C_f might therefore be different. Also, the addition of a layer of material with low rigidity, the glue, can influence the measured value of C_f. The authors estimated the thickness of the adhesive layer by profilometry to be between 10 and 50 µm. When considering an elastic modulus of 4 GPa, they computed a compliance of 0.002 µm/N for the glue and were incidentally able to correct the measured value of C_f.

The results of this study conducted by Van Vliet et al. [126] showed that C_f was on average 1.4 % higher upon loading than unloading, demonstrating a small influence of the loading direction. No significant influence of the load was observed upon unloading and a small diminution of C_f with increasing load was observed upon loading. The results from several indirect measurements methods were compared to that obtained by Van Vliet et al. [126] and differences ranging from 3.7% to 25% were recorded. This demonstrates the relevance of a direct measurement method for C_f to better correct the raw indentation data.

2.2.2 Effect of scale of indentation

When attempting to extract the bulk properties of metals, care must be taken to ensure that the scale of indentation is sufficiently large to sample a representative volume of material. Particularly, a minimum number of grains must be within the deformed zone as to obtain an averaged behaviour representative of the macroscopic tensile curve. Previous studies have estimated that a deformed zone including a minimum of 12 grains is required to represent the bulk behaviour of most materials, but a higher number of grains is preferable [28, 45]. Indentation data obtained on populations of grains which are not numerous enough will be influenced by crystallographic orientation and is not expected to result in accurate estimations of the bulk elasto-plastic behaviour. The interaction between grains would also not be well sampled in this case.

2.3 Extraction of elastic properties by instrumented indentation

During an indentation test, the stiffness observed does not reflect only that of the specimen, but actually that of the interaction between the specimen and indenter. The reduced modulus, E_r, was developed to characterize this interaction. It is derived from Hertz's small strain theory of elastic frictionless contact between a plane surface and a spherical inden-

ter [43, 61, 67]. E_r is defined by:

$$\frac{1}{E_r} = \frac{1-\nu^2}{E} + \frac{1-\nu_i^2}{E_i}, \tag{2.3}$$

where E_i and E are the elastic modulii of the indenter and specimen, respectively. ν_i and ν are the Poisson's ratios of the indenter and specimen, respectively. E_r can be estimated from indentation, and the specimen's elastic modulus, E, can then be obtained through equation (2.3). To do so, the elastic properties of the indenter as well the Poisson's ratio of the specimen must be known or estimated.

Two approaches exist to extract E_r by instrumented indentation: methods based on the loading curve and methods based on the unloading curve. The methods based on the loading curve use Hertz's contact equations to fit the beginning of the indentation loading curve and then solve for E_r [36, 55]. This approach relies on the assumption that the behaviour is purely elastic in this region of the curve, and requires a spherical indenter tip. Since plastic deformation appears early in the indentation curve and it is difficult to find the transition point between elastic and elasto-plastic behaviour, this approach is not commonly used.

The most commonly used approach to extract E_r uses the indentation unloading curve, resting on the hypothesis that the strain recovery during unloading is purely elastic and thus independent of plastic properties [52,97]. E_r can then be computed from the contact stiffness, $S = \frac{dP}{dh}$, at h_{max} through the following relationship:

$$E_r = \frac{1}{2\beta}\frac{dP}{dh}\bigg|_{h_{max}} \frac{\sqrt{\pi}}{\sqrt{A_p(h_c)}}, \tag{2.4}$$

where β is a geometrical factor empirically derived and varying with the indenter used and $A_p(h_c)$ is the area function of the indenter. Equation (2.4) was first derived from the contact between two elastic bodies and was shown to be valid for rigid indenters with an axisymmetric geometry [109, 116]. It was then shown that it can actually be applied to any indenter geometry [109].

The contact depth, h_c, is computed by:

$$h_c = h_{max} - \frac{\epsilon P_{max}}{\frac{dP}{dh}\Big|_{h_{max}}}. \tag{2.5}$$

The second term of the right side of this equation corresponds to the deviation of the surface from its original position, at h_{max}. It was developed from the profile of the surface in the

vicinity of an indent as described by Sneddon's elastic contact theory [116]. The constant ϵ varies with the indenter used. Equation (2.5) only takes into account the displacement of the surface due to elastic deformation, which is always a sinking-in of the surface. The piling-up phenomenon, which arises from the plastic behaviour of the material, cannot be considered by this model. Over-estimations of the extracted elastic modulus may arise, especially for materials with low strain hardening behaviours.

Another important source of error associated with these methods falls from the precision with which the contact stiffness can be measured. Indeed, this parameter is highly sensitive to the machine compliance, since the deformation of the specimen upon unloading is purely elastic and therefore small, when compared to the total depth. The deformation of the experimental setup can therefore decrease the measured value of S, and lead to underestimations of E_r.

2.4 Extraction of elasto-plastic properties by instrumented indentation

This section presents different methods using instrumented indentation to extract elasto-plastic constitutive parameters capable of estimating true stress-true strain curves for isotropic materials. They are separated into three categories: (i) empirical methods (Section 2.4.1), (ii) dimensional analysis methods (Section 2.4.2) and (iii) optimization methods (Section 2.4.3). A comparison of all three approaches is presented in Section 2.4.4

2.4.1 Empirical methods

Stress and strain fields generated by indentation are complex and triaxial. Tabor [120] attempted to simplify the analysis of indentation data by introducing the concepts of indentation stress, σ_{ind}, and indentation strain, ε_{ind}. These are effective values that represent the stress and strain fields by a single scalar. Empirical methods thus use empirically developed direct relationships between the indentation data and values of σ_{ind} and ε_{ind}, which together estimate the position of a point on the tensile curve of the studied material. No finite element simulations are necessary to apply these methods, making them simple and quick to use.

The average pressure applied to the specimen during the indentation test is defined by:

$$p_m = \frac{P}{A_c}. \tag{2.6}$$

Using Hill's slip line theory [69] and the Hubert-Mises plasticity criterion, Tabor [120] developed an analytical relationship between p_m and σ_{ind} for flat punch indentations. This relationship was developed for materials with a perfectly plastic behaviour and a fully de-

veloped plastic zone, but was later found to be valid for other indenter shapes and plastic behaviours. σ_{ind} is defined by:

$$\sigma_{ind} = \frac{p_m}{\Psi} = \frac{P}{A_c \Psi}, \tag{2.7}$$

where Ψ is a constant called the constraint factor determined empirically. Its value varies with different studies because it depends upon the materials used to obtain it [66, 115].

The indentation strain, ε_{ind}, is defined so its value is equivalent to the strain which generates a stress, σ_{ind}, on the tensile curve of the studied material. With indentation and tensile experiments or simulations, empirical relationships between the indenter geometry and ε_{ind} were found by different authors [2, 62, 120]. Details of specific methods developed for sharp and spherical indenters are given below.

Sharp indenters

Because of the geometrical similarity of sharp indenters, Tabor [120] found that for the same material and sharp indenter combination, the average pressure obtained during a test did not vary with indentation depth. It follows that σ_{ind} and ε_{ind} are also constant with indentation depth. Therefore, with empirical methods, sharp indenters can only lead to the extraction of a single point on the stress-strain curve. Thus, the number of inferred points on the tensile curve is limited to the number of available sharp indenters with varying geometries. Examples of ε_{ind} for commonly used indenters are 0.08 for the Vickers and Berkovich indenters and 0.22 for a cube-corner indenter.

Spherical indenters

Spherical indenters do not have the geometrical similarity property, which means that the values of σ_{ind} and ε_{ind} vary with indentation depth. This is a major advantage, since many points on the tensile curve can be found with a single indenter [94]. Instead of conducting many different indentation tests at different depths, the use of multiple load-unload cycles, where the load increases in each cycle, is used. As many (ε_{ind}, σ_{ind}) couples as the number of preformed cycles can be found from a single indentation curve.

For spherical indenters, σ_{ind} is still defined by equation (2.7). In this case, $A_c = \pi a^2$, where a is the contact radius of indentation. The physical significance of a is shown in Figure 2.4, as well as the influence of sink-in and pile-up phenomena on this parameter.

The ideal contact radius, a_{id}, can be computed based on the contact depth, h_c, given by

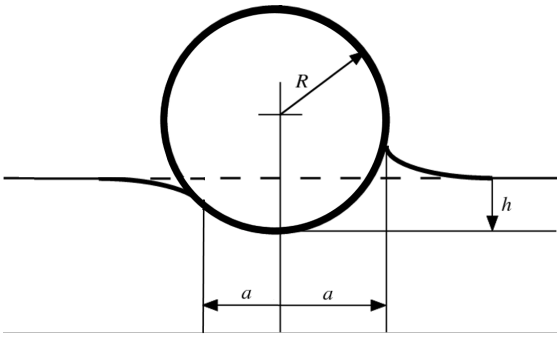

Figure 2.4 Illustration of spherical indentation parameters for empirical methods: the indenter radius, R, the indentation depth, h, and the contact radius, a, when sinking-in (left) or piling-up (right) occurs (adapted from [92]).

equation (2.5) and the indenter radius, R, by:

$$a_{id} = \sqrt{2Rh_c - h_c^2}. \tag{2.8}$$

This equation is based on the assumption of a perfect spherical geometry, as well as the absence of piling-up of the surface due to plastic deformation. The latter assumption follows from the definition of h_c (Eq. (2.5)). It was quickly found that the use of a_{id} in empirical methods led to significant errors because of these assumptions. A correlation between a, the real contact radius including pile-ups, and the hardening coefficient, n, of the studied material was observed by Matthews et al. [89].

A correction factor, c^2, was proposed as:

$$c^2 = \left(\frac{a}{a_{id}}\right)^2. \tag{2.9}$$

This dimensionless factor, c^2, is computed through different empirical relationships which are functions of n and were found by various authors. Since the hardening coefficient of the studied material is unknown, an iterative method must be used. An initial value for n is thus set and the $(\sigma_{ind},\ \varepsilon_{ind})$ couples forming a tensile curve determined by the empirical method can be used to update the value of n for the next iteration. This process is repeated until convergence of n and c^2.

Table 2.1 presents a summary of five different empirical methods using spherical indenters. It shows the definitions used for the contact radius, a, the constraint factor, Ψ, the correction factor, c^2, and the indentation strain, ε_{ind}. The four first methods shown, as developed by Ahn and Kwon [2], Tabor with Hill [68, 120], Habbab et al. [62] as well as Taljat et al. [122],

Table 2.1 Summary of five empirical methods using spherical indentation. The definitions of contact radius, a, constraint factor, Ψ, correction factor, c^2, and indentation strain, ε_{ind}, are shown. h_{max}, h_r, h_c and h_e are respectively the maximum, residual, contact and elastic indentation depths, E_r is the reduced modulus, P is the applied load, n is the material hardening coefficient and R is the indenter radius. FEA is short for finite element analysis.

Method	Radius of contact, a	Ψ	Pile-up correction factor, C^2	ε_{ind}
Ahn and Kwon [30]	From ideal contact area: $a_{id} = \sqrt{2Rh_c - h_c^2}$	From empirical results: $\psi = 3$	From FEA: $c^2 = \frac{5(2-n)}{2(4+n)}$	From veritcal displacement: $\varepsilon_{ind} = \frac{0.1}{\sqrt{1-\left(\frac{a}{R}\right)^2}}\frac{a}{R}$
Tabor with Hill [26, 35]				Tabor's definition of indentation strain : $\varepsilon_{ind} = \frac{0.2a}{R}$
Habbab et al. [31]			From FEA, considering the influence of indentation depth: $c^2 = \frac{5(2-n)}{2(4+n)}\sqrt{1.125\left(\frac{h_r}{h_{max}}\right)^3 + \left(\frac{h_e}{h_{max}}\right)^3}$	
Taljat et al. [36]		From empirical results: $\psi = 2.87$	From FEA: $c^2 = \frac{1}{4}(5 - 3n^{7/10})$	
Kalidindi et al. [27-42]	From Hertz theory: $a = \sqrt[3]{\frac{3PR^*}{4E_r}}$ With $R^* = \frac{9P^2}{16(h_{max}-h_r)^3E_r^2}$	From FEA: $\psi = 2.2$	N.A.	Modeling strain as of a cylinder in compression of radius a and height $2.4a$: $\varepsilon_{ind} = \frac{1}{1.3}\left(\frac{4h_t}{3\pi a^2} - \frac{\sigma_{ind}}{E_r}\right) + \frac{\sigma_{ind}}{2E_r}$

make use of the correction factor, c^2. Supplemental details can be found in the respective references and are not shown here for brevity. All these methods were presented with good experimental validations. However, they could perform well for materials similar to those used to create the empirical relationships, but may fail for materials that have different microstructures or tensile behaviours.

The last method shown in Table 2.1, developed by Kalidindi et al. [73,98–102], uses a different approach without the correction factor, c^2. They define the contact radius, a, with the Hertz equations for a sphere in contact with a plane. Since this plane curves while contact happens, the contact is no longer between a sphere and a flat surface. An effective indenter radius is then used which was found to give the best approximation of a. This method was validated with numerical indentation tests, but no experimental validation was presented.

2.4.2 Dimensional analysis

This second category of elasto-plastic properties extraction methods is the most commonly used in the literature. The approach is separated in the following steps:

1. Direct analysis : generation of indentation data for known elasto-plastic properties:
   (a) Assumption of a tensile model for the stress-strain curve (*e.g.* elastic-perfectly plastic [37], power law [41, 48, 95], bi-linear [104], etc.);
   (b) Development of dimensionless relationships between indentation parameters (C, h_{max}, S, h_r, etc.) and material elasto-plastic properties (E, σ_y, n, ν, etc.) with Buckingham's theorem;
   (c) Development of an instrumented indentation finite element model (FEM) and simulation of the indentation process for large quantity of elasto-plastic properties. The outputs of the FEM are the simulated indentation data of interest for the particular method.
   (d) Fitting of the indentation data, obtained by the FEM, as a function of elasto-plastic properties based on the dimensionless relationships developed in (b). A non-linear equation system is thus created for which the solution is the group of sought material properties as a function of indentation data.
2. Experimental indentation of the material to characterize and calculation of the necessary indentation data.
3. Inverse analysis: solving of the non-linear equation system with the experimental indentation data for the extraction of elasto-plastic properties.

An example of the process used for such methods is shown in Figure 2.5, where a relationship between the ratio $\frac{h_r}{h_{max}}$ and n, and the ratio $\frac{\sigma_y}{E_r}$, is developed.

A difficulty of this method is the complexity of the non-linear equation system to solve. To reduce the number of variables involved, the concept of representative strain, ε_r (not to be confused with indentation strain, ε_{ind}, used in empirical methods), was introduced. ε_r is defined as a strain value for which the relationship between the indentation curvature, C, and the reduced modulus, E_r, is independent of the hardening coefficient, n [48]. This can be visualized in Figure 2.6.

After the introduction of this parameter, various authors found different values for ε_r, even when using the same indenter (*e.g.* for a Vickers indenter: ε_r =0.034-0.042 [5], 0.0115 [75] and 0.025-0.095 [66]). These different findings demonstrate that a universal value of ε_r cannot be found. ε_r depends upon many parameters of the developed dimensional analysis methods as well as material properties of the studied materials [23, 82, 83]. Also, for spherical indenters, ε_r depends upon the maximum indentation depth because of the absence of geometrical similarity in the indenter shape [29]. For these reasons, many authors choose not to use such a representative strain in their dimensional analysis methods [34, 40, 41, 70, 106].

Limitations: assumption of a tensile model

A notable flaw of dimensional analysis inverse methods is the necessity to assume a pre-defined shape of the tensile curve (*e.g.*: power law [85, 137], bi-linear [104], presence of a Lüders plateau [106, 107]) to extract the elasto-plastic properties, whilst the actual shape of the true stress-true strain curve is unknown. The precision of the true stress-true strain curve obtained with such methods directly depends on the chosen hardening model's capacity to accurately fit the experimentally observed behaviour.

The most commonly used models for the extraction of elasto-plastic properties by indentation are power laws. However, there are different models used to describe power law true stress-true strain behaviour (*e.g.*: Ramberg-Osgood [92], Hollomon [85, 137], Swift [5]), for which the quality of the approximation of the tensile behaviour will vary for different materials. For instance, materials with high strain hardening behaviour will be badly represented by the Hollomon model. A method developed assuming one of these models would lead to results of different quality, depending on the studied materials. There are also materials having tensile curves which cannot be approximated by a power law, for instance, structural steels including a Lüders plateau. In such cases, the extracted true stress-true strain curve would carry significant errors, especially near the elastic limit.

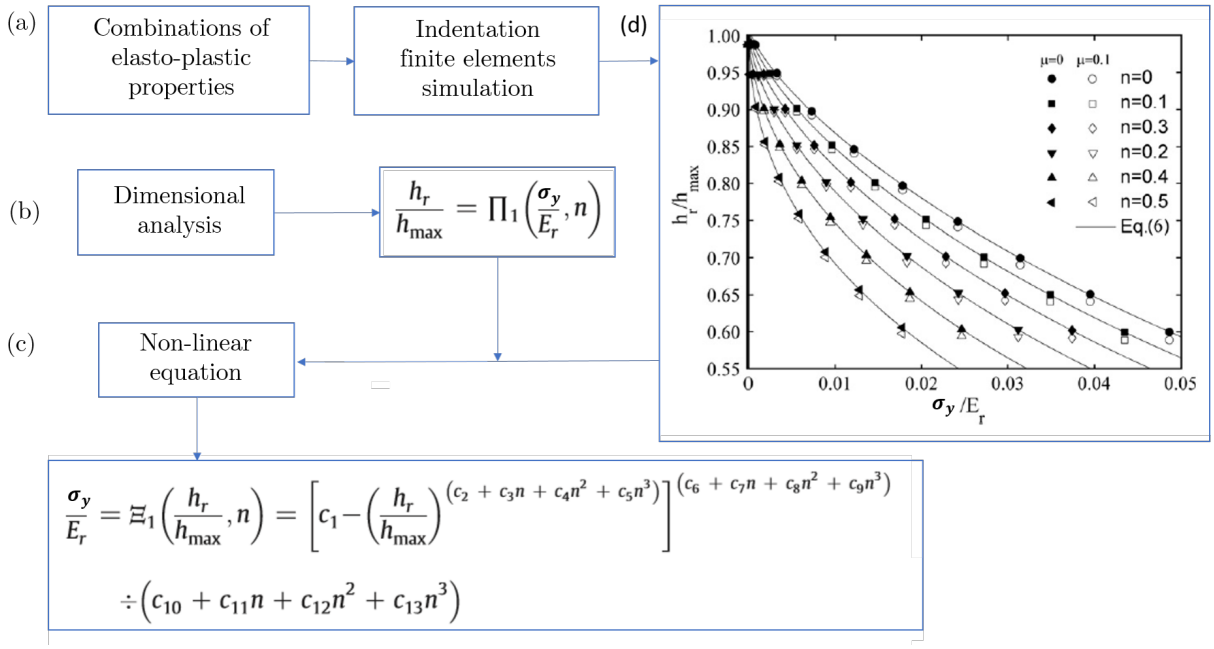

Figure 2.5 Flowchart displaying an example of application of a dimensional analysis method for elasto-plastic properties extraction by instrumented indentation: (a) simulations of indentation tests for many elasto-plastic properties combinations; (b) development of dimensionless relationships; (c) creation of the non-linear equation fitting the simulated data; (d) relationship between the indentation data and mechanical properties, including the effect of varying the friction coefficient. Graph taken from [110].

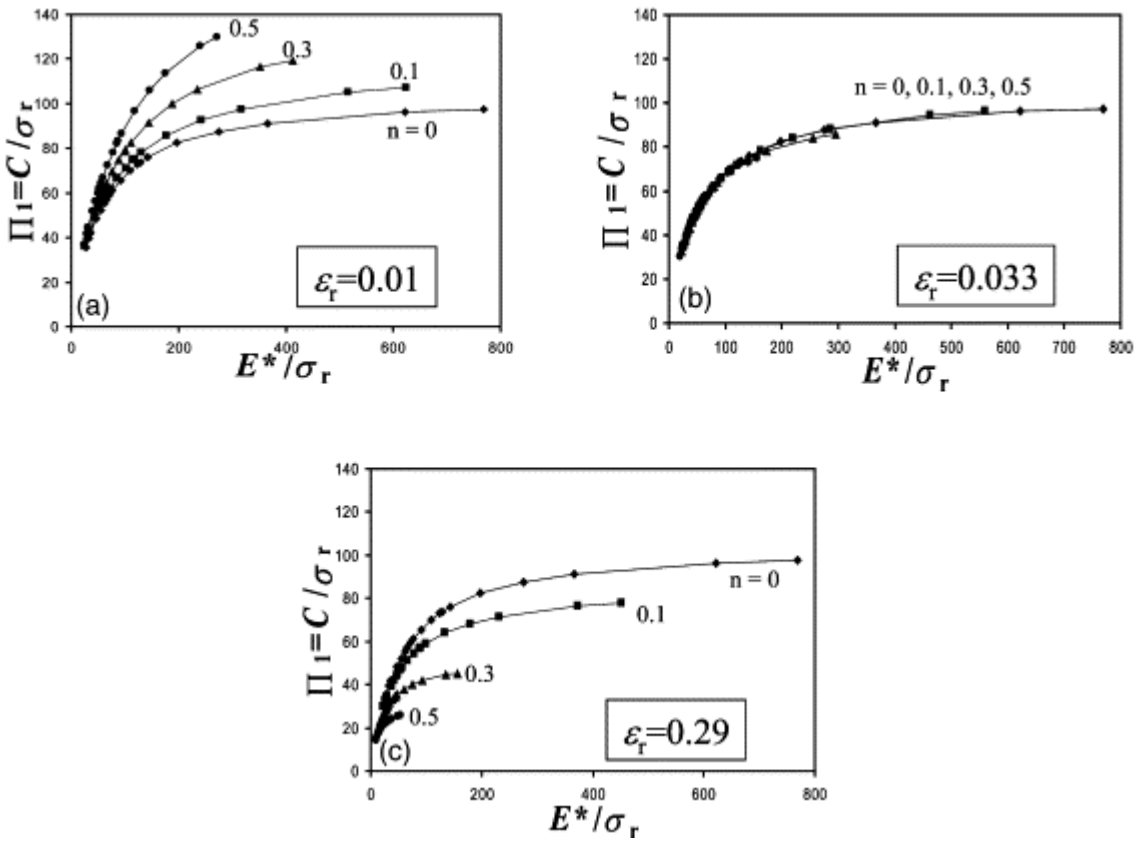

Figure 2.6 Dimensionless function Π_1 constructed using three different values of ε_r using a Vickers indenter. A value of $\varepsilon_r = 0.033$ gives the sought independence from the hardening coefficient. Taken from [48].

Limitations: uniqueness of the solution

Another issue with these inverse methods is the possible non-uniqueness of the solution caused by the reduced sensitivity of the indentation curve to certain material characteristics. It has been shown that there exists materials, called mystical materials, that have different tensile properties which yield indiscernible indentation curves [33, 37, 41, 42].

To improve the performance of these methods by reducing the risks of non-uniqueness, several approaches were used. First, the use of more than one sharp indenter with different half-angles, θ, yields indentation curves obtained with diverse strain distributions under the indenter, rendering the problem sensitive to a larger region of the tensile curve [75, 85]. The necessity to conduct more than one indentation however makes the extraction of very localized elasto-plastic properties difficult since the indents cannot be made in the exact same location. This can be problematic when studying a weld, for instance, since the properties constantly change within the heat affected zone (HAZ).

A second approach to improve the uniqueness of the solution is the use of a spherical indenter. Since the strain field under the indenter evolves with depth, an indentation with a spherical indenter is the equivalent of using many sharp indenters [51]. The use of a spherical indenter also leads to other advantages [28]:

- Indenter wear is slower than for pyramidal indenters as the spherical geometry is smoother;
- Indenter manufacturing is easier since no sharp edges are present;
- Finite element simulations converge better and contact detection is less problematic, when compared to sharp indenters;
- Finite element simulations can take advantage of the axisymmetrical geometry, leading to considerably faster calculation times.

When using a spherical indenter, it is imperative to apply a sufficient load to obtain a maximum depth, h_{max}, which is high enough with respect to the indenter radius, R [37, 82, 137]. Indeed, mystical materials will present indistinguishable indentation curves at low indentation depths, and will then separate if a higher indentation depth is applied. An example of this phenomenon is shown in Figure 2.7. This explains why better identification of elasto-plastic properties is achieved when using a higher h_{max}/R ratio.

Lu et al. [85] combined the use of a Berkovich and a spherical indenter. Their method led to a good precision of the extracted value for E ($< 1.7\%$), but the precision of the extracted σ_y and n were not significantly better than when using two sharp indenters (see Table 2.2).

Limitations: little to no experimental validation

Another weakness of many studies conducting the extraction of elasto-plastic properties with dimensional analysis is the lack of experimental validation. The validation of the method is the testing of its performance for known material properties. Most methods are validated through a numerical study, which uses indentation data generated by finite element simulations rather than experiments as the input to the inverse method. This eliminates the influence of modeling errors, which arise from the precision with which the model can represent the experimental indentation results, as well as experimental errors, on the obtained results. This creates a difficulty in the interpretation of the precision of the extracted properties.

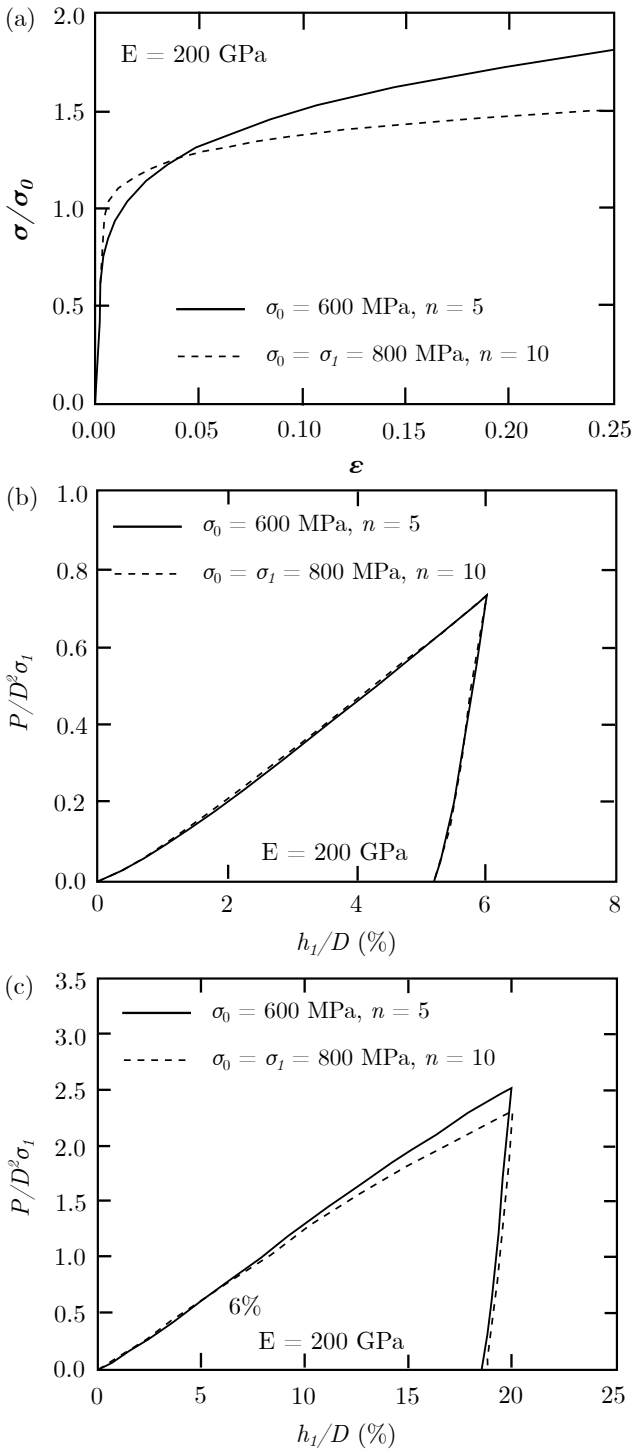

Figure 2.7 Example of the influence of the ratio of maximum indentation depth to indenter radius, h_{max}/R, on the indentation data of mystical materials: (a) tensile curves of the two mystical materials, (b) indentation data when h_{max}/D =0.06, and (c) indentation data when h_{max}/D =0.20. D is the indenter diameter, σ_0 is the yield stress and σ_1 is a constant. It can be observed that the indentation curves become separated as h/D increases, meaning that higher h/D values reduce the risk of non-uniqueness issues. Reproduced from [82].

Some authors conduct sensitivity studies of their results by applying random perturbations to the numerical indentation data, to simulate experimental data. The errors on extracted properties are then increased by much more than the value of the perturbation that was applied to the numerical data [44]. For example, Heinrich et al. [65] applied an error of 5% to P_{max}, for one of the two sharp indenter used in their study and saw the error on the extracted σ_y rise from 0.16% to 11.05%, and that of E, from 3.53% to 66.36%. Hyun et al. [70] observed similar effects, when the errors on extracted properties more than doubled after the application of a random $\pm 2\%$ perturbation of the indentation data. This shows an instability of the methods studied and their results might not be reliable when applied to experimental indentation data.

To demonstrate this, Guelorget and François [60] tested the accuracy of different dimensional analysis methods presented in the literature that only presented numerical validations. They reproduced five methods [29–31, 95, 137] and extracted the elasto-plastic plastic properties of a copper, an aluminum and a 316L steel, using experimental indentation data. Out of these five methods, four presented errors that were much higher than those reported for numerical indentation data. The worst increase in error happened with the method developed by Zhao et al. [137], which used a single spherical indenter. In the original study, the precision obtained with numerical indentation data was better than 1% for the identified values of E, σ_y and n. However, the application of this method to experimental data led to extracted values $\sigma_y = 1034$ MPa et $E = 108$ GPa, which are far from the expected values for this steel ($\sigma_y \approx 290$ MPa and $E \approx 200$ GPa). Similar deterioration of the results were obtained when testing with copper and aluminum. The other three methods that presented significantly lower accuracy with experimental data were those of Ogasawara et al. [95] as well as two methods by Cao et al. [30,31]. These applications to experimental data show that validations done solely on numerical data must be interpreted with caution when evaluating the performance of a method. The fifth method tested by Guelorget and François, another one by Cao et al. [29], identified material parameters with reasonable precision. The errors for σ_y were lower than 20%, for all three tested materials. The errors for n were between 26% and 38%.

Synthesis

The reliability and performance of the dimensional analysis methods vary greatly depending on the choices made by the authors regarding the definition of non-linear equation system: the indentation parameters used, the use of ε_r and its value(s), the number and geometry of indenter(s), as well as the hypothesis made for the definition of the FEM.

Table 2.2 compares the accuracy of several numerically validated methods presented in the literature while specifying their respective characteristics. All these examples suppose a Hollomon power-law hardening model. It can be noticed that not all methods aim to extract all three elasto-plastic parameters of a Hollomon power law (E_r or E, σ_y and n). The errors of the extracted E_r or E are small and improve with the use of more than one indenter. This improvement is also present for the precision of σ_y, though the errors on this parameter are higher. The worst errors appear in the extraction of the hardening coefficient, n. This can be explained by a very small sensitivity of this parameter to the indentation curve. It was shown, however, that the residual imprint of indentation carries a much higher sensitivity to n [6,14,15,17,34,91,121]. The use of data on the residual imprint is very hard to incorporate in the dimensionless functions since no parameter can represent the full topography of the residual imprint. It is therefore not really used for dimensionless analysis methods. Casals and Alcalà [34] used the parameter $\alpha = \frac{A_p(h_c)}{A_p(h_{max})}$ (Figure 2.2), but instead of measuring its value directly from the residual imprint, two values of α were estimated from two material properties sets that generated the same indentation curve, and the general aspect of the imprint was used to choose between the two values.

Table 2.3 shows the same information as the previous table, but for experimentally validated methods. General increases in the errors on E and σ_y are observed, showing again the importance of conducting an experimental validation of the developed methods.

Table 2.2 Comparison of the accuracy of several dimensional analysis methods assuming a power law presented in the literature and validated with numerical indentation data. Indenters B, C and S signify Berkovich, conical and spherical, respectively. Indentation parameters W_t, W_e and W_p are the total, elastic and plastic indentation works, respectively.

Authors	Indenter(s)	ε_r	Indentation parameters	ΔE_r or ΔE	$\Delta\sigma_y$	Δn
Ogasawara et al. [95]	B	0.0115	C, h_{max}, W_t, S	-	-	3.3-20%
Casals and Alcalà [34]	B	-	C, h_{max}, h_r, h_e	5.88%	0.22%	22.2%
Hyun et al. [70]	C ($\theta = 70.3°$), C ($\theta = 45°$)	-	$C_{(\theta=70.3°)}$, $C_{(\theta=45°)}$, $S_{(\theta=70.3°)}$	$< 4\%$	<5 %	$< 5\%$
Heinrich et al. [65]	C ($\theta = 70.3°$), C ($\theta = 60°$)	-	$P_{max(\theta=70.3°)}$, $P_{max(\theta=60°)}$ $S_{(\theta=70.3°)}$	0.01-1.3%	0.07-17.04%	20-97.3%
Liu et al. [85]	B, S	-	$C_{(B)}$, $h_{max(S)}$, $W_{e(S)}$,$W_{e(B)}$, $W_{t(S)}$, $W_{t(B)}$	0.1-1.7%	0.3-9.3%	1.6-22.5%
Cao and Lu [29]	S with $\frac{h_{max(1)}}{R} = 0.01$, $\frac{h_{max(2)}}{R} = 0.06$	Varies with h_{max}	$P_{max(1)}$, $P_{max(2)}$	-	0.48-10.7%	0.67-27.8%
Zhao et al. [137]	S with $\frac{h_{max(1)}}{R} = 0.13$, $\frac{h_{max(2)}}{R} = 0.3$	0.0374, 0.0674	$C_{(1)}$, $C_{(2)}$, $S_{(2)}$, $h_{max(1)}$, $h_{max(2)}$	0.4-1.12%	0.8-9.33%	3.7-22.5%

Table 2.3 Comparison of the accuracy of several dimensional analysis methods assuming a power law presented in the literature and validated with experimental indentation data. Indenters B, C and S signify Berkovich, conical and spherical, respectively. Indentation parameters W_t, W_e and W_p are the total, elastic and plastic indentation works, respectively.

Authors	Indenter(s)	ε_r	Indentation parameters	ΔE_r or ΔE	$\Delta\sigma_y$	Δn
Dao et al. [48]	B	0.033	C, h_r, h_{max}, $\frac{W_p}{W_t}$, S	0.1-1.63%	2.36-6.51%	12.3-30%
Chollacoop et al. [44]	B, C ($\theta = 60°$)	0.033, 0.057	$C_{(B)}$, $C_{(\theta=60°)}$, $h_{r(B)}$, $h_{max(B)}$, $S_{(B)}$	0.1-8.03%	10-16.12%	-

2.4.3 Inverse method by numerical optimization

The last approach often exploited in the literature uses optimization algorithms to find the tensile properties which minimize the difference between indentation data obtained from experiments and that obtained by finite element simulations for a given material [15, 17, 28, 129]. The development of such methods is separated in the following steps:

1. Assumption of a tensile model for the stress-strain curve;
2. Development of an instrumented indentation FEM;
3. Development of the objective function to be optimized which characterizes the difference between indentation data obtained from experiments and simulation as a function of tensile properties;
4. Development of an optimization algorithm, or choice of an existing one, applicable to the obtained optimization problem.

Once the method is developed, its application for the extraction of elasto-plastic properties follows the flow-chart shown in Figure 2.8.

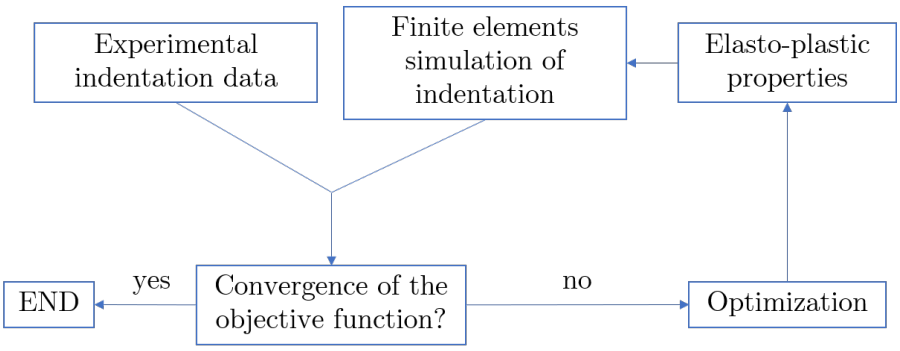

Figure 2.8 Flow-chart describing the inverse method by numerical optimization for the extraction of elasto-plastic properties by instrumented indentation.

Different types of optimization algorithms can be used with this approach and they are discussed in Section 2.6

Limitations: assumption of a tensile model

Just like dimensional analysis methods, optimization methods presented in the literature mostly suppose a hardening model, often a power-law, to extract the elasto-plastic properties.

However, an inverse method which avoided such an assumption was developed by Bouzakis et al. [20–22] for a Berkovich indenter. In their approach, the indentation curve was divided into small increments, for each of which a point was found on the tensile curve by optimizing the slope $\mathrm{d}\sigma/\mathrm{d}\varepsilon$ after the previous point computed. No application of the method to materials with known properties was presented by the authors to validate its performance, making it difficult to evaluate the reliability and robustness of this method. Also, to use the residual imprint in such an approach, one would need to indent up to a certain depth, unload, take a topography measurement, and repeat. This process would represent a great experimental challenge because of how difficult it would be to realign the indenter in the exact same position at each cycle. The lack of this supplementary experimental information, particularly because a sharp indenter was used, means that the method could suffer from non-uniqueness issues [37]. Except for that of Bouzakis et al., no optimization method which does not suppose a hardening model was found in the literature.

Jeong et al. [72] applied Bouzakis et al.'s incremental method and were able to extract the different tensile curves for the ferrite, bainite and martensite phases of a steel. With multi-scale modeling using these extracted elasto-plastic properties, the macroscopic tensile curve of the steel was obtained and compared to that obtained experimentally. A maximum difference of 9% was observed, showing the potential of this approach which does not rely on any assumed constitutive theory for the mechanical response.

Limitations: uniqueness of the solution

Non-uniqueness issues are also a limitation of numerical optimization methods, causing increased errors because of a lack of sensitivity to material parameters. The hardening coefficient, n, is the parameter most affected by non-uniqueness issues. For instance, Kang et al. [76] obtained an extraction error of 68 % on n, when applying their method which used only the indentation curve obtained from a sharp indenter. Just as in the case of dimensional analysis methods, authors have shown that the use of more than one sharp indenter or the use of a spherical indenter improves the quality of the extracted elasto-plastic properties [14, 28, 51].

Other authors use the topography of the residual imprint of indentation as supplementary indentation data to the method. Bolzon et al. [17] developed an objective function which takes into account both the indentation curve and the position of a number of points on the residual imprint topography. They have shown that the accuracy with which power-law hardening parameters can be extracted is significantly better when considering the residual imprint (see Table 2.4). This was then supported by Meng et al. [91].

More recently, a new trend appeared in optimization-based methods, which is the use of exclusively the residual imprint topography as indentation data in the objective function [27, 127,128]. This has only been done with spherical indenters. In these methods, the indentation curve is completely ignored, which greatly simplified the data acquisition during the test. Indeed, it is difficult (some say impossible) to obtain a precision better than 1% on the depth measurement during an indentation test [27]. This is mainly due to the deformation of the testing apparatus during the test, which is measured by the displacement sensor additionally to the actual penetration depth. The extent of this effect depends on the machine compliance, C_f, a parameter which is challenging to estimate (see Section 2.2.1).

On the other hand, the measurement of the maximum load applied during the indentation test is much easier to conduct owing to the many available high-quality load cells [27]. Hence, when using the maximum applied load as the boundary condition in the finite element simulation of indentation, the experimental and numerical residual imprints can be compared without the necessity to measure the displacement during the test. The results obtained when using this approach are similar to when the indentation curve is used in combination to the residual imprint. They vary with the ratio of maximum depth to indenter ratio, h_{max}/R, just as when the indentation curve is used. Wang et al. [127, 128] conducted indentation tests at two loads, 612 N and 1838 N, using a spherical indenter with R =1.25 mm. The corresponding h_{max}/R ratios obtained were 0.0415 and 0.123, respectively. They found that the optimization method was much more stable with the high load and thus higher h_{max}/R ratio. The use of lower load yielded different results depending on the used starting point for the optimization. The best accuracy was however obtained when both imprint topographies were used to identify the sought elasto-plastic parameters (see Table 2.5). Figure 2.9, taken from this study, shows the imprints simulated for three different materials, which are indistinguishable under the first load of 612 N, but separate under the second load of 1 838 N.

Campbell et al. [27] studied the average strain generated by an indentation test through finite element analysis and concluded that a minimum value of 0.25 for h_{max}/R is needed to maximize the sensitivity of the indentation process to the tensile curve of the studied material. They also found that this value can increase to 0.4 in the case of materials with a high strain hardening behaviour.

Limitations: little to no experimental validation

Numerical optimization methods are often only validated with numerical indentation data. Since the same FEM is used to generate these target data as well as in the optimization, all experimental and modeling errors are neglected and the optimization algorithm will con-

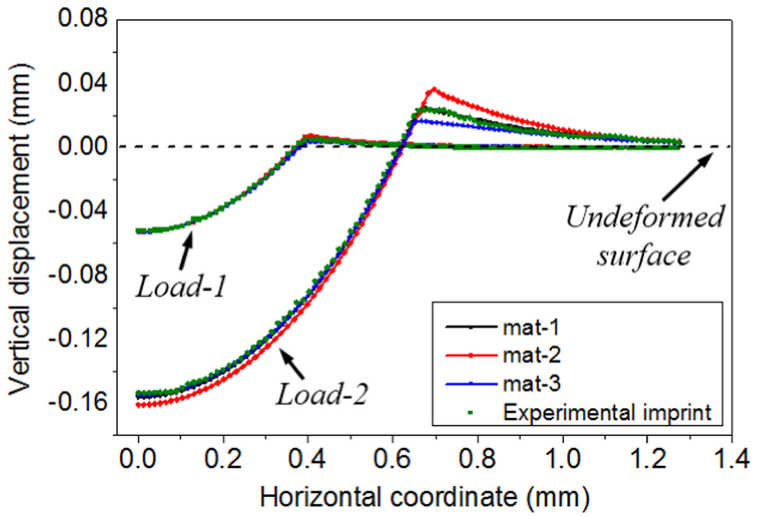

Figure 2.9 Effect of ratio h_{max}/R on the distinguishability of simulated indentation residual imprints for three materials. Load 1 corresponds to 612 N, leading to $h_{max}/R = 0.0415$ and load 2 corresponds to 1838 N, leading to $h_{max}/R = 0.123$. With a higher load for the same indenter, the pile-up heights become different. Taken from [128].

sequently lead the objective function to a lower value and at a better convergence rate. It is difficult to predict how the method would perform for experimental data and validations under these conditions would greatly improve the quality of such studies.

Synthesis

Tables 2.4 and 2.5 present the accuracy of extracted elasto-plastic parameters obtained by different optimization-based methods when a numerical or experimental validation is presented, respectively. The methods reported in these tables all assumed a power-law tensile model.

Table 2.4 Comparison of the accuracy of several numerical optimization methods presented in the literature assuming a power law and validated with numerical indentation data. Indenters B and V signify Berkovich and Vickers, respectively.

Authors	Indenter	Optimization algorithm	Indentation data used	ΔE_r or ΔE	$\Delta\sigma_y$	Δn
Meng et al. [91]	B	Shape collector	Curve and imprint	-	0-2.84%	0.01-2.1%
Bolzon et al. [17]	V	Non-linear least squares	Curve and imprint	<1%	<1%	<1%

Table 2.5 Comparison of the accuracy of several numerical optimization methods presented in the literature assuming a power law and validated with experimental indentation data. Indenters B and S signify Berkovich and spherical, respectively.

Authors	Indenter	Optimization algorithm	Indentation data used	ΔE_r or ΔE	$\Delta\sigma_y$	Δn
Kang et al. [76]	B	Non-linear least squares	Curve	6.7-7%	1.05-2.7%	67.2-69.1%
Wang et al. [128]	S	Internal point	Imprint	7%	0.65%	2.89%
Wang and Wu [127]	S	Internal point	Imprint	-	7.99%	4.16%

2.4.4 Comparison of the three approaches with regard to potential applications to welds

To characterize the elasto-plastic behaviour of hydraulic turbines and their welded joints (base metal, HAZ, weld metal), a method must be developed which enables the extraction of the local tensile curves. This method must be versatile enough to be efficient through the heterogeneous microstructure of a weld, while remaining reliable enough to ensure the accuracy of the extracted tensile curves. Instrumented indentation is an experimental technique which offers many advantages to carry out this task, particularly the inherent simplicity of the indentation test and its non-destructive nature. From the three approaches described in Section 2.4, a choice must be made as to which approach is most suitable for the objective of this research work.

Owing to the formation of residual stresses in welds during cooling, the developed method must also be applicable in the presence of residual stresses. These can be measured by another non destructive technique like XRD and then be incorporated into the method as known variables. It is imperative to consider their presence since they have non-negligible effects on the indentation experimental parameters and could therefore alter the results (see Section 2.7). Of the three approaches presented, the optimization based and the dimensional analysis based methods can include residual stresses in their analysis since these can be added to the finite element models. However, the empirical methods have not been developed to include the effects of residual stresses.

Table 2.6 lists the advantages and limitations of the different categories of methods. When comparing the methods, it can first be observed that those who do not use any finite element simulations are simpler to implement and do not require the assumption of a pre-defined

tensile model. However, the precision of the obtained results vary with the studied material due to the empirical nature of these methods. Adding the fact that empirical methods cannot account for residual stresses, it is concluded that a method based on dimensional analysis or numerical optimization would be better suited for the application to a welded joint.

To make a choice between a dimensional analysis or numerical optimization approach, these two families of methods are compared on a deeper level as follows. The use of material parameters which avoid the assumption of a pre-defined hardening model would be very challenging using a dimensional analysis approach. Indeed, this would require an increase in the number of variables and add complexity to the definition of the dimensionless functions. Also, since all necessary finite elements simulations are conducted at once, with specific conditions, the parameters like indenter geometry as well as the load and depth ranges are fixed during the definition of the dimensionless equations. A change in these parameters thus leads to the necessity to create a new method with new dimensionless equations which requires a great number of finite elements simulations. For example, after a certain number of experimental indentation tests, the indenter will wear and its geometry will change and the dimensionless functions previously developed will not be applicable. These changes are easier to make with numerical optimization based methods because only the finite element model needs to be adapted when the indentation experimental setup is modified. The method can directly be used without the need to develop new dimensionless equations. Optimization methods also offer more flexibility regarding the variables being extracted, which makes it easier not to assume a pre-defined tensile model. An good example of this is the incremental method developed by Bouzakis et al [21].

As mentioned in Section 2.4.2, the level of piling-up or sinking-in of the material around the indenter carries sensitivity to the hardening behaviour of materials. Another advantage of numerical optimization based methods, when compared to dimensional analysis methods, is that the topography of the residual imprint can be incorporated in the objective function to be optimized. Including the entirety of the residual imprint geometry in a small number of parameters to be used in the development of dimensionless functions would be a great challenge. Some authors used the parameter α, which is the ratio of the real contact area to the projected contact area at the maximum depth. However, different imprints could lead to the same value of α since this parameter does not contain information regarding the full imprint.

Since an optimization-based method can be adapted to avoid the use of a hardening model, offer more flexibility for experimental set-up changes, and can simply include the whole residual imprint, such an approach is best suited to the application sought in this work, *i.e.*,

Table 2.6 Principal advantages, disadvantages and limitations of methods to extract elasto-plastic properties by instrumented indentation based on dimensional analysis, numerical optimization and spherical or sharp indentation empirical methods.

Method	Advantages	Disadvantages and limitations
Dimensional analysis	• Finite element simulations only necessary to develop the dimensionless relationships; • Possibility of taking residual stresses into account.	• Necessary assumption of a pre-defined tensile model; • Necessary development of new dimensionless functions for any change (indenter change or wear, tensile model, load or depth range, residual stresses); • Non-uniqueness issues if not enough indentation parameters are used; • Large volume of simulations necessary *a priori*.
Numerical optimization	• Possibility of extracting the tensile curve without a pre-defined hardening model; • Possibility of taking residual stresses into account; • Possibility of incorporating information regarding the full residual imprint topography into the objective function.	• Numerous finite elements simulations needed for every indentation analyzed; • Non-uniqueness issues if not enough indentation parameters are used.
Spherical indentation empirical methods	• No assumption of a pre-defined tensile model; • No finite element simulations needed to apply the method.	• Result quality depends on studied material; • Necessary load-unload indentation tests; • No possibility to take residual stresses into account.
Sharp indentation empirical methods	• No assumption of a pre-defined tensile model; • No finite element simulations needed to apply the method.	• No possibility to extract elastic properties; • No possibility to take residual stresses into account. • Several indenters with different geometries needed to obtain a significant amount of points on the tensile curve.

the local characterization of welded joints.

To further prevent non-uniqueness issues, the use of several indenters or of a spherical indenter is a solution to consider. Since local tensile curves are sought, the use of more than one indenter, is not suited. The distance required between two indents (a minimum of three times the indenter diagonal or diameter [56]) can be significant, especially for soft materials, and the material behaviour could vary between two adjacent points. A spherical indenter offers an improved sensitivity to the tensile properties while only requiring a single indentation.

From all the previous considerations, the methodology developed in this work is thus an inverse method for spherical indentation based on numerical optimization which does not assume a pre-defined hardening model and uses the residual imprint topography as supplementary experimental information.

2.5 Finite elements modeling of instrumented indentation

Finite element modeling of instrumented indentation tests is central to numerical optimization methods. It is thus imperative to understand the different aspects of the approaches that have been presented in the literature and to compare them. The following section presents different approaches used in indentation modeling regarding the geometry, boundary conditions, meshing, material behaviour, friction and size effects.

2.5.1 Geometry

The geometry modeled in instrumented indentation simulations is separated into two parts: the specimen and the indenter. Regarding the specimen, the majority of authors choose a cylindrical shape [6, 81, 93] or square-based prisms [84, 114, 134]. The size of the specimen in radius or length must be sufficient to behave as a semi-infinite solid. The thickness of the specimen must also be large enough to not influence the indentation results obtained from the model. These geometries simulate the entirety of the specimen, but it is possible to model only a fraction of this geometry by taking advantage of different indenter and material symmetry [63, 119]. For example, only 1/8 the of the specimen needs to be modeled if using a Vickers indenter with an isotropic material, substantially reducing computation time.

Spherical indenters are generally incorporated into axisymmetrical models as half-spheres, usually using the theoretical radius of the indenter as provided by the manufacturer [121,128]. Other authors have shown however that the actual geometry of a spherical indenter can be significantly different from that specified by the manufacturer and choose to directly measure the geometry by profilometry or atomic force microscopy [46, 50, 124] with the objective of

improving the accuracy of the finite element model.

2.5.2 Boundary conditions

The boundary conditions applied to instrumented indentation finite element models developed in the literature are restrictions to the movement of the nodes at the bottom of the specimen. These are fixed vertically but can move freely in the radial direction [14, 20, 78]. The outer nodes of the specimen are not constrained to avoid increasing the rigidity of the specimen.

2.5.3 Meshing

The meshing approaches are different for the indenter and the specimen. For the indenter, a commonly used assumption is that it can be modeled as a perfectly rigid surface since its rigidity is higher than that of the specimen. This reduces the number of degrees of freedom in the model and improves computation times. For spherical indenters however, Dean et al. [51] recommend taking into account the elastic deformation of the indenter because the lateral deformation caused by the Poisson effect can affect the shape of the residual imprint.

In axisymmetrical models, the specimens are usually modeled using four-node bi-linear elements [33, 72] or eight-node quadratic elements [63, 85]. However, Lee et al. [81] showed that for their model, the axisymmetrical eight-node elements (specifically ABAQUS software CAX8 elements) led to discontinuities in the values of strain evaluated in their central node. They concluded that four-node bi-linear elements (specifically ABAQUS CAX4 elements) gave better results for simulating the indentation process. In 3D models, the most commonly used elements are three-linear eight-node isoparametric hexahedrons [5, 73, 92]. Some authors opted for 20-node hexahedrons, C3D20 elements in the software ABAQUS [64, 118].

The size of the elements is a parameter which needs to be fixed with precaution in the contact region and in its peripheral region. The mesh must be fine enough to enable an efficient contact detection as well as a precise description of the generated stress and strain fields in this region [87]. Since numerical indentation studies are conducted within large ranges of maximum depths and material properties, no general rule exists as to the fineness of the mesh which leads to optimal results. Convergence studies are necessary and most authors choose to compare the value of reaction force obtained at maximum indentation depth for an increasingly fine mesh [6]. Other authors have used the maximum pile-up height in the residual imprint as the parameter of interest for the mesh convergence study [81]. A compromise is then often necessary between accuracy and computation time.

A strategy to reduce the computation time, that is always used in the specimen and in the indenter, if it is meshed, is to gradually increase the size of the elements as moving away from the contact region. A convergence study of the size of the region where the elements are most refined is therefore also necessary to ensure reliable results.

2.5.4 Material behaviour and yield criteria

Many indentation studies consider macroscopic material behaviour and thus model homogeneous and isotropic materials through the input of the uni-axial tensile curve. Classical plasticity with associated flow rule is then implemented or used within commercially available softwares. The yield criterion used is usually Von-Mises', except for studies which consider anisotropic materials and therefore apply Hill's yield criterion [6, 15, 39].

Different hardening models are used to define material behaviour in the literature. Isotropic hardening is used since it is assumed that no plasticity occurs during unloading. Some authors use elastic-perfectly plastic behaviour [22, 25, 37] or bi-linear behaviour [104]. However, the vast majority of studies use a power law type tensile model such as those developed by Hollomon [24, 65, 78], Ludwik [46], Swift [5, 71] or Ramberg-Osgood [92]. Another type of tensile model was developed by the group of Pham and Kim [106, 107]. Its particularity was that it included a Lüders plateau, which is characteristic of structural steels. The accuracy of these tensile models depends strongly on their respective capacity to fit experimental tensile data. This will change for different material-tensile model combinations.

The new method which is developed in this work does not use a hardening model. To compare its performance with methods assuming a hardening model, two existing models are investigated: those developed by Hollomon and Ramberg-Osgood.

Both models rely on a separation of elastic and elasto-plastic strains as per:

$$\varepsilon = \varepsilon_{el} + \varepsilon_p, \tag{2.10}$$

where ε_{el} and ε_p are the elastic and plastic parts of the total strain, ε, respectively. For both models, ε_{el} is defined with Hooke's law:

$$\varepsilon_{el} = \frac{\sigma}{E}, \tag{2.11}$$

where E is the elastic modulus and σ is the applied stress. For the Hollomon model, the

stress in the elastic-plastic region of the tensile curve is defined by:

$$\sigma = \sigma_y \left(1 + \frac{E}{\sigma_y}\varepsilon_p\right)^n, \tag{2.12}$$

where σ_y is the yield stress and n is the hardening coefficient.

The plastic behaviour following the Ramberg-Osgood model is described by:

$$\sigma = \sigma_y + K\varepsilon_p^n, \tag{2.13}$$

where K is a plasticity constant.

2.5.5 Contact and friction

The contact algorithm used, which prevents the interpenetration of the indenter and specimen in contact, is either the penalty method [34, 88] or the augmented Lagrangian method [5, 6], depending on which yielded the best convergence in the specific models developed.

Being faced with a contact problem, it is imperative to determine the effects of friction between the indenter and the specimen on the simulated indentation results. Many authors decide to neglect friction in their model [14,21]. The validity of the assumption depends upon the studied material, the indenter used, as well as the indentation data of interest. When friction is included in the models, it is done by using the classical Coulomb law [15, 95].

Bucaille et al. [24] showed that when using conical indenters with high half-angles, θ =60° and θ =70.3°, the increase of the friction coefficient, μ, from 0 to 0.3 led to a maximum increase of 3% in the load of the indentation curve. For indenters with smaller half-angles (θ <50°), this difference rises to 20%. The authors thus concluded that neglecting friction was a valid assumption for indenters with θ >60°, if only the indentation curve is used. This was confirmed by other studies [6, 63, 113].

For spherical indenters, studies showed that the effects of friction on the indentation curve were more important in cases when the ratio $\frac{h_{max}}{R}$ was over 0.08 [29, 32, 82]. The extent of the friction effects thus depend upon the applied indentation depth for spherical indenters. Frictionless contact can thus be assumed for $\frac{h_{max}}{R}$ <0.08, if only the indentation curve is considered [32].

The effect of friction is much more significant when studying the topography of the indentation residual imprint [24,88,121]. Indeed, friction adds a resistance to the upwards movement of the material on the surface of the indenter. This therefore promotes the sinking-in of the

surface and creates an obstacle to the piling-up phenomenon. Mata and Alcala [88] studied the effect of friction on simulated residual imprints obtained with sharp indenters. They observed an increase of up to 20% in the size of the plastic strain field generated by the indentation process when increasing μ from 0 to 0.2. The characteristics of the plastic strain field have a significant effect on the sinking-in or piling-up of the surface. When considering the residual imprint topography in an indentation study, with any indenter, it is imperative not to neglect the presence of friction in finite element modeling.

The exact value of the friction coefficient, μ, between the indenter and the surface is not known and is challenging to measure experimentally. Bucaille et al. [24] determined that the sensitivity of the indentation simulated results to the value of μ were very important between 0 and 0.1, moderate between 0.1 and 0.2 and then saturated. Heinrich et al. [65] then described similar effects, but found the saturation to appear after a friction coefficient value of 0.3. Most studies therefore choose a value of μ between 0.15 and 0.2 to model friction during the indentation process [63, 88, 95].

2.6 Numerical optimization

Since the methodology proposed in this thesis is based on an optimization problem, this section presents relevant background information on numerical optimization. In general, such a problem can be cast as:

$$\underset{\mathbf{X}}{\arg\min} \quad f(\mathbf{X}) \tag{2.14a}$$

$$\text{subjected to} \quad c_k(\mathbf{X}) \leq 0, \ \forall \ k \tag{2.14b}$$

where $\mathbf{X}$ is the variable vector, $f(\mathbf{X})$ is the objective function, and $c_k(\mathbf{X})$ are the different constraints of the problem. The constraints are defined by inequalities: if $c_k(\mathbf{X}) \leq 0$, then constraint k is respected and variables $\mathbf{X}$ that satisfy all constraints form an acceptable solution candidate.

The problem studied in this work is a complex blackbox optimization problem [10], *i.e.*, a problem in which the objective function cannot be analytically derived. The objective function depends on a finite element simulation. This prohibits the use of derivative based optimization algorithms. Even though numerical derivatives could be computed, this would be prohibitive due to the time required to perform this calculation. Also, since the optimization problem is constrained and local minima might exist, the numerical derivatives may lead the optimization to such a local minimum. A blackbox optimization approach is thus

preferred to solve the problem.

2.6.1 Optimization algorithm

Different types of optimization algorithms have been used to solve blackbox optimization problems aiming to estimate the material true stress-true strain curve from indentation tests. Trust region algorithms [14, 15, 17, 76], well known in the field of non-linear optimization, are the most commonly used. Others include the interior-point [127, 128] and the Nelder-Mead simplex [27, 28, 35] algorithms. Even though these algorithms may use strategies to escape local minima, it was shown that there exist situations where these strategies can fail and the algorithm still converges to a local minimum [10]. These algorithms are not designed to handle optimization constraints.

The algorithm used in this work is the Mesh-Adaptive-Direct-Search algorithm [8] using orthogonal directions (OrthoMADS) [1]. This algorithm is available through the software NOMAD, version 3.9.1 was used with the Matlab interface [1, 10, 11, 80]. The choice of this algorithm is justified by its aptitude to escape of local minima and its high performance even in the presence of highly constrained problems. To the knowledge of the authors, direct-search algorithms have not been applied to indentation inverse problems [3].

Each iteration, associated with an iteration number, i, of this algorithm is divided into a search step and a poll step. For both of these steps, the trial points of the objective function must be located on a discretisation of the variable space called the *mesh*. The fineness of the mesh varies as iterations are completed, based on the mesh size parameter, δ_i.

The search step used in this work is an adaptation of the Nelder-Mead algorithm where the vertices of the simplex are rounded to the mesh and the ordering of the trial points is also adapted to account for variable constraints [12]. When the search step is successful, *i.e.*, when a new solution is found, the mesh becomes coarser, with the aim of escaping local minima.

If the search step fails, then the poll step serves to explore the variable space more locally. The poll step uses a direct search approach which determines trial points on the mesh inside a frame which limits the region of the variable space sampled. The more points on the mesh are present inside the frame, the more available sampling directions are possible. The frame is generated using the frame size parameter, Δ_i, which also varies along with δ_i. In this step, both parameters can increase, in the case of a success, or decrease, in the alternative. Upon unsuccessful poll evaluations, δ_i decreases faster than Δ_i, which ultimately creates a dense set of directions from which the algorithm can generate the sample points. The poll

step enables the convergence of the algorithm, which happens when the frame and mesh size become theoretically infinitely small. In reality, a chosen minimum limit of these sizes defines the convergence of the algorithm, unless another criterion is set (*e.g.*: a tolerance on the objective function or a maximum number of function evaluations).

2.6.2 Handling of constraints

The MADS algorithm is well equipped to deal with constraints. Two types of constraints exist: non-relaxable and relaxable [10]. When a non-relaxable constraint is violated, the objective function $f(\mathbf{X})$ cannot be evaluated from the variables. For example, an error could result from the finite element model and therefore no $f(\mathbf{X})$ value can be obtained. These constraints are dealt with by the use of the extreme barrier algorithm, which simply gives a value of infinity to $f(\mathbf{X})$ when the constraint is violated. This creates jumps in $f(\mathbf{X})$ and leads to additional difficulties for the algorithm to navigate the variable space.

On the other hand, when a relaxable constraint is violated, $f(\mathbf{X})$ can still be evaluated, but the set of variables cannot be the optimal solution. When such constraints are violated, the computed values of the objective function for this set of variables can help the algorithm reach a physically acceptable solution in a faster manner. The values of the relaxable constraints, $c_k(\mathbf{X})$, quantify the degree to which the variables are far from being acceptable. The progressive barrier algorithm is then used to minimize $c_k(\mathbf{X})$ and $f(\mathbf{X})$ simultaneously until the constraint is respected [9].

2.6.3 Optimization using quadratic models

By default, the OrthoMADS algorithm builds quadratic models [47] based on approximations of the numerical derivatives of the function, $f(\mathbf{X})$, and constraints, $c_k(\mathbf{X})$, to obtain the trial points which will form the initial simplex in the search step. The use of such models should improve the performance of the optimization algorithm. However, in the presence of local minima, these models sometimes lead the algorithm in wrong directions. Also, when non-relaxable constraints are not respected, jumps appear in the objective function. The derivatives can therefore slow down the optimization procedure instead of making it more efficient. This feature can thus be kept activated or disabled depending on the problem studied. Both options are used in different steps of the methodology proposed in this work.

2.6.4 Surrogate function strategy

A common strategy in blackbox optimization is the use of a surrogate function [18]. Such a function behaves in a similar fashion to the objective function, while requiring a shorter computation time (typically at least 10 times shorter) [10]. When finite element simulations are used in the objective function, the surrogate function can be created, for instance, by using a simplified version of the finite element model. While the value of this function remains an approximation of the actual objective function, it is assumed that the variables generating the local minima and the global minimum should be similar for both functions. In this work, a surrogate function is used to obtain a suitable starting point for the optimization procedure.

2.6.5 Performance analysis tool: identifiability index

The group of Richard et al. [112] developed an identifiability index (or I-index) which quantifies the richness of the experimental indentation data used to extract different properties by optimization-based indentation analysis. The lower the value of this index, the more efficient the identification of sought material parameters will be. Using this index, the inverse method developed can be improved through the choice of experimental indentation data used in the objective function. It can also help determine how many, and which material properties, can be extracted in a reliable manner.

To compute the I-index, a set of reference material parameters $\boldsymbol{\eta}$ is chosen and a finite element simulation of indentation is conducted for this combination of parameters. Then, simulations are conducted sequentially with a relative perturbation of ξ applied to each of the parameters, with the other parameters unchanged. Renner et al. [111] chose a value of $\xi = 10^{-3}$.

An I-index considering only the indentation curve as experimental information was developed by Renner et al. [111] and can be computed through the following steps. First, the sensitivities of the indentation reaction load at different indentation depths to the parameters $\boldsymbol{\eta}$ can be defined through:

$$S_{kj}^{C} = \frac{\eta_j}{P_{max}\sqrt{T}} \frac{\partial P_k}{\partial \eta_j}, \tag{2.15}$$

where $\frac{\partial P_k}{\partial \eta_j}$ is the partial derivative of the indentation reaction load at the kth point on the indentation curve as a function of jth studied material parameter. The derivative is then scaled by the reference material parameter η_j and the maximum load of the indentation curve, P_{max}, to obtain a relative sensitivity. T is the total number of points on the indentation curve

and superscript C refers to the fact that the indentation curve is studied.

The dimensionless matrix, $\mathbf{H}$, is then computed by:

$$H_{ij} = \sum_{k=1}^{T} S_{ki}^{C} S_{kj}^{C}, \tag{2.16}$$

in which the sensitivities are summed for all points on the indentation curve. This matrix serves to expose parameters to which the indentation curve has a low sensitivity as well as multicollinearity between some of the S_{ki}^{C}. The I-index, I, is then computed from this matrix by:

$$I = \log_{10}\left(\frac{\lambda_{max}}{\lambda_{min}}\right), \tag{2.17}$$

where λ_{max} and λ_{min} are the maximum and minimum eigenvalues of $\mathbf{H}$.

Renner et al. [111] state that the the following conclusions can be inferred regarding the identifiability of the sought parameters, depending on the value of I:

- if $I \leq 2$, all parameters can be identified;
- if $2 < I \leq 3$, the parameters can be identified, but with difficulty;
- if $I > 3$, the parameters cannot be identified.

The definition of the I-index can easily be adapted to include additional indentation experimental information, like for instance the residual imprint topography. To do so, a second sensitivity matrix, $\mathbf{S}^{I}$, where I refers to imprint, can be created. This matrix contains the sensitivity of the height of the residual imprint profile at different positions on the imprint to the material parameters in $\boldsymbol{\eta}$. The matrix $\mathbf{H}$ then sums the contribution of both experimental information.

Recently, Renner et al. [111] used the I-index to determine the possibility of extracting parameters governing a Méric Cailletaud crystal plasticity model when using only the indentation curve or when using the topography of one, two or three residual imprints obtained on indentations in grains with different orientations. The sought material parameters were the critical resolved shear stress, τ_0, the six coefficients of the interaction matrix for FCC structures, h_1, h_2, h_3, h_4, h_5 and h_6, and two parameters which define the isotropic hardening behaviour, q and b. They used pre-defined values for the elastic and viscosity parameters to reduce the number of parameters to extract. They observed a decrease in the index value

from using the indentation curve only ($I > 6$), to using one, ($I = 3.6$), two ($I > 2.4$), or three ($I > 2.1$) residual imprint topographies. Their conclusion was that the topography of at least three imprints was necessary to efficiently identify all nine of the material parameters of interest.

2.7 Instrumented indentation and residual stresses

Residual stress fields can appear in different parts and components following their fabrication or after a repair, as is the case for hydraulic turbine blades. Several methods exist to quantify these residual stresses, such as the contour method, hole drilling, or X-ray diffraction (XRD) [74]. The methods for the extraction of elasto-plastic properties by instrumented indentation presented in Section 2.4 neglect the presence of residual stresses. This is an acceptable assumption in many cases, but when studying material specimens from parts which were fabricated or repaired by welding, for instance, significant errors can arise in the extracted properties. Indeed, the indentation parameters have such a sensitivity to residual stresses that many studies developed methods to quantify residual stresses by indentation.

2.7.1 Effect of existing residual stresses on instrumented indentation results

The presence of residual stresses has effects on both the indentation curve as well as the topography of the residual imprint. Many studies showed that compressive residual stresses in a material increase the reaction load needed to obtain the same maximum depth, while decreasing the residual depth after unloading, meaning the increase of elastic recovery [49, 86, 114, 130, 131, 136]. Also, Lu et al. [86] found that compressive stresses led to a decrease in the curvature, C of the indentation curve. As could be expected, the presence of tensile residual stresses had the opposite effects on these parameters of the indentation curve. Figure 2.10 shows the effect of equi-biaxial compressive or tensile residual stresses on experimental Vickers indentation loading curves conducted on an aluminum 2024 [86]. Figure 2.11 shows indentation curves, normalized for their respective maximum load and maximum depth, obtained by finite element simulation of conical indentation. This normalization puts forth the effect on the residual depth of indentation [132].

The size of the generated plastic zone induced by the indentation in the presence of compressive residual stresses decreases in size and the pile-up height therefore increases [38, 131–133]. Tensile residual stresses will contrarily favour the sinking-in of the surface around the indent and thus lower the pile-up height. The extent of this effect can be observed in Figure 2.12, which shows several residual imprint profiles obtained by finite element simulation of conical

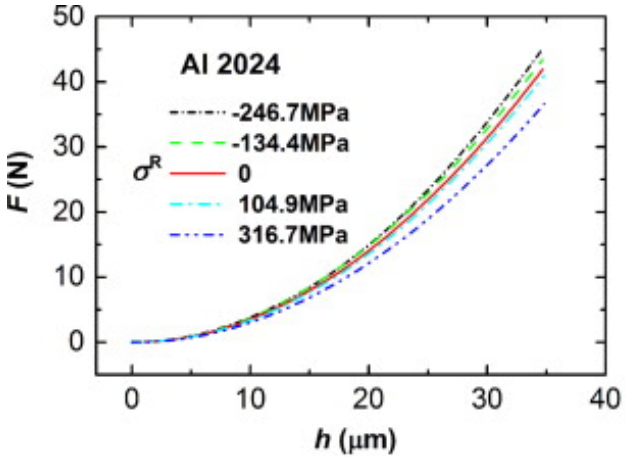

Figure 2.10 Effect of the presence of compressive or tensile equi-biaxial residual stresses on the experimental Vickers indentation results on 2024 aluminum alloy with $\sigma_y = 350.8$ MPa. Compressive residual stresses induce an increase in reaction force for the same indentation depth and the opposite is true for tensile residual stresses. Taken from [86].

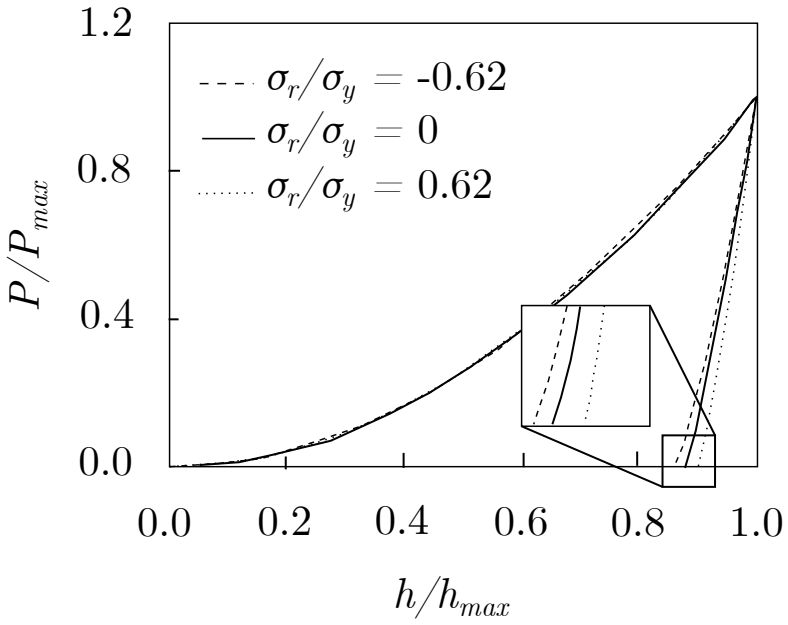

Figure 2.11 Indentation curves normalized by their respective max load, P_{max}, and max depth, h_{max}, obtained by conical indentation finite elements simulations on specimens containing different states of residual stress. A compressive residual stress creates a decrease in residual indentation depth and the opposite is true for a tensile residual stress. Reproduced from [132].

indentation on specimens containing different states of equi-biaxial residual stress.

2.7.2 Measurement of residual stresses by indentation

Different approaches are used for the extraction of residual stresses by instrumented indentation. First, there are methods which focus solely on the quantification of residual stresses, using a material with known elasto-plastic properties. For example, Lu et al. [86] developed dimensionless functions relating the curvature parameter, C, of the indentation curve to a value of equi-biaxial residual stress. They conducted an experimental validation of their method with four materials, which were each imposed four different equi-biaxial residual stress values. The errors on the extracted residual stresses varied between 1.6% and 28.3%.

However, residual stresses are rarely equi-biaxial. With this in mind, Bocciarelli et al. [16] developed a numerical optimization method which used the asymmetry of the residual imprint topography to determine the complete three-dimensional residual stress state. They obtained a rapid convergence towards the correct values of residual stress components in a numerical validation. However, when applying their method to experimental indentation data, the method became unstable and led to errors in the identification of residual stress varying from 2.2% to 92%. Moreover, the algorithm sometimes extracted values higher than 100 MPa in a direction in which no residual stress was physically present.

Some authors attempted to extract residual stress simultaneously to the elasto-plastic properties. Chen et al. [38, 133, 136] established dimensionless relationships between parameters of the indentation curve as well as a parameter characterizing imprint pile-up and values of E, σ_y as well as a value of equi-biaxial residual stress. For a material with linearly elastic, perfectly plastic behaviour, a maximum error of 10% was obtained for all parameters in a numerical validation [136].

Recently, Pham and Kim [108] used dimensional analysis considering only the indentation curve to extract parameters of a tensile model which was composed of a Lüders plateau followed by a power law, and the present equi-biaxial residual stress, σ_R. Even though the indentation curve is not very sensitive to the hardening coefficient, the authors claim to have successfully extracted σ_y, n, σ_R and $l_{plateau}$ (a parameter quantifying the length of the Lüders plateau) using only four dimensionless functions and no information from the residual imprint. They conducted an experimental validation on structural steel specimens containing tensile residual stresses and obtained errors ranging from -2.3% to 5.5% for σ_y, from -0.8% to 5.2% for n, from -2.4% to 6.2% for $l_{plateau}$ and from -1.5% to 2.7% for σ_R. No validation is presented in the presence of compressive residual stresses. This method seems to work very well, even though no experimental data is taken from the residual imprint of indentation.

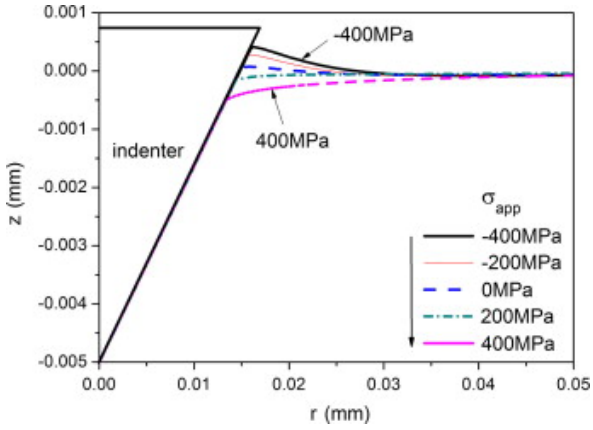

Figure 2.12 Effect of equi-biaxial compressive or tensile residual stresses on the residual imprint profiles obtained by conical indentation finite elements simulations for a material with $\sigma_y = 400$ MPa. Compressive residual stresses cause an increase in pile-up height while tensile residual stresses have the opposite effect. Taken from [131].

2.8 Application of instrumented indentation to welded joints

Numerous studies focused on the application of different methods presented in Section 2.4 to extract local tensile curves in welded joints. In many of these studies, the presence of residual stresses is completely ignored. The results obtained must then be interpreted with caution because of the sensitivity of the indentation curve and residual imprint to the presence of residual stresses, as described in Section 2.7.1. Some studies however present satisfying validations of the extracted tensile curves, demonstrating that the presence of residual stresses might not have a detrimental effect on the extracted tensile curves in some cases.

Ye et al. [135] used the dimensional analysis based method using two sharp indenters developed by Dao et al. [48] through a welded joint which was composed of 304L steel as the base metal and 316L steel as the weld metal. Their study showed that σ_y and n were higher in the weld metal than the base metal and that these two parameters varied linearly in the HAZ. A validation was presented for the base and weld metals, comparing the elasto-plastic properties extracted in these zones of the welded joint to that obtained from macroscopic tensile tests of the respective metal. For the base metal, errors of 21.2, 5.5 and 23.7 % were obtained on the value of σ_y, n and E, respectively. For the weld metal, the errors are smaller, with values of 1.6, 0.5 and 7 %. These results represent the average properties in the base and weld metals studied, where in reality, a slight gradient was present in the values of σ_y and n. We could hypothesize that this gradient, which should not be attributed to microstructural changes since they were obtained outside the HAZ, could be caused by the presence of varying residual stress which affect indentation results and thus the extracted

properties.

Pham et al. [107] extracted the tensile properties through a SM490 steel welded joint using a method based on dimensional analysis and a Berkovich indenter. The assumed tensile model was one including a Lüders plateau, followed by a power law. For the validation of the results, the authors first used the rule of mixtures to evaluate the precision of the extracted elastic modulus. They computed an equivalent modulus taking into account the extracted values in the base metal, weld metal and HAZ, and then compared this value to the elastic modulus as measured with a tensile test on a specimen taken through the welded joint. The average difference was 7.5%. The authors then undertook the validation of the elasto-plastic properties extracted in the weld [79]. To do so, they developed a finite element model of a tensile specimen including the welded joint and applied the extracted properties by indentation to the base metal, weld metal and the HAZ. The loading direction was perpendicular to the weld line, so the different weld zones were assembled in series along the loading direction. Average values for each zone were used to simplify the model. The gradient of properties present in the HAZ was then neglected. Despite this simplification, differences below 3% were estimated between the simulated and associated experimental tensile curves, as can be observed in Figure 2.13. However, the obtained tensile curve for the weld is very similar to that of the base metal without the weld, with differences estimated from Figure 2.13 to be below 6%. This was expected since the total elongation of the specimen is measured and the base metal, which is the least resistant and thus contributes the most to the elongation, has the largest volume fraction in the specimen. Even large errors in the extracted tensile curves in the weld metal and HAZ would not have had an important effect on the macroscopic tensile curve so this validation should therefore be interpreted with caution.

Sun et al. [117] used a numerical optimization approach with a Vickers indenter to obtain the tensile curves in a dual phase high strength steel welded joint. They also used a finite element model to simulate the behaviour of the complete weld under tensile loading. In this case, the loading direction was parallel to the weld line. A good correspondence was obtained between the simulated tensile curves using extracted properties and the experimental tensile curve, with an approximated maximum error of 10%. To deepen their analysis, the authors also used digital image correlation (DIC) to compare experimental and simulated strain distributions. The distributions were qualitatively similar. The maximum strain values in the experiment and simulation at different total strain values were quantitatively compared and the difference remained under 20% for all total strain values. However, the maximum strain value did not necessarily appear at the same localization in the welded joint when taken from the simulation or experiment.

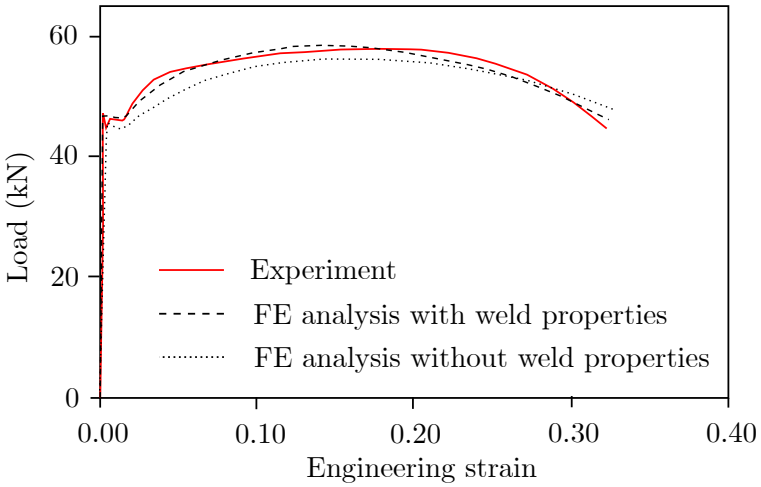

Figure 2.13 Comparison of the tensile curve obtained from an experiment on a SM490 steel welded joint to the tensile curves simulated from finite element models using the extracted tensile curves by instrumented indentation and using only the base metal properties. A satisfying correspondence is achieved even though no residual stresses were considered in this study. Reproduced from [79].

It is difficult to draw conclusions regarding the results obtained by these studies, since the nature of the residual stress fields present are unknown. To actually determine if it is a valid assumption to neglect the presence of residual stresses in welds, a study of the effect of the presence of residual stresses on the extracted tensile curve by instrumented indentation should be conducted. Indeed, by measuring the stress fields present in a specimen by another non-destructive method before the indentation tests, it would be possible to compare the extracted tensile curves obtained by taking into account the presence of residual stresses to those obtained by neglecting their presence.

2.9 Literature review synthesis and relevance to the research project

The findings from this literature review are as follows regarding the development of a method for the local characterization of welded joints by instrumented indentation:

1. The indenter geometry and experimental setup compliance must be measured in a direct manner to reduce the effect of these parameters on the experimental indentation results;

2. A numerical optimization approach is best suited for the studied application;

3. To reduce the risk of non-uniqueness issues, the most suitable strategies are the use of

a spherical indenter as well as the topography of the residual imprint as supplementary experimental information;

4. An important lack of experimental validation is present in the literature, and such a validation is essential to ensure the method is stable enough to be used in the presence of experimental and modeling errors.

5. The effect of residual stresses on the indentation curves and residual imprints are understood. However, the magnitude of the errors induced on the extracted properties using an inverse method when neglecting these residual stresses are unknown. Since welded joints contain residual stresses, this must be understood to ensure a reliable estimation of their local material properties.

CHAPTER 3 RESEARCH OBJECTIVES AND ORIGINALITY

3.1 General objective

The general objective of this thesis is the following:

Develop a reliable and versatile inverse methodology for the estimation of bulk elasto-plastic tensile properties of metals using spherical instrumented indentation and apply it to a welded joint.

3.2 Specific objectives

The general objective is separated into the four following specific objectives:

1. Study of the effect of experimental parameters on indentation results to ensure reliable experimental indentation data and development of a method to directly measure the machine compliance;
2. Develop a finite element model for the indentation process and experimental validation;
3. Develop a numerical optimization inverse method using the indentation curve and residual imprint obtained by a spherical indenter which enables the estimation of elasto-plastic properties without the assumption of a pre-defined tensile model;
4. Apply the developed inverse method to a welded joint in the as-welded state and following a stress relief annealing treatment to study the influence of residual stresses on the extracted properties.

3.3 Originality

The principal novelty of this work is the extraction of the tensile curve without assuming a pre-defined tensile model like a power-law. This greatly complexifies the optimization problem to solve by adding variables and constraints, but it permits the extracted tensile curve to take whatever physically acceptable shape and leads to a method which is more versatile than other methods presented in the literature. Other novelties are the method for the direct measurement of the machine compliance and the analysis of the effect of the presence of residual stresses in a weld on the accuracy of extracted true stress-true strain curves.

CHAPTER 4 EXPERIMENTAL INDENTATION STUDY AND DIRECT MEASUREMENT OF THE MACHINE COMPLIANCE

Chapter 4 presents the experimental study, which was conducted to complete the first specific objective of this research. The materials and methods are first described in Section 4.1, followed by the associated results and discussion in Section 4.2.

4.1 Materials and methods

The methodology used for the accomplishment of the indentation experimental study is presented in the following sections. First, the four materials used in the project are described in Section 4.1.1 followed by the details regarding the indentation tests methods in Section 4.1.2. Then, the methodology used to study the effect of experimental parameters on indentation results is presented in Section 4.1.3, followed by the novel method developed for the direct measurement of the machine compliance in Section 4.1.4.

4.1.1 Materials

Four steels with different tensile behaviours were investigated in this study: the eutectoïd steel SAE 1080, the carbon steel ASTM A516, the martensitic stainless steel AISI 415 and the austenitic stainless steel AISI 304L. The general characteristics of these steels are given in Table 4.1. These steels were used for the study of experimental effects on indentation data, as well as for the validation of the finite elements models and of the developed inverse method.

Isotropy and macroscopic homogeneity

Anisotropy and in-homogeneity, *i.e.*, varying mechanical properties in different locations in the material specimens, have effects on indentation data. The method developed in this work is not designed to take these effects into consideration. They must then be minimal in the studied materials. Isotropy and macroscopic homogeneity studies were completed through Rockwell hardness measurements using a Zwick/Rohell ZHU250 testing machine on all steels except SAE 1080, which was added later in the project. SAE 1080 steel was assumed homogeneous ans isotropic since it had received a recrystalisation treatment at 800°C for 40 minutes to obtain equiaxed grains. The homogeneity specimens were machined

Table 4.1 General characteristics of the four steels studied in this work. The hardening coefficient is defined by the slope of a linear fit of the logarithm of the true stress as a function of the logarithm of the true strain as measured by the tensile tests in the elasto-plastic region.

Material	Eutectoïd steel SAE 1080	Carbon steel ASTM A516	Stainless steel AISI 415	Stainless steel AISI 304L
Microstructure	Pearlitic	Ferrito-pearlitic	Martensitic	Austenitic
Material form	Bar, $0.75'' \times 0.75''$	Plate, $96'' \times 48'' \times 1''$	Plate, $210''\times78''\times2.5''$	Plate, $12'' \times 6'' \times 1''$
Metallurgical state	Recrystallized	Normalized	Double tempered	Annealed
Hardening coefficient	0.284	0.226	0.151	0.377
Yield stress (MPa)	498	345	500	200
Lüders plateau	Present	Present	Absent	Absent

conventionally with the geometry shown in Figure 4.1, which also shows the approximate positions of hardness measurement.

Variations of hardness were observed in the as-received AISI 304L plate and it was thus heat-treated at 1060°C for 80 minutes to obtain homogeneity and isotropy in the plate. The hardness was then re-tested in the thickness of the plate and was found stable, so the material was deemed to have acceptable homogeneity to be used in this project.

The ASTM A516 and the AISI 415 steels were found homogeneous, as presented in Table 4.2. For AISI 415, the largest difference between the average hardness measurements in two directions being 0.3 HRC (26.3 and 26.6 HRC for planes L and S, respectively). The standard deviation in the short transverse (S) plane is about twice that of the other planes. This might be caused by the smaller amount of sampled hardness measurements in the S plane due to smaller specimen size, when compared to L and T planes. The homogeneity of the specimen was considered acceptable for this project as the maximum standard deviation is 1.81 HRC.

For ASTM 516, the largest difference between the average hardness of two planes is 4.6 HRB (planes L and T). The standard deviations of the hardness values obtained within each planes are also satisfactory, with a maximum of 1.28 HRB. The homogeneity and isotropy of ASTM A516 was also considered acceptable for this project.

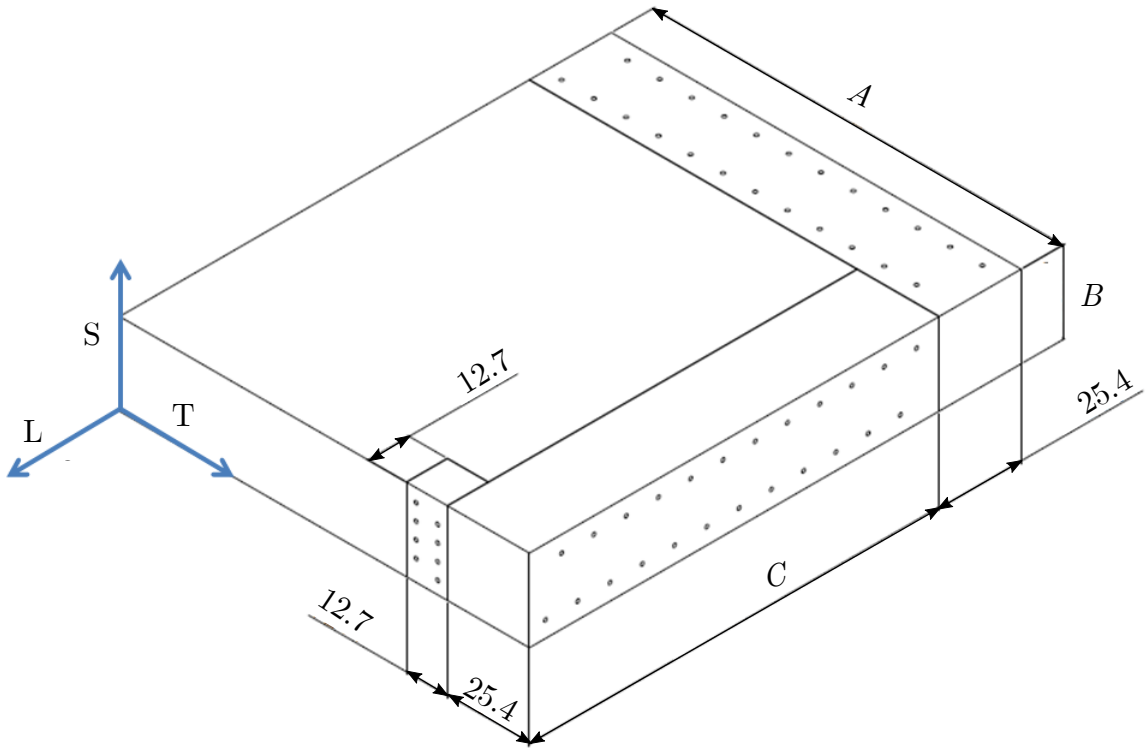

Figure 4.1 Geometry of specimens for homogeneity and isotropy study as well as approximate position of hardness tests. The positioning of each hardness test was done manually, in locations previously marked as guided by a standard ruler. The typical distance between indents was 10 mm along the L and T directions and 5 mm in the S direction. For ASTM A516 and AISI 304L steels: $A = 152.4$ mm, $B = 25.4$ mm, $C = 127$ mm; and for AISI 415 steel: $A = 101.6$ mm, $B = 63.5$ mm and $C = 101.6$ mm.

Table 4.2 Measurements of hardness variations across plates of AISI 415 and ASTM A516 steels. Both materials are considered to have sufficient isotropy and homogeneity for the present research project. L refers to longitudinal, T refers to long transverse and S refers to short transverse directions.

Material	Normal of indented plane	Sampling direction	Average hardness	Standard deviation
Acier 415	L	T	26.3 HRC	1.81 HRC
	T	L	26.5 HRC	0.98 HRC
	S	T	26.6 HRC	0.92 HRC
	Total average		26.5 HRC	1.39 HRC
Acier A516	L	S	76.3 HRB	1.28 HRB
	T	L	80.9 HRB	0.74 HRB
	S	T	77.4 HRB	0.98 HRB
	Total average		78.2 HRB	2.56 HRB

Chemical compositions

The chemical compositions of the studied materials were measured by spectroscopy using a LECO GDS 850A. For increased accuracy on carbon and sulphur contents, the analysis for these two elements were done by combustion analysis using a LECO CS230. For AISI 304L and AISI 415, the oxygen and nitrogen contents were measured using the inert gas fusion technique on a LECO ONH826. The chemical compositions are presented in Tables 4.3 to 4.6. All measured compositions were within the limits of the respective standards for the four steels, except for the manganese content in SAE 1080, which was measured at 0.91% while the standard states values between 0.6% and 0.9%.

Microstructure

The microstructures of the four studied steels are shown in Figures 4.2 to 4.5. The indicated directions, longitudinal (L) or long transverse (T), correspond to that of the normal of the plane observed. For SAE 1080, the material is in bar form, so only the L direction is observed. This steel has a predominantly pearlitic microstructure characterized by equiaxed grains. Some ferrite grains are also observed. The three other steels are in plate form, so both L and T directions are observed. ASTM A516 is composed of ferrite and pearlite arranged in layers (typical band structure) which are aligned with the L direction. It can be observed that the layers are not as aligned parallel to the T direction, so the microstructure is slightly different in both observed planes.

For AISI 415 and AISI 304L, no significant variation is observed between the sampled directions. AISI 415 presents a martensitic microstructure, while AISI 304L presents an austenitic microstructure.

Macroscopic true stress-true strain curves

The true stress-true strain curves were obtained by conventional tensile tests with an Instron 1332 hydraulic universal testing machine in accordance with the ASTM E8/E8M-11 standard [7]. The specimens were cylindrical with a diameter of 9.5 mm and a length of 57.2 mm. An extensometer was used with a gauge length of 25 mm to accurately measure

Table 4.3 Chemical composition (% wt.) of SAE 1080.

C	Mn	P	S	Fe
0.81	0.90	0.02	0.01	Remainder

Table 4.4 Chemical composition (% wt.) of ASTM A516.

Fe	C	Mn	P	S	Si	Ni
98.1	0.17	0.96	0.013	0.0017	0.24	0.092
Cr	Cu	Mo	V	Ti	Al	
0.087	0.26	0.019	0.0034	0.0012	0.028	

Table 4.5 Chemical composition (% wt.) of AISI 415.

Fe	C	Mn	P	S	Si	Ni	Cr	O
81.1	0.019	0.80	0.015	0.003	0.50	4.59	12.2	0.005
Cu	Mo	V	Ti	Al	Nb	Co	N	
0.14	0.66	0.039	0.0012	0.0011	0.031	0.0046	0.012	

Table 4.6 Chemical composition (% wt.) of AISI 304L.

Fe	C	Mn	P	S	Si	Ni	Cr	O
70.2	0.024	1.78	0.030	0.003	0.24	8.14	18.6	0.004
Cu	Mo	V	Ti	Al	Nb	Co	N	
0.34	0.32	0.069	0.008	0.0055	0.082	0.13	0.092	

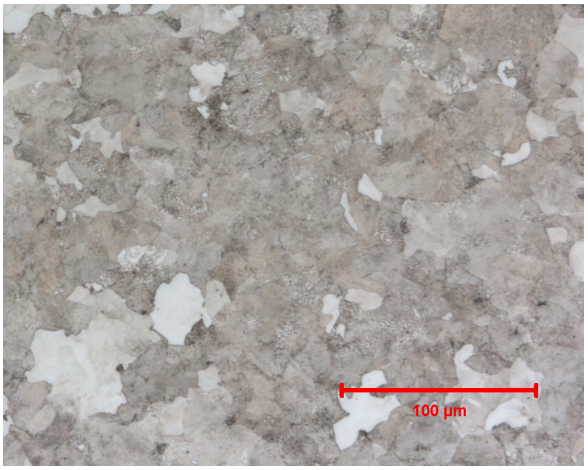

Figure 4.2 Microstructure of SAE 1080 steel in the L direction. The specimen was etched with a solution of 2 % nital in ethanol.

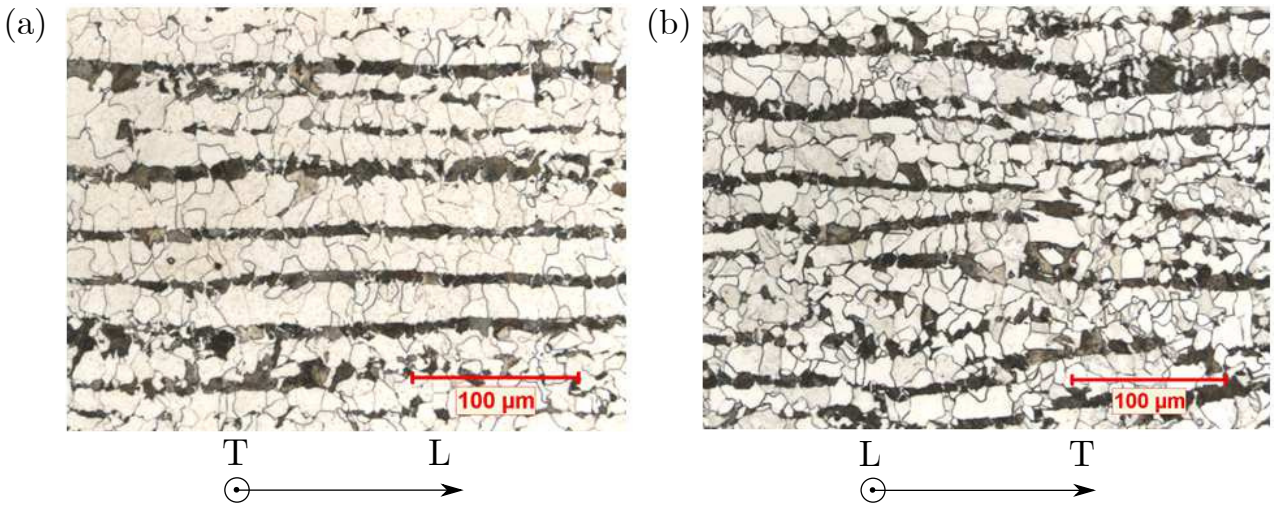

Figure 4.3 Microstructure of ASTM A516 steel in the: (a) T; and (b) L directions. The specimens were etched with a solution of 2 % nital in ethanol.

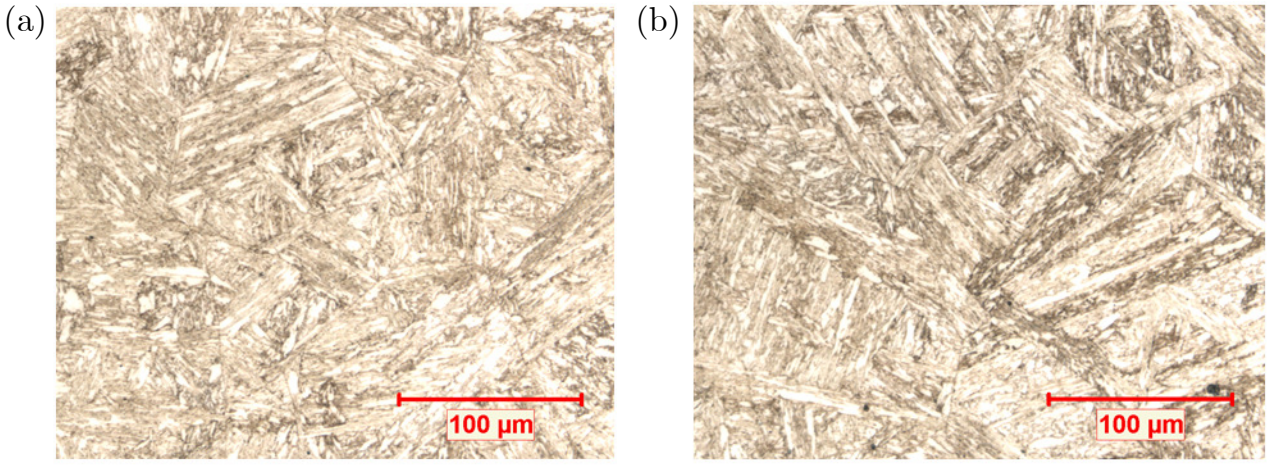

Figure 4.4 Microstructure of AISI 415 steel in the: (a) T; and (b) L directions. The specimens were etched in a solution of 5 ml HCl in 100 ml of ethanol with 1 g of picric acid.

(a) 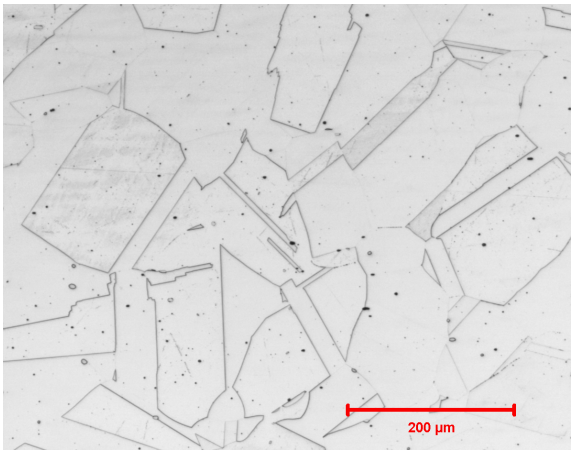

(b) 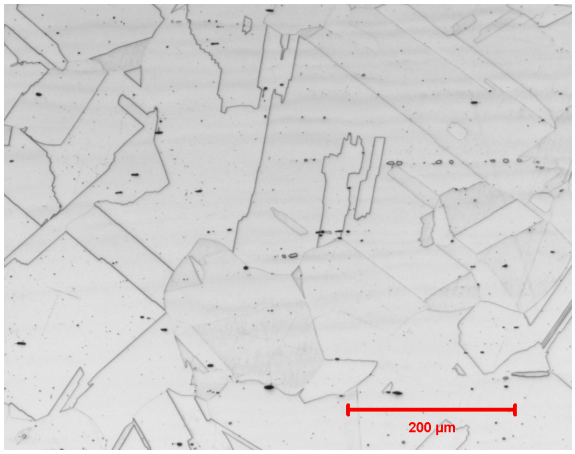

Figure 4.5 Microstructure of AISI 304L steel in the: (a) T; and (b) L directions. A 6 V electrolytic etch was performed on the specimens using a solution of 10% oxalic acid in water.

the strain. The displacement rate applied by the tensile machine was 1 mm/min. For ASTM A516 and AISI 304L, two specimens were tested per direction (L and T) to observe isotropy. For ASTM 1080, 3 specimens were tested in the L direction as the material was supplied in bar form. For AISI 415, four specimens were tested in the L direction.

Figure 4.6 presents the obtained true stress-true strain curves for the four materials, up to the strain at which the necking was observed in the engineering stress-engineering strain curves. Table 4.7 shows the average of the elastic modulus, $\overline{E}$, and the yield stress, $\overline{\sigma_y}$, as well as the standard deviation of these values over all specimens, s_E and s_{σ_y}, respectively. The average of the standard deviation of the curves within the hardening region, *i.e.*, for all strains between the yield strain and the maximum strain, $\overline{s}_{[\varepsilon_y,\ \varepsilon_{max}]}$, is also shown to quantify the general variability of the curves obtained in the same material. It can be observed that the variability of the extracted curves is more important for ASTM A516 and SAE 1080 than for AISI 415 and AISI 304L. However, for the elastic modulus, the variability is more significant in the cases of ASTM A516 and AISI 415 than the other two steels.

4.1.2 Instrumented indentation

Indentation curves

The micro-indentation experiments were conducted using a MHT micro-indentation tester, manufactured by Anton-Paar. Spherical indenters compatible with the indentation machine characterized by a sphero-conical shape. A diamond sphero-conical indenter with a cone half-angle of 45° and a theoretical tip radius, R, of 50 µm was used in this study. The

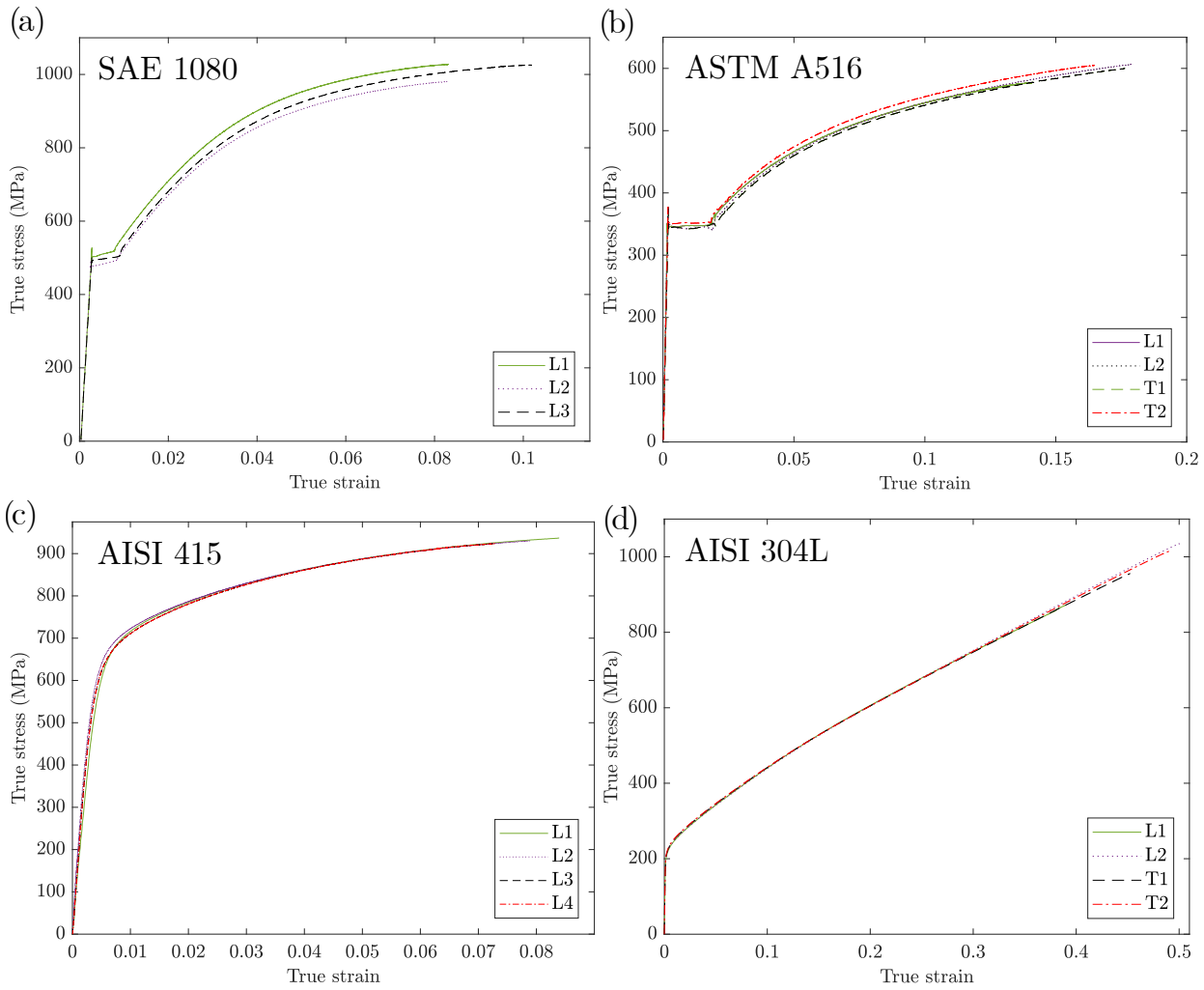

Figure 4.6 Experimental true stress-true strain curves obtained for the four studied steels.

Table 4.7 Average of the elastic modulus, $\overline{E}$, and the yield stress, $\overline{\sigma_y}$, calculated from the experimental tensile curves, as well as the standard deviation of these values, s_E and s_{σ_y}, respectively. The average of the standard deviation of the curves within the hardening region, *i.e.*, for all strains after the yield strain to the maximum strain, $\overline{s}_{[\varepsilon_y,\ \varepsilon_{max}]}$, is also shown to quantify the general variability of the curves obtained in the same material.

Material	$\overline{E}$ (GPa)	s_E (%)	$\overline{\sigma_y}$ (MPa)	s_{σ_y} (%)	$\overline{s}_{[\varepsilon_y,\ \varepsilon_{max}]}$ (%)
SAE 1080	205.8	1.48	491.3	2.77	2.65
ASTM A516	205.3	8.05	346.8	0.89	1.16
AISI 415	187.3	9.24	511.8	2.8	0.84
AISI 304L	194.9	2.17	205.8	0.61	0.42

actual geometry of the indenter tip was measured, for accurate modeling in the finite element simulations, using an Olympus LEXT OLS4100 laser scanning 3D microscope made available for this work by the École de Technologie Supérieure (ÉTS). It was estimated that the transition from a spherical to a conical geometry began around an indentation depth of 12 µm. A comparison of the measured and ideal geometries is shown in Figure 4.7.

The indentation tests were load-controlled and 20 indents were performed in each of the four materials applying a maximum load of 5 N. This load was chosen as it led to a good repeatability between indentation curves and averaged residual imprints for all materials, supporting that bulk properties are sampled, while creating indents which were small enough to enable a spacing of 1 mm between them. At this load, the contact region remained in the purely spherical part of the indenter. The indentation position matrix and reference coordinate system used in the analysis are shown in Figure 4.8.

The loading and unloading durations were set to 30 s and a dwell period of 30 s was included at the maximum load to prevent any creep effect on the unloading portion of the indentation curve. Figure 4.9 shows an example of the progression of the indentation load and depth as a function of time for ASTM A516. It can be observed that the indentation depth increases a total of 0.41 µm during the dwell period at a load of 5 N. The rate of increase of the depth when the load first reached 5 N was 0.151 µm/s, but it reduced to less than 0.003 µm/s right before the onset of unloading. It is concluded that creep will not have a significant effect on the unloading curve as the rate of increase of the displacement with time has reduced sufficiently during the 30 s dwell period.

Details of specimen and surface preparation are given in Section 4.1.3 for the different tests conducted.

Measurement of residual imprints

The residual imprints were measured with an Olympus LEXT OLS4100 laser scanning 3D microscope. The resolution of the height measurement for this equipment is 10 nm. The step size between positions where heights were sampled in the imprints and pile-up regions was set to 0.25 µm.

Figure 4.10 (a) shows a typical residual imprint measurement. The topography is not perfectly axisymmetrical. This was not due to material anisotropy, since isotropy was verified for the studied materials (see Section 4.1.1). The asymmetry of the imprint could also be caused by heterogeneity at the micrometer scale. However, the indent presented in Figure 4.10 was conducted in ASTM A516, and for this material, a circle approximating the size

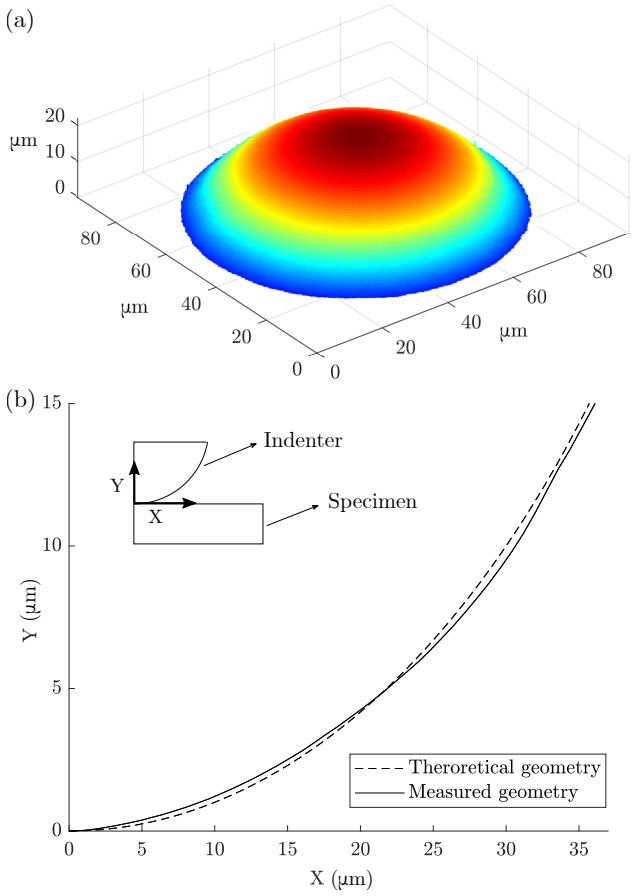

Figure 4.7 Geometry of the indenter used in this work: (a) 3D geometry measured with a laser scanning 3D microscope; (b) Comparison of the average measured profile of the indenter as modeled in simulations compared with that of the theoretical geometry for a spherical tip with a radius $R = 50$ μm. It can be observed that the tip does not follow a perfectly spherical shape.

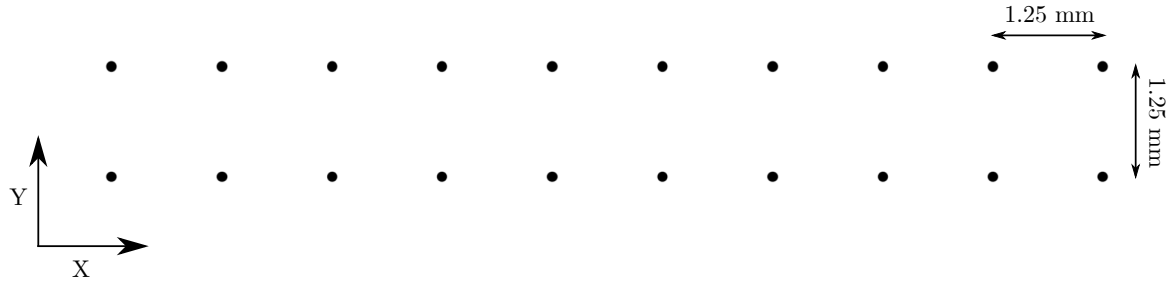

Figure 4.8 Position matrix of indentations (10 × 2 indents) with reference coordinate system. This matrix was used for all tests on all specimens except the welded joints.

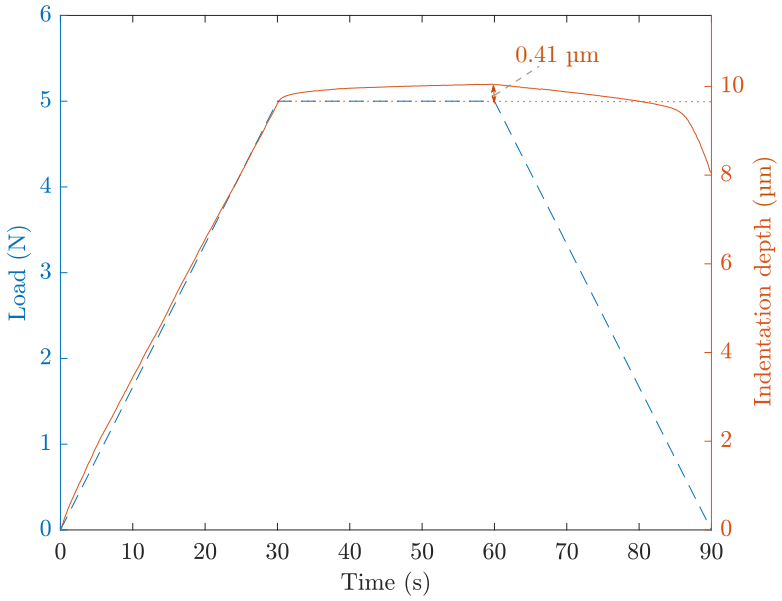

Figure 4.9 Indentation load and depth as a function of time for ASTM A516 steel.

of the plastically deformed zone with a radius of 80 µm on the surface contained approximately 80 grains. This number should be sufficient to limit the effect of material micro-scale heterogeneity on the pile-up height. What can be seen in Figure 4.10(a) is instead caused mainly by unavoidable setup misalignment between the indenter and the surface. Indeed, when observing the imprints, a preferential direction was noticed (in the north-east quadrant of the indents) in which the pile-up was always higher. This did not change upon rotating the specimen, and rotating the indenter, which points to an inherent misalignment in the setup. Using shims to align the specimens, the angle characterizing this misalignment was estimated to be under 0.5°. These shims could not be used to conduct the indentation tests as this led to an increased compliance since the specimens were no longer rigidly supported on the specimen holder of the testing machine.

We therefore obtained the average experimental profile to enable a comparison with the axisymmetrical profile generated by the finite element simulations. The averaging procedure was developed with ASTM A516 steel, and it was found to yield a satisfactory approximation by comparison with simulated imprints for this steel. Further details are given in Section 5.4.1. To obtain the average profile, 3D cylindrical coordinates centred at the tip of the indent were projected on the $r - z$ plane. This allowed plotting all the measured data on a single 2D graph, amounting to over 400 000 points per indent, as shown in Figure 4.10 (b). The radial axis was separated into intervals of 0.1 µm and the average height of all points within each interval was computed to obtain an average profile which was accurate for all

radial positions. Such an averaged profile is shown in Figure 4.10 (b).

A comparison between a residual imprint profile for ASTM A516 steel and the indenter geometry is shown in Figure 4.11. The indenter is illustrated at its loaded position, at a depth of 10.1 µm, while the residual imprint corresponds to the unloaded state. The extent of the elastic recovery of the imprint can be observed to be almost constant through the whole imprint.

4.1.3 Study of the effect of experimental parameters on indentation results

Before considering the extraction of material parameters to estimate the true stress-true strain curves of materials by instrumented indentation, efforts must be dedicated to the improvement of the quality of the experimental indentation results. To do so, the effect of four experimental parameters on indentation results were studied:

1. Installation of specimens onto the testing apparatus;
2. Fabrication process of the specimens;
3. Surface preparation of the specimens;
4. Correction for the machine compliance.

Baseline specimens preparation

The experimental effects studies regarding the fabrication process and the specimen installation approach were conducted on ASTM A516 steel specimens. For the effect of surface preparation and machine compliance, the study was conducted on all materials, namely, SAE 1080, ASTM A516, AISI 415 and AISI 304L steels.

The baseline specimens, A516-B, 1080-B, 415-B, and 304L-B serve as a comparison basis for the applicable studies using ASTM A516, SAE 1080, AISI 415 and AISI 304L steels, respectively. These specimens were prepared by electric discharge machining (EDM) to avoid strain hardening the material in the region of interest. Their dimensions were 25 $\times$ 24 $\times$ 22 mm^3, as measured in the L $\times$ T $\times$ T directions. These dimensions were large enough so the specimen could be directly deposited on the machine specimen holder, removing all effects of the installation approach of the specimen on the machine. Figure 4.12 shows an example of the baseline specimens installation setup onto the specimen holder of the micro-indentation apparatus (specimen A516-B).

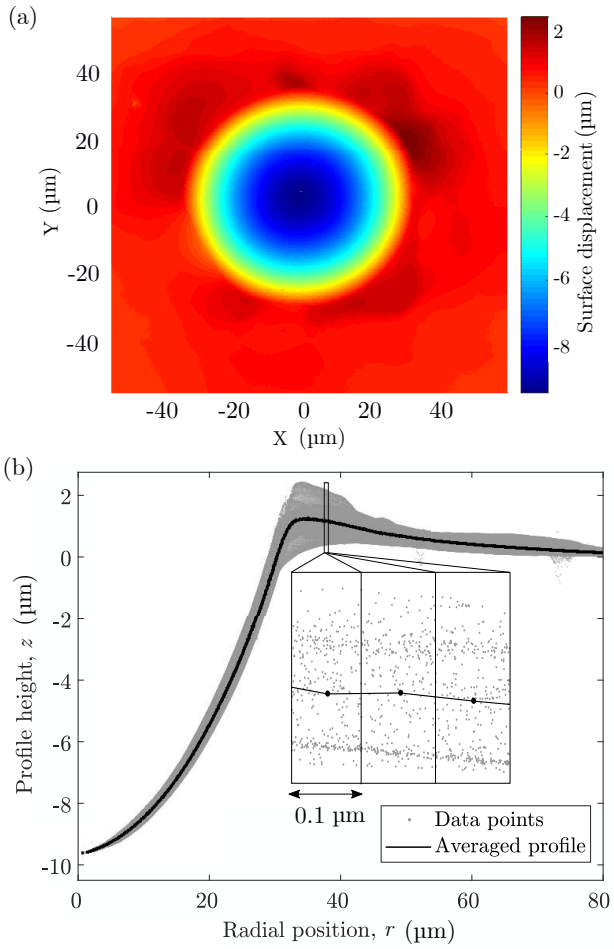

Figure 4.10 Example of the residual imprint of an indentation performed with a spheroconical indenter of radius $R = 50$ µm and a maximum load of 5 N in an ASTM A516 steel specimen: (a) full imprint topography; and (b) corresponding projection of the data points on the $r - z$ plane of a 3D cylindrical coordinates system centred at the tip of the indent. Also shown is the corresponding average profile, obtained by averageing the height of all the projected data points in intervals of 0.1 µm of the radial position.

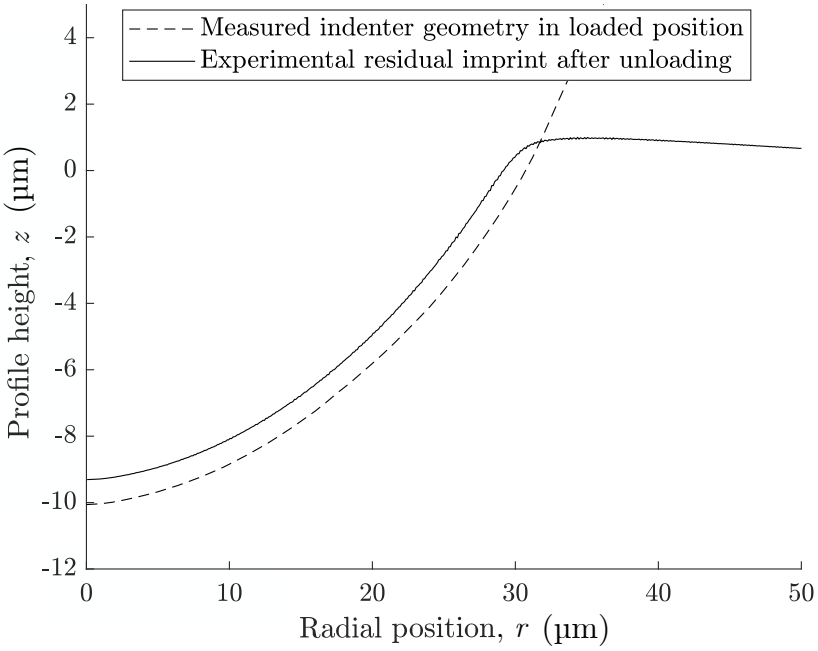

Figure 4.11 Comparison between the residual imprint of an indentation in ASTM A516 steel and the geometry of the indenter, positioned at the maximum indentation depth achieved during the test. The extent of the elastic recovery of the imprint can be observed to be almost constant through the whole imprint.

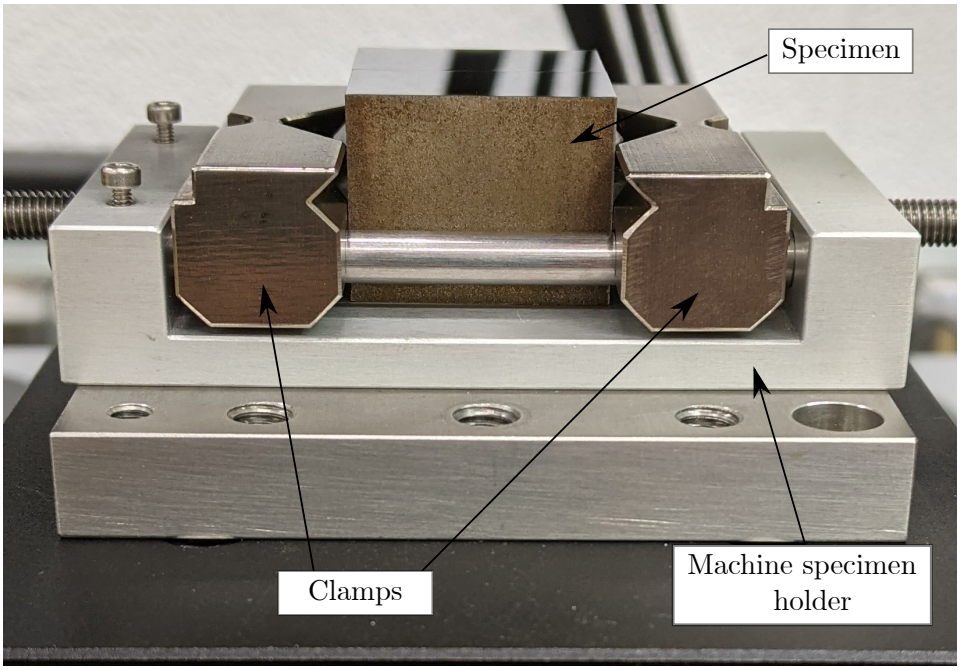

Figure 4.12 Installation setup of a baseline specimen, A516-B, which is large enough to be deposited directly onto the machine specimen holder. With this setup, the specimen is very stable as the clamps have a high contact area with the sides of the specimen.

The specimen surfaces were ground sequentially with silicon carbide paper with grits of 600 and 800 particles/in^2. The surfaces were then polished sequentially with 6 µm, 3 µm and 1 µm diamond suspensions deposited on Struers MD-Pan, MD-Mol and MD-Nap cloths, respectively. This surface preparation procedure is referred to by the size of the particles of its finest polishing stage, *i.e.*, 1 µm.

A summary of the different manufactured specimens for the experimental effects studies and their preparation methods is given in Table 4.8. The studies are detailed in the following sections.

Effect of the technique used to install the specimen on the testing apparatus

Anton-Paar, the manufacturer of the micro-indentation machine used in this work, provides circular aluminum supports on which it is instructed to glue the specimens. The geometry of these aluminum supports was conceived to maximize specimen stability during the indentation tests. Figure 4.13 illustrates the specimen installation setup as proposed by Anton-Paar.

An issue with this installation technique is the necessity of using a layer of glue to attach the specimen to the aluminum support. The adhesives recommended are cyanoacrylate glues. Such glues have a very low stiffness, typically $E \approx 1.25$ GPa, and their presence in the experimental setup can influence the machine compliance. This effect can have varying intensities, depending on the thickness of the glue layer. Furthermore, because of the short curing time of the glue, it is difficult to control the thickness of the applied layer, and its uniformity. A layer of low stiffness glue with varying thickness will lead to a variable machine compliance, depending on the indented position on the specimen. This also causes a misalignment of the surface of the specimen, deviating from the desired perpendicularity with the indenter axis.

To study the effect of the glue in the setup, specimen A516-G, was prepared by EDM with dimensions of $8 \times 25 \times 25$ mm^3, in the L $\times$ T $\times$ S directions and its surface was prepared using the previously defined 1 µm polishing method. The specimen was then manually glued with a layer of Loctite 401 cyanoacrylate glue. A small drop of glue was used to attempt minimizing the thickness of the layer obtained. Indentation tests were then conducted and the results were compared to that obtained with the baseline specimen, the dimensions of which were chosen to avoid the use of the aluminum support and maximizing the contact area of the clamps and the specimen to avoid movement during the tests (Figure 4.12).

Table 4.8 Summary of the characteristics of the specimens used for the studies of different experimental effects on indentation results. In the specimen designation, the material is first stated, followed by a suffix referring to the particularity of this specimen: baseline (B), use of conventional machining (CM), use of glue in installation (G), and refining of surface preparation (SP).

Specimen	Fabrication process	Surface preparation	Dimensions L × T × S (mm^3)	Study
A516-B	EDM	1 µm	25 × 24 × 22	Baseline for fabrication process, specimen installation and surface preparation
A516-CM	VM	1 µm	8 × 25 × 25	Fabrication process
A516-G	EDM	1 µm	8 × 25 × 25	Specimen installation
304L-B	EDM	1 µm	25 × 24 × 22	Baseline for surface preparation
415-B	EDM	1 µm	25 × 24 × 22	
1080-B	EDM	1 µm	25 × 24 × 22	
A516-SP	EDM	0.05 µm	25 × 24 × 22	Surface preparation and machine compliance
304L-SP	EDM	0.05 µm	25 × 24 × 22	
415-SP	EDM	0.05 µm	25 × 24 × 22	
1080-SP	EDM	0.05 µm	25 × 24 × 22	

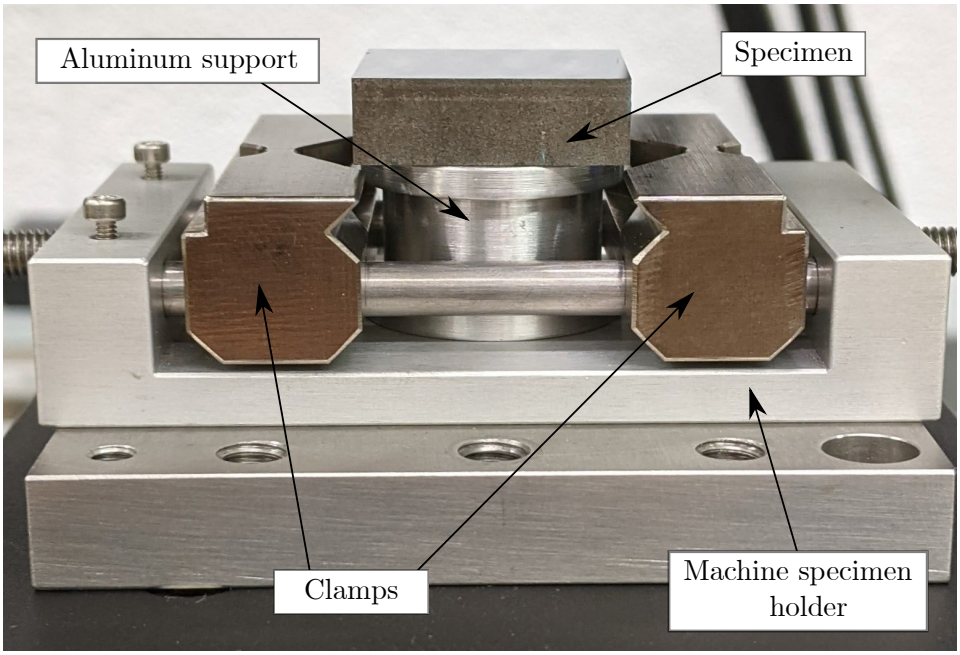

Figure 4.13 Installation setup as proposed by the manufacturer of the micro-indentation machine, Anton-Parr. The specimen, A516-G, is glued with a cyanoacrylate adhesive to a circular aluminum support to be well supported by the clamps on the machine.

Effect of specimen fabrication process

The machining process induces the hardening of a thin layer at the surface of the specimens. The indentation tests performed in this work are at the macroscopic scale, so it is interesting to study if this micro-scaled hardened layer affects the obtained results. To verify this, indentation tests were made on a conventionally machined specimen (A516-CM) and were compared to that obtained on the baseline specimen A516-B which is fabricated by EDM to minimize surface hardening.

The conventionally machined specimens had dimensions of $8 \times 25 \times 25$ mm^3, in the L $\times$ T $\times$ S directions, which were supposed to enable installation on the aluminum support. To permit the comparison to the baseline specimen, the effect of the installation of the specimen must be removed. Since the specimens were not thick enough to simply be deposited on the specimen-holder as can be done with the baseline specimen, they were instead deposited on a machined square based prism with the same dimensions. No glue was used in between this support and the specimen. Positioning of the specimens was secured by the pressure applied by the clamps of the specimen-holder. Also, the quality of the machined surfaces led to a good contact between the surfaces of the stacked specimen and support and it is thus assumed that they behave together as would have a single specimen of larger thickness. Figure 4.14 shows this installation setup.

Effect of surface preparation

To verify that the surface preparation procedure ending with a 1 µm particle size led to a surface roughness that does not influence the indentation results, a more refined surface preparation procedure was tested. This refined procedure consisted of the addition of a polishing step, using Mastermet 0.05 µm colloidal silica deposited onto a Struers MD-Chem cloth. Also, precision cuts were added in the EDM procedure, to minimize the quantity of matter which needs to be removed in the grinding steps of the surface preparation of the specimen.

The specimens A516-SP, 1080-SP, 415-SP and 304L-SP were thus prepared the same way as the baseline specimen in terms of dimensions and fabrication method, but a surface preparation with a last polishing stage using particles of 0.05 µm was used instead of stopping at particles of 1 µm. Indentations conducted on specimens with both surface preparations were then compared for all materials.

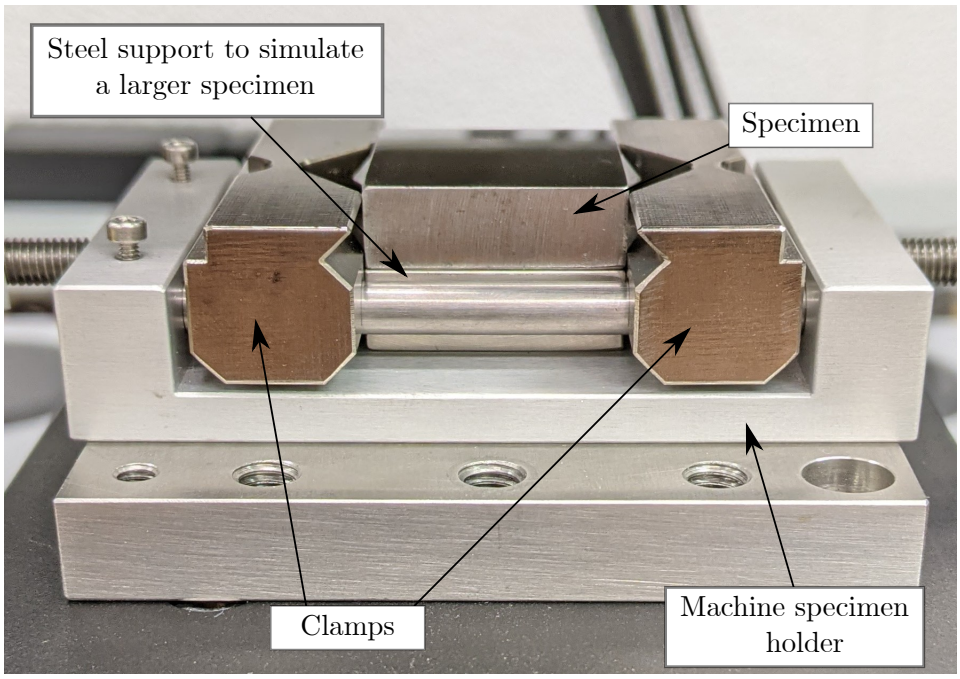

Figure 4.14 Installation setup of the conventionally machined specimen, A516-CM, by depositing the specimen onto a steel block of the same dimensions, in order to avoid using the aluminum support and glue and lead to a better comparison with the baseline specimen, A516-B.

Effect of machine compliance

The effect of the machine compliance was studied for all materials using indentation curves obtained on specimens A516-SP, 1080-SP, 415-SP and 304L-SP. The raw data was then treated using either a compliance of $C_f = 0$ µm/N or the values calculated from the direct calibration method described in the following Section 4.1.4. The resulting indentation curves were then compared.

4.1.4 Direct measurement of the machine compliance

The data treatment software, *Indentation*, provided with the MHT micro-indentation machine manufactured by Anton-Paar specifies by default a value of 0 µm/N for the machine compliance, C_f. However, through the analysis of the raw indentation data obtained on specimens A516-SP, 1080-SP, 415-SP and 304L-SP using Oliver and Pharr's equations [97] described in Section 2.3, it can be observed that C_f is not actually zero (see Section 4.2.2).

Indirect calibration procedures for C_f are not applicable to the apparatus used in this work. Indeed, these procedures use pyramidal indenters on reference materials like fused silica, in which a maximum load of 400 mN can be applied before the emergence of cracks in the corner regions of the indenter. These cracks alter the indentation results and data obtained with loads higher than this limit cannot be used to reliably calibrate C_f. Using loads below 400 mN with the MHT micro-indentation machine is not recommended since the threshold for maximum precision in the load-depth curves is said to be at a minimum of 500 mN. It is thus not possible to obtain reliable indentation data enabling C_f calibration from this machine without the apparition of cracks in the reference material used.

This supports the conclusions of Section 2.2.1, particularly that a direct measurement method for C_f would be more appropriate to maximize the precision of the obtained value and to study the effects of this parameter on indentation tests. A direct measurement method for C_f was therefore developed by using a similar approach to that used by Van Vliet et al. [126] and applied to the experimental setup used in this work. This direct procedure is possible through the conducting of an indentation test using a flat punch indenter with a large radius on a very rigid material. The contact area generated by the test is thus large, creating a small stress on the specimen. The high stiffness of the specimen limits even further its deformation. These conditions enable the hypothesis that all the displacement measured by the machine during the test is entirely attributable to the deformation of the experimental setup, which is directly linked to the machine compliance.

Materials and indenters

The indenter used for the direct calibration of C_f was a tungsten carbide flat punch indenter with a radius $R = 1$ mm. Two aluminum oxide specimens were used, AO-1 and AO-2, with a square surface of 25×25 mm^2 and a thickness of 8 mm.

To study the effect of the applied load, 10 indentation tests were made for maximum forces of 5, 10, 15, 20, 25 and 30 N on both specimens AO-1 and AO-2. 30 N is the maximum load that can be applied with the testing machine.

Alignment

Van Vliet et al. [126] observed alignment issues between the cylindrical platen they used to replace the indenter and the specimen. Even with a specimen presenting an excellent parallelism with the surface of the testing apparatus on which it was deposited, alignment issues remained. These are due to the unavoidable misalignment in the experimental setup itself, as well as in the flat punch indenter, where the axis of the indenter may not be perfectly normal to the flat surface of the indenter [103].

To overcome the alignment problems and enable proper contact between the specimen and indenter surfaces, the specimen installation was modified. A new specimen holder was machined and added to the setup. It is a steel block containing a cavity in which a self-leveling material was deposited, followed by the specimen. With the indenter, a displacement was then imposed towards the specimen and upon contact, the specimen pivoted in the self-leveling material until its surface was in contact with the indenter surface. The displacement was then held constant until the hardening of the self-leveling material was complete. The new specimen holder, the final result of the installation as well as an illustration of the alignment procedure are shown in Figure 4.15.

The choice of self-leveling material was based on its stiffness after hardening, its viscosity before hardening as well as its hardening time. The material had to have an elastic modulus which was as high as possible to avoid increasing too much the compliance of the experimental setup, which would then contribute to the overestimation of C_f. The viscosity of the material before hardening had to be low enough to enable the pivoting of the specimen and the minimizing of its final thickness, while not too low to avoid the specimen sinking at the bottom of the cavity in the specimen holder under its own weight. Finally, the hardening time had to be over about 3 minutes to permit the installation and application of the displacement on the indenter, but not too long, again to avoid the sinking of the specimen into the self-leveling material.

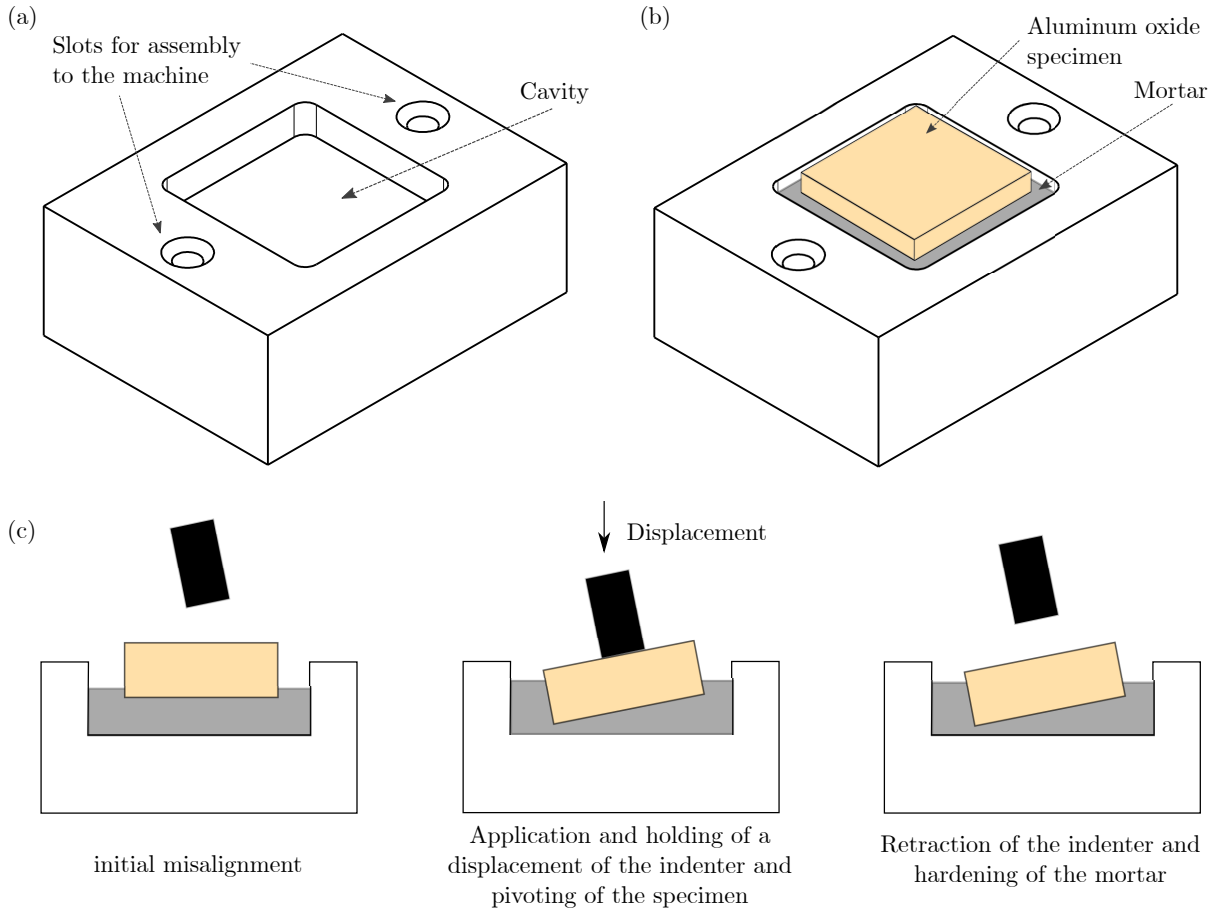

Figure 4.15 Illustration of the specimen installation conceived to overcome alignment issues: (a) New specimen holder designed to enable the alignment; (b) Final installation setup including specimen, self-leveling material (mortar) and the new specimen holder; and (c) Illustration of the alignment process through the application of a displacement to the indenter towards the specimen and pivoting of the specimen upon contact (exaggerated misalignment for schematic purpose).

Several adhesives and polymers like cyanoacrylate glue and epoxy were fist considered but their low stiffness (typically $E < 4$ GPa) and low viscosity did not fulfill the requirements. It was finally determined that a cement material would fulfill the requirements, since these materials have higher stiffnesses ($E > 15$ GPa after ageing) and higher viscosities, being more of a paste than a liquid before hardening. Particularly the SikaQuick 2500 mortar was selected, which is characterized by the manufacturer as having an elastic modulus of 35 GPa after ageing in ideal conditions.

A small quantity of mortar and water were mixed following the prescribed ratio of 11.2 ml of water to 100 g of mortar. The hardening time needed to reach the final geometry before ageing was estimated to an hour, during which the displacement was held constant by the indenter. After this, the assembled specimen-mortar-specimen holder setup was removed from the MHT micro-indentation machine and ageing of the mortar for 28 days was done before conducting the direct C_f calibrations. During this period, the mechanical properties of the mortar increased, which then lowered the deformation of the mortar during the tests and minimized the corresponding error on the calibrated value of C_f. During the ageing period, the indentation machine was not used and no modifications were made to the setup until the calibrations of C_f were conducted, in order to preserve the quality of the alignment.

Figure 4.16 shows the resulting assembled specimen-mortar-specimen holder setup for specimen AO-2 after ageing was completed.

Corrections applied to the measured value of C_f

During the direct calibration tests for C_f, it must be noted that the machine is not exactly in the same state as when typical indentation tests are conducted. Indeed, the usual specimen holder was removed and replaced by a new design. Also, a layer of mortar was added under the specimen. Finally, if the compliance of the machine only is sought, the aluminum oxide specimen also constitutes an addition. The calibrated value of the machine compliance must then be corrected for all these changes. To do so, the contribution to the compliance of all these additions, or retractions, when compared to the typical setup can be estimated and removed, or added, to the calculated compliance value C_f^*. The corrected compliance is thus computed through:

$$C_f = C_f^* + C_O - C_N - C_M - C_{AO}, \tag{4.1}$$

where C_f is the corrected machine compliance and C_f^* is the compliance directly calculated with the flat punch indenter. The compliances, C_O, C_N, C_M and C_{AO} are those associated

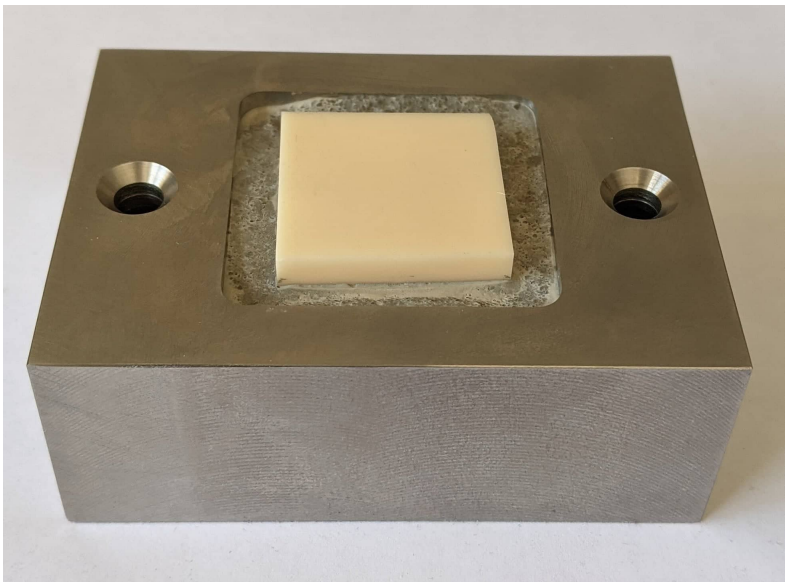

Figure 4.16 Final setup for direct calibration of the machine compliance with specimen AO-2 after the ageing of the mortar.

with the original specimen holder, the new specimen holder, the mortar and the aluminum oxide specimen, respectively.

The contribution of the aluminum oxide specimen deformation, C_{AO}, in which the stress and strain fields are complex, was estimated through a finite element simulation. The details of this model are given in Section 5.3.

An advantage of using a flat punch indenter geometry is the corresponding constant contact area, which leads to a theoretically linear indentation curve. This means that the compliance expected from the coupling specimen-indenter is constant with the application of the load and is thus easy to correct.

The elastic properties of aluminum oxide used in the finite element model were measured by ultrasound with a 16-channel Z-Scan multi-element transducer from Zetec. For the elastic modulus, the V112-RM compression probe with 10 MHz frequency from Olympus was used. To obtain the Poisson's ratio, V156-RM vertical shear probe with 5 MHz frequency from Olympus was used. Data treatment was done through the Ultravision software, version 1.5.

This technique necessitates the density of the material to estimate the elastic properties. Density measurements were thus conducted with a density determination kit enabling to use Archimedes' principle with a OHAUS balance. Five measurements were made for each aluminum oxide specimen.

The values of C_O, C_N and C_M can be obtained with uniaxial elastic compression analysis by:

$$C_i = \frac{l_i}{A_i E_i}, \tag{4.2}$$

where l_i is the thickness of the considered component, A_i is the surface on which the load is applied and E_i is the elastic modulus of the component. The index i refers to the three components considered for the calculation. Table 4.9 shows the corresponding values of l_i, A_i and E_i used as well as the compliances C_O, C_N and C_M obtained with those values.

The load being applied to the specimen, it was assumed that it was evenly distributed on the surface under the specimen (25 × 25 mm^2) before reaching the mortar or the specimen holder. Since the mortar has the lowest stiffness of the setup, it was assumed that the area on which the load is applied remained the same when transferred to the specimen holder without dispersing further into the mortar.

4.2 Results and discussion

The results of the experimental indentation study are presented in the following sections. Specifically, the studies of the effect of different experimental parameters on indentation data are presented in Section 4.2.1, followed by the outcomes from the direct calibration of the machine compliance in Section 4.2.2.

4.2.1 Study of the effect of experimental parameters on indentation results

This section demonstrates the effects of the technique used to install the specimens on the testing apparatus, the fabrication process used to cut the specimens and the surface preparation procedure on indentation data. The effect of the machine compliance is studied in

Table 4.9 Values of thickness, l_i, area, A_i, and elastic modulus, E_i, used to calculate the compliances C_O, C_N and C_M with Eq. (4.2), associated with the original specimen holder, the new specimen holder and the mortar.

Component	Material	l_i (mm)	A_i (mm^2)	E_i (MPa)	C_i (mm/N)
Original specimen holder	Aluminum	4.8	25 × 25	70 000	$C_O = 1.10\times 10^{-7}$
New specimen holder	Steel	22.5	25 × 25	210 000	$C_N = 1.71\times 10^{-7}$
Self-leveling material	Sika Quick 2500 mortar	2	25 × 25	35 000	$C_M = 9.14\times 10^{-8}$

Section 4.2.2, along with the description of the result obtained by applying the direct calibration method previously described in Section 4.1.4.

Effect of the technique used to install the specimen on the testing apparatus

The expected effect of using the aluminum support which requires the addition of a layer of glue to the sample was an increase of the overall compliance of the experimental setup. A non-uniformity in the compliance with the position in the specimen where the indentation tests are made was also expected, since the thickness of the glue is not perfectly uniform.

The obtained results from the indents made in the baseline specimen, A516-B, and the specimen which required the aluminum support and the glue, A516-G, are shown in Figure 4.17 and confirm both these hypotheses. Figures 4.17(a) and (b) compare the contact stiffness, S, computed for the indents as a function of their different positions in both specimens (position matrix previously shown in Figure 4.8). It can be observed that the average value of S is 4.9% lower in the case of the glued specimen, which indicates a higher compliance of the experimental setup since the stiffness is the inverse of the compliance. Also, an effect of the position is present for the indents performed in this specimen. Indeed, the values of S show a decreasing trend as the X position increases. In the Y direction, the values of S are lower for $Y = 2.25$ mm than for $Y = 1$ mm for all indents except at $X = 8$ mm. The results obtained with the baseline sample do not show such trends. S is steadier with X and no general trend is observed in the Y direction.

Figure 4.17(c) shows the obtained indentation curves for both specimens. The effect of the increased compliance caused by the glue can once again be inferred from these curves, where the maximum depth, h_{max}, is on average 5.4% higher for the glued specimen, when compared to the baseline specimen. A higher h_{max} is caused by the increased deformation in the experimental setup due to the high compliance of the glue.

Since the layer of glue can have varying thicknesses from specimen to specimen, the effect of the use of an adhesive in the experimental setup for indentation tests can vary and is thus difficult to correct. The geometry of the baseline specimen must then be used instead of the installation of a smaller sample to the aluminum support as proposed by the micro-indentation machine manufacturer.

Effect of sample fabrication process

Figure 4.18 shows the indentation curves obtained on the baseline specimen, A516-B, which was manufactured by EDM, and compares them to those obtained with the convention-

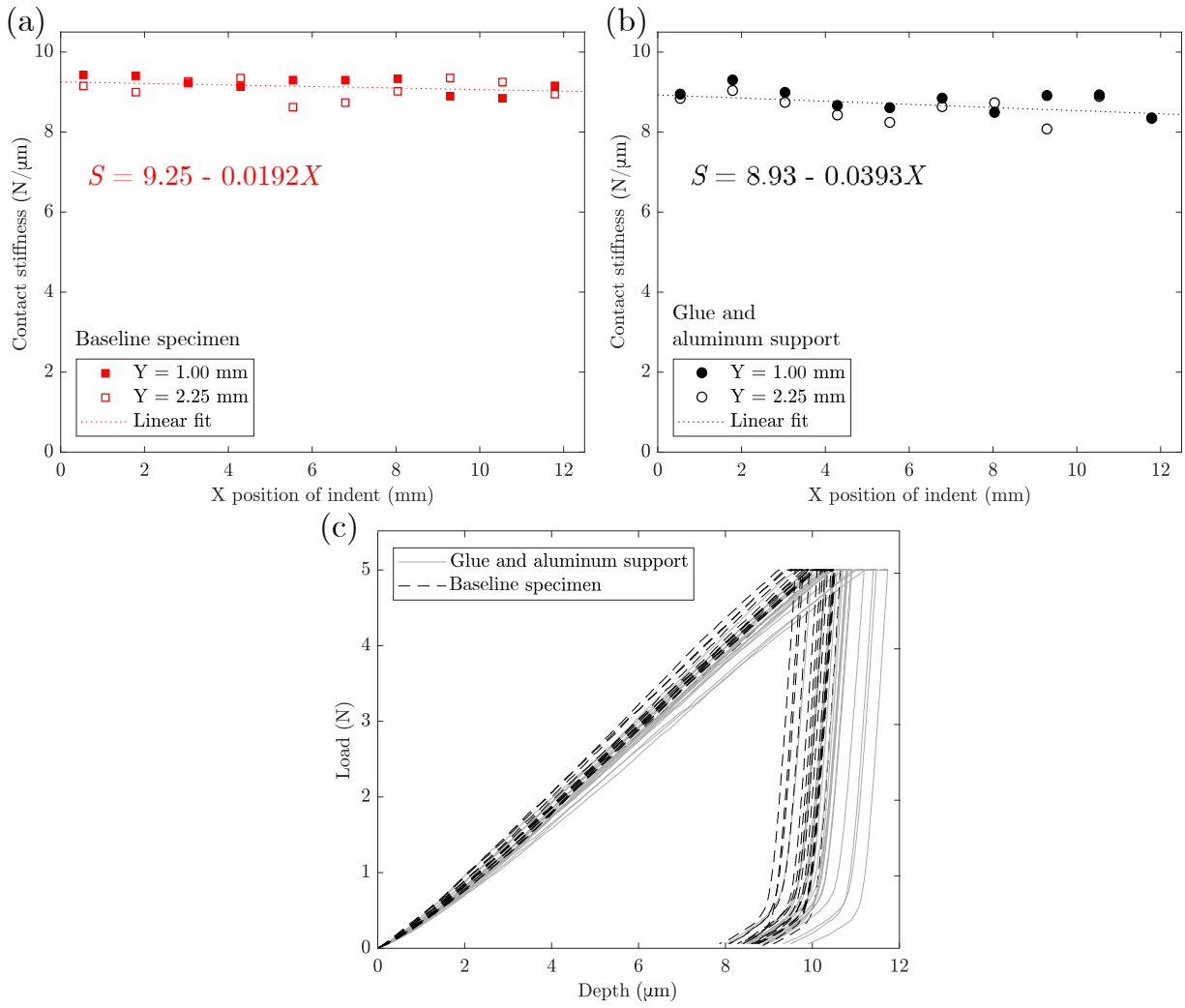

Figure 4.17 Comparison of indentation results from the ASTM A516 steel baseline specimen and the specimen installed with an aluminum support and a layer of glue: (a) and (b) contact stiffness, S, measured as a function of position in the specimens; and (c) comparison of the obtained indentation curves from both specimens. This figure shows both the increased compliance, demonstrated as a decrease in S, as well as the variability of the compliance with position in the glued sample, when compared to the baseline specimen.

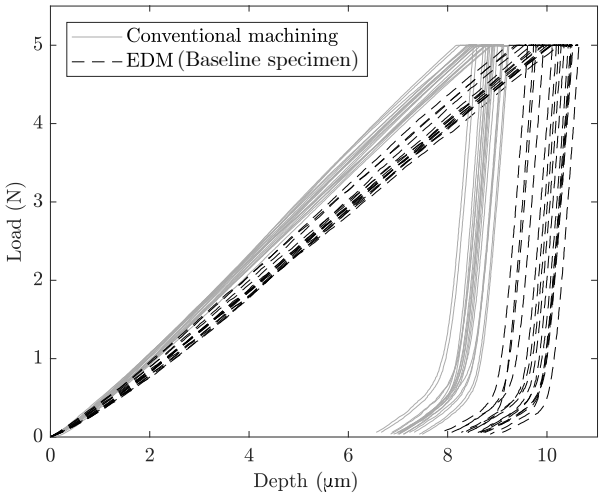

Figure 4.18 Comparison of indentation curves obtained on the ASTM A516 steel baseline specimen, A516-B, which was manufactured by EDM, with those obtained on the conventionally machined specimen, A516-CM. Significant hardening of the surface is concluded to have taken place in the conventionally machined specimen as observed by the decrease in maximum indentation depth, when compared to the baseline specimen.

ally machined specimen, A516-CM. For the same load, the average maximum depth, h_{max}, obtained in the conventionally machined sample is 12.6% lower than that obtained in the baseline sample. This demonstrates that significant surface hardening took place during the machining of specimen A516-CM which influences the indentation curves. EDM is therefore the fabrication process which must be used to manufacture specimens to reduce the amount of surface hardening and increase indentation results reliability.

Effect of surface preparation

Figure 4.19 shows the indentation curves and imprints obtained for all baseline specimens, for which the last step of the surface preparation was a polishing with 1 µm particles (A516-B, 1080-B, 304L-B and 415-B), when compared to those obtained for specimens which were polished further with 0.05 µm particles (A516-SP, 1080-SP, 304L-SP and 415-SP). The differences between the maximum load, P_{max}, contact stiffness, S, residual depth, h_r, and maximum pile-up height, u_{max}, obtained for both surface preparation procedures are quantified in Table 4.10.

It can be observed that the obtained loading curves produced with both surface preparation procedures are highly similar, with differences smaller than 2% over the curves for all materials. The contact stiffness is also unchanged, with differences under 1.3% for all materials except ASTM A516, for which the error is 5.7%. Since no trend is observed in the variation

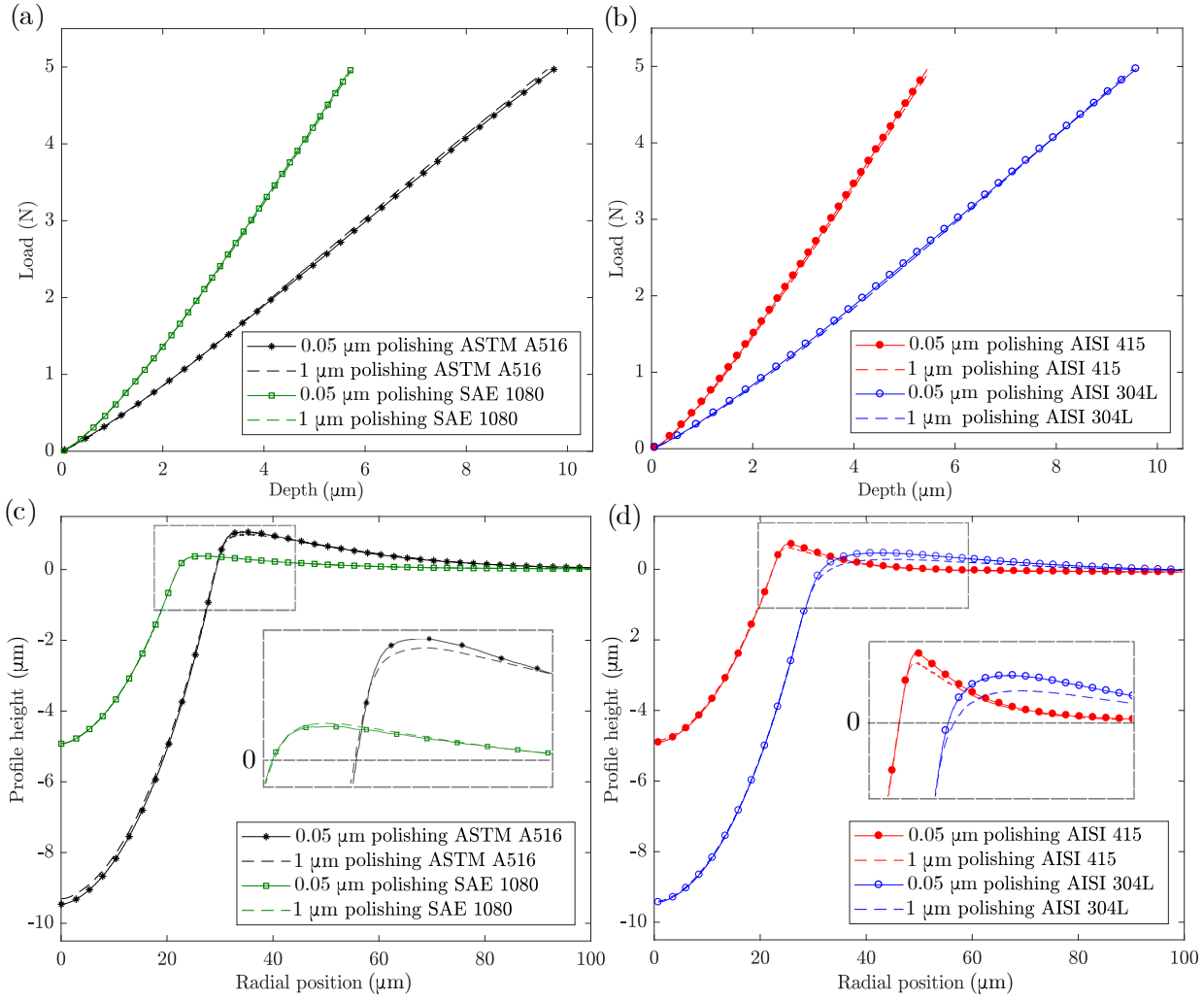

Figure 4.19 Comparison of experimental indentation data obtained on the baseline specimens, for which the last step of the surface preparation was a polishing with 1 µm particles (A516-B, 1080-B, 304L-B and 415-B), when compared to those obtained on specimens which were polished further with 0.05 µm particles (A516-SP, 1080-SP, 304L-SP and 415-SP): (a) and (b) indentation curves; and (c) and (d) residual imprints. Only two materials are displayed per graph for clarity. An increase in the pile-up height is observed when surface preparation is refined, ranging from 4.4% for SAE 1080 to 45.6% for AISI 304L.

Table 4.10 Differences in maximum load, ΔP_{max}, contact stiffness, ΔS, residual depth, Δh_r, and maximum pile-up height, Δu_{max}, observed when refining the surface preparation procedure from that ending with a polishing step using 1 µm particles, to using 0.05 µm particles. The most significant effect is an increase in pile-up height for all materials when the polishing is done with smaller particles.

Material	ΔP_{max} (%)	ΔS (%)	Δh_r (%)	Δu_{max} (%)
SAE 1080	-0.5	-0.2	0.2	4.4
ASTM A516	1.3	5.7	1.6	6.9
AISI 415	-1.3	1.3	1.0	14.2
AISI 304L	0.6	1.0	0.3	45.7

of S with surface preparation when comparing the different materials, it is hypothesized that the higher change in S for ASTM A516 has not been caused by the surface preparation refinement but by other experimental errors, like perhaps a slight difference in material properties from specimen A516-B to A516-SP.

The effect of the surface preparation is more pronounced on the indentation residual imprint, but only in the pile-up region. Indeed, the residual imprint topographies in the contact region are very close, the highest difference in this region being at the residual depth, h_r, and is below 2% for all materials. The difference appearing in the pile-up region is more significant, with errors on u_{max} ranging from 4.4% to 45.7% for the studied steels. These results support the fact that the polishing procedure affects mostly a small layer at the surface of the specimen. Also, the trend is an increase in the pile-up height, meaning that the material is more easily deformed in this region with a better polishing procedure. This was expected, since the addition of a finer polishing step removes material which could have been hardened during the mechanical grinding of the specimens, leaving softer material exposed. Furthermore, a smoother surface finish leads to a smaller friction coefficient, which makes it easier for the material to slide under the indenter, favouring piling-up behaviour.

It is interesting to note that the magnitude of the effect induced by refining the final polishing step on pile-up height varies significantly with the materials studied. The material which is the most affected, AISI 304L, is also the one which presents the highest strain hardening behaviour (see Table 4.1), and is thus most suitable for surface hardening during mechanical grinding. However, the second most affected material is AISI 415, which is the material with the lowest strain hardening behaviour. An explanation could be that the polishing using a final step with 1 µm particles on specimen 415-B was of lower quality than for the other materials, showing an increased difference between the two procedures. The difference in pile-up height induced by refining the polishing procedure for ASTM A516 and SAE 1080

are quite similar, with values of 4.4% and 6.9% respectively. These materials have comparable strain hardening behaviours and both present a plastic plateau, but ASTM A516 has a lower yield stress and thus has a lower hardness. Surface preparation is harder and leads to a lesser quality when softer materials are used. Perhaps there was more surface hardening in the specimen polished up to 1 µm particles for ASTM A516, when compared to SAE 1080, and the removal of this hardened layer with a polishing using 0.05 µm particles would then have a greater effect for ASTM A516.

Since the pile-up region of the imprint can be highly affected by surface preparation, depending on the material, the refined polishing procedure using 0.05 µm particles will be used in subsequent indentation tests. It is possible that using a final polishing step with 0.05 µm is not sufficient to remove all effect of surface preparation. Further work could be conducted to investigate if further refining the polishing procedure would have a significant impact on the indentation residual imprints.

4.2.2 Direct measurement of the machine compliance and its effect on indentation curves

This section first presents the analysis of indentation results without correcting the raw data for the contribution of the machine compliance, C_f, followed by the results of the direct measurement of C_f. Finally, the extent of the effect of the measured C_f on the indentation curves for the studied materials is analyzed.

Results using $C_f = 0$

Table 4.11 shows the different elastic moduli computed with the Oliver and Pharr [97] method when assuming a machine compliance $C_f = 0$ µm/N as well as the errors on these values, when compared to the moduli measured by tensile tests. The contact area was estimated by calculating the area of residual imprints of indentation to consider the material piling-up.

The errors on the evaluation of E range from -21.8% to -26.8%. Since these values are significantly high, similar in magnitude for all materials, and are negative, it can be hypothesized that the machine compliance is in fact not 0 µm/N. A correction for the machine compliance would have the effect of increasing the contact stiffness of the indentation curve and thus increasing the value of the extracted elastic modulus.

Table 4.11 Elastic moduli computed with the Oliver and Pharr method and a machine compliance of 0 µm/N when using an experimentally measured contact area for indentations conducted on specimens 1080-SP, A516-SP, 415-SP and 304L-SP, E_0, compared to the experimental elastic moduli, E, calculated from tensile experiments. The errors induced by neglecting the compliance, ΔE_0, are also shown. Subscripts refer to the compliance value. Errors are similar and negative for all materials, pointing to a non-null compliance of the indentation testing apparatus.

Specimen	E (GPa)	E_0 (GPa)	ΔE_0 (%)
1080-SP	205	158.6	-22.6
A516-SP	208	152.3	-26.8
415-SP	195	152.5	-21.8
304L-SP	199	151.0	-24.1

Direct measurement of C_f

Figure 4.20(a) shows the raw flat punch indentation curves obtained on specimen AO-2 for a maximum load of 30 N. Similar curves were obtained on specimen AO-1. The results show that the contact detection is inconsistent and the indentation curves do not have the perfectly linear aspect expected for flat punch indentations. These observations lead to the hypothesis of an imperfect contact between the indenter and the specimen, even after the alignment procedure. Also, the curves show a residual permanent displacement, observed by the difference in the loading and unloading parts of the curve. Since the aluminum oxide specimen and the indenter are expected to have elastic behaviours, this residual displacement could have been caused by micro-cracking of the mortar, leaving a residual displacement of the ceramic specimen into the mortar. No experiments were conducted to observe the micro-cracking so this remains a hypothesis. To avoid the effect of this permanent displacement, the analysis conducted is done solely using the unloading curve data, which is considered purely elastic.

Figure 4.20(b) shows an example of indentation curves for each applied load on specimen AO-2, where a correction for contact detection was applied. It can be observed that the loading curves at the different applied loads coincide, showing good repeatability. Since the loading time is 30 s, no matter the maximun load, the loading rate increases with the applied load. It is thus concluded that the loading rate has no effect on these measurements and hence, on the machine compliance.

Figure 4.21 shows the average contact stiffness, S, measured at the onset of unloading as a function of the applied load, for both specimens, AO-1 and AO-2. The residual misalignment evidenced by the contact detection inconsistency is also shown by the increase and

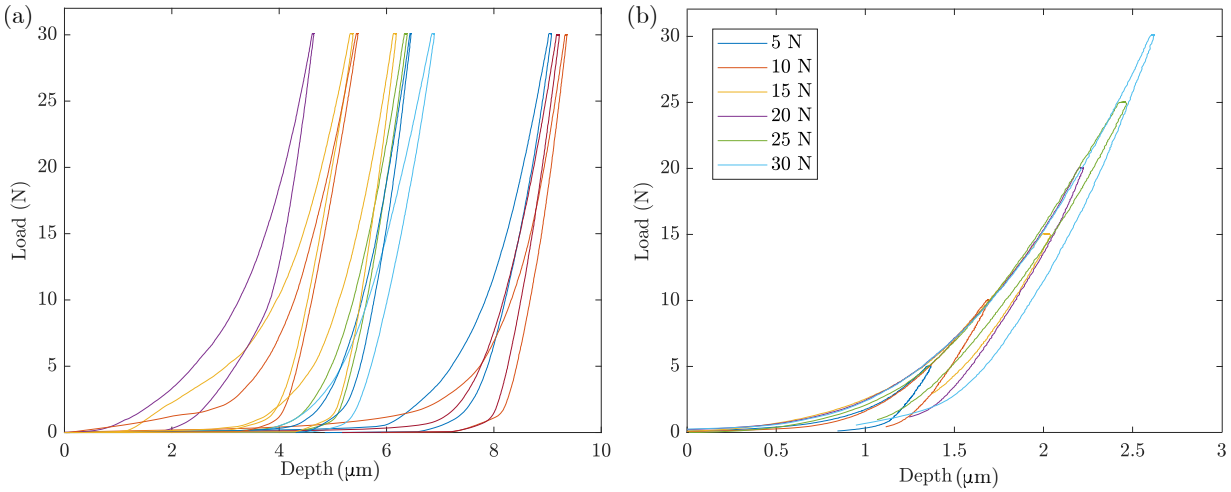

Figure 4.20 Flat punch indentation results obtained on specimen AO-2: (a) raw indentation curves obtained with a maximum load of 30 N and (b) example curves for each applied load with contact detection correction. These graphs show contact detection inconsistency as well as a residual displacement in the indentation curves, which were expected to be linear [58].

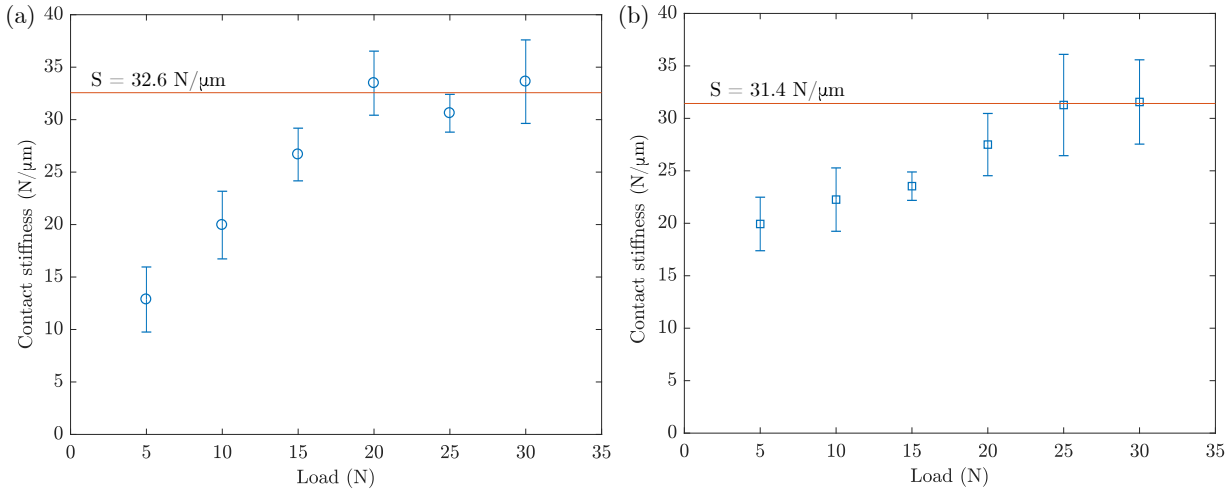

Figure 4.21 Average contact stiffness measured at the onset of unloading as a function of applied load, for both specimens: (a) AO-1; and (b) AO-2. Error bars represent one standard deviation. The stiffness increases with applied load, because of the increase in contact area, until it reaches a plateau once a complete contact has been reached between the surface of the specimen and the indenter.

stabilization of S with increasing load. Indeed, as the load increases, so does the contact area, until the point where the whole surface of the indenter is in contact with the surface of the specimen, whereupon S reaches a stable maximum value. It can also be observed that the alignment was different for both specimens. This is seen through the value of S of specimen AO-1 at 5 N being smaller than that of specimen AO-2 for the same load by 35.5%. The rate of increase of S as a function of the applied load is also different for both specimens: that of specimen AO-1 is estimated to be 2.5 times that of specimen AO-2. However, since both specimens converge to very similar values of S ($\Delta S = 3.5$ %), we can conclude that the misalignment was small enough to be corrected by the applied loads and that it did not affect the reliability of the directly calibrated machine compliance. The average value of S at the plateau for both specimens is 32.0 N/µm, which leads to a total compliance of the setup $C_f^* = 0.0313$ µm/N.

To compute the actual machine compliance, C_f, though Eq. (4.1), the compliance due to the deformation of the specimen must estimated. The density of the aluminum oxide specimens was measured at 3.91 g/cm^3 with a standard deviation of 0.0011 g/cm^3. This value led to the computation of the elastic properties of the aluminum oxide specimens with ultrasonic tests as $E = 385.5$ GPa and $\nu = 0.233$, with respective standard deviations of 2.9 GPa and 0.0018. Using these values as material properties in the flat punch indentation finite element model, the compliance of the specimen to be removed from the direct measurement, C_{AO}, was estimated at 1.235 $\times 10^{-3}$ µm/N (see Section 5.4.3 for details on the finite element analysis). The corrected machine compliance is then computed at 0.0299 µm/N.

Effect of machine compliance

Table 4.12 shows the different elastic moduli computed with the Oliver and Pharr [97] method when using the directly calibrated value of the machine compliance, $C_f = 0.0299$ µm/N, for the four studied materials. The differences between these extracted moduli and to those obtained by tensile tests are also given and compared to that obtained previously when assuming a machine compliance of 0 µm/N (see Table 4.11).

The computed elastic moduli are improved by the compliance correction, evidenced by a reduction of the error with the value measured by tensile tests ranging from 58.1 % to 84.5 % for the different materials. The remaining error on the extracted elastic modulus ranges from 3.5 % to 10.1 %, demonstrating that the extracted machine compliance was reliably measured, as well as the importance of correcting for this parameter in indentation analysis.

Figure 4.22 shows the raw indentation curves obtained on specimens 1080-SP, A516-SP, 415-SP and 304L-SP, when compared to those corrected for the contribution of the machine

Table 4.12 Elastic moduli, $E_{0.0299}$, computed with the Oliver and Pharr method and the measured machine compliance of 0.0299 µm/N when using an experimentally measured contact area for indentation conducted on specimens 1080-SP, A516-SP, 415-SP and 304L-SP; error on the estimation of the elastic moduli compared to the expected values measured by tensile experiments, $\Delta E_{0.0299}$, and improvement on the absolute value of the error, when compared to when using a null machine compliance.

Specimen	E	$E_{0.0299}$ (GPa)	$\Delta E_{0.0299}$ (%)	$\frac{\lvert\Delta E_{0.0299}\rvert - \lvert\Delta E_0\rvert}{\lvert\Delta E_0\rvert} \times 100$ (%)
1080-SP	205	212.2	3.5	-84.5
A516-SP	208	228.0	9.6	-64.2
415-SP	195	205.0	5.1	-76.6
304L-SP	199	219.0	10.1	-58.1

compliance using the directly calculated value $C_f = 0.0299$ µm/N. It can be seen that not taking into account the compliance introduces errors on the indentation loading curves below 2.6 % for all materials. It is also shown that the effect is greater for harder materials, SAE 1080 and AISI 415, since the same displacement results from the machine deformation at the same load, but the material displacement is lower, leading to a higher relative error on the measured indentation depth.

The highest effect of not correcting for C_f is observed on the unloading curves, the difference on S ranging from 21.9 % to 29.1 %. A difference between harder and softer materials is also observed here. For harder materials, the depth for the same load is smaller, and so is the contact area which leads to a smaller S. Since the correction is applied as a function of load, the relative error on a smaller S will be higher. Since the extraction of the elastic modulus is highly dependent on S, the effect of C_f on this parameter explains the large errors on E obtained when neglecting to correct for machine compliance, especially for harder materials.

4.3 Conclusions

The results shown in this chapter led to the elaboration of the experimental indentation tests done to validate the developed inverse methodology to estimate the true stress-true strain curves of metals. Specifically, it was demonstrated that for all subsequent indentation tests, specimens A516-SP, 1080-SP, 304L-SP and 415-SP must be used to avoid:

- The increased and variable compliance due to the presence of the glue in the setup for the installation method of the specimens proposed by Anton-Paar;
- The surface hardening caused by the conventional machining of the specimens;

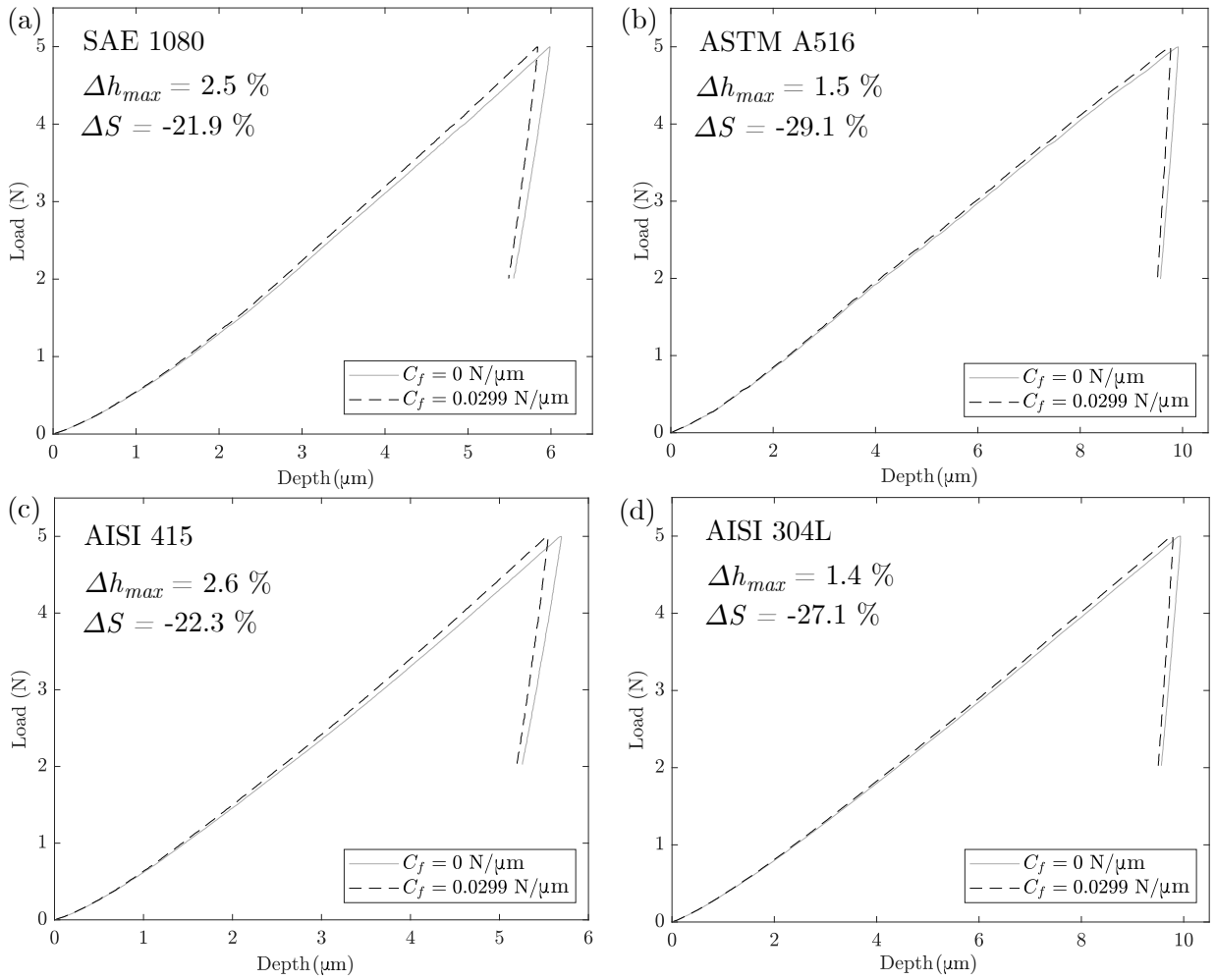

Figure 4.22 Effect of machine compliance correction on indentation curves for the four studied steels using the calibrated C_f of 0.0299 µm/N. Also shown are the relative differences in the maximum indentation depth, Δh_{max}, and contact stiffness, ΔS, induced by neglecting to correct for the machine compliance. The effect is less important on the loading curves, but the values of S are significantly affected.

- The surface hardening due to the surface preparation method.

Also, it was demonstrated that neglecting the machine compliance leads to significant errors in the contact stiffness and C_f must then be considered in indentation analysis. Finally, the method developed to directly calibrate the machine compliance led to $C_f = 0.0299$ µm/N.

CHAPTER 5 DEVELOPMENT OF INDENTATION FINITE ELEMENT MODELS

The inverse methodology developed in this thesis requires two finite element models of spherical indentation:

1. The detailed model, which is accurate and represents an experimental indentation test as closely as possible;
2. The surrogate model, which is a simplified version of the detailed model. It is therefore less accurate, but requires shorter computational times than the detailed model.

The detailed model was developed first and then simplified to create the surrogate model. In this chapter, the models are thus presented in this order. However, in the inverse method, they are used in the opposite order, as the surrogate model first serves to find a suitable starting point for the final optimization step which then uses the detailed model.

Additionally, a third finite element model, this one of a flat punch indentation, was required in the direct calibration of the machine compliance methodology (see Section 4.1.4). All three models are described below, in Sections 5.1 to 5.3. The performances of the two spherical indentation models are then discussed in Section 5.4, along with the results of the flat punch indentation model.

The majority of the methods and results presented in the current Chapter and Chapter 6, were published in 2021 in the *International Journal of Solids and Structures* [123]. Some experimental methods described in Chapter 4 were also included in the publication. The reviewers of this paper contributed to the improvement of the research work that follows by suggesting to add discussions on the scale of indentation and to elaborate further on the convergence behaviour of the developed method as compared to when hardening models are used.

5.1 Spherical indentation: Detailed model

The spherical indentation test was modeled through axisymmetric finite element modeling using the commercial software ANSYS Mechanical APDL 19.2. A large strain kinematics with an updated Lagrangian formulation was used. The load was applied through displacement control of the indenter, which leads to better convergence, especially when Lüders plateaus are involved.

Geometry

The specimen was modeled as a cylinder with a height h_d = 323.7 µm and radius r_d = 522.6 µm. These dimensions, determined through a convergence study, were large enough for the specimen to respond to indentation tests as a semi-infinite solid would. The geometry of the indenter was modeled to match the measured indenter profile, as described in Section 4.1.2.

Mesh refinement

The mesh comprised of 3 801 4-node general axisymmetric elements (SOLID272) and is shown in Figure 5.1(a). The smallest element size in the specimen, s_d, was 0.65 µm. The element size in the most refined region of the indenter, $s_{i,d}$, was set to be twice as large as that in the specimen, *i.e.*, 1.3 µm. This ratio is believed to lead to a better convergence of finite element simulations when contact pairs are involved [4]. The most refined region of the mesh contained $60 \times 40 = 2400$ elements and the size of the elements increased gradually as moving away from this refined region to reduce the required computational time. These mesh dimensions were found after a convergence analysis of important indentation parameters, *i.e.*, the maximum load, P_{max}, the contact stiffness (the slope at the onset of unloading in the indentation curve), S, the residual depth, h_r, and the maximum pile-up height, u_{max}. The stress distributions were also studied and were observed to have converged, except for very high values in the contact region (less than 0.5 µm into the surface). Since the indentation parameters had converged, it was assumed that this had no consequence on the model results.

Boundary conditions

The vertical displacement of the bottom nodes of the specimen was restricted but not their radial displacement.

Material constitutive model

The constitutive behaviour of the specimen was modeled as a rate-independent elasto-plastic material with isotropic hardening. The von Mises yield criterion was used and an associated flow rule plasticity was adopted. The true stress-true strain curve was entered as an input through ANSYS's *Multilinear Isotropic Hardening Model* to eliminate the assumption of a pre-defined hardening model. This was done by prescribing several points of the true stress-true strain curve, *i.e.*, the optimization variables (defined in Section 6.1.2). Poisson's ratio was set to $\nu = 0.33$ and was not included as an optimization variable.

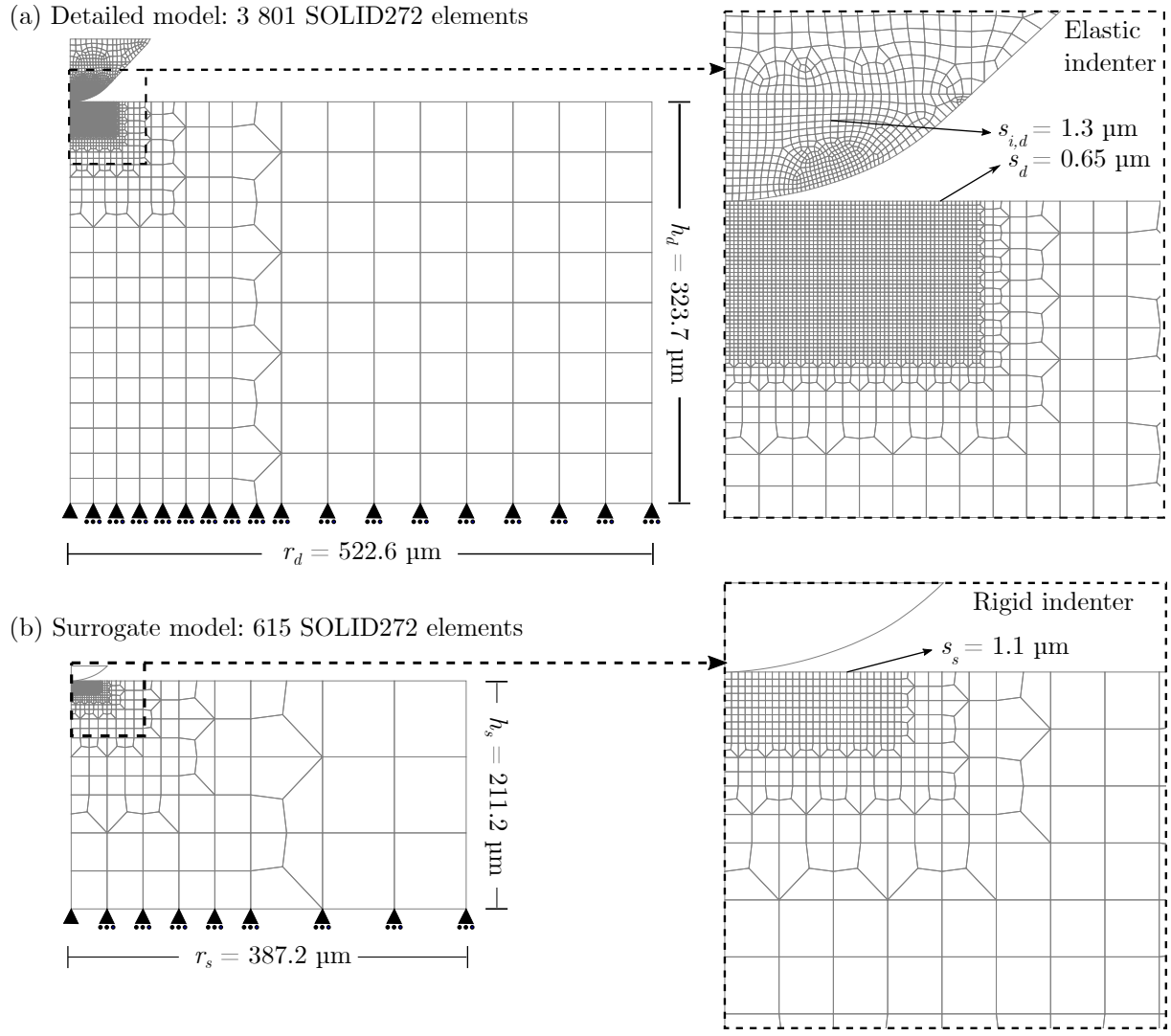

Figure 5.1 Finite element meshes for spherical indentation tests with $R = 50$ µm, used in the: (a) detailed model; and (b) surrogate model. For each model, the height, h_d or h_s, and radius, r_d or r_s, of the specimen are shown as well as the smallest element size in the specimen, s_d or s_s. The element size set in the most refined region of the indenter, $s_{i,d}$, is also shown for the detailed model.

To compare the performance of the proposed method to when a predefined hardening model is assumed, additional simulations are conducted using the Hollomon or Ramberg-Osgood hardening models, previously described in Section 2.5.4. Some materials exhibit tensile curves that cannot be approximated by a power law, like structural steels showing a Lüders plateau. A hybrid model was therefore developed to incorporate a plastic plateau in the plastic behaviour of the Ramberg-Osgood model. The Ramberg-Osgood model was chosen because it led to the best fit of the hardening region of the tensile curve, defined by the region where

strains are larger than the strain at the end of the plastic plateau, for the studied steels ASTM A516 and SAE 1080. In this hybrid model, the strain is divided into elastic and plastic parts, as in Eq. (2.10). The elastic strain is again defined by Hooke's law, Eq. (2.11). The plastic behaviour of the hybrid model is described by:

$$\sigma = \begin{cases} \sigma_y, & \text{if } \varepsilon_y \leq \varepsilon_p \leq \varepsilon_{pl} \\ \sigma_y + K(\varepsilon_p - \varepsilon_{pl})^n, & \text{otherwise,} \end{cases} \tag{5.1}$$

where ε_y is the yield strain and ε_{pl} is the strain at the end of the Lüders plateau. The length of the plateau, called the yield point elongation, is defined by $\varepsilon_{pl} - \varepsilon_y$.

The material behaviour of the indenter was modeled as linearly elastic with the properties of diamond: Young's modulus $E = 1\,141$ GPa and Poisson's ratio $\nu = 0.07$.

Contact and friction

The interaction between the indenter and the specimen was modeled through the augmented Lagrangian method available in ANSYS for node-to-surface contact problems. The indenter surface was defined as the target surface and meshed using contact elements TARGE169, which overlay the solid elements at the boundary of the indenter. The contact surface was defined on the top of the specimen to extend up to a radial position equal to the radius of the indenter. This contact surface was meshed using contact elements CONTA175, each defined by one node associated to an existing node on the specimen surface.

The effect of friction was incorporated in the model by adopting Coulomb's friction law. The exact value of the friction coefficient, μ, between the indenter and the surface is not known, and it is challenging to measure this quantity experimentally. However, studies have shown that the effect of friction generally saturates at a value larger than $\mu = 0.2$ and many authors used this limiting value as an estimate for the friction coefficient [28, 65].

Values of μ between 0.1 and 0.3, at intervals of 0.025 were tested for all materials. It was found that the effect of varying μ on the indentation curves and on the contact region of the residual imprint was negligible. The difference between the maximum loads and residual depths obtained with $\mu = 0.1$ and $\mu = 0.3$ were under 2% and 1%, respectively, for all materials. The effect was more pronounced in the pile-up region of the residual imprint. Increasing μ from 0.1 to 0.3 resulted in a decrease of 17% to 27% in the maximum pile-up height, depending on the material. The effect of varying μ decreased with increasing μ, saturating around a value of 0.225 ± 0.025, depending on materials. A value of $\mu = 0.2$ led to the best agreement between simulation and experimental indentation residual imprints, and

this value was thus used in the finite element models.

5.2 Spherical indentation: Surrogate model

The surrogate model is a simplified version of the detailed model, which uses a pre-defined hardening model to describe material behaviour.

Simplifications to the detailed model

We looked for simplifications that reduced the computational time while inducing variations lower than a threshold of 20% in important indentation parameters for simulated indentations with a maximum load of 5 N on all materials. These parameters are the maximum load, P_{max}, the contact stiffness (the slope at the onset of unloading in the indentation curve), S, the residual depth, h_r, and the maximum pile-up height, u_{max}.

The first simplification that was investigated was the assumption of a frictionless contact, which resulted in an error above 20% in the residual imprints profiles.

Two investigated simplifications had the desired effect of reducing the computation time while not deteriorating excessively the solution. A comparison between indentation data obtained from the surrogate and detailed models is given in Section 5.4.2. These simplifications are:

1. Modeling the indenter as a rigid surface instead of as a deformable body;
2. Reducing the number of elements in the mesh from 3801 SOLID272 elements to 615 by:
   (a) increasing the smallest element size from $s_d = 0.65$ to $s_s = 1.1$ µm in the specimen;
   (b) reducing the size of the most refined region from 60×40 to 26×10 elements;
   (c) reducing the dimensions of the specimen from $h_d = 323.7$ µm and $r_d = 522.6$ µm to $h_s = 211.2$ µm and $r_s = 387.2$ µm.

The mesh of the surrogate model is shown in Figure 5.1(b). The computational time for this model was between 8 to 10 times shorter than the detailed model, depending on the material modeled.

Material elasto-plastic behaviour

The elasto-plastic behaviour of the specimen was modeled using a Ramberg-Osgood power-law (Eq. (2.13)) instead of using the *Multilinear Isotropic Hardening Model* to reduce the

number of variables and eliminate the constraints. This particular power law model was chosen since it leads to the best preliminary approximations for all four studied materials.

5.3 Flat punch indentation for direct calibration of machine compliance

The same approach regarding the boundary conditions, contact and friction were used for the flat punch indentation model as those used in the detailed spherical indentation model.

Geometry

The specimen was modeled as cylindrical with a height $h = 8$ mm and radius $r = 16.08$ mm. The height is that of the true specimen and the radius was large enough as to not influence the simulated indentation curve.

The geometry of the indenter was modeled using the geometry provided by the manufacturer, that is a cylinder with a height $h_i = 250$ µm and a radius $r_i = 1$ mm. The sharp corners of the indenter induced high local stress values. However, this was found not to influence the computed specimen compliance. Indeed, modeling a blunter radius at the edge of the indenter did reduce local stress values, but did not influence the resulting indentation curve.

Mesh refinement

The mesh was built with the same approach as for the detailed spherical indentation model, but was scaled because of the larger dimensions and adapted to achieve the exact 8 mm height of the specimen. The mesh thus comprised of 3208 4-node general axisymmetric elements (SOLID272) and is shown in Figure 5.2. The smallest element size in the specimen, s, was 20 µm and the smallest element size in the indenter, s_i, was 40 µm.

Material behaviour

The specimen being a ceramic material, the material behaviour was modeled as linearly elastic with an elastic modulus of 385.5 GPa and a Poisson's ratio of 0.23. These values were found by ultrasound analysis of the aluminum oxide specimens, as described in Section 4.1.4.

The material behaviour of the indenter was also modeled as linearly elastic with the elastic properties for tungsten carbide given by the manufacturer of 640 GPa for elastic modulus and 0.21 for Poisson's ratio.

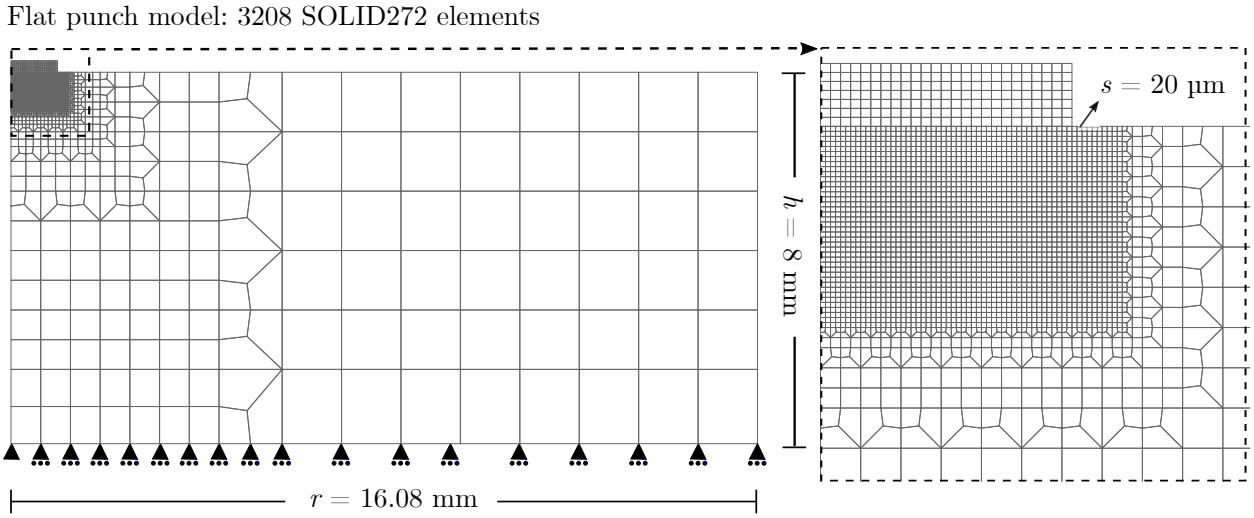

Figure 5.2 Finite element mesh of the flat punch indentation model. The height, h, and radius, r, of the specimen are shown as well as the smallest element size in the specimen, s.

5.4 Performance of the indentation finite element models

This section presents the study of the performance of the two spherical indentation models and the results obtained with the flat punch indentation model. First, the detailed model is analyzed, including a comparison of finite element results with experimental results. Then, a study of the surrogate model is conducted, which compares simulated indentation data resulting from the surrogate and detailed models. Finally, the indentation curve obtained from the flat punch indentation model is presented and briefly discussed.

5.4.1 Detailed model

The detailed model needs to approximate the indentation experiments with the highest accuracy possible. Figure 5.3 shows a comparison between experimental and numerical indentation data used to validate the detailed finite element model. The simulated indentation data were obtained using the average experimental true stress-true strain curves of each material as the input material behaviour to observe how well the model can reproduce the indentation experiments when the correct tensile curves are used.

For further comparison, Table 5.1 quantifies the modeling errors for the indentation parameters P_{max}, S, h_r and u_{max}. It can be observed that the finite element model captures the material behaviour during the indentation test with a better precision in the case of ASTM A516 and SAE 1080 steels, when compared to the two others. The error on u_{max} for AISI 415 reaches a value of -47% and the error on S and P_{max} for AISI 304L reach values

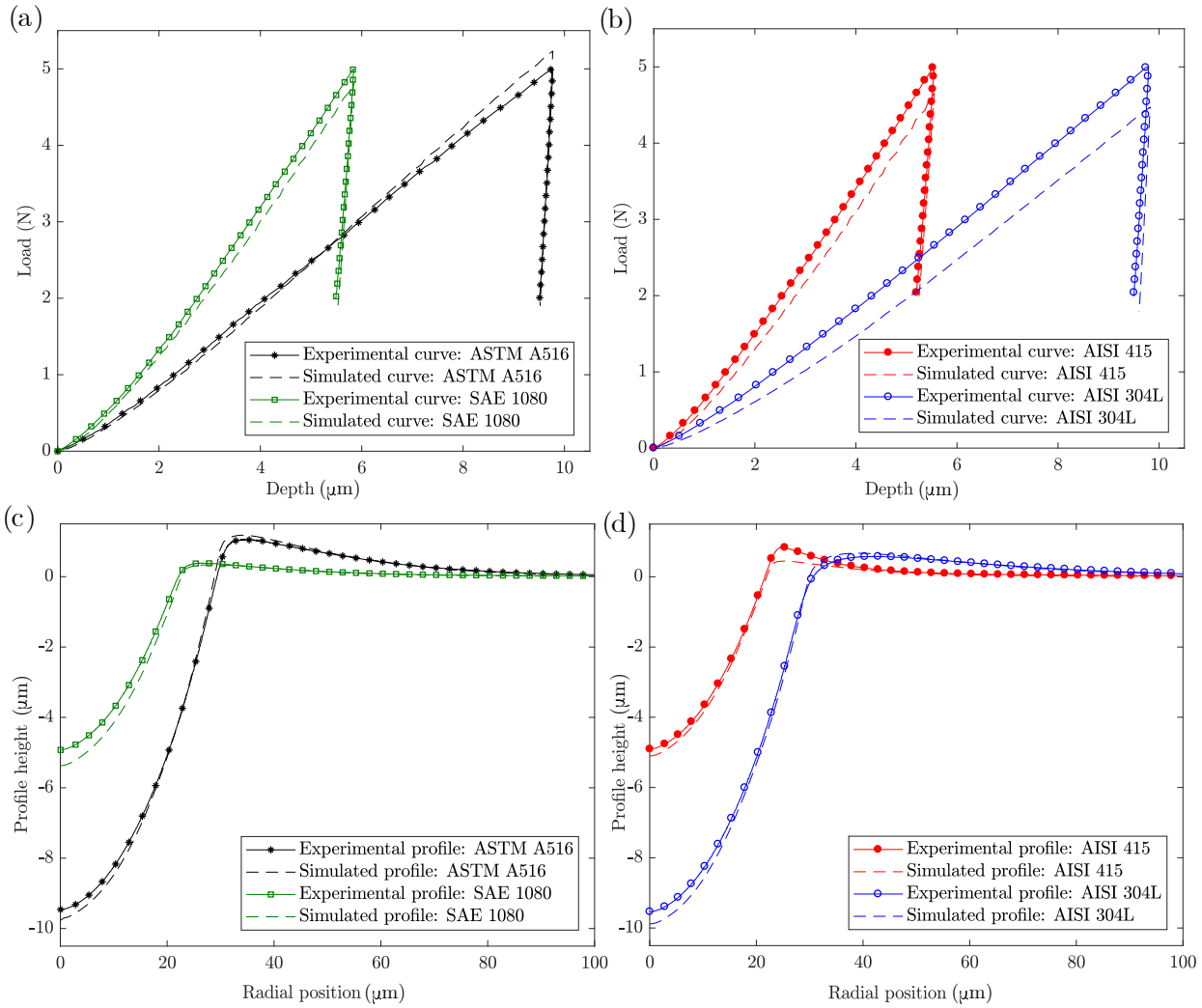

Figure 5.3 Comparison of numerical and experimental indentation data obtained with a sphero-conical indenter with $R = 50$ µm, by applying a maximum load of 5 N: (a) and (b) indentation curves; and (c) and (d) residual imprints. Only two materials are displayed per graph for clarity. The model is capable of accurately representing the indentation behaviour for ASTM A516 and SAE 1080 steels, but errors are higher for AISI 304L and AISI 415 steels.

of 20% and 10.6%, respectively. The experimental validation of the proposed methodology is thus expected to perform better for ASTM A516 and SAE 1080 steels than for AISI 304L and AISI 415 steels.

Two hypotheses were identified which could explain the increased modeling error for AISI 415 and AISI 304L: an effect of the scale of indentation, and possible strain-induced transformations taking place during the indentation process.

Table 5.1 Differences between indentation maximum load, P_{max}, contact stiffness, S, residual depth, h_r, and maximum pile-up height, u_{max}, obtained from experiments and those obtained by the detailed finite element model. Errors are particularly high in regards to u_{max} for AISI 415 steel as well as S and P_{max} for AISI 304L.

Material	ΔP_{max} (%)	ΔS (%)	Δh_r (%)	Δu_{max} (%)
SAE 1080	-3.8	1.7	9.2	-14.2
ASTM A516	4.6	5.0	3.3	9.4
AISI 415	-6.8	-2.5	4.0	-47.0
AISI 304L	-10.6	20.6	3.7	14.6

Scale of indentation

To investigate if the scale of indentation led to the sampling of a sufficient number of grains for each steel, metallographic observations of the undeformed specimen surfaces were undertaken and the number of grains or martensite blocks included in the plastic zone was estimated, as shown in Table 5.2. The size of the plastic zones were approximated from the residual imprint profiles as a circle extending to the radial position at which the pile-up height had reduced by half of its maximum value. This criteria was established from the equivalent plastic strain distributions after indenter unloading, which are presented in Figure 5.4 for the four studied steels.

Keeping in mind that layers of grains are present in the plastic zone below the surface, the indentations performed in ASTM A516 sample at least 300 grains. As a minimum number of 12 grains is suggested in the literature [28, 45], the indentation results are considered representative of the bulk behaviour for this material. This is in line with the correspondence of the finite element model and the experimental indentation data. The plastic zone of SAE 1080 is also considered to contain a sufficient amount of grains, *i.e.*, approximately 30 grains if including grains under the surface. Furthermore, considering the satisfactory correspondence between the finite element results and experimental indentation data, we conclude that the bulk properties are sampled.

The same cannot be said for the indentations in AISI 304L and AISI 415 steels, which contain on average 4 grains and 8 martensite blocks, respectively. For these materials, we consider that only the grains or martensite blocks observed on the surface are sampled as they are too large to assume that more of them are deformed deeper in the material. This could contribute to the errors observed in Figure 5.3 and Table 5.1. However, the indentation results for these two materials were very repeatable, for both the indentation curves and residual imprints after averaging, which could indicate a bulk response. A larger indenter

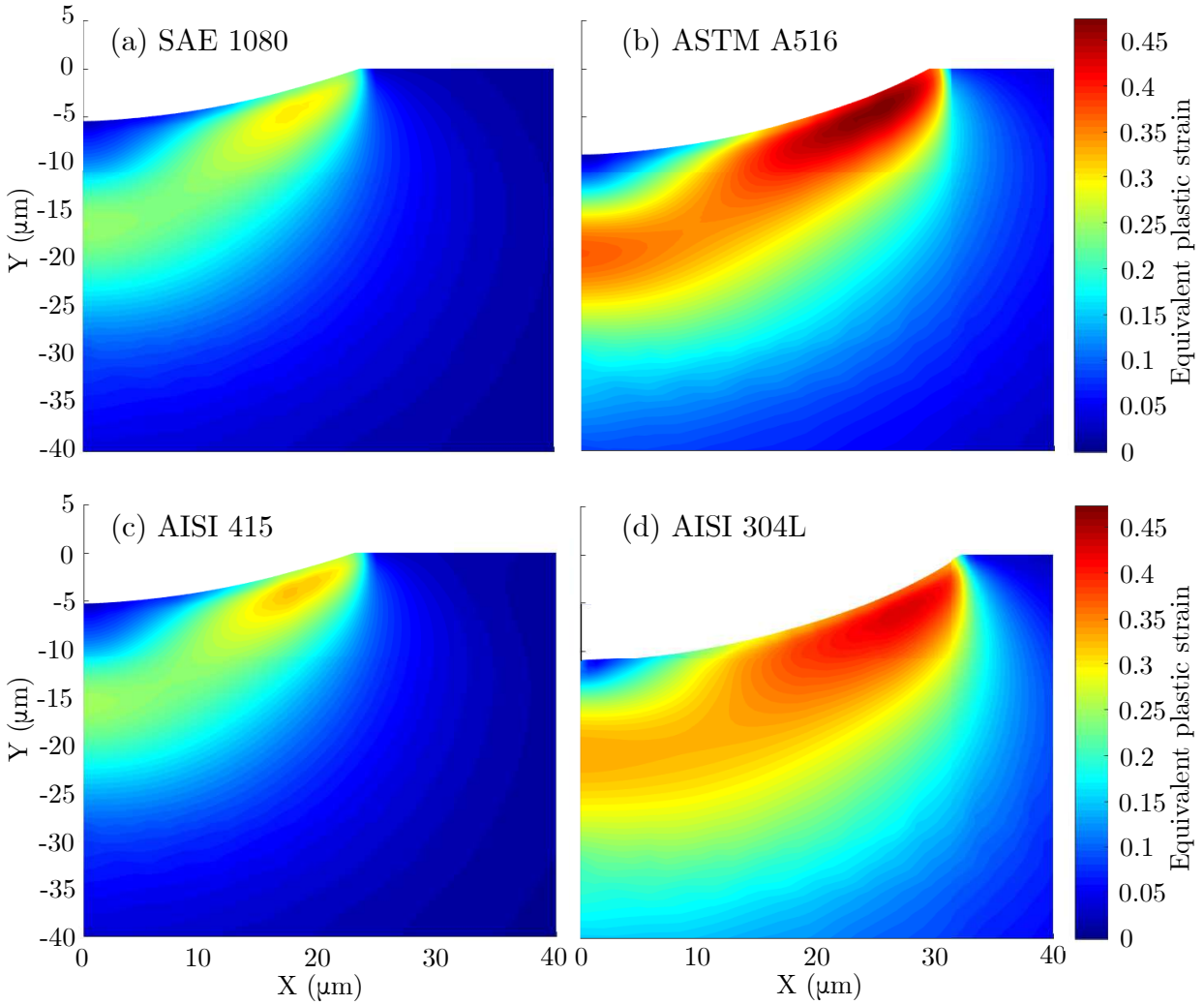

Figure 5.4 Simulated equivalent plastic strain distributions obtained with a sphero-conical indenter with $R = 50$ µm, by applying a maximum load of 5 N using the detailed finite element model. The size of the plastic zone and value of the maximum equivalent plastic strain varies for the different materials, even when the maximum indentation depth is similar (*e.g.*, ASTM A516 and AISI 304L). The maximum equivalent plastic strain is located close to the edge of the indent.

Table 5.2 Average number of grains (SAE 1080, ASTM A516, AISI 304L) or martensite blocks (AISI 415) contained within a plastic zone, as approximated from the residual imprint topography, on the undeformed surface prior to indentation. These values refer to the number of grains visible on the surface, not the number of grains in the three-dimensional plastic zone.

Material	Plastic zone radius (µm)	Average number of sampled grains or blocks on the surface
SAE 1080	30	12
ASTM A516	50	80
AISI 415	30	8
AISI 304L	60	4

along with higher loads could be used in further studies with these two materials to verify if a better correspondence with the detailed finite element model can be achieved with such experiments.

Strain-induced transformations

The increased error present for AISI 415 and AISI 304L steels could also perhaps be explained by strain-induced phase transformations from austenite to martensite which could take place at higher strains locally present during the indentation process [105]. The emergence of martensite after deformation was observed after the tensile tests for AISI 304L through a verification of the material magnetic behaviour with a simple magnet. The tensile specimens did not present a magnetic capacity before the tensile tests, but the specimens became magnetic after the tensile tests, indicating a transformation from a non-magnetic phase (austenite) to a magnetic phase (martensite). However, due to the lack of equipment to make precise magnetic properties measurements, the proportion of material which underwent this transformation is unknown. It was also attempted to observe this phase transformation by performing several EBSD scans on the cross-section of a large indent in AISI 304L. However, this was inconclusive since the high level of plastic deformation rendered the indexation of phases difficult. Thus, any attempt to calculate the distribution of phases underneath the indentation would have lead to a significant bias.

Since martensite is a harder phase than austenite and has a higher volume, its emergence would increase P_{max}, when compared to the simulated curve, in which this phase transformation is not modeled. The effect on u_{max} and S of this phase transformation are more difficult to analyze and will be studied in future works.

AISI 304L has an austenitic microstructure and a fraction of about 15-20% of residual or reformed austenite is present in the AISI 415 used in this work, as measured by XRD in a previous study [59]. ASTM A516 and SAE 1080 do not contain any austenite, and therefore cannot be affected by this phenomenon. Austenite to martensite strain-induced transformations are highly dependent upon the stress state (tension vs. compression, uni-axial vs. triaxial) [105]. This effect cannot therefore be captured in a single tensile test. Further investigation must be undertaken to determine if strain-induced transformations could explain the higher modelling errors for AISI 304L and AISI 415 steels. This would require modifications to the finite element models to include such constitutive behaviour to observe the effects on indentation data.

Size of the plastic zone

A last observation was made during the study of the performance of the detailed finite element model. The generated equivalent plastic strain fields previously shown in Figure 5.4 display the relationship between the size of the plastic zone and the hardening coefficient of the material. Indeed, observing the strain fields of ASTM A516 and AISI 304L for which the maximum indentation depth is less than 0.5% apart, the plastic zone of ASTM A516 is smaller by approximately 20%. From Table 4.1, it can be observed that the hardening coefficient of ASTM A516 is 40% smaller than that of AISI 304L. Indentations in materials which harden more with increasing strain will thus present a larger and more diffused plastic strain field.

5.4.2 Surrogate model

The surrogate model was created to obtain an approximation of indentation results, while reducing computational time. It was developed by incorporating simplifications to the detailed model. It is important, however, that these simplifications do not introduce significant differences on the simulated indentation data, when compared to the detailed model. A threshold of 20% was deemed an acceptable limit. Table 5.3 shows the differences between the values of P_{max}, S, h_r and u_{max} obtained from the surrogate and the detailed model.

It can be observed that the least affected parameters are the max load, P_{max}, and the residual depth, h_r. The effect of the simplifications is more apparent in the maximum pile-up height, u_{max}, differences reaching 16.2% and 18% for AISI 415 and ASTM A516, respectively. The contact stiffness is also significantly affected, but the differences remain under 10%.

Table 5.3 Differences introduced by the simplifications applied to the detailed model to create the surrogate model on the indentation maximum load, P_{max}, contact stiffness, S, residual depth, h_r, and maximum pile-up height, u_{max}. The most influenced parameters are S and u_{max} which can help explain the weights applied in the surrogate function defined in Section 6.1.1.

Material	ΔP_{max} (%)	ΔS (%)	Δh_r (%)	Δu_{max} (%)
SAE 1080	3.3	-3.6	1.6	-5.0
ASTM A516	4.4	-6.7	0.58	-18.0
AISI 415	2.4	-8.4	0.51	-16.2
AISI 304L	0.47	-4.7	1.7	-6.6

5.4.3 Flat punch indentation model

This model was developed to estimate the compliance of the aluminum oxide specimens used in the direct method for the calibration of the machine compliance. This estimated compliance of the specimens was necessary to be removed from the total measured compliance (see Section 4.1.4). Figure 5.5 shows the indentation curve obtained from the flat punch indentation model when applying a displacement of the indenter leading to a reaction force of 30 N, the maximum force attained by the indentation testing machine. The curve is perfectly linear, as expected for plat punch indentation [58] with a slope of 809.7 N/µm. This leads to a compliance of $C_{AO} = 1.235 \times 10^{-3}$ µm/N, which was used in Section 4.2.2. The specimen behaves in a perfectly elastic way, as the loading and unloading curves are coincident, meaning no residual imprint is generated by the indentation process.

5.5 Conclusions

This chapter detailed the developed finite element models used in this work. The performance of the spherical indentation models were studied and the following conclusions were drawn:

- The detailed model was found to accurately simulate the indentation process for ASTM A516 and SAE 1080 steels. For these steels, the indentation parameter most affected by modeling errors was the maximum pile-up height, u_{max}.
- The detailed model was not capable of capturing the behaviour of AISI 415, for which u_{max} was underestimated by 47%, and of AISI 304L, for which the maximum load, P_{max}, was underestimated by 10.6%, the contact stiffness, S, was overestimated by 20.6% and u_{max} was overestimated by 14.6%. Two hypotheses are given for this modeling failure. The first is the possible strain induced transformation happening during indentation

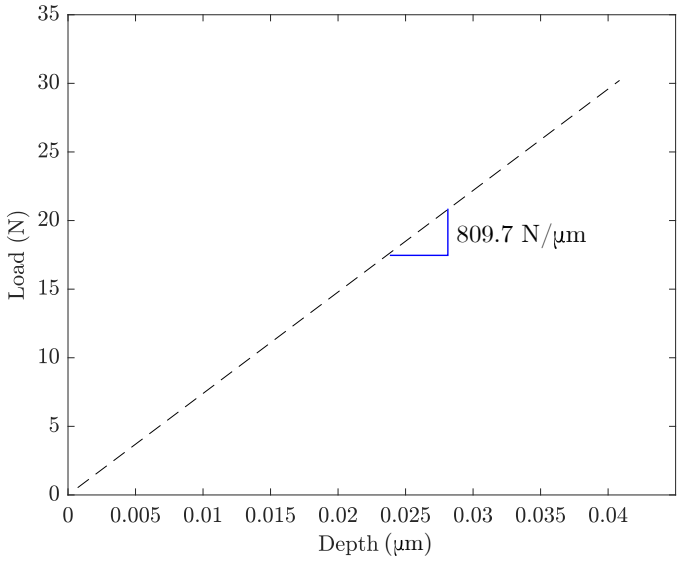

Figure 5.5 Simulated flat punch indentation curve and calculated slope of 809.7 N/µm. The curve is linear, as expected for a flat punch indentation.

which is not captured in the material behaviour of the model and the second is that an insufficient number of grains were sampled during the experimental indentation.

- The surrogate model was found to yield indentation parameters which present differences of less than 20% with the same parameters obtained by the detailed model. The parameter affected the most by the simplifications done to the detailed model is u_{max}. These induced differences are deemed to be small enough for the surrogate model to be efficient in the inverse method developed in the following chapter.

CHAPTER 6 INVERSE METHODOLOGY FOR THE ESTIMATION OF TRUE STRESS-TRUE STRAIN CURVES BY INDENTATION WITHOUT THE ASSUMPTION OF A PRE-DEFINED HARDENING MODEL

This Chapter presents the novel inverse methodology developed in this thesis for the extraction of tensile curves by indentation and its performance. The method is first detailed in Section 6.1, followed by the approaches used to evaluate its performance in Section 6.2. An analysis of the capacity of the tensile curves of the studied materials to be fitted by specific hardening models is presented in Section 6.3, to demonstrate the advantage of eliminating the need for the assumption of a hardening model. Finally, the results and discussion regarding the performance of the proposed method are given in Section 6.4.

6.1 Description of the method

The inverse methodology for estimating the true stress-true strain curves proposed in this thesis is summarized in the flow chart shown in Figure 6.1. It is separated into two steps: the surrogate step and the optimization step. The details of both steps of the optimization procedure are described in this section.

The surrogate step is a loop in which, for each iteration i, the surrogate finite element model is used to obtain the numerical indentation curve and imprint for a set of variables $\mathbf{Y} = \mathbf{Y_i}$, containing the material parameters of a Ramberg-Osgood model. The obtained numerical indentation data is then used in combination with the experimental indentation curve and residual imprint to compute the surrogate function, $\tilde{f}(\mathbf{Y})$, to be minimized by optimization. The problem defined in the surrogate step is unconstrained. If one of the stopping criteria is met, *i.e.*, either $\tilde{f}(\mathbf{Y})$ is less than ϵ_S, the tolerance for the surrogate function, or the number of function evaluations is higher than a predetermined maximum, the variable vector $\mathbf{Y}$ is the solution of this first step. Otherwise, the OrthoMADS optimization algorithm moves to iteration $i + 1$, generates a new variable vector $\mathbf{Y} = \mathbf{Y_{i+1}}$ and the process is repeated until one of the stopping criteria is met.

The solution of the surrogate step is used to generate the starting point, $\mathbf{X_0}$, for the optimization step, which is another loop following the same structure as the surrogate step. For iteration j, the variables in the optimization step, $\mathbf{X} = \mathbf{X_j}$, define a group of 6 points on the true stress-true strain curve and the elastic modulus. The set of constraints, $C(\mathbf{X})$, is computed to verify that the variables are physically acceptable (no oscillations or softening

behaviour are present) and will not cause convergence problems for the finite element simulations (no sharp increases in stress after a plastic plateau). The mathematical definitions of the constraints are detailed in Section 6.1.2

The numerical indentation curve and imprints are obtained with the detailed finite element model using $\mathbf{X}$ to define material behaviour. From the simulated and experimental indentation data, the objective function $f(\mathbf{X})$ is computed and the algorithm verifies if a stopping criterion is met. In the affirmative, $\mathbf{X}$ defines the final estimate of the material true-stress-true strain curve and in the negative, a new variable vector, $\mathbf{X} = \mathbf{X_{j+1}}$, is generated to begin the next iteration $j + 1$. The stopping criteria for the optimization step are a tolerance on $f(\mathbf{X})$, ϵ_O, and a maximum size of the algorithm mesh, δ_{max}.

6.1.1 Surrogate step: determination of suitable starting point for subsequent optimization step

Optimization variables of the surrogate step

Using a Ramberg-Osgood power law requires only four variables to be optimized, namely, the elastic modulus, E, the yield stress, σ_y, the hardening coefficient, n, and the hardening constant, K, forming the vector:

$$\mathbf{Y} = \Big[E, \sigma_y, n, K\Big]\,. \tag{6.1}$$

The lower and upper bounds, $\boldsymbol{Y}_l$ and $\boldsymbol{Y}_u$, applied to vector $\mathbf{Y}$, as well as the starting point of this surrogate optimization step, $\mathbf{Y}_0$, are set to the following values:

$$\boldsymbol{Y}_l = \Big[170\text{ GPa}, 100\text{ MPa},\ 0.1,\ 500\Big]\,, \tag{6.2a}$$

$$\boldsymbol{Y}_u = \Big[230\text{ GPa}, 1\,000\text{ MPa},\ 0.9,\ 2\,500\Big]\,, \tag{6.2b}$$

$$\mathbf{Y}_0 = \Big[200\text{ GPa}, 400\text{ MPa},\ 0.5,\ 1\,500\Big]\,. \tag{6.2c}$$

Since the elastic modulus of steels is known to be around 200 GPa, tight bounds were set, corresponding to a +/- 15% variation around this expected value. The bounds on σ_y were chosen to include the tensile behaviour of different types of steels. The hardening coefficient, n, can theoretically take values ranging from 0 to 1. However, values of n too close to these theoretical limits often result in convergence problems in the finite element simulation. Bounds of 0.1 and 0.9 were found to be the limits which avoided such convergence issues. Finally, the bounds on K were chosen in a similar fashion to those on n, to include as many

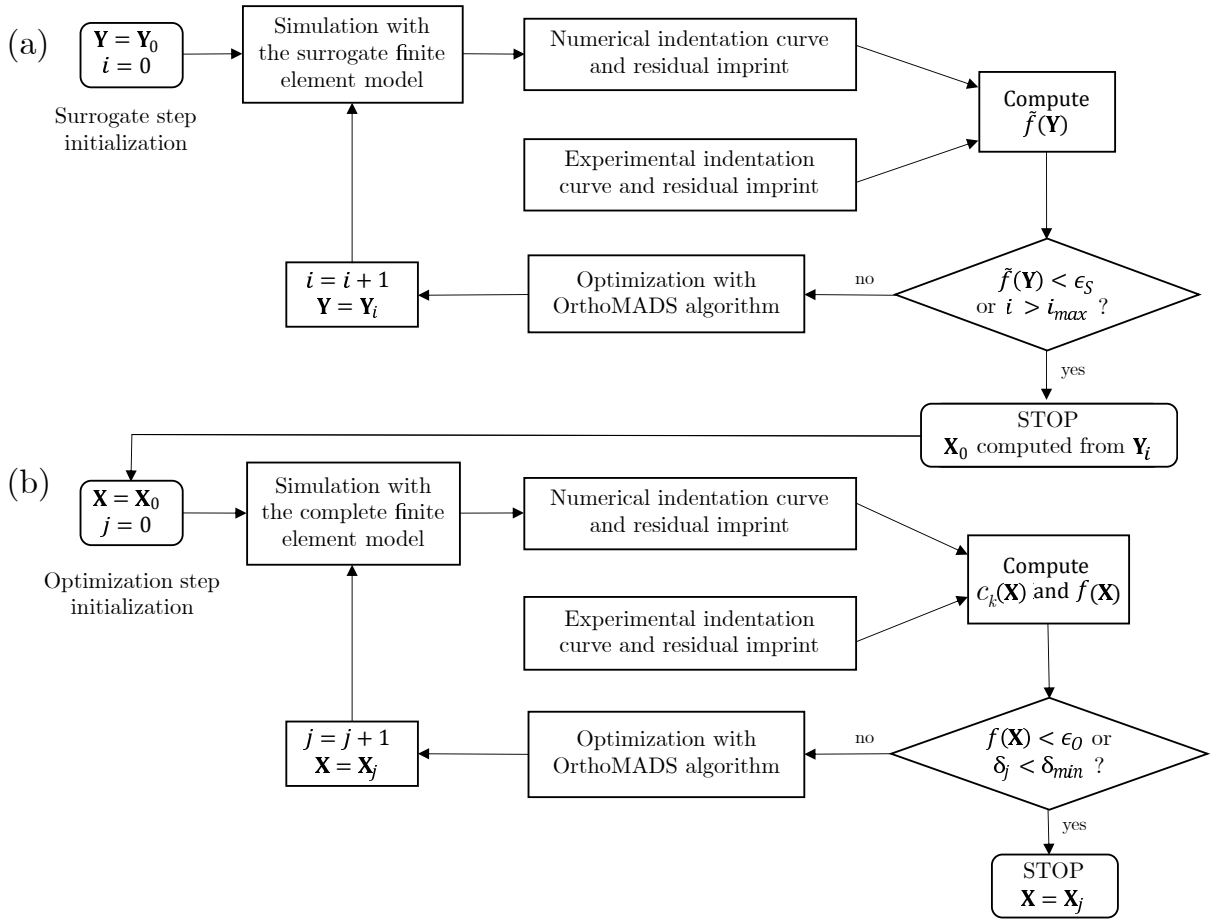

Figure 6.1 Flowchart describing the inverse methodology proposed in this thesis: (a) The surrogate step, a loop in which the surrogate finite element model is used to obtain the numerical indentation curve and imprint for a set of variables $\mathbf{Y}$ which is then used in combination with the experimental indentation curve and residual imprint to compute the surrogate function, $\tilde{f}(\mathbf{Y})$. If one of the stopping criteria is met, *i.e.*, either $\tilde{f}(\mathbf{Y})$ is less than ϵ_S, the tolerance for the surrogate function, or the number of function evaluations is higher than a predetermined maximum, i_{max}, the variable vector $\mathbf{Y}$ is taken as the solution of this step. Otherwise the OrthoMADS optimization algorithm is used to generate a new variable vector and the process is repeated until convergence. $\mathbf{Y_0}$ is the starting point of this step. The solution of the surrogate step is used to obtain the starting point, $\mathbf{X_0}$, for the optimization step; (b) The optimization step, a loop which follows the same structure as the surrogate step. The differences are that the variables optimized are in the vector $\mathbf{X}$, that the objective function $f(\mathbf{X})$ is computed instead of $\tilde{f}(\mathbf{Y})$ and the constraints, $c_k(\mathbf{X})$, are also computed. ϵ_O is the tolerance for the objective function and δ_{max} is the minimum mesh size which is assumed for algorithmic convergence.

materials as possible while avoiding convergence issues. The starting point, $\mathbf{Y}_0$, was chosen with values in the middle of the intervals.

Surrogate function

The surrogate function $\tilde{f}(\mathbf{Y})$ quantifies the difference between indentation data obtained from simulation with the surrogate model and the target experimental indentation data. It is defined as the weighted sum of four sub-functions:

$$\tilde{f}(\mathbf{Y}) = w_L \tilde{f}_L(\mathbf{Y}) + w_{IC} \tilde{f}_{IC}(\mathbf{Y}) + w_{IF} \tilde{f}_{IF}(\mathbf{Y}) + w_S \tilde{f}_S(\mathbf{Y}), \tag{6.3}$$

where w_L, w_{IC}, w_{IS} and w_S are the weights attributed to the sub-functions accounting for the indentation loading curve (L), the residual imprint in the contact region (IC), the residual imprint in the free surface region (IF), and the contact stiffness (S). Each of these four sub-functions compare a different portion of the indentation experimental and numerical data, which are illustrated in Figure 6.2.

Indentation loading curve, $\tilde{f}_L(\mathbf{Y})$

$\tilde{f}_L(\mathbf{Y})$ quantifies the difference between the numerical and experimental indentation loading curves and is defined by a normalized, dimensionless, sum of squares, as follows:

$$\tilde{f}_L(\mathbf{Y}) = \sum_{n=1}^{N} \frac{1}{N} \left(\frac{P_{exp,n} - P_{num,n}(\mathbf{Y})}{P_{max}} \right)^2, \tag{6.4}$$

where $P_{num,n}(\mathbf{Y})$ is the load computed at the nth depth of the numerical indentation curve and $P_{exp,n}$ is the load interpolated at the same depth on the target experimental curve. P_{max} is the maximum load measured experimentally and N is the total number of points being investigated on the numerical curve. N depends on the number of sub-steps used by the finite element simulation to achieve convergence.

Residual imprint, $\tilde{f}_{IC}(\mathbf{Y})$ and $\tilde{f}_{IF}(\mathbf{Y})$

The sub-functions $\tilde{f}_{IC}(\mathbf{Y})$ and $\tilde{f}_{IF}(\mathbf{Y})$ quantify the difference between the experimental and numerical residual imprints in the contact region and in the free surface region, respectively. To separate these regions, the M^{th}_{max} nodal position is first derived as the nodal position at which the maximal pile-up height of the numerical imprint is observed. None of the studied materials presented a sink-in behaviour in their residual imprints so this situation was not included in the method at this time. The radial nodal position approximating the separation of the contact and free surface zones of the residual imprint, the M^{th}_{C} node, is defined by:

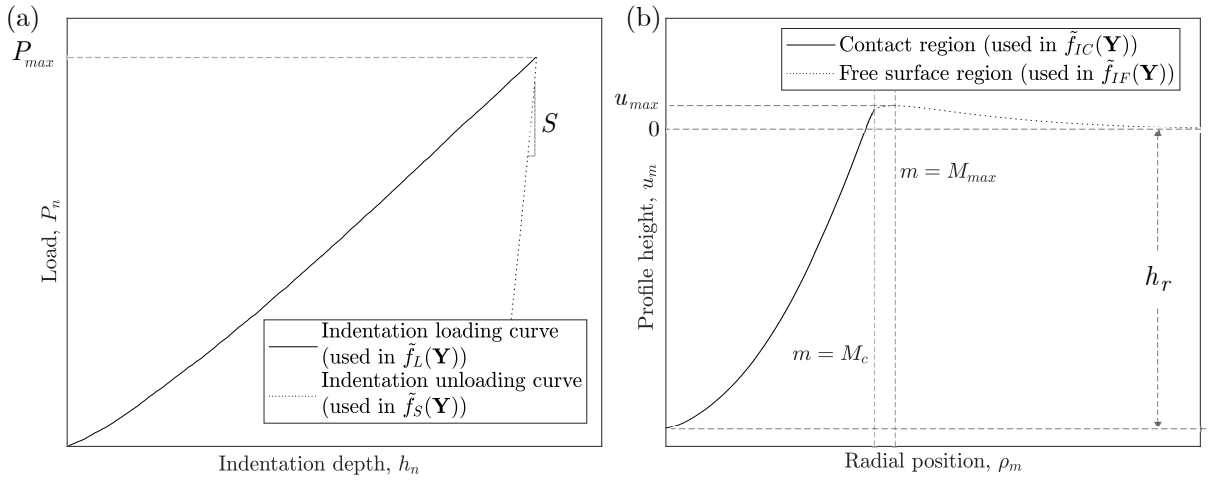

Figure 6.2 Typical indentation data: (a) indentation curve comprised of loading and unloading parts and (b) indentation residual imprint profile separated in contact and free surface regions. The maximum pile-up height, u_{max}, is at the M_{max}^{th} nodal position, which is used to find the M_c^{th} node by using Equation (6.5) to approximate the separation of the contact and free surface zones of the residual imprint.

$$M_C = M_{max} - 4. \tag{6.5}$$

This definition was found by finite element simulations to lead to the best compromise to approximate the position of the separation between contact and free-surface regions for all the materials studied in this thesis. Figure 6.2 shows an example of the M_{max}^{th} and M_C^{th} node radial positions.

$\tilde{f}_{IC}(\mathbf{Y})$ and $\tilde{f}_{IF}(\mathbf{Y})$ are defined by normalized, dimensionless, sums of squares, as follows:

$$\tilde{f}_{IC}(\mathbf{Y}) = \sum_{m=1}^{M_C} \frac{1}{M_C} \left(\frac{u_{exp,m} - u_{num,m}(\mathbf{Y})}{h_r} \right)^2, \tag{6.6}$$

$$\tilde{f}_{IF}(\mathbf{Y}) = \sum_{m=M_C+1}^{M} \frac{1}{M - M_C} \left(\frac{u_{exp,m} - u_{num,m}(\mathbf{Y})}{u_{max}} \right)^2, \tag{6.7}$$

where $u_{exp,m}$ and $u_{num,m}(\mathbf{Y})$ are the heights of the experimental and numerical residual imprint profiles, at the mth radial distance from their center, respectively. M is the total number of points contained in the numerical profile. These M locations correspond to the coordinates of the nodes on the surface of the specimen in the finite element model. The experimental profile is interpolated at the same M radial locations. Parameters h_r and u_{max}

are respectively the residual depth, and maximum pile-up height, of the experimental residual imprint profile.

The sub-functions $\tilde{f}_{IC}(\mathbf{Y})$ and $\tilde{f}_{IF}(\mathbf{Y})$ were not combined into a single sub-function because such a combination results in the contact region driving most of the value of the overall sub-function. Indeed, the difference in height between experimental and numerical imprints in both regions would then be normalized by the same value, for example h_r, and the absolute difference is larger in the contact region, giving this region a higher weight in the sub-function. This would have a detrimental effect on the estimated strain hardening behaviour of the analyzed materials because the pile-up region of the residual imprint is very sensitive to the material hardening behaviour. By normalizing the separated sub-functions by their respective peak values, the sub-functions are more representative of the relative differences in height for both regions. A demonstration of this is given in Section 6.4.3.

Another approach which was attempted was to obtain the relative error in each point, by normalizing the squared difference $(u_{exp,m} - u_{num,m})^2$ with the squared experimental height at the point of interest, $u^2_{exp,m}$. However, this led to a substantial increase in relative difference for points located at a height close to zero, taking up most of the value of the sub-function, and a significant decrease in the performance of the method.

Contact stiffness, $\tilde{f}_S(\mathbf{Y})$

$\tilde{f}_S(\mathbf{Y})$ is defined as:

$$\tilde{f}_S(\mathbf{Y}) = \left(\frac{S_{exp} - S_{num}(\mathbf{Y})}{S_{exp}} \right)^2, \tag{6.8}$$

where S_{exp} and $S_{num}(\mathbf{Y})$ are the contact stiffness of the experimental and numerical indentation curves, respectively.

Weight values

The weights were attributed to the sub-functions after trial and error runs with different weight values combinations with the objective to obtain starting points which were the closest to the target curves for a limited amount of function evaluations. The target indentation data used in these runs were obtained by finite element simulation with the detailed model and the tensile curves of the four studied materials. These weights were $w_L = 50$, $w_{IC} = w_{IF} = 10$ and $w_S = 1$. Since the tensile behaviour of the four studied materials are quite different (see Table 4.1), it is hypothesized that these weights could be applied to other types of materials.

The performance of the surrogate finite element model, presented in Section 5.4.2, can help explain the weight values obtained for the surrogate function. Indeed, the weight value attributed to the sub-function accounting for the loading curve has the highest weight in the surrogate function, with a value of 50. Since the loading curve is well approximated by the surrogate model, it makes sense that a higher weight for this sub-function renders better results since more weight is attributed to more reliable information in the surrogate function. The weights attributed to the residual imprint are five times lower, with a value of 10, since the pile-up region is less well approximated by the surrogate model. The lowest weight was attributed to the sub-function regarding the contact stiffness, with a value of 1. Since the errors on S are lower than for u_{max}, the weight of the sub-function accounting for the contact stiffness would have been expected to be higher than that accounting for the residual imprint. The fact that the opposite gave better results may be explained by the sensitivities of the sub-functions to different material parameters. The residual imprint carries sensitivity to the elastic modulus as well as the whole hardening behaviour of the material, while the contact stiffness is mostly influenced by the elastic modulus. To obtain a sufficient sensitivity to the hardening behaviour of the material, a higher weight needs to be attributed to the sub-function taking the residual imprint into account.

Optimization algorithm

The unconstrained blackbox optimization problem for this step can be written as:

$$\underset{\mathbf{Y}=[E,\sigma_y,n,K]}{\arg\min} \quad \tilde{f}(\mathbf{Y}). \tag{6.9}$$

The OrthoMADS algorithm (previously described in Section 2.6.1) is used to solve this problem. The quadratic model feature was kept activated because doing so resulted in starting points which were the closer to the target curves. The first stopping criterion is a convergence value for $\tilde{f}(\mathbf{Y})$ of $\epsilon_S = 10^{-3}$. If the algorithm cannot find the variables $\mathbf{Y}$ which result in $\tilde{f}(\mathbf{Y}) < \epsilon_S$, a maximum number of function evaluations, i_{max}, is set to 150. In this step, the maximum number of evaluations is expected to be the limiting factor. The tolerance ϵ_S is set to a low value to let the algorithm reach the smallest value it can in the allowed number of surrogate function evaluations. For the four materials studied, increasing i_{max} did not lead to significant improvements in the obtained starting points for the optimization step.

6.1.2 Optimization step: final estimation of true stress-true strain curves

Optimization variables used in the optimization step

A set of pre-defined true strain values is computed prior to the optimization process in such a way that only the stress values at these pre-defined strains are optimized along with the elastic modulus to obtain a group of six points on the estimated true stress-true strain curve. The pre-defined strains are determined in two steps, the first is the determination of the complete range of strains, followed by the positioning of the intermediate strains within this interval.

The range of strains of the estimated tensile curve is the interval between the yield strain, ε_y, and a maximum strain value, ε_{max}, defining the strain position of the last point extracted. The maximum plastic stain values, ε_{max}, were obtained for the four steels studied in this thesis with finite element simulations of an indentation with a maximum load of 5 N, using their experimental true stress-true strain curves obtained from macroscopic tensile tests. The results are shown in Table 6.1. Since the actual true stress-true strain curves of the materials are unknown when the method is applied, it must be estimated from indentation parameters. To do so, Tabor's indentation strain, ε_{ind}, defined in Table 2.1, was computed for all materials using the contact radius obtained from the simulated residual imprint [120]. An approximate correlation between the values of ε_{max} obtained by finite element simulations and the values of ε_{ind} calculated from the simulated indentation data was found to be:

$$\varepsilon_{max} \approx \alpha \, \varepsilon_{ind}, \tag{6.10}$$

where, α is a constant. The average value of α obtained by finite element simulations for the materials studied in this work was 3.52, with a relative standard deviation of 16%, as shown in Table 6.1. Since the tensile behaviour of the four studied steels are quite different, a value of $\alpha = 3.5$ is assumed to be a good approximation for most steels and is used in the proposed methodology. The relationship $\varepsilon_{max} \approx 3.5 \, \varepsilon_{ind}$ can then be used to estimate the position of the last point to extract on the tensile curve, as ε_{ind} can be obtained from experimental indentation data.

The yield strain, defined as $\varepsilon_y = \sigma_y/E$, and the value of ε_{max}, limit of the total interval of the strain values of the points to be estimated on the tensile curve. From this interval, the intermediate strain values, representing the positions of the 2nd to 5th points to estimate, are computed by adopting a geometric progression. This choice of progression serves to obtain a higher density of points on the true stress-true strain curve at lower strains and a lower

Table 6.1 Finite element study for the obtention of the contact radius, a, from which Tabor's indentation strain, ε_{ind}, is computed, and the maximum equivalent plastic strain after unloading, ε_{max}. The ratio of ε_{max} to ε_{ind} is computed to investigate if a stable relationship exists between these two parameters which would enable the estimation of ε_{max} from ε_{ind}. It is concluded that a relationship $\varepsilon_{max} \approx 3.5\ \varepsilon_{ind}$ is an acceptable estimation.

Material	a (µm)	ε_{max}	$\varepsilon_{ind} = 0.2a/R$	$\varepsilon_{max}/\varepsilon_{ind}$
SAE 1080	23.4	0.301	0.0936	3.21
ASTM A516	29.2	0.472	0.117	4.03
AISI 415	23.4	0.320	0.936	3.42
AISI 304L	31.2	0.427	0.125	3.42
Average				3.52

density of points at higher strains. This approach was used to capture more features near the yield stress, like abrupt changes in hardening or a Lüders plateau. The geometric progression used is defined by:

$$\varepsilon_i = \varepsilon_y + \sum_{j=2}^{i} \gamma 2^{j-2}, \quad i = 2, 3, 4, 5, \tag{6.11}$$

where

$$\gamma = \frac{\varepsilon_{max} - \varepsilon_y}{\sum_{i=2}^{6} 2^{i-2}}. \tag{6.12}$$

Hence, the material parameters to be identified are the elastic modulus, E, and the yield stress, σ_y, which together deliver the yield strain, ε_y, as well as the true stress values, σ_2 to σ_6, at pre-defined strains, ε_2 to $\varepsilon_6 = \varepsilon_{max}$. The variable vector $\mathbf{X}$ and the pre-defined strain vector, $\boldsymbol{\varepsilon}$, are:

$$\mathbf{X} = [E, \sigma_y, \sigma_2, \sigma_3, \sigma_4, \sigma_5, \sigma_6], \tag{6.13a}$$

$$\boldsymbol{\varepsilon} = \left[\frac{\sigma_y}{E}, \varepsilon_2, \varepsilon_3, \varepsilon_4, \varepsilon_5, \varepsilon_{max}\right], \tag{6.13b}$$

corresponding to an input true stress-true strain curve with six data points and an optimization problem comprising seven variables. This number of points was found to be the best compromise between stability and the capability to represent the shape of tensile curves accurately. Using these variables, the tensile curve is estimated between the points by linear interpolation. A graphical representation of these vectors and the true stress-true strain curve obtained is shown in Figure 6.3.

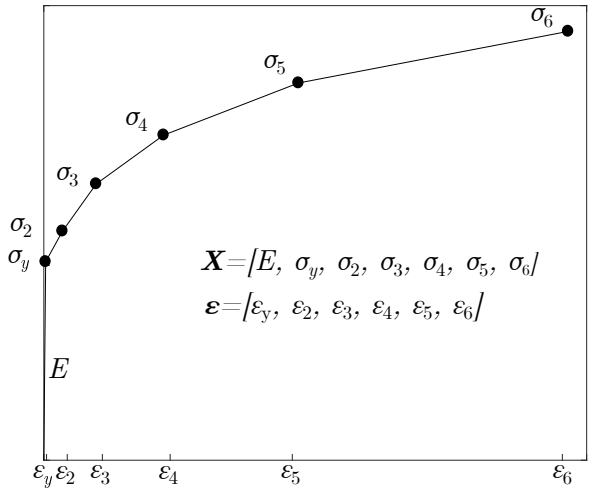

Figure 6.3 Illustration of the variables for the optimization step. The variable vector, $\mathbf{X}$, contains the elastic modulus, the yield stress and 5 values of true stress associated with pre-defined strains, obtained with Eqs (6.10) to (6.12), that define a tensile curve formed of 6 data points. Linear interpolation is used between estimated points.

From the power law parameters obtained by the surrogate step, the stresses corresponding to the pre-defined strains, $\boldsymbol{\varepsilon}$, are computed to obtain the vector $\mathbf{X}_0$, which is the starting point for the optimization step. The vectors $\mathbf{X}_L$ and $\mathbf{X}_U$, representing the lower and upper bounds of the variables are defined as:

$$\boldsymbol{X}_L = [170\ 000, 100, 100, 100, 100, 100, 100, 100, 100, 100]\ \text{MPa}, \tag{6.14a}$$

$$\boldsymbol{X}_U = [230\ 000, 1\ 000, 1\ 000, 1\ 000, 1\ 500, 1\ 500, 1\ 500, 1\ 500, 1\ 500]\ \text{MPa}. \tag{6.14b}$$

The same bounds as in the surrogate step were applied to the values of E and σ_y. The bounds on σ_2 to σ_6 were chosen to be sufficiently wide for the variables to yield materials with various resistances and strain hardening behaviours.

Optimization constraints

Two non-relaxable constraints, $c_1(\mathbf{X})$ and $c_2(\mathbf{X})$, and one relaxable constraint, $c_3(\mathbf{X})$, are applicable to this optimization step and are defined below. Examples of true stress-true strain curves which do not respect each of these constraints are illustrated in Figure 6.4, as well as a tensile curve which respects all constraints.

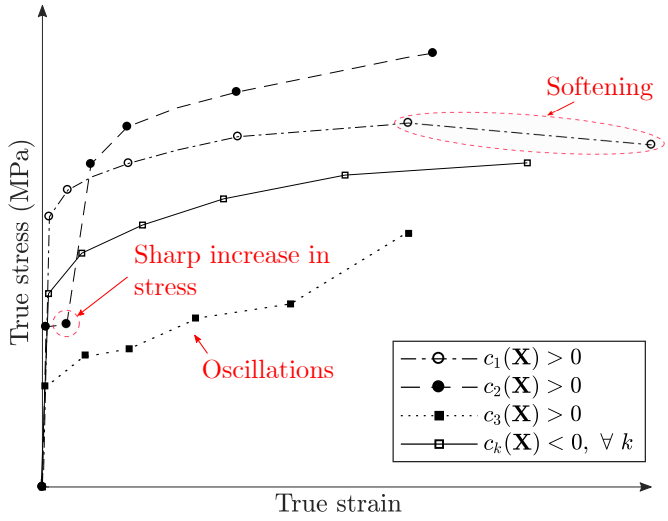

Figure 6.4 Examples of true stress-true strain curves which do not respect each of the constraints, in which case the value of the constraint is greater than 0: $c_1(\mathbf{X})$, which serves to avoid softening behaviour in the tensile curves; $c_2(\mathbf{X})$, which serves to avoid sharp increases in stress resulting in convergence failure of finite element simulation; and $c_3(\mathbf{X})$, which serves to avoid oscillations in the tensile curve; when compared to a true stress-true strain curve which respects all constraints ($c_k(\mathbf{X}) < 0 \ \ \forall \ k$).

Non-relaxable constraint $c_1(\mathbf{X})$: avoid softening

The first non-relaxable constraint, $c_1(\mathbf{X})$, is respected if all the tangent moduli, $(E_T)_i$, in the plastic portion of the true stress-true strain curve are positive, *i.e.*, when there is no softening. The material is then said to be stable in a Drucker's sense [54]. The tangent moduli, $(E_T)_i$ are defined by:

$$(E_T)_i = \frac{X_{i+2} - X_{i+1}}{\varepsilon_{i+1} - \varepsilon_i}, \quad i = 1, 2, 3, 4, 5, \tag{6.15}$$

where $\mathbf{X}$ and $\boldsymbol{\varepsilon}$ are the variables and pre-defined strains vectors, respectively. For example, $(E_T)_1$ is the slope of the first segment after the yield strain.

This constraint is non-relaxable because an error results from the finite element software if this constraint is not respected. $c_1(\mathbf{X})$ is expressed as follows:

$$c_1(\mathbf{X}) = \begin{cases} 0, & \text{if } (E_T)_i > 0, \ \forall \ i \\ 1, & \text{otherwise.} \end{cases} \tag{6.16}$$

Non-relaxable constraint $c_2(\mathbf{X})$: avoid sharp increases in stress

Sharp increases in stress on the tensile curve lead the simulation towards a convergence failure. This happens when E_T after a plastic plateau is very high, making the change in the slope of the tensile curve very abrupt at the end of the plateau. Non-relaxable constraint $c_2(\mathbf{X})$ thus sets a limit of 30 GPa on the change in E_T. This value was found, by trial and error, to allow the finite element simulations to converge. Furthermore, abrupt increases of over 30 GPa in the tangent modulus at the end of a plastic plateau is not physically observed in metals.

Defining the vector $\mathbf{\Delta E_T}$ as the changes in E_T at each applicable discrete point on the curve:

$$\Delta(E_T)_j = (E_T)_{j+1} - (E_T)_j, \quad j = 1, 2, 3, 4, \tag{6.17}$$

$c_2(\mathbf{X})$ is then expressed as:

$$c_2(\mathbf{X}) = \begin{cases} 0, & \text{if } \Delta(E_T)_j < 30 \text{ GPa}, \ \forall \ j \\ 1, & \text{otherwise.} \end{cases} \tag{6.18}$$

Relaxable constraint $c_3(\mathbf{X})$: avoid oscillations

The relaxable constraint was implemented to remove oscillations in the optimized tensile curve. To do so, E_T must always decrease as strain increases, and the vector $\mathbf{\Delta E_T}$ should as a consequence only contain negative values, unless a plastic plateau exists. Indeed, the existence of a plateau would imply an increase of E_T at its end.

The first step in creating a mathematical description for this constraint is the definition of a new vector, $\mathbf{\Delta E_T^+}$, which is obtained from the vector $\mathbf{\Delta E_T}$ by changing the negative values to zero. The sum of the elements in $\mathbf{\Delta E_T^+}$ can then serve as the value of $c_3(\mathbf{X})$ if no plastic plateau is present. For example, if: $\boldsymbol{\Delta E_T} = \begin{bmatrix} -2 & 3 & -4 & 2 \end{bmatrix}$ GPa, then $\boldsymbol{\Delta E_T^+} = \begin{bmatrix} 0 & 3 & 0 & 2 \end{bmatrix}$ GPa and $c_3(\mathbf{X}) = 5$ GPa. The larger the value of $c_3(\mathbf{X})$, the more pronounced are the oscillations observed in the tensile curve formed by the variables. If a plastic plateau exists, only the values in $\mathbf{\Delta E_T^+}$ associated to points after the strain marking its end, ε_{pl}, would be summed.

It must then be determined if a plastic plateau exists in the tensile curve defined by $\mathbf{X}$. The limit of the slope in the plastic plateau for the steels studied in this work was 1.25 GPa which is also applicable to most steels presenting a plastic plateau. The initial values of E_T are then compared to this threshold. However, a difficulty arises in the determination of the

strain value that marks the end of the plateau, ε_{pl}, since it could, in reality, lie in an interval between two pre-defined strains. We therefore find the limits of this interval to complete the definition of $c_3(\mathbf{X})$. The lower limit of this interval is the strain value after which E_T increases over the limit of 1.25 GPa. The higher limit of the interval is simply the next point on the curve. With these limits known, the index, j_0, of the first $(\Delta E_T^+)_j$ appearing after the plastic plateau can be obtained, which corresponds to the point on the tensile curve after the higher limit of the interval containing ε_{pl}.

$c_3(\mathbf{X})$ is then defined by:

$$c_3(\mathbf{X}) = \sum_{j=j_0}^{4} (\Delta E_T^+)_j. \tag{6.19}$$

Examples of tensile curves with ε_{pl} in three different intervals are presented in Figure 6.5. In each case, the corresponding value of j_0 is shown. This figure also shows how these curves could be adjusted, if needed, to estimate the true position of ε_{pl} once the optimization is completed.

Objective function, $f(\mathbf{X})$

The objective function, $f(\mathbf{X})$, is constructed in the same way as the surrogate function, $\tilde{f}(\mathbf{Y})$, except that the numerical information comes from the detailed finite element model instead of the surrogate model. The objective function is therefore the sum of four sub-functions:

$$f(\mathbf{X}) = v_L f_L(\mathbf{X}) + v_{IC} f_{IC}(\mathbf{X}) + v_{IF} f_{IF}(\mathbf{X}) + v_S f_S(\mathbf{X}), \tag{6.20}$$

where $f_L(\mathbf{X})$, $f_{IC}(\mathbf{X})$, $f_{IF}(\mathbf{X})$ and $f_S(\mathbf{X})$ are the sub-functions accounting for the indentation loading curve (L), the residual imprint in the contact (IC) and free surface (IF) regions, and the contact stiffness (S), respectively. The constants v_L, v_{IC}, v_{IF} and v_S correspond to the weights attributed to the four parts of the function. Contrary to the surrogate step, a value of 1 for all four weights led to an efficient identification of the true stress-true stress curves. An optimization of weights using the I-index was attempted, but was not conclusive. The details of this study and its results are presented in Sections 6.2 and 6.4.3.

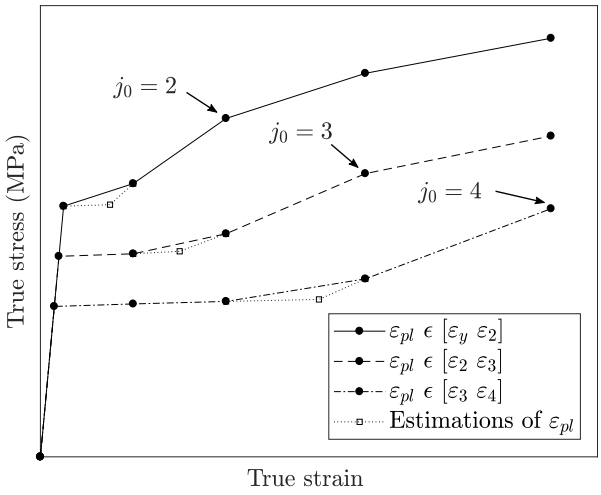

Figure 6.5 Examples of tensile curves obtained with different $\mathbf{X}$ in which ε_{pl} lies within the intervals $[\varepsilon_y, \varepsilon_1]$, $]\varepsilon_1, \varepsilon_2]$ and $]\varepsilon_2, \varepsilon_3]$ and extrapolations to estimate the actual position of ε_{pl}.

Optimization algorithm

For the optimization step, the constrained black-box optimization problem can be written as:

$$\underset{\mathbf{X}=[E,\sigma_y,\sigma_2,\sigma_3,\sigma_4,\sigma_5,\sigma_6]}{\arg\min} \quad f(\mathbf{X}) \tag{6.21a}$$

$$\text{subjected to} \quad c_1(\mathbf{X}) \leq 0,\ c_2(\mathbf{X}) \leq 0,\ c_3(\mathbf{X}) \leq 0. \tag{6.21b}$$

This optimization problem is solved using the OrthoMADS algorithm, but in this case the feature creating quadratic models was disabled. The constraints involved in this step made the quadratic models lead the algorithm in the wrong direction. Two stopping criteria were used for this step. The convergence value of $f(\mathbf{X})$ is set to $\epsilon_O = 10^{-5}$. If this limit is not reached, a minimum mesh size, δ_{min}, is set to 100 MPa for the elastic modulus, E, and 10^{-2} MPa for the stress values σ_y to σ_6.

Table 6.2 shows a summary of the parameters used in the surrogate and optimization steps which together constitute the proposed methodology.

Table 6.2 Summary of the parameters defining the optimization problems to be solved in the surrogate and optimization steps of the proposed methodology.

	Surrogate step	Optimization step
Variables	Ramberg-Osgood power law : $\mathbf{Y} = [E, \sigma_y, n, K]$	No pre-defined hardening model: $\mathbf{X} = [E, \sigma_y, \sigma_2, \sigma_3, \sigma_4, \sigma_5, \sigma_6]$
Constraints	None	$c_1(X)$, $c_2(\mathbf{X})$, $c_3(\mathbf{X})$
Weights	$w_L = 50$, $w_{IC} = 10$, $w_{IS} = 10$, $w_S = 1$	$v_L = 1$, $v_{IC} = 1$, $v_{IS} = 1$, $v_S = 1$
Starting point	$\mathbf{Y_0} =$ $[200\text{ GPa}, 400\text{ MPa}, 0.5, 1500]$	$\mathbf{X_0}$ derived from the solution of surrogate step
Finite element model	Surrogate model	Detailed model
Stopping criteria	$\epsilon_S = 10^{-3}$, $i_{max} = 150$	$\epsilon_O = 10^{-5}$, $\delta_{min}(E) = 100$ MPa, $\delta_{min}(\sigma_y \text{ to } \sigma_6) = 10^{-2}$ MPa
Use of quadratic models	Enabled	Disabled

6.2 Methods used for the performance study of the developed inverse method

The performance of the proposed methodology is studied through a numerical application, analysis with the identifiability index and an experimental application. The details of the approach taken in these studies are given in this section.

Numerical application

The first step in assessing the performance of the proposed methodology is a numerical study, which eliminates the influence of modeling errors, namely the errors induced by the finite element modeling hypotheses, and experimental errors. The numerical study serves to test the efficiency of the algorithm chosen to solve the optimization problem, and to quantify the precision with which tensile curves of different materials can be estimated with the method under ideal conditions.

This is undertaken by using indentation test data generated by finite element simulations, rather than experiments, as the input to the inverse method. The true stress-true strain curves used to numerically generate the target indentation data were obtained from extrapolations of the experimental tensile curves and are called the target tensile curves. In the case of ASTM A516 and SAE 1080 steels, the plastic plateau region was modeled by a straight line, eliminating experimental fluctuations and the instability at the upper yield point. Only a single experimental tensile curve for each material was used to generate the target curves

instead of the average of all curves, so the values for E and σ_y do not correspond to the averages given in Table 4.7.

Experimental validation

To demonstrate that the method can perform well in the presence of experimental and modeling errors, it is applied to experimental indentation data obtained with the experimental parameters determined by the conclusions of Chapter 4.

Identifiability index study

The I-index developed by the group of Richard et al. [111], described in Section 2.6.5, was adapted to the format of the objective function, $f(\mathbf{X})$, used in this work.

Since the objective function is separated into four sub functions, four sensitivity matrix exist to account for the sensitivity of the function to the different indentation characteristics. For the sub-function accounting for the indentation loading curve, $f_L(\mathbf{X})$:

$$S_{nj}^{L} = \frac{X_j}{P_{max}\sqrt{N}} \frac{\partial P_{num,n}}{\partial X_j}. \tag{6.22}$$

For the sub-function accounting for the contact stiffness, $f_S(\mathbf{X})$:

$$S_{j}^{S} = \frac{X_j}{S_{exp}} \frac{\partial S_{num}}{\partial X_j}. \tag{6.23}$$

For the sub-function accounting for the contact region of the residual imprint topography, $f_{IC}(\mathbf{X})$:

$$S_{mj}^{IC} = \frac{X_j}{h_r\sqrt{M_c}} \frac{\partial u_{num,m}}{\partial X_j}. \tag{6.24}$$

For the sub-function accounting for the contact region of the residual imprint topography, $f_{IF}(\mathbf{X})$:

$$S_{mj}^{IF} = \frac{X_j}{u_{max}\sqrt{M - M_c}} \frac{\partial u_{num,m}}{\partial X_j}. \tag{6.25}$$

The dimensionless matrix $\mathbf{H}$ is then obtained by:

$$H_{ij} = v_L \sum_{n=1}^{N} S_{ni}^{L} S_{nj}^{L} + v_S S_i^S S_j^S + v_{IC} \sum_{m=1}^{M_c} S_{mi}^{IC} S_{mj}^{IC} + v_{IF} \sum_{m=M_c+1}^{M} S_{mi}^{IF} S_{mj}^{IF}, \tag{6.26}$$

where the coefficients v_L, v_{IC}, v_{IS} and v_S are weights attributed to the different sub-functions.

Equation (2.17) is then used to compute the I-index.

The following aspects were studied using this adapted I-index:

1. Number of optimized variables leading to estimates of the true stress-true strain curves made up of different number of points:
   - Comparison of I-indices obtained when the identified material parameters generate 4, 5, 6, 7 or 8 points on the true stress-true strain curve.
2. Experimental information used in the objective function and sub-function weights:
   - Comparison of I-indices obtained when the objective function considers only the indentation curve, only the residual imprint, both the indentation curve and the residual imprint, and the full function with all experimental information;
   - Comparison of using a single sub-function for the imprint or separating it into two sub-functions accounting for its contact region and the pile-up region (see Eqs 6.27 to 6.29);
   - Minimization of the I-index through variation of the values of the weights v_L, v_S, v_{IC} and v_{IF} between 0 and 1.
3. Ratio of maximum indentation depth to indenter radius, h_{max}/R:
   - Comparison of I-index obtained with different h_{max}/R ratios generated by applying maximum loads of 2.5 N, 5 N and 7.5 N which modifies the maximum depth attained during the indentation.

The sub-function considering the whole residual imprint is defined as:

$$f_I(\mathbf{X}) = \sum_{m=1}^{M} \frac{1}{M} \left(\frac{u_{exp,m} - u_{num,m}(\mathbf{X})}{h_r} \right)^2, \tag{6.27}$$

which leads to a sensitivity of this sub-function defined by:

$$S^I_{mj} = \frac{X_j}{h_r \sqrt{M}} \frac{\partial u_{num,m}}{\partial X_j}, \tag{6.28}$$

and the dimensionless matrix $\mathbf{H}$ then becomes:

$$H_{ij} = v_L \sum_{n=1}^{N} S^L_{ni} S^L_{nj} + v_S S^S_i S^S_j + v_I \sum_{m=1}^{M}, S^I_{mi} S^I_{mj}. \tag{6.29}$$

where v_I is the weight associated with the sub-function accounting for the full residual imprint.

6.3 Tensile properties and power law curve fitting

This section serves to demonstrate the ability of hardening models to fit experimental tensile data. No indentation data is used in this section. Figure 6.6 shows the experimental true stress-true strain curves for the four studied materials as well as the best fitting Ramberg-Osgood, Hollomon and hybrid hardening models for these curves.

It can be observed that different models fit the tensile curves better for the different materials. For instance, AISI 304L can be very accurately represented by a Ramberg-Osgood model, with an average error of 0.35% across the hardening region, but not by a Hollomon model, in which case the yield stress is underestimated by 87% to compensate the inability of this model to fit a linear hardening behaviour. The fit of the hybrid model to the AISI 304L experimental data found a plateau characterized by a yield point elongation of $0.15\varepsilon_y = 1.56 \times 10^{-4}$, which is not significant, and therefore the fit was very similar to that of the Ramberg-Osgood model.

The strain hardening behaviour of AISI 415 can be approximated within an error of 2% with all three models after a strain value of 5×10^{-3}, but there is always an overestimation of the yield stress, ranging from 17%, for the Hollomon model, to 24%, for the hybrid model. In addition, when the hybrid model is used, a non-negligible plateau characterized by a yield point elongation of $0.45\varepsilon_y = 1.42 \times 10^{-3}$ appears. The plateau improves the fit to the experimental data in the hardening region by shifting the onset of strain hardening. The apparition of a plateau that does not actually exist demonstrates the inability of this hardening model to be used with materials exempt of a plastic plateau.

As expected, the tensile curves of the two steels which actually have a Lüders plateau in their true stress-true strain curves, *i.e.*, SAE 1080 and ASTM A516, cannot be well represented by the Ramberg-Osgood and Hollomon models, particularly for strains below 3×10^{-2}. The use of the hybrid model improves the fit, but, for both materials, the yield point elongation is overestimated by at least 20%. For ASTM A516, the strain hardening behaviour is better captured with the hybrid model, when compared to the other two models. This is not the case for SAE 1080 steel, whose strain hardening cannot be accurately captured by the Ramberg-Osgood part of the hybrid model.

With these results, it can be concluded that none of these models can accurately fit the entire tensile curve of the four materials studied in this thesis. Assuming one of these models beforehand could therefore lead to significant errors in the identified tensile cures, depending

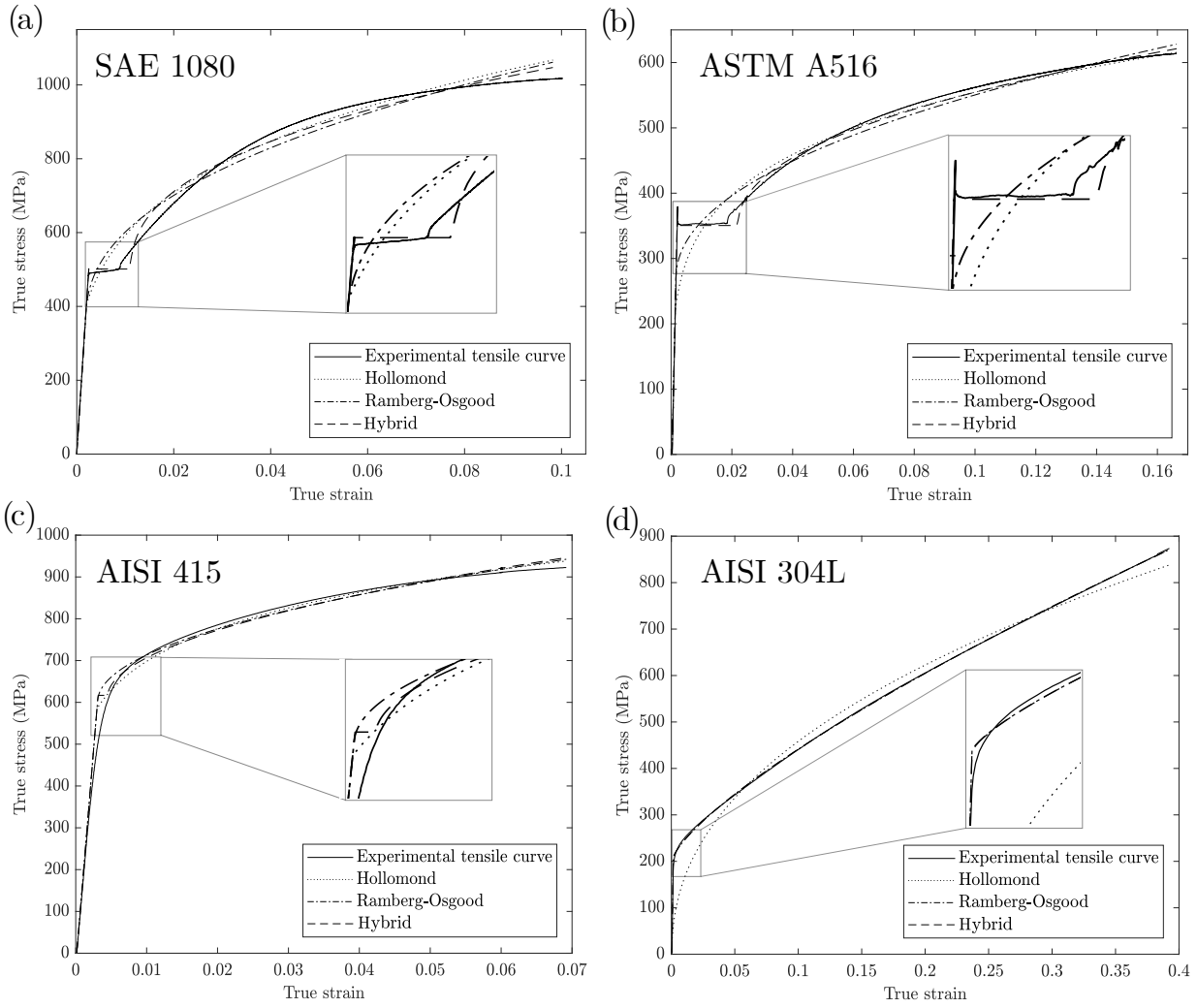

Figure 6.6 Experimental true stress-true strain behaviour of four steels compared to the tensile curves obtained by fitting the models developed by Hollomon, Ramberg-Osgood and the hybrid model, to the experimental tensile curves: (a) SAE 1080; (b) ASTM A516; (c) AISI 415; and (d) AISI 304L. This figure shows that some hardening models can better approximate the experimental true stress-true strain curves than others depending on the material and it is concluded that no hardening model can represent the whole tensile curve of all materials.

on the material/model combination. This demonstrates the potential of the novel method developed in this work which does not assume a hardening model.

It must be noted that it is possible that new models developed in the future may be able to fit more materials with more accuracy, especially regarding materials including a plastic plateau, for which hardening models are not commonly available at this time.

6.4 Results of the performance study of the developed inverse methodology

This section presents the results of the performance studies regarding the numerical application of the inverse methodology, the experimental application and the analysis using the I-index.

6.4.1 Numerical application

Estimated tensile curves

Table 6.3 shows the Ramberg-Osgood parameters obtained by the surrogate step of optimization for the four steels studied in this thesis. The target values for the elastic modulus, E, and yield stress, σ_y, are also shown for comparison. The obtained starting points are within +/- 1.5% and 24% of the target tensile properties E and σ_y, respectively. This demonstrates that a suitable starting point for the optimization step is found through the surrogate step and that the surrogate finite element model is effective.

The true stress-true strain curves generated by the surrogate step and upon completion of both steps of the proposed methodology are shown in Figure 6.7 for the four steels studied. For comparison purposes, Figure 6.7 also shows the estimated true stress-true strain curves if instead of optimizing the variables in $\mathbf{X}$, the parameters of a Hollomon (Eq. (2.12)), Ramberg-Osgood (Eq. (2.13)), or hybrid (Eq. (5.1)) hardening model were used as variables in the optimization step.

With the proposed methodology, the estimated curves lie very close to the target curves for all four studied materials. This demonstrates the capability of the proposed method to obtain different shapes of tensile curves with a good accuracy. It is also noticeable that assuming a hardening model either deteriorates the estimation of the overall shape of the tensile curve (*e.g.* SAE 1080 steel) or gives equivalent results (*e.g.*, hybrid model for ASTM 516 and Ramberg-Osgood model for AISI 304L). The proposed methodology is therefore more versatile because it can lead to accurate results for materials with varying tensile behaviours.

Table 6.4 lists the errors on elastic modulus, ΔE, and yield stress, $\Delta\sigma_y$, associated with the estimated tensile curves shown in Figure 6.7. The proposed methodology evaluates E and σ_y with maximum errors of 0.5% (AISI 304L) and 11.1% (AISI 415), respectively. Assuming a hardening model in the optimization step either increases the error on σ_y, or leads to similar errors, and has no significant impact on the estimation of E. This can be explained by the increased error in the strain hardening region of the estimated curve when using a hardening model that cannot fit this region properly. The yield stress is then altered to compensate

Table 6.3 Ramberg-Osgood parameters obtained by the surrogate step of the optimization procedure and target values of elastic modulus, E, and yield stress, σ_y, for comparison. These parameters were obtained using numerical indentation data.

	SAE 1080				ASTM A516			
	E (GPa)	σ_y (MPa)	K (MPa)	n	E (GPa)	σ_y (MPa)	K (MPa)	n
Surrogate step	207	520	1693	0.59	209	350	618	0.660
Target values	205	498	N.A.	N.A.	208	345	N.A.	N.A.
	AISI 415				AISI 304L			
	E (GPa)	σ_y (MPa)	K (MPa)	n	E (GPa)	σ_y (MPa)	K (MPa)	n
Surrogate step	192.0	620	700	0.36	200	230	1250	0.821
Target values	195	500	N.A.	N.A.	199	200	N.A.	N.A.

that effect.

The precision of the estimated true stress-true strain curves with regard to the target curves in the hardening region is quantified through $|\overline{\Delta\sigma_p}|$. This parameter is obtained by interpolating the estimated and target true stress-true strain curves at true strain values incremented by 5×10^{-4}, leading to at least 600 data points for each material. For each interpolated point, the error of the estimated curve, when compared to the target curve, is computed. The parameter $|\overline{\Delta\sigma_p}|$ is then the average of the absolute value of these errors, to give a general appreciation of the quality of the estimated curve. For each material. The values of $|\overline{\Delta\sigma_p}|$ are shown in Table 6.4. For all materials, this average error is lowest when using the proposed methodology, reaching a maximum value of 2.42% in the case of ASTM A516.

The presence of a plastic plateau was successfully identified in the estimated tensile curves of ASTM A516 and SAE 1080 steels. For ASTM A516, a plateau with a tangent modulus below the limit of 1.25 GPa set in constraint $c_3(\boldsymbol{X})$ is found, *i.e.*, a plateau which is almost horizontal, so no further manipulation is necessary. However, for SAE 1080, the strain value marking the end of the plateau, ε_{pl}, was not precisely identified. The first tangent modulus of the identified curve is lower than the second, but the plateau is not close to a horizontal line. Figure 6.8 displays the results obtained by extrapolation of the line between σ_2 and σ_3 to create a horizontal plateau. The yield point elongation then matches very well with that of the target curve. However, since the position of the strains are not optimized, an important error can arise in the estimation of ε_{pl}: for ASTM A516, this value is underestimated by 19.1%.

It was attempted to add the strain values as optimization variables, but the corresponding increase in the number of degrees of freedom made the determination of the tensile curve

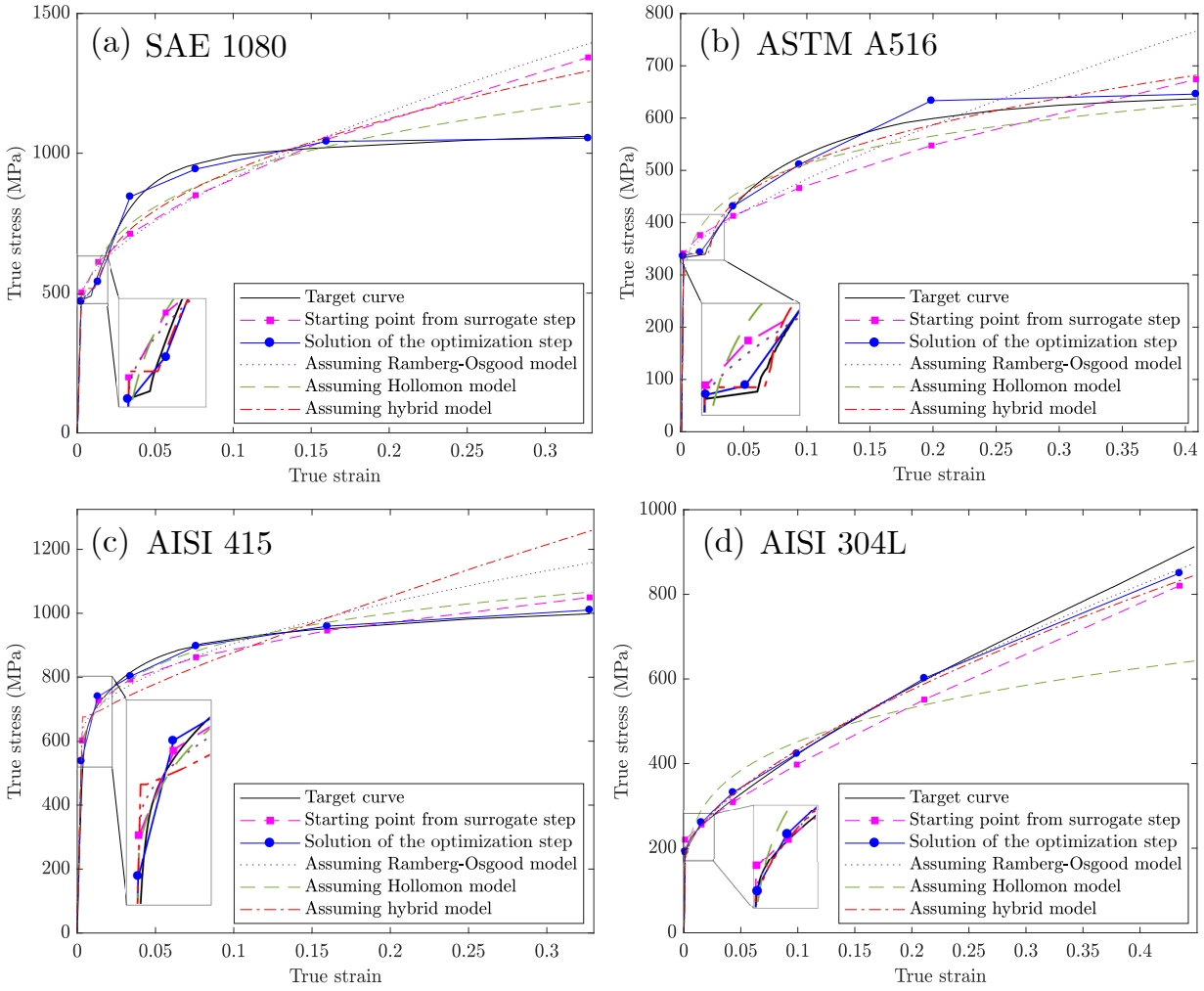

Figure 6.7 Comparison of the target true stress-true strain curves to the starting points obtained from the surrogate step, and those estimated with the optimization step when using the proposed methodology and when assuming either the Ramberg-Osgood, Hollomon or hybrid hardening model. The target indentation data used was numerically generated. This figure shows the capacity of the proposed method to approach the general shape of the sought true stress-true strain curves for all materials, which is not the case when assuming hardening models.

parameters unstable. For example, the extracted material parameters obtained when using the same method, but adding a single variable to modify the strain values by scaling the geometric progression, led to a tensile curve resulting in an averaged difference with the strain hardening region of the experimental tensile curve which was 10 times higher, when compared to when strains were pre-defined for a test done on ASTM A516 steel.

Another issue to point out about the strain values is the limited strain range of the estimated tensile curve. Applications may require the knowledge of the plastic behaviour at strains

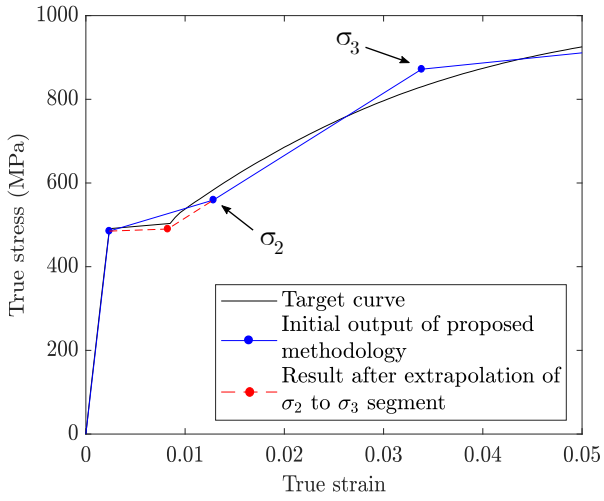

Figure 6.8 Estimation of the actual yield point elongation by extrapolation of the σ_2 to σ_3 segment of the true stress-true strain curve obtained for SAE 1080 steel. This figure shows how the value of the strain at the end of the plateau can be well estimated even when it falls in between two values of pre-defined strains.

Table 6.4 Errors on the estimated elastic modulus, ΔE, and yield stress, $\Delta\sigma_y$, and the average of the absolute value of the error over the hardening region of the true stress-true strain curve derived from the extracted material parameters, $|\overline{\Delta\sigma_p}|$, obtained by the optimization step when using the proposed methodology and when assuming either the Ramberg-Osgood, Hollomon or hybrid hardening model. The optimization was conducted using numerically generated indentation data.

	SAE 1080			ASTM A516		
	ΔE (%)	$\Delta\sigma_y$ (%)	$\lvert\overline{\Delta\sigma_p}\rvert$ (%)	ΔE (%)	$\Delta\sigma_y$ (%)	$\lvert\overline{\Delta\sigma_p}\rvert$ (%)
Proposed methodology	0.2	-2.6	1.24	0.3	1.8	2.42
Assuming Ramberg-Osgood model	0.2	1.7	13.4	0.1	-1.1	9.15
Assuming Hollomon model	-0.2	-9.2	6.12	-0.4	-17.0	4.31
Assuming hybrid model	0.3	7.6	9.19	-0.1	1.5	3.19
	AISI 415			AISI 304L		
	ΔE (%)	$\Delta\sigma_y$ (%)	$\lvert\overline{\Delta\sigma_p}\rvert$ (%)	ΔE (%)	$\Delta\sigma_y$ (%)	$\lvert\overline{\Delta\sigma_p}\rvert$ (%)
Proposed methodology	0.0	11.1	0.96	-0.5	0.2	1.53
Assuming Ramberg-Osgood model	-0.3	28.0	6.67	-0.5	0.5	1.78
Assuming Hollomon model	-0.5	20.8	3.21	-1.5	-24.0	15.08
Assuming hybrid model	0.1	39.6	10.17	-0.6	1.9	3.28

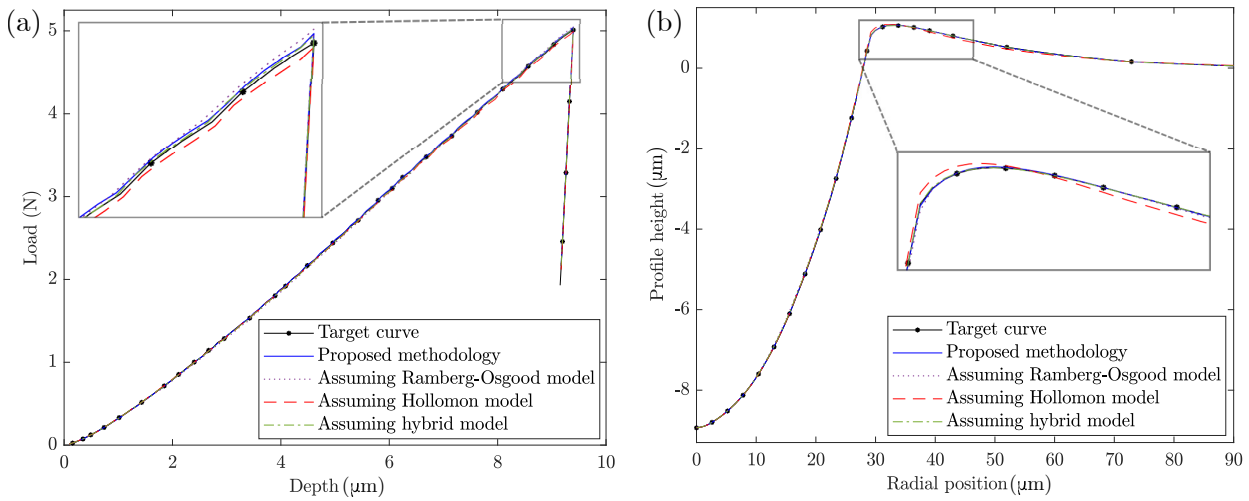

Figure 6.9 Indentation data obtained by finite element simulation using the target curve, and the estimated true stress-true strain curves using the proposed methodology, and when assuming either the Ramberg-Osgood, Hollomon or hybrid hardening model for ASTM A516 steel. It can be observed that even though the estimated true stress-true strain curves are different (see Figure 6.7(b)), the simulated indentation data are similar, pointing towards possible non-uniqueness issues.

higher than ε_{max}. In this work, the estimated tensile curves of ASTM A516, SAE 1080 and AISI 415 tended to perfect plasticity at high strains, and that of AISI 304L displayed a hardening behaviour very close to linear. The estimated true stress-true strain curves could then extrapolated using a linear equation to approximate the true stress-true strain behaviour at higher strains. However, other relationships might be better suited for other materials, like power-laws or polynomial equations.

Figure 6.9 shows the simulated indentation data obtained with the target curve compared to that obtained with the true stress-true strain curves estimated by the proposed methodology or when assuming either the Ramberg-Osgood, Hollomon or hybrid hardening model for ASTM A516 steel. For this material, the difference between the estimated true stress-true strain curves and the target curves varied with the assumed model or lack thereof. Particularly, the error on the yield stress ranged from -1.1% to -17% and the value of $|\overline{\Delta\sigma_p}|$ ranged from 2.42% to 9.15%. However, these variations in the tensile curves did not lead to very large differences in the simulated indentation curves and imprints. Indeed, the errors on the maximum load P_{max} ranged from -0.31% to 1.0% and the errors on u_{max} were all below 1%, except when the true stress-true strain curve estimated assuming a Hollomon hardening model was used, in which case the error reached 2.7%. The similarity in the simulated indentation curves and imprints obtained with the different estimated tensile curves points to the

possibility of non-uniqueness issues. A higher depth could perhaps be used in further studies to increase the value of the ratio h_{max}/R and improve the sensitivity of the indentation data to the material parameters used to estimate the tensile curve. However, with the indenter used in this work, the conical region could be reached and the indentation would then not be purely spherical.

Convergence plots

The convergence behaviour of the method must also be analyzed to infer its overall performance. Figure 6.10 presents the convergence plots of the surrogate and optimization steps of the proposed method for all four materials. These stairstep curves display the value of $\tilde{f}(\mathbf{Y})$ or $f(\mathbf{X})$ corresponding to the incumbent solution, as a function of number of function evaluations.

For the surrogate step, the maximum number of $\tilde{f}(\mathbf{Y})$ evaluations is reached for all materials before the tolerance based stopping criterion $\tilde{f}(\mathbf{Y}) < \epsilon_S = 10^{-3}$. The scale used for this step does not show the initial values of $\tilde{f}(\mathbf{Y})$ to better observe the behaviour at lower $\tilde{f}(\mathbf{Y})$ values, not because the starting point did not lead to an acceptable solution.

For the optimization step, the tolerance based stopping criterion ($f(\mathbf{X}) < \epsilon_O = 10^{-5}$) was reached for all materials, except for AISI 304L, for which the minimum mesh size was reached beforehand. The proposed methodology performed the best for AISI 415 steel, reaching convergence in 594 $f(\mathbf{X})$ evaluations. The convergence plot of the algorithm for SAE 1080 steel particularly illustrates the capability of the OrthoMADS optimization algorithm to get out of local minima. Indeed, the value of $f(\mathbf{X})$ does not improve significantly between 350 and 600 evaluations for that material, since the solution is then trapped into the neighborhood of a local minimum. After 600 evaluations however, the algorithm successfully escapes this local minimum, and the value of $f(\mathbf{X})$ starts to decrease effectively and reaches the convergence criterion after an additional 200 evaluations.

To evaluate the use of adding the surrogate step, the optimization step was launched directly with the starting point of the surrogate step (given in Eq. (6.2c)). The convergence plots show that omitting the surrogate step has an important effect for ASTM A516 and AISI 304L, for which the number of necessary function evaluations to reach one of the stopping criteria is increased by a factor of 2.6 and 2.5, respectively. Also, in the case of ASTM A516, the tolerance based stopping criterion is not reached, meaning that the obtained solution is farther from the target curve obtained using the surrogate step. For AISI 415 and SAE 1080, the number of function evaluations necessary was 2.9% higher and 0.3% smaller, respectively. These differences are considered negligible. Even though only two of the four studied mate-

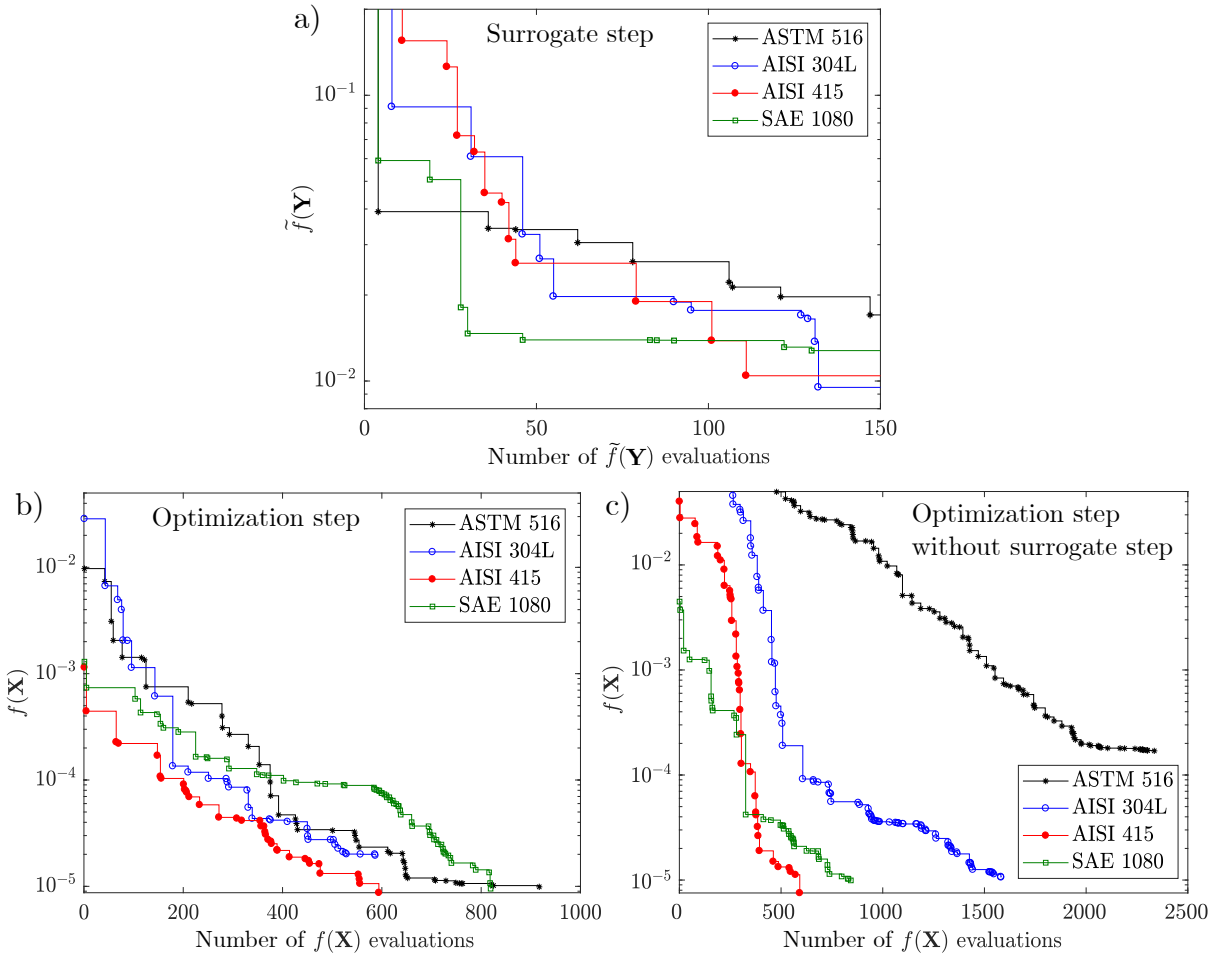

Figure 6.10 Convergence plots of the proposed method for four materials using numerically obtained target indentation data for: (a) the surrogate step; (b) the optimization step; and (c) the optimization step without the surrogate step. This figure shows the efficient convergence behaviour of the chosen optimization algorithm for all materials and the importance of including the surrogate step in the methodology. For the surrogate step, the scale used does not show the initial values of $\tilde{f}(\mathbf{Y})$ to better observe the behaviour at lower $\tilde{f}(\mathbf{Y})$ values, not because the starting point did not lead to an acceptable solution.

rials were affected by the use of the surrogate step, it is still imperative to include it in the method to ensure the performance is optimized for all materials.

Figure 6.11 displays the convergence plots corresponding of the optimization step when using the proposed methodology and when assuming either the Ramberg-Osgood, Hollomon or hybrid hardening models. A general, expected, increase in computational time is observed for the proposed methodology since it optimizes more variables. The worst decrease in computational efficiency is observed for SAE 1080, for which the use of all three hardening models led to a value of $f(\mathbf{X})$ very close to their respective converged result within 80 function evaluations. The proposed method required 819 function evaluations, an increase by a factor of ten. For the proposed method, this number includes 104 evaluations for which the non-relaxable constraints were not respected. The evaluation time is under a tenth of a second for such evaluations as no finite element simulations are conducted. The time required for an evaluation respecting constraints during the optimization step was between 100 to 150 seconds, using a regular workstation with an Intel(R) Core(TM) i9-9900K CPU processor. The time to reach 80 evaluations for SAE 1080 steel using a hardening model was thus around 2.75 hours, and about 25 hours for the proposed method, an increase by a factor of 9.

Even though the proposed method is slower, its use leads to a final value of $f(\mathbf{X})$ which is below the tolerance ϵ_O, while it is not the case for the use of the hardening models, which converged by reaching the minimum mesh size values. A lower $f(\mathbf{X})$ was observed with the proposed method for all materials, except for the Ramberg-Osgood model used with AISI 304L in which case the results are comparable. This is in line with results presented in Figure 6.7, since a lower $f(\mathbf{X})$ is associated with a better estimation of the true stress-true strain curve.

From these results, it is apparent that the proposed method is more time consuming than when assuming a hardening model. It does however render more accurate estimations of tensile curves in cases when the experimental true stress-true strain curve is not adequately fitted by popular hardening models. The added value of using this novel method thus depends upon the requirements of the user in terms of precision and restrictions in terms of computation time. This method could therefore be better suited for a research environment rather than an industrial environment.

6.4.2 Experimental application

The true stress-true strain curves obtained by the surrogate and optimization steps of the proposed methodology using experimental indentation data for all steels are shown in Figure 6.12, as well as the corresponding macroscopic experimental tensile curves for comparison.

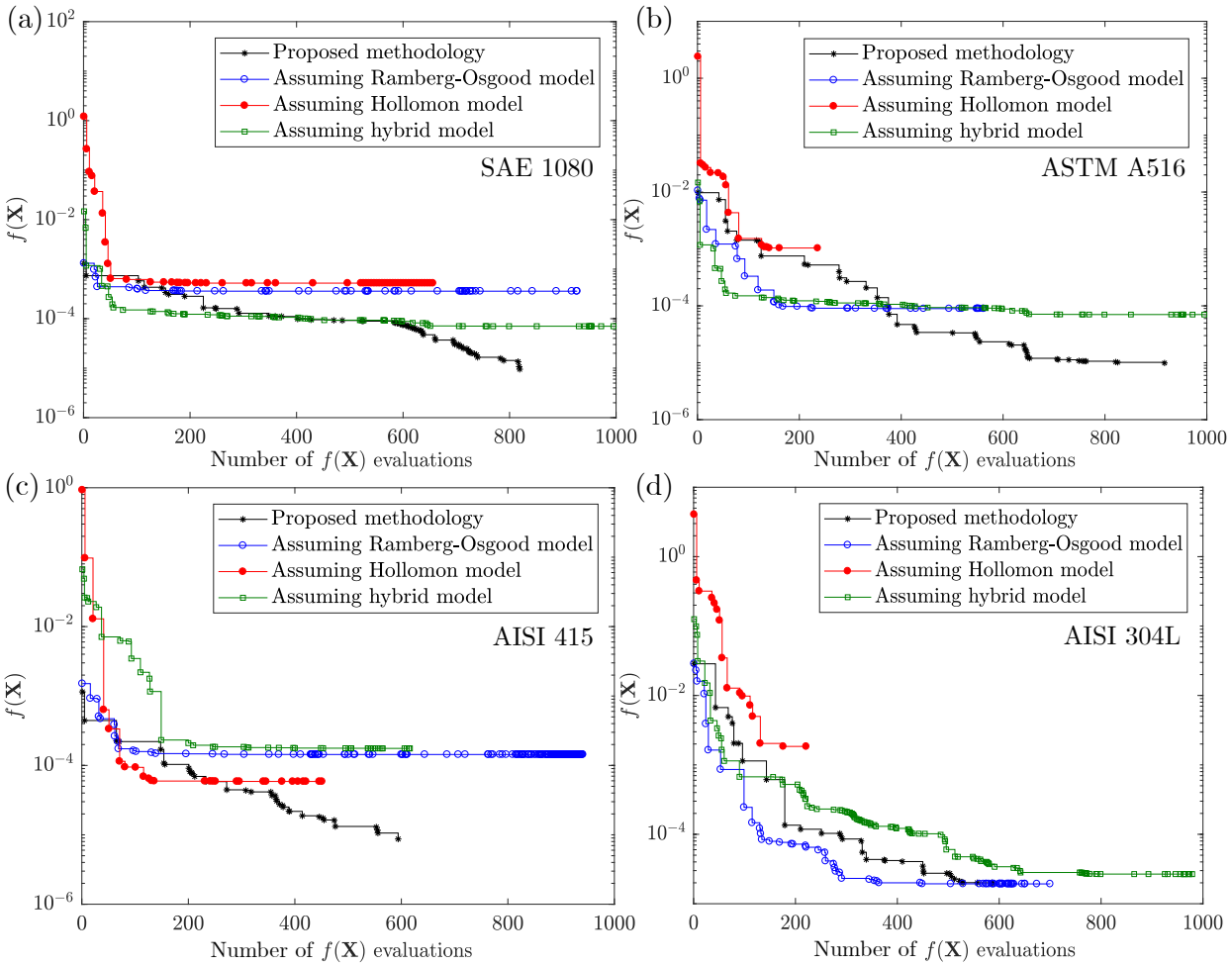

Figure 6.11 Comparison of the convergence plots of the optimization step when using the proposed methodology and when assuming either the Ramberg-Osgood, Hollomon or hybrid hardening model. The target indentation data used was numerically generated. This figure shows a general increase in computation time using the proposed method, due to the increased number of variables. However, it is also apparent that the value of $f(\mathbf{X})$ reached by the optimization is lower with the proposed method, meaning a more precise estimation of the true stress-true strain curve.

In the case of SAE 1080, the extrapolation procedure used in Figure 6.8 was used to improve the estimation of ε_{pl}, since the first tangent modulus was above the limit of 1.25 GPa. This was not required for ASTM A516, as in the numerical application. Extrapolations of the experimental true stress-true strain curves up to values of ε_{max} are also shown since data is not available after the onset of necking. The transition from experimental to extrapolated data is shown by orange squares in Figure 6.12.

The parameters extracted from the surrogate step are shown in Table 6.5. The values of E and σ_y, found in the optimization step, as well as their relative errors, when compared to the average experimental values obtained by tensile tests and the average error over the hardening region, $|\overline{\Delta\sigma_p}|$, are shown in Table 6.6. To include the variability of the experimental tensile curves in the analysis, Table 6.7 re-iterates the standard deviations of E and σ_y as well as the average of the standard deviation in the hardening regions of the curves. This table also gives the variability around the average tensile curves which represents the 95th percentile, calculated by taking the standard deviation multiplied by a factor of 1.96. These values give the variability of the experimental tensile parameters within which 95% of the experimental tensile curves are expected to lie.

The results demonstrate that the proposed inverse method performs well for ASTM A516 and SAE 1080, while performing poorly for AISI 415 and AISI 304L. This was expected, as described in Section 5.4.1: the behaviour of the former two steels is captured more accurately by the finite element model than the later two steels.

For SAE 1080 steel, the presence of a plastic plateau is well identified. However, an overestimation of the stress is observed for all but the last pre-defined true strain value, leading to an average error in the hardening region, $|\overline{\Delta\sigma_p}|$, of 3.7%. This overestimation is maximum at the yield stress, where it reaches 22.1%, an error significantly larger than that of the 95th percentile, $\Delta\sigma_{95} = 5.43\%$. These differences can partly be explained by the modelling errors for this steel (see Figure 5.3). Table 6.8 shows the difference between important indentation parameters obtained from indentation experiments, and those obtained from simulation with the detailed model using either the average experimental true stress-true strain curve or the optimized true stress-true strain curve. Only the average experimental tensile curve is used in this comparison, because even though simulations using different experimental tensile curves led to slight variations in the indentation parameters, the same trends were observed and thus the same conclusions could be drawn, for all materials.

The modelled indentation curve using the average experimental tensile curve for SAE 1080 shows a 3.8% lower reaction force, P_{max}, for the same indentation depth, when compared to the indentation experiment. To minimize the error between the numerical and experimental

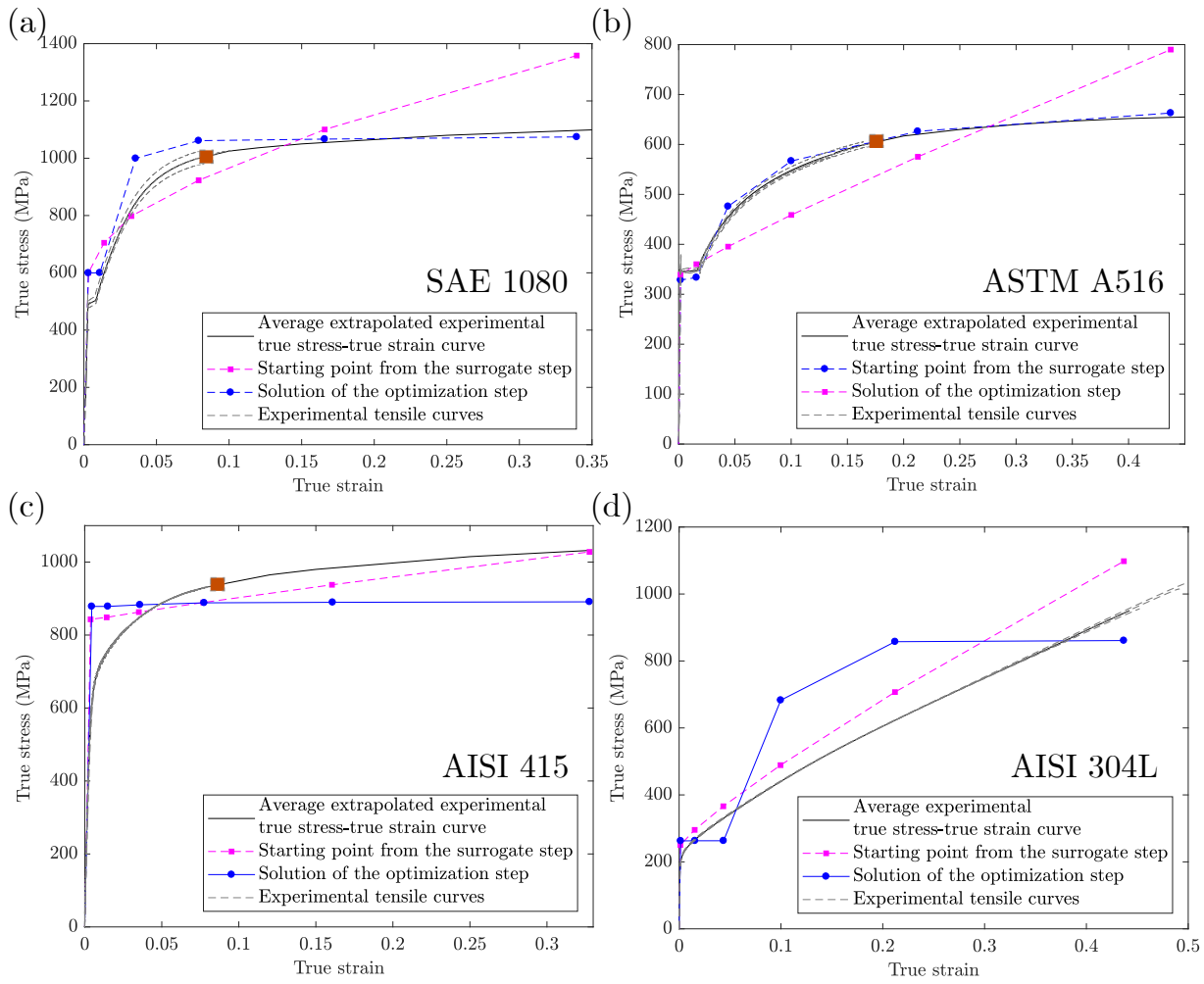

Figure 6.12 Comparison of the experimental true stress-true strain curves to those estimated by the surrogate step and optimization step using experimentally obtained target indentation data. The orange squares indicate the point at which the extrapolation of experimental data begins when necessary. The method can be observed to be accurate only in the case of SAE 1080 and ASTM A516 steels, for which the finite element model is also more precise (see Section 5.4.1).

Table 6.5 Optimization starting points defined by elasto-plastic parameters of a Ramberg-Osgood hardening model obtained by the surrogate step of the optimization procedure. These optimization starting points were obtained using experimental indentation data.

	SAE 1080				ASTM A516			
	E (GPa)	σ_y (MPa)	K (MPa)	n	E (GPa)	σ_y (MPa)	K (MPa)	n
Surrogate step	193	600	1421	0.57	208	339	917	0.89
Target values	206	491	N.A.	N.A.	205	347	N.A.	N.A.
	AISI 415				AISI 304L			
	E (GPa)	σ_y (MPa)	K (MPa)	n	E (GPa)	σ_y (MPa)	K (MPa)	n
Surrogate step	221	840	509	0.9	203	250	1800	0.85
Target values	187	512	N.A.	N.A.	195	206	N.A.	N.A.

Table 6.6 Values of the extracted elastic moduli, E, and yield stresses, σ_y, as well as their relative errors with respect to the experimental tensile curves, ΔE and $\Delta\sigma_y$, and the average of the absolute value of the error over the hardening region of the estimated true stress-true strain curve, $|\overline{\Delta\sigma_p}|$, obtained by the material parameters identified in the optimization step of the method. Experimental indentation data were used in the application of the method.

SAE 1080					ASTM A516				
E (GPa)	ΔE (%)	σ_y (MPa)	$\Delta\sigma_y$ (%)	$\lvert\overline{\Delta\sigma_p}\rvert$ (%)	E (GPa)	ΔE (%)	σ_y (MPa)	$\Delta\sigma_y$ (%)	$\lvert\overline{\Delta\sigma_p}\rvert$ (%)
192.8	-6.3	599.4	22.1	3.7	187.0	-8.8	328.5	-5.3	2.1
AISI 415					AISI 304L				
E (GPa)	ΔE (%)	σ_y (MPa)	$\Delta\sigma_y$ (%)	$\lvert\overline{\Delta\sigma_p}\rvert$ (%)	E (GPa)	ΔE (%)	σ_y (MPa)	$\Delta\sigma_y$ (%)	$\lvert\overline{\Delta\sigma_p}\rvert$ (%)
190.8	2.0	878.5	71.6	9.9	170.0	-12.8	262.6	27.4	22.8

Table 6.7 Standard deviations of E and σ_y as well as the average of the standard deviation in the hardening regions of the curves. Also shown are the variability around the average tensile curves which represents the 95th percentile, calculated by taking the standard deviation multiplied by a factor of 1.96. These values, ΔE_{95}, $\Delta\sigma_{95}$ and $\Delta\overline{s}_{95\ [\varepsilon_y,\ \varepsilon_{max}]}$ represent the variability of the elastic modulus and yield stress, and the average variability of the stress values in the hardening region which are statistically expected to include 95% of the experimental tensile curves.

SAE 1080						ASTM A516					
s_E (%)	ΔE_{95} (%)	s_{σ_y} (%)	$\Delta\sigma_{95}$ (%)	$\overline{s}_{[\varepsilon_y,\ \varepsilon_{max}]}$ (%)	$\Delta\overline{s}_{95\ [\varepsilon_y,\ \varepsilon_{max}]}$	s_E (%)	ΔE_{95} (%)	s_{σ_y} (%)	$\Delta\sigma_{95}$ (%)	$\overline{s}_{[\varepsilon_y,\ \varepsilon_{max}]}$ (%)	$\Delta\overline{s}_{95\ [\varepsilon_y,\ \varepsilon_{max}]}$ (%)
1.48	2.90	2.77	5.43	2.65	5.20	8.05	15.7	0.89	1.74	1.16	2.27
AISI 415						AISI 304L					
s_E (%)	ΔE_{95} (%)	s_{σ_y} (%)	$\Delta\sigma_{95}$ (%)	$\overline{s}_{[\varepsilon_y,\ \varepsilon_{max}]}$ (%)	$\Delta\overline{s}_{95\ [\varepsilon_y,\ \varepsilon_{max}]}$	s_E (%)	ΔE_{95} (%)	s_{σ_y} (%)	$\Delta\sigma_{95}$ (%)	$\overline{s}_{[\varepsilon_y,\ \varepsilon_{max}]}$ (%)	$\Delta\overline{s}_{95\ [\varepsilon_y,\ \varepsilon_{max}]}$
9.24	18.1	2.8	5.49	0.84	1.65	2.17	4.25	0.61	1.20	0.42	0.82

indentation curves, the optimized true stress-true strain curve for SAE 1080 consequently corresponds to a material which is more resistant to plastic deformation. Using the optimized parameters, the values of P_{max} obtained by simulation is 3.0% higher than for indentation experiments. Table 6.8 shows a better approximation of indentation parameters using the optimized tensile curve for this material except for the contact stiffness. This may explain the least precise estimation of the elastic modulus, for which the error with the average experimental value is -6.3% while $\Delta E_{95} = 2.90$.

In the case of ASTM A516 steel, the overall shape of the curve is better approximated, when compared to SAE 1080, with $|\overline{\Delta\sigma_p}| = 2.1\%$, which is below the value of $\Delta\overline{s}_{95\ [\varepsilon_y,\ \varepsilon_{max}]} = 2.27$ %. The yield stress is also better estimated for this material, with an error of -5.3%, although

Table 6.8 Differences between indentation maximum load, P_{max}, contact stiffness, S, residual depth, h_r, and maximum pile-up height, u_{max}, obtained from experiments and those obtained by the detailed finite element model using experimental true stress-true strain curves (labelled Sim.) and the optimized true stress-true strain curves (labelled Opti.).

Material	ΔP_{max} (%)		ΔS (%)		Δh_r (%)		Δu_{max} (%)	
	Sim.	Opti.	Sim.	Opti.	Sim.	Opti.	Sim.	Opti.
SAE 1080	-3.8	3.0	1.7	-6.0	9.2	7.6	-14.2	-3.2
ASTM A516	4.6	3.0	5.0	-3.9	3.3	2.3	9.4	-1.8
AISI 415	-6.8	-2.4	-2.5	0.1	4.0	3.2	-47.0	-10.5
AISI 304L	-10.6	2.3	20.6	3.0	3.7	2.1	14.6	-2.0

it is above $\Delta\sigma_{95} = 1.74$ %. This shows that except in the plastic plateau region, the extracted curve is within the 95th percentile of the experimental tensile curves. This was expected since the modelling errors are smaller for ASTM A516 as shown in Table 6.8. All indentation parameters from this table are better estimated by simulation with the optimized true stress-true strain curve than with the experimental curve.

For AISI 415 steel, the yield stress is overestimated by 71.6% and the estimated true stress-true strain curve presents almost no strain hardening, leading to an average error in the strain hardening region of 9.9%. The extracted tensile curve significantly falls outside the 95th percentile of the experimental tensile curves. It is shown in Table 6.8 that the maximum pile-up height, u_{max}, is underestimated by 47% by the finite element simulation using the experimental tensile curve. To better approximate the experimental residual imprint, the strain hardening of the optimized tensile curve was decreased, leading to the error on the pile-up height decreasing to 10.7%. This lower strain-hardening leads to a decrease in hardness, and the yield stress must then increase for the simulated indentation curve to approach the experimental one. The error on P_{max} reduced from -6.8% to -2.4% using the optimized parameters.

For AISI 304L steel, the estimated true stress-true strain curve is overestimated as a whole, and has a completely different shape than the experimental curve, presenting a long plastic plateau and non-linear strain hardening. For this material also, the extracted curve is significantly far from the 95th percentile of the experimental tensile curves. It can also be observed that the surrogate step led to a better approximation of the tensile curve, leading to $|\overline{\Delta\sigma_p}| = 12.52$ while the optimization step led to $|\overline{\Delta\sigma_p}| = 22.8\%$. For this steel, there was an underestimation of 10.6% of P_{max} observed when using the experimental tensile curve. The optimized estimated true stress-true strain curve being more resistant to plastic deformation, the difference on P_{max} reduced to 2.3%.

It is concluded that the proposed methodology is thus capable of estimating true stress-true strain curves with satisfying precision in the presence of experimental errors and moderate modeling errors. For the two steels respecting these conditions, *i.e.*, ASTM A516 and SAE1080, the proposed method was shown to be capable of approaching the general shape of the experimental tensile curve without the use of a hardening model. For the other two steels, AISI 415 and AISI 304L, the improvement of the finite element model by taking into account the martensitic transformations and/or increasing the scale of indentation (Section 5.4.1) could help in obtaining better results with the proposed method.

6.4.3 Analysis using the identifiability-index

This section presents the different studies enabled by the use of the I-index. The following analysis is focused on the optimization step of the inverse method. All of the conclusions were however applied to the surrogate step to improve its performance.

Number of points

Table 6.9 displays the I-index values quantifying the identifiability of different sets of material parameters for each material. These sets contain different quantities of variables which led to estimations of the true stress-true strain curves defined with different numbers of points. The number of points is always the number of parameters minus 1 since the parameters contain the elastic modulus. The pre-defined strain values were computed using Eq. (6.13b) and the values for ε_{max} were taken from the numerical application (see Section 6.4.1) with a maximum load of 5 N. The value ε_{max} is constant for each material, regardless of the number of material parameters used to estimate the tensile curve, as it only depends upon the residual imprint of indentation.

It is observed that the I-index gets smaller, denoting a better identifiability, as the number of parameters decreases. However, the objective of avoiding the use of a tensile model is to obtain estimated true stress-true strain curve which fit the experimental tensile data more accurately. Lowering the number of points with which the tensile curve is constructed will lessen the quality of the fit and increase errors. To consider this, the parameters were fitted to the experimental tensile curves, to investigate what the minimal identification error could be without the optimization. Table 6.9 thus also shows the average of the absolute value of the error of this fit over the strain hardening region, $|\overline{\Delta\sigma_p}|$, as well as the maximum error of the fit, $\Delta\sigma_{max}$.

As expected the general trend is an increase in the error of the fit with the decreasing of parameter numbers. Some exceptions are present, for instance in the case of ASTM A516, for which both $|\overline{\Delta\sigma_p}|$ and $\Delta\sigma_{max}$ are minimum when using 7 points. This can be explained by the computed strain values that are better capable of capturing different features of the tensile curve, like the plastic plateau.

A compromise must be done between the identifiability of the parameters and their capacity to fit the experimental true stress-true strain curve with precision. This thus explains the choice of using of 7 parameters, leading to an estimated true stress-true strain curve comprising of 6 points.

Table 6.9 I-index, I, quantifying the identifiability of sets containing between 5 and 9 parameters leading to estimated true stress-true strain curves comprising of 4 to 8 points. The parameters were fitted to the experimental tensile curves, to observe the minimal identification errors without the optimization, $|\overline{\Delta\sigma_p}|$ and $\Delta\sigma_{max}$. The minimum values for $|\overline{\Delta\sigma_p}|$, $\Delta\sigma_{max}$ and I are emphasized by using a bold font. It is concluded that the best compromise between possible precision of the estimated tensile curve and identifiability is obtained by using 7 paramters.

		SAE 1080			ASTM A516		
		$\lvert\overline{\Delta\sigma_p}\rvert$ (%)	$\Delta\sigma_{max}$ (%)	I	$\lvert\overline{\Delta\sigma_p}\rvert$ (%)	$\Delta\sigma_{max}$ (%)	I
9 parameters	8 points	**0.27**	4.13	4.36	0.88	4.72	2.94
8 parameters	7 points	0.28	**3.03**	3.76	0.66	3.99	3.16
7 parameters	6 points	0.45	8.7	3.69	**0.41**	**3.32**	2.71
6 parameters	5 points	0.82	12.3	3.60	0.79	10.1	2.55
5 parameters	4 points	0.73	10.7	**3.22**	1.1	12.1	**2.16**
		AISI 415			AISI 304L		
		$\lvert\overline{\Delta\sigma_p}\rvert$ (%)	$\Delta\sigma_{max}$ (%)	I	$\lvert\overline{\Delta\sigma_p}\rvert$ (%)	$\Delta\sigma_{max}$ (%)	I
9 parameters	8 points	0.28	6.33	4.03	0.37	1.67	2.93
8 parameters	7 points	**0.25**	**4.18**	3.67	**0.25**	**0.98**	2.95
7 parameters	6 points	0.36	10.0	3.74	**0.25**	4.42	2.91
6 parameters	5 points	0.74	15.3	3.69	0.47	7.2	**2.73**
5 parameters	4 points	1.78	20.1	**3.29**	0.89	9.2	3.01

Experimental information used in the definition of the objective function: combinations of indentation data

Table 6.10 shows the computed I-indices when using different experimental information in the objective function: the indentation curve only, the residual imprint only, or a combination of both. Here, the indentation curve includes both the loading curve and the contact stiffness, and the residual imprint includes both the contact and free surface regions. The results show that the identification is optimized for the combination of the residual imprint and indentation curve, since the I-index is the lowest value in this case for all materials.

Contrary to the results of Renner at al. [111], the use of the residual imprint only does not improve the identifiability of the material parameters, when compared to the use of the indentation curve only. However, in their study, the parameters were those of a Méric Cailletaud crystal plasticity model and their sensitivity to the indentation data is different from the parameters used in the present study, which characterize the bulk behaviour of materials.

Experimental information used in the definition of the objective function: separation of the residual imprint

In the developed inverse method, the imprint is separated into two sub-functions in $f(\mathbf{X})$ (see Eqs (6.6) and (6.7)). To demonstrate why this choice was made, Table 6.11 shows the I-indices computed when replacing these two sub-functions in $f(\mathbf{X})$ by a single sub-function to account for the residual imprint, as in Eq. (6.27), when compared to those obtained with the developed inverse method. For all materials, an increase in the I-index is observed when using the full imprint in a single sub-function, meaning a lower identifiability of the material parameters. This is explained by the the fact that using the full residual imprint in a single

Table 6.10 I-indices obtained for the identification of $\mathbf{X} = [E, \sigma_y, \sigma_2, \sigma_3, \sigma_4, \sigma_5, \sigma_6]$ using different indentation data in the objective function: the indentation curve only, the residual imprint only, or a combination of both. The lowest value for the I-index is obtained when both the indentation curve and the residual imprint are used, leading to the best identifiability for $\mathbf{X}$ with these indentation data.

Experimental information	SAE 1080	ASTM A516	AISI 415	AISI 314L
Indentation curve only	5.23	3.30	4.66	3.09
Residual imprint only	4.5	4.28	4.6	4.36
Indentation curve and residual imprint	3.69	2.71	3.74	2.91

sub-function results in the contact region driving most of the value of the sub-function. This has a detrimental effect on the sensitivity of $f(\mathbf{X})$ to the strain hardening behaviour of the materials since the pile-up or sink-in regions are where the experimental information is the richest in the residual imprint.

Experimental information used in the definition of the objective function: optimization of sub-function weights

One last thing which was studied regarding the experimental information used in the objective function was the weights attributed to each sub-functions in Eq. (6.20). To find the weight combinations which rendered the best posed problem according to the I-index definition, the I-index was minimized by varying the weights between 0 and 1 for all materials. The weights found as well as the I-index values are displayed in Table 6.12.

It can first be observed that the obtained I_{min} are indeed smaller than those obtained with unit weights. This should mean that the method performs better with the optimized weights. However, the trends present in the obtained weights are unexpected. First, the highest weight is attributed to the contact region of the residual imprint, v_{IC}, which is not a portion of the indentation data which is known to carry the most sensitivity to material parameters, while the weight associated with the free surface region of the residual imprint, v_{IF}, is between 135 and 650 times smaller than v_{IC}. Many studies have shown that it is essential to consider the pile-up region of the imprint to estimate the hardening region of the tensile curve by indentation. With the optimized weights, this portion of the indentation data will have a negligible impact on the overall objective function value.

Also, the weight attributed to the contact stiffness portion of the objective function, v_S, is either null or again of a negligible magnitude, when compared to v_{IC}. The contact stiffness

Table 6.11 I-indices obtained for the identification of $\mathbf{X} = [E, \sigma_y, \sigma_2, \sigma_3, \sigma_4, \sigma_5, \sigma_6]$ using the indentation curve and either the full residual imprint topography in a single sub-function (see Eq. (6.27)) or the residual imprint separated into two sub-functions accounting for the contact (see Eq. (6.6)) and free surface (see Eq. (6.7)) regions of the imprint. The lowest value for the I-index is obtained when separating the residual imprint into two sub-functions.

	SAE 1080	ASTM A516	AISI 415	AISI 314L
Indentation curve and full residual imprint	4.68	2.84	4.44	3.03
Indentation curve and residual imprint separated into contact and free surface regions	3.69	2.71	3.74	2.91

Table 6.12 I-indices obtained for the identification of **X** using weight values which were optimized to obtain the smallest I-Index for each material, I_{min}. For comparison, the value of the I-index obtained with weights of unity value is given as I_{unity}. An improvement in the I-index is observed from the weight optimization.

	v_L	v_{IC}	v_{IF}	v_S	I_{min}	I_{unity}
SAE 1080	0.07	1	0.0083	0.004	2.83	3.69
ASTM A516	0.09	1	0.0028	0.003	1.39	2.71
AISI 415	0.11	0.847	0.0013	0	2.76	3.74
AISI 304L	0.24	0.82	0.006	0	1.35	2.91

is the indentation data which makes the method able to accurately estimate the elastic modulus. Removing this part of the indentation data is expected to reduce performance for the estimation of this parameter.

To investigate if these weights do indeed result in a better performance of the proposed inverse method, it was tested while using the optimized weights and experimental indentation data for ASTM A516 and SAE 1080 steels. The I-index should indicate how stable a problem is, and its effect should be mainly observed when experimental data is used, since more errors are present and can influence the results. Since the method with unity weights gave satisfying results for these two materials, it is interesting to see how it will behave with the optimized weights. Figure 6.13 shows the obtained true stress-true strain curves with optimized or unity weights. It is observed that using the optimized weights reduces the quality of the obtained results. Indeed, as expected, since the pile-up region of the residual imprint is almost neglected, the hardening region of the true stress-true strain curve does not follow the experimental curve at all. For both materials, the plastic plateau was not identified with the optimized weights. Also, the error on the estimated value of E increased from 6% and 10.1% with unity weights to 12.8% and 17.8% with optimized weights for SAE 1080 and ASTM A516, respectively. In the case of optimized weights, the obtained values were on the lower boundary of 170 GPa for both materials, so the method could have further underestimated the values of E if it was not for this boundary. This demonstrates that the sub-function accounting for the contact stiffness is absolutely necessary to obtain an accurate estimation of E.

It is unclear why the minimization of the I-index through the optimization of the weights reduced the performance of the developed inverse method. The other conclusions drawn from the analysis with the I-index (number of points, which combinations of indentation curve and imprint to use and combination and separation of the residual imprint) were all conclusive in the sense that they did indeed increase the performance of the method.

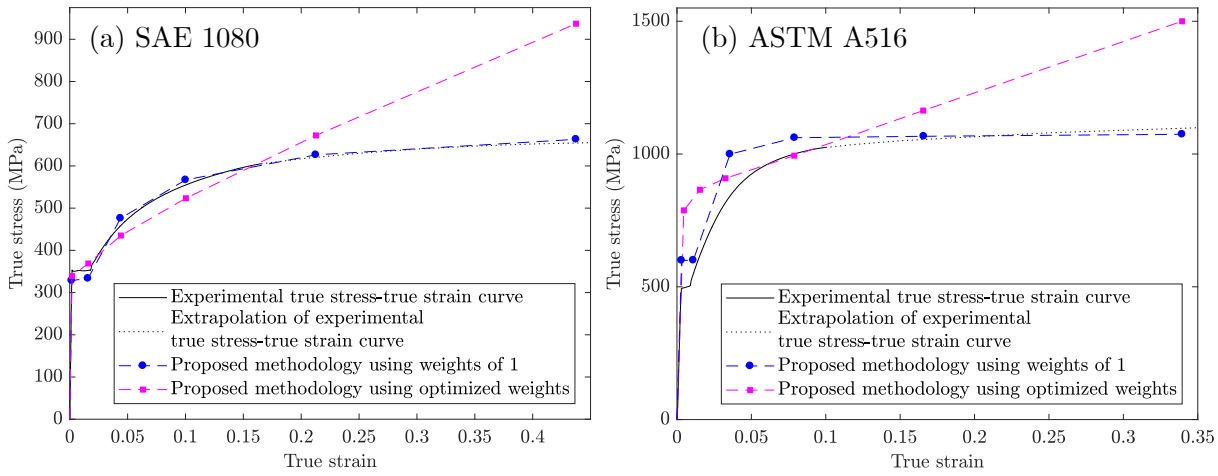

Figure 6.13 Comparison of the experimental true stress-true strain curves to those estimated with the proposed methodology using unity weights or optimized weights to minimize the I-index value for ASTM A516 and SAE 1080 steels. The use of the optimized weights actually decreases the performance of the method, even though this approach leads to lower I-index values, which should be associated with better performance.

Effect of the ratio h_{max}/R

The last aspect of the inverse method studied through the I-index is the influence of the ratio of maximum indentation depth to indenter radius, h_{max}/R. The I-index values were computed for the developed method, but varying the applied load to values of 2.5 N, 5 N, and 7.5 N, to vary h_{max} and thus vary h_{max}/R. This was done with numerically generated indentation data, as no experiments were conducted at loads of 2.5 N and 7.5 N. Table 6.13 displays the obtained results.

It can be observed that the minimal I values, which should be associated with increased

Table 6.13 I-index values, I, found through a numerical study varying indentation maximum load of 2.5 N, 5 N, and 7.5 N, as well as the corresponding h_{max}/R ratios for all materials. A trend of decreasing I with decreasing h_{max}/R exists, which is contrary to expectations that a higher h_{max}/R ratio leads to better performance of inverse methods to estimate tensile curves by indentation. For each material, the minimum values of I is emphasized by using a bold font.

	SAE 1080		ASTM A516		AISI 415		AISI 304L	
Applied load (N)	h_{max}/R	I	h_{max}/R	I	h_{max}/R	I	h_{max}/R	I
2.5	0.069	**2.36**	0.101	**2.71**	0.067	**2.38**	0.121	**2.58**
5	0.122	3.69	0.188	**2.71**	0.119	3.74	0.217	2.91
7.5	0.172	3.11	0.284	2.88	0.168	2.86	0.313	3.08

performance appear for the lowest values of h_{max}/R. However, it is well documented in the literature that the value of this ratio must be as large as possible to obtain the largest sensitivity to the hardening region of the tensile curve [37, 82, 137]. Similarly to the study of the optimized weights, the I-index seems to go against previously established findings.

A numerical application of the method using the varying loads was conducted to determine the effect of the load on the inverse method developed in this work. Figure 6.14 shows the estimated tensile curves for all three loads and all materials. The true stress-true strain curves for a load of 5 N are the same as previously shown in Figure 6.7. The results for all loads seem similar, the proposed method being able to estimate the general shape of the tensile curve. When using a smaller load, the contact radius is smaller and thus the value of the maximum strain of the estimated tensile curve, calculated with Eq. (6.10), decreases. This means that no matter the I-index analysis, if the behaviour of the material is sought at higher strains, the maximum load must be set accordingly.

To compare the accuracy more in depth, Table 6.14 displays the errors of the estimated elastic modulus, E, and yield stress, σ_y, as well as the average error over the hardening region, $|\overline{\Delta\sigma_p}|$. Observing the load at which the minimum error occurs for each material and parameter combinations, it is apparent that the load which gives the best results depends on the material studied. For AISI 415 and AISI 304L, the errors for all parameters are minimized for a load of 5 N, which was not the load for which the I-index was minimized, *i.e.*, 2.5 N. For SAE 1080 and ASTM A516, ΔE is minimized for a load of 5 N, but $\Delta\sigma_y$ and $|\overline{\Delta\sigma_p}|$ are minimized with 2.5 N or 7.5 N, respectively. It is thus difficult to evaluate the effect of the h_{max}/R ratio, as no evident trend exists.

To give further insight, Figure 6.15 displays the convergence plots obtained for the optimization step using the varying loads. It can be observed that, as predicted by the I-index values, the load of 7.5 N yields the worst performance, always necessitating a larger number of function evaluations to reach convergence. The performance for the loads of 2.5 N and 5 N varies with the materials. These results go against the conclusions obtained in past studies that increasing the h_{max}/R ratio increases performance. This can maybe be explained by the fact that the hardening portion of the tensile curve is linked through an equation (defined by a hardening model) in popular methods with which these conclusions were drawn. In the method proposed in this work, the stresses at higher strains and at lower strains are not rigidly linked together, and can move independently. At a higher load, the strains reached during the indentation process are on average very high. This could have the effect of reducing the sensitivity of the indentation data to the beginning of the tensile curve, when compared to the higher strains. It would then become more difficult for the algorithm to

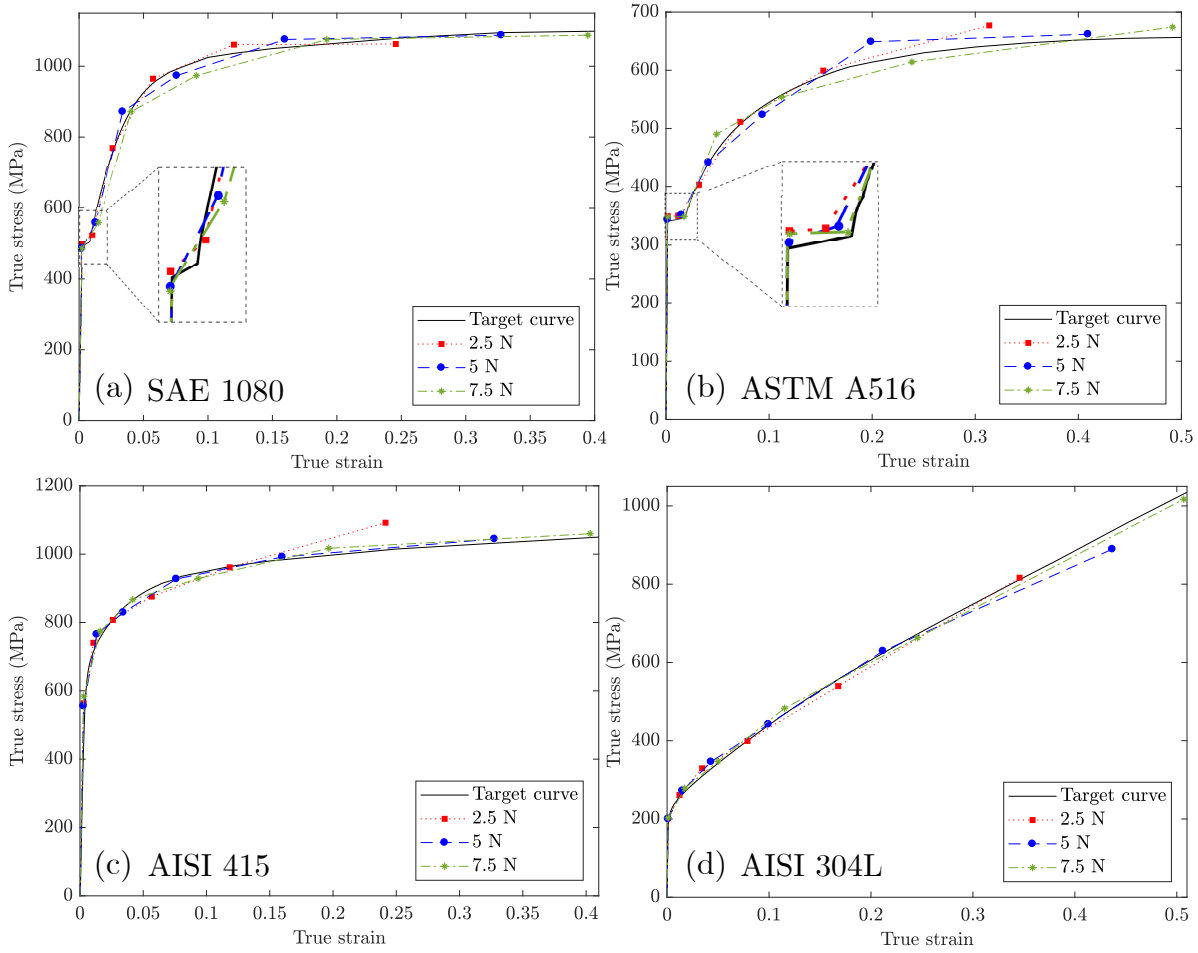

Figure 6.14 Comparison of the target true stress-true strain curves to those estimated with the optimization step when using maximum indentation loads of 2.5 N, 5 N and 7.5 N. The target indentation data used was numerically generated. This figure shows that when using numerically generated indentation data, the method is capable of estimating the general shape of the true stress-true strain curves for all applied loads.

Table 6.14 Errors on the estimated elastic modulus, ΔE, and yield stress, $\Delta\sigma_y$, and the average of the absolute value of the error over the hardening region of the true stress-true strain, $|\overline{\Delta\sigma_p}|$, obtained by the optimization step when using the proposed methodology with maximum loads of 2.5, 5 or 7.5 N generating different h_{max}/R ratios. The optimization was conducted using numerically generated indentation data. The minimum errors for each parameter and material combination is emphasized by using a bold font.

Applied load (N)	SAE 1080			ASTM A516		
	ΔE (%)	$\Delta\sigma_y$ (%)	$\lvert\overline{\Delta\sigma_p}\rvert$ (%)	ΔE (%)	$\Delta\sigma_y$ (%)	$\lvert\overline{\Delta\sigma_p}\rvert$ (%)
2.5	-0.3	**-0.1**	**0.99**	-0.5	1.6	1.84
5	**0.2**	-2.6	1.24	**0.3**	1.8	2.42
7.5	-0.4	-3.4	1.99	-0.7	**0.8**	**1.72**
Applied load (N)	AISI 415			AISI 304L		
	ΔE (%)	$\Delta\sigma_y$ (%)	$\lvert\overline{\Delta\sigma_p}\rvert$ (%)	ΔE (%)	$\Delta\sigma_y$ (%)	$\lvert\overline{\Delta\sigma_p}\rvert$ (%)
2.5	-0.8	12.7	2.94	-1.0	0.8	2.13
5	**0.0**	**11.1**	**0.96**	**-0.5**	**0.2**	**1.53**
7.5	-0.9	16.8	1.36	-1.0	1.5	1.54

reach its optimal solution. When a hardening model is used, a single parameter defines the whole hardening region of the tensile curve, so this effect would be less noticeable.

Since numerical indentation data was used for this analysis, the problem is stable. It would be very necessary to conduct the same analysis using experimentally obtained indentation data, to observe the stability of the method using various h_{max}/R ratios in the presence of experimental and modeling errors. In this situation, the problem would be less stable and more reliable conclusions could be drawn.

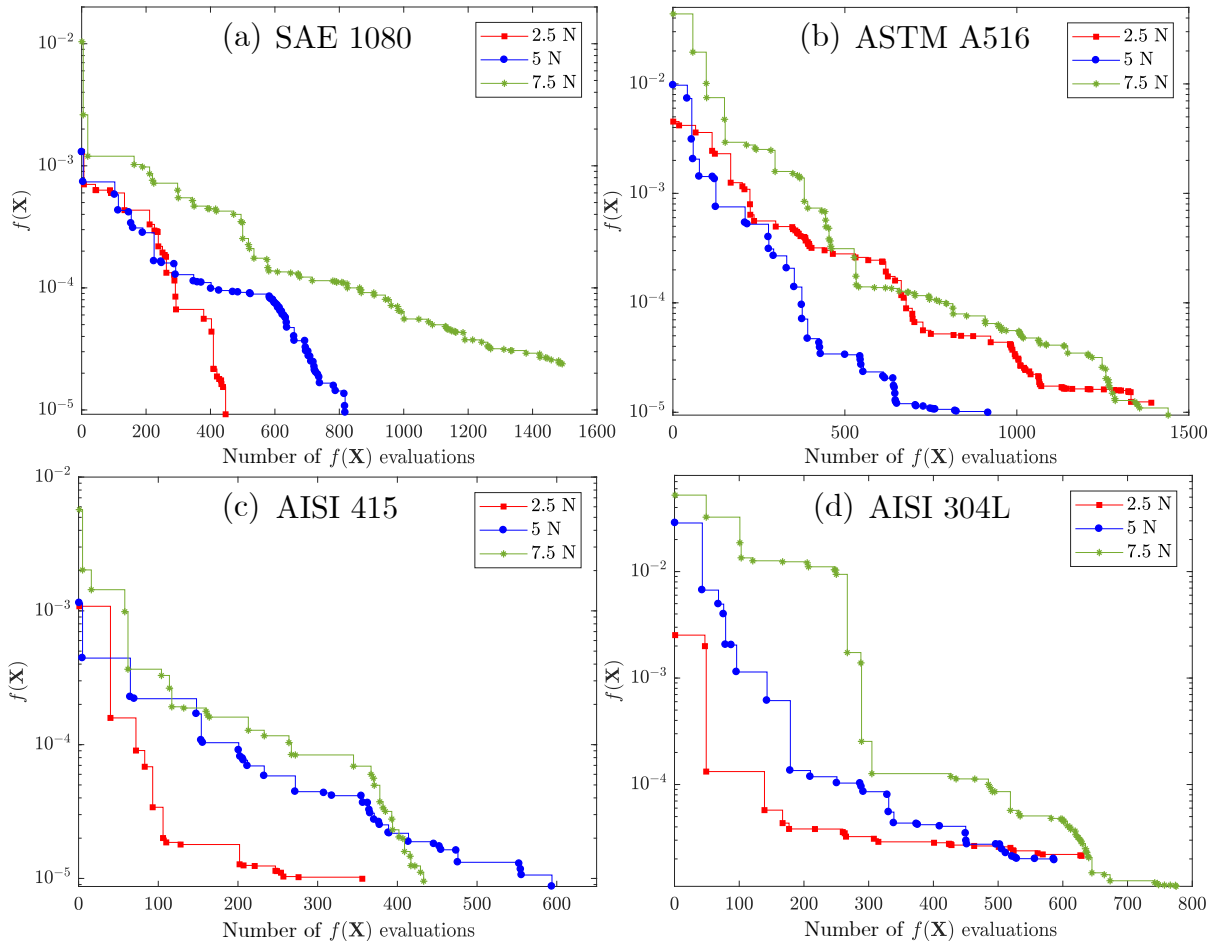

Figure 6.15 Convergence plots of the optimization step of the proposed method for four materials using numerically obtained target indentation data and maximum indentation loads of 2.5 N, 5 N and 7.5 N to vary the ratio h_{max}/R. The largest load leads to the worst performance and the results vary for loads of 2.5 and 5 N.

6.5 Conclusions

In this chapter, a methodology was developed to estimate the true stress-true strain curves by spherical indentation while avoiding the assumption of a hardening model. The numerical and experimental studies of the method brought to light the following conclusions:

- The proposed method, when used with a spherical indenter ($R = 50$ µm), an applied maximal force of 5 N and numerically generated indentation data, is capable of generating a true stress-true strain curve which fits the shape of the target macroscopic tensile curves of four different steels. The average error between the estimated and experimental tensile curves ranged from 0.96% to 2.42%. It was shown that the estimated tensile curves were either closer to the targets when using the proposed method rather than assuming a hardening model or similar results were obtained. *The proposed method is therefore more versatile than other common methods that assume a hardening model;*

- The choice of the optimization algorithm, OrthoMADS, is justified for this complex problem because of its capacity of performing well on constrained problems. Such an algorithm is not necessary for common methods assuming a hardening model since no constraints are present. The convergence plots of the proposed methodology for four materials, show convergence is efficient and an example of the algorithm escaping a local minimum is shown in the case of the application to SAE 1080 steel. *This algorithm behaves satisfactorily within the proposed methodology;*

- The computation time required for the convergence of the proposed method can be substantially longer than when using a hardening model. For SAE 1080 steel, for example, using a hardening model required a time of about 2.75 hours, while the proposed method required about 25 hours. The user must weigh if the added precision is worth the significant increase in required time for their application;

- The study using the I-index demonstrated the reasoning behind some choices made in the development of the inverse method. This includes the number of estimated points on the true stress-true strain curve, the use of both residual imprint and indentation curve data in the objective and surrogate functions, and the separation of the residual imprint into two sub-functions. The optimization of the sub-function weights was also attempted but was inconclusive. Lastly, the effect of the ratio h_{max}/R was investigated with the I-index and it was found that with numerical indentation data, the method did not perform better when increasing this ratio as is seen in the literature. It was

hypothesized that this could be explained by the nature of the variables which avoid the use of a hardening model;

- The experimental application of the method showed that the presence of a plastic plateau for both studied carbon steels, SAE 1080 and ASTM A516, was captured by the proposed method. The average differences between the estimated and experimental tensile curves over their hardening regions are 3.9% for SAE 1080 and 0.9% for ASTM A516. The general overestimation of the extracted true stress-true strain curve for SAE 1080 steel can be explained by the errors induced by the finite element modelling hypotheses. *The proposed method is shown to perform well even when using experimental indentation data for these two materials;*

- The limitations of the method include the pre-defined strain values, which can lead to significant errors in the estimation of the length of a plastic plateau, if present (*e.g.*, $\Delta\varepsilon_{pl} = -19.1\%$ for ASTM A516 in the numerical study). Another important limitation is the capability of the studied material to be modelled by classical plasticity using von Mises yield criterion and isotropic hardening. Materials exhibiting, for example, strain-induced phase transformations will not be accurately modelled since these effects are not taken into account in the current finite element model and the method will yield erroneous results. This was observed for AISI 415 and AISI 304L steels.

CHAPTER 7 APPLICATION OF THE PROPOSED INVERSE METHODOLOGY TO A WELD

An objective of this work is to observe how well the inverse method developed in this thesis is capable of capturing the changes expected within each region of a weld. The subject of the following chapter is the application of the proposed inverse methodology to a weld.

An analysis of the method's behaviour in the presence or absence of residual stresses is also presented. The residual stresses in a weld in the as-welded and heat treated states were measured by X-ray diffraction (XRD). Indentation tests were then conducted in the same locations as the residual stress measurements. The local true stress-true strain curves were then estimated by applying the proposed inverse methodology while considering or neglecting the residual stress values. The residual stresses can be included in the inverse method through the finite element simulation as a known variable. It is then possible to study the suitability of the often used assumption that neglecting the presence of residual stresses will not significantly influence extracted local elasto-plastic properties within welds by instrumented indentation.

The methodology used for this application is detailed in Section 7.1, followed by the results and relevant discussion in Section 7.2.

7.1 Approach used for the application of the proposed methodology to a weld

This section contains details of the methodology used for the application of the inverse method to a weld. First, the materials used and welding method are described in Section 7.1.1, followed by the approach taken for the preparation of specimens in Section 7.1.2 and the residual stress measurements in Section 7.1.3. Then, the methods used for indentation tests are presented in Section 7.1.4, followed by the approach used to incorporate the residual stresses into the spherical indentation finite element models in Section 7.1.5. Finally the details regarding the general application of the inverse method are given in Section 7.1.6.

7.1.1 Materials and welding

The base metal of the weld studied was a normalized low carbon steel ASTM A516 with a ferrito-pearlitic microstructure. The plate of ASTM A516 was not from the same batch than that used in Chapters 4 through 6. The weld metal was an AWS ER70s-6 steel, which has a very similar composition to the base metal. The chemical compositions of both materials

are given in Table 7.1.

The weld studied was reproduced from the methodology used in a past study by Bouffard et al. [19]. The base metal plate had dimensions of 455 × 245 × 24 mm. A single weld bead was deposited in the center of the plate, in the longitudinal direction by gas metal arc welding (GMAW) using a robotic arm. The gas protection used was argon with 8% CO_2. The arc was characterized by a current of 255 A, a tension of 28.5 V and advanced at a speed of 6 mm/s.

7.1.2 Specimen preparation

To prepare the specimens, the welded plate was cut into two halves perpendicularly to the deposited weld, as shown in Figure 7.1. The first half was kept in the as-welded (AW) state while the second half was heat treated (HT) at 600 °C for 1 hour to relieve the residual stresses which appeared during the welding process. Two specimens, sampling the welded section from each half plate, were then cut by electrical discharge machining (EDM), as illustrated in Figure 7.1. The specimens were taken close to the plane where the plate was cut, which represents the centre of the original welded plate, to avoid boundary effects.

To study repeatability, the surfaces to be studied from the specimens of the same state (as-welded or heat treated) must be as close to each other as possible in the longitudinal axis of the plate. The surfaces along the cutting planes identified as C_s in Figure 7.1 were thus used. The distance between the surface of each specimen with its counterpart in the same state is estimated to be a maximum of 4 mm. This value is approximated knowing the thickness of the EDM cuts, 0.35 mm, and the removal of an additional 1 mm of thickness for each specimen after the residual stress measurements (see following Section 7.1.3). Also, it is estimated that the surface removal from surface preparation (mechanical grinding and polishing) should be less than 1 mm in total.

The surfaces were prepared as described in Section 4.1.3, using a final polishing step with particles of 0.05 µm as recommended in the results of Section 4.2.1.

Table 7.1 Chemical composition (% wt.) of the ASTM A516 steel used as the base metal for the application to a weld and the weld metal, AWS ER70s-6 steel.

	C	Mn	S	Si	Ni	Cu	Cr	Mo
ASTM A516	0.20	0.77	0.014	0.20	0.02	0.06	0.06	0.01
AWS ER70s-6	0.13	1.00	0.011	0.65	0.05	0.05	0.06	0.01

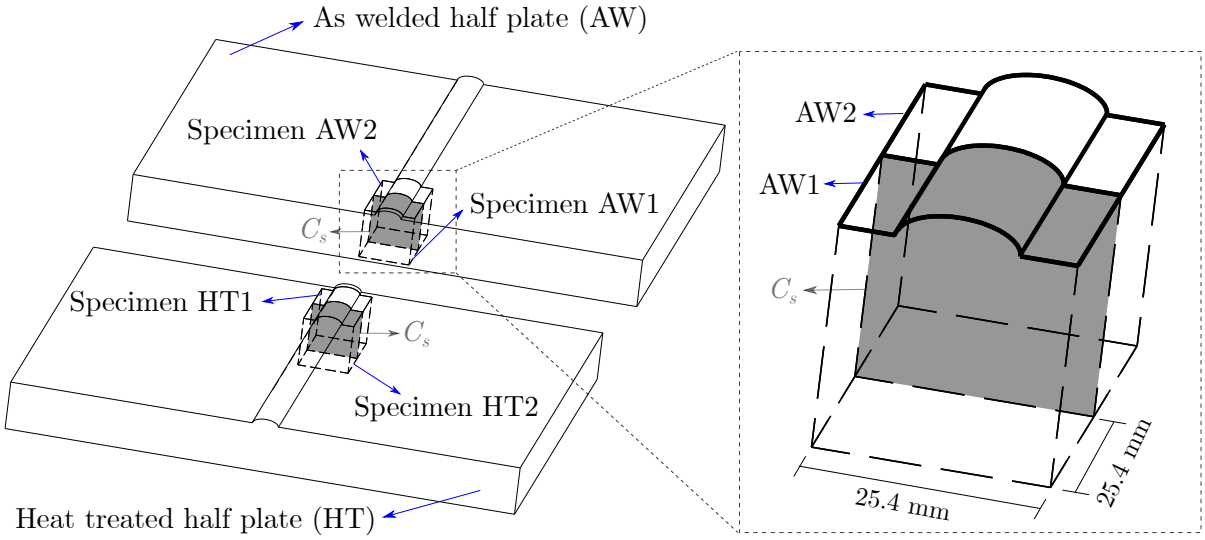

Figure 7.1 Illustration of the geometry, locations and states (as-welded, AW, or heat treated, HT) of the specimens within the welded plate. Two specimens are cut by EDM for each half plate and the surfaces to be analyzed are mirroring each other at the planes identified as C_s. This strategy serves to minimize the distance between studied surfaces which enables to study repeatability of the method since the material properties are expected to be similar between the two specimen surfaces of each state.

7.1.3 Residual stress measurements

The residual stress measurements were conducted by American Stress Technologies. They employed a StressTech Xstress DR45 X-ray diffractometer with a Cr-Kα radiation source ($\gamma = 0.229$ nm). The radiation tube was powered with 30 kV and 9 mA. The analysis was performed through an elliptical least squares fit of the obtained inter-planar spacing, d, vs. $\sin\psi^2$ data. The variable ψ is the angle between the normal of the specimen and the normal of the diffracting plane. The elastic properties of the specimens were assumed by American Stress Technologies to be standard values for steel, *i.e.*, an elastic modulus of 211 GPa and a Poisson ratio of 0.3.

Prior to the residual stress measurements, the zone of interest of the surfaces were electropolished to remove a thickness of 100 µm, as seen in Figure 7.2(a). This was done to eliminate residual stresses which could have appeared during surface preparation. This thickness was verified to be sufficient to remove surface preparation induced stresses through a preliminary profile measurement of the residual stresses at 10 depths between 0 and 500 µm. The stresses were observed to stabilize at a depth of approximately 75 µm.

The locations of the residual stress measurements are shown in Figure 7.2(b). They are the same as the locations at which the indentation tests will be made, and create a line passing

through the base metal, heat affected zone (HAZ) and weld metal. At each location, the residual stresses were measured in three directions: in the long transverse (X) and short transverse (Y) directions of the welded plate, as well as at an angle of 45° between these two directions in order to enable the computation of the principal stresses.

It would not have been possible to conduct indentation with the surface geometry obtained after electropolishing as illustrated in Figure 7.2a. Therefore, after the residual stress measurements, a thickness of 1 mm was removed by EDM from the surface of all specimens to remove the section which had been electropolished and reveal the underlying metal. The surface preparation sequence described in Section 4.1.3 was then repeated. It was assumed that the residual stresses at the same in plane locations would not change significantly with this longitudinal position change of 1 mm.

7.1.4 Instrumented indentation

The indentation tests and residual imprint measurements were conducted as described in Section 4.1.2. The positions of the indents were as illustrated in Figure 7.2(b), after the removal of the groove created by the electropolishing.

7.1.5 Inclusion of residual stresses in the finite element models

The spherical indentation finite element models presented in Section 5 were adapted to include the experimentally measured residual stresses. To achieve this, a radial displacement was applied to the circumferential surface of the specimen, prior to the simulation of the indentation process. This produced an equi-biaxial stress within the specimen in the plane perpendicular to the loading direction. The value of this stress was scaled by the applied radial displacement to replicate the measured values.

Since the measured residual stress values were not in reality equi-biaxial, an equivalent equi-biaxial stress was computed as a first approximation by taking the average of the two in-plane principal residual stresses in each measurement position.

Figure 7.3 illustrates the meshes of the detailed and surrogate models including the radial displacement used to model the residual stresses.

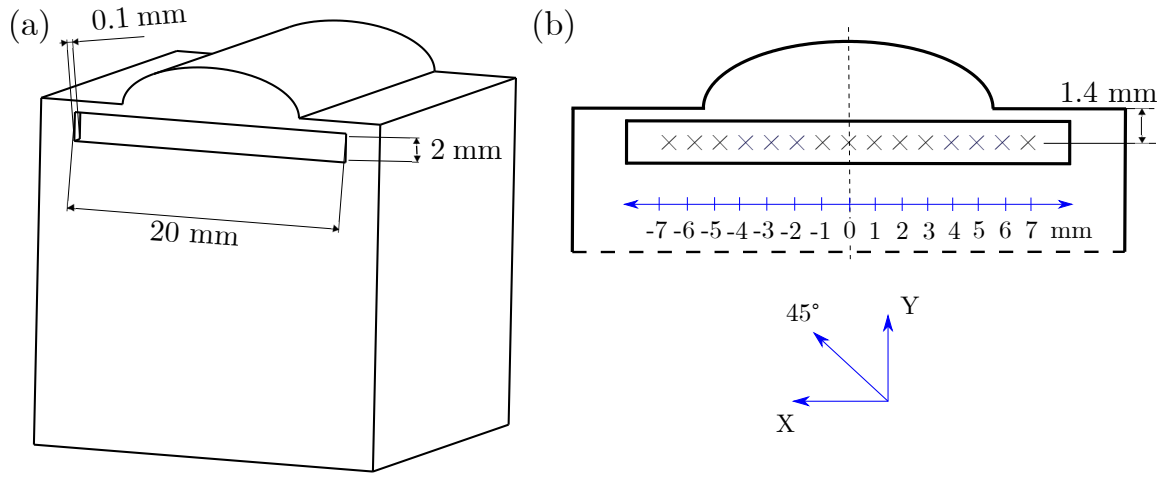

Figure 7.2 Residual stresses measurements characteristics: (a) size and position of the electropolished zone for elimination of residual stresses induced by surface preparation; and (b) locations and directions of the residual stresses measurements. The same in plane locations are used for the indentation measurements, but prior to these tests, a thickness of 1 mm was removed from the specimens in order to obtain a flat surface without the groove caused by electropolishing.

7.1.6 Extraction of local true stress-true strain curves in the weld through the application of the developed inverse methodology

The method described in Section 6.1 was applied for the indentation measurements done on specimens HT1 and HT2 while neglecting the presence of residual stresses and for the measurements done on specimens AW1 and AW2 while both considering and neglecting the presence of residual stresses.

Because of the known nature of the base material, ASTM A516 steel, a value of 208 GPa can be set for the elastic modulus, which was previously measured by macroscopic tensile testing. The modulus is not expected to change within the base metal, HAZ and weld metal. Since the elastic modulus does not need to be extracted, the sub-functions pertaining to the indentation unloading curve in the objective and surrogate functions, $f_S(\mathbf{X})$ and $\tilde{f}_S(\mathbf{Y})$, were no longer useful. Indeed, these sub-functions had been added to the objective and surrogate functions with the sole purpose of adding sensitivity to the elastic modulus. These sub-functions were therefore removed for the application to the weld, and the objective and surrogate functions, Eqs (6.3) and (6.20), were reduced to:

$$\tilde{f}(\mathbf{Y}) = w_L \tilde{f}_L(\mathbf{Y}) + w_{IC} \tilde{f}_{IC}(\mathbf{Y}) + w_{IF} \tilde{f}_{IF}(\mathbf{Y}), \tag{7.1}$$

$$f(\mathbf{X}) = f_L(\mathbf{X}) + f_{IC}(\mathbf{X}) + f_{IF}(\mathbf{X}), \tag{7.2}$$

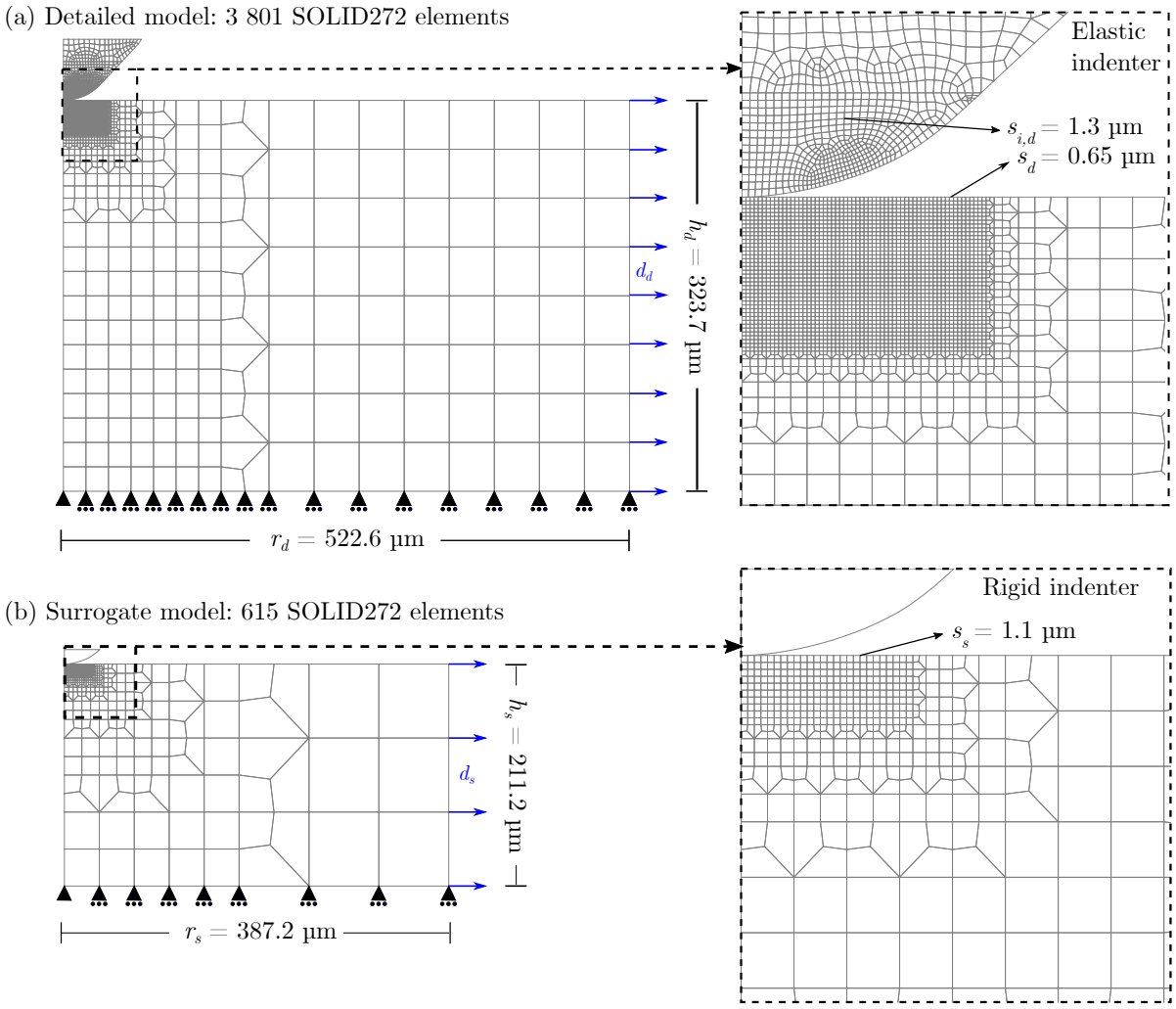

Figure 7.3 Finite element meshes for spherical indentation tests, used in the: (a) detailed model; and (b) surrogate model, including the radial displacement used to generate the residual stresses, d_d, and d_s. For each model, the height, h_d or h_s, and radius, r_d or r_s, of the specimen are shown as well as the smallest element size in the specimen, s_d or s_s. The element size set in the most refined region of the indenter, $s_{i,d}$, is also shown for the detailed model.

where only the sub-functions pertaining to the indentation loading curve (L) as well as the residual imprint in the contact (IC) and free surface (IF) regions are considered.

7.2 Results and discussion

This section presents the results of the application of the proposed method to a weld. First, the measured residual stresses are given and discussed in Section 7.2.1. An analysis of the microstructure of the weld specimens is then presented in Section 7.2.2, including a hardness study. Finally, the estimated true stress-true strain curves in both states, considering and neglecting residual stresses are compared and analyzed in Section 7.2.3.

7.2.1 Residual stress measurements

Figure 7.4 shows the measured residual stresses as a function of positions in the specimens, in the directions previously illustrated in Figure 7.2. The error bars represent the least square error of the elliptical fit of d vs. $\sin\psi^2$.

It can be observed that the residual stress values are of lower magnitude in the heat treated specimens, as expected. All measured stress values for heat treated specimen HT1 are below 50 MPa. Considering the measurement errors, this leads to the conclusion that the heat treatment eliminated the residual stresses effectively. However, the measured stresses in specimen HT2 are higher in magnitude, reaching a maximum compressive value of 123 MPa in the X direction. In that same location in the HT1 specimen, the stress value was measured to be $\sigma_x = 12$ MPa in compression. There is no physical reason for the residual stress to increase by a factor of ten between the specimens, *i.e.*, at the same in-plane location and less than 4 mm apart in the welding direction. It is thus assumed that the higher stresses in specimen HT2 were caused by specimen preparation or other errors inherent to the XRD measuring method. For the remainder of the analysis, specimens HT1 and HT are considered to be stress free as the measured stress values are considered negligible.

When observing only the results for the as-welded specimens, it is noticed that the stress values are of a mostly compressive nature. In the X and 45° directions, the residual stress distributions approximately follow a parabolic distribution centred in the middle of the specimen, where the compressive stress is the highest in magnitude. In the Y direction, the distribution resembles two plateaus, separated at the centre of the specimen, one neighbouring a null value of residual stress, and the other a compressive stress of approximately 100 MPa. Except for a few aberrant positions (*e.g.*, -1 mm for directions X and 45°), the residual stresses follow the same distribution trends between the two AW1 and AW2 specimens.

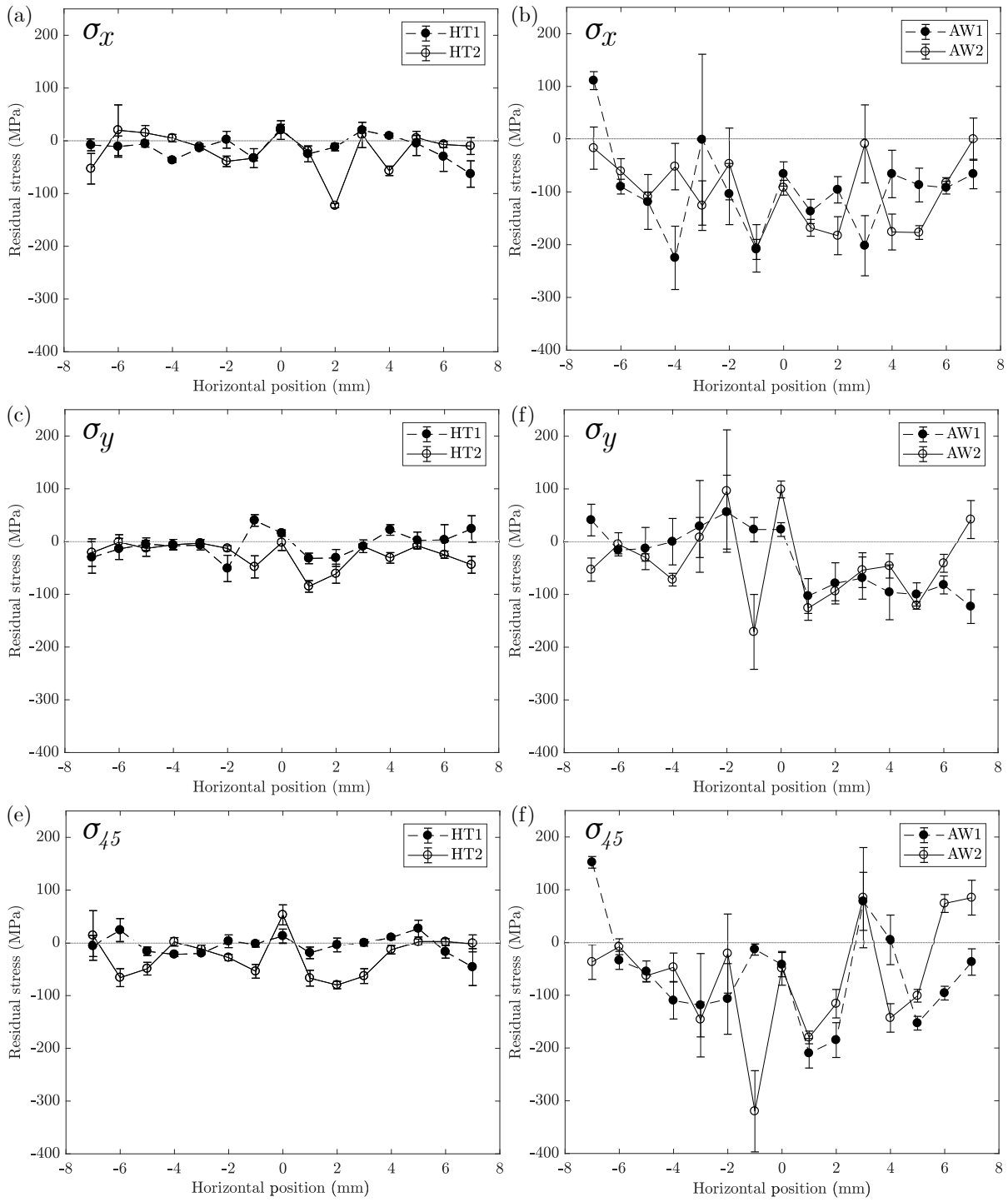

Figure 7.4 Residual stresses measured by XRD in the heat treated (HT1 and HT2) and as-welded (AW1 and AW2) specimens in the positions and directions previously illustrated in Figure 7.2.

To input the residual stress values into the finite element models, as described in Section 7.1.5, the principal residual stress values were calculated by American Stress Technologies and their average was computed for each position where measurements were made. The principal stresses and their averages are shown in Figure 7.5.

7.2.2 Microstructure analysis

Figure 7.6 shows the surface of the specimens AW1 and HT1 after indentation. The surfaces were etched using a 2% nital solution in ethanol to reveal the varying microstructure through the weld. The positions of the indents relatively to the microstructure indicate that the indents in positions 0 and 1 are located in the weld metal, the indents in positions 2 to 6 are located in the HAZ and the indent in position 7 is located in the base metal.

When comparing the two specimens, it is observed that the indents in specimen AW1 are smaller in size than those in specimen HT1. This was expected as the heat treatment relaxed the compressive residual stresses present in the as-welded condition. However, the effect is far too significant to be solely caused by the relief of residual stresses. Indeed, the heat treatment conducted at 600 °C to relax the residual stresses is also within the temperature and time range of a tempering treatment for low carbon steels [53]. The treatment is thus expected to lead to an important decrease in hardness.

For further analysis, observations of the microstructure are conducted as well as a hardness study. Figures 7.7 to Figure 7.10 show the microstructure at a higher magnification of indents in all positions for specimens AW1 and HT1.

The apparent Brinell hardness was calculated for every position in the weld and compared with these expected values. The designation of apparent hardness is used because of the residual stresses present in the as-welded specimens, which could slightly alter the hardness values. The apparent Brinell hardness is defined as:

$$BHN = \frac{2P_{max}}{\pi D(D - \sqrt{D^2 - d^2})}, \tag{7.3}$$

where D is the indenter diameter, set as 100 µm, the nominal value provided by the manufacturer, and d is the imprint diameter as measured directly from residual imprints.

As previously shown in Table 7.1, the carbon content of the ASTM A516 steel used for the application to a weld is 0.2%, and that of the weld metal is 0.13%. Since the total of alloying elements is low ($< 2\%$), the expected hardness of different phases and constituents can be estimated using the carbon content [26]. For the base metal (0.2% C), the Brinell hardness of

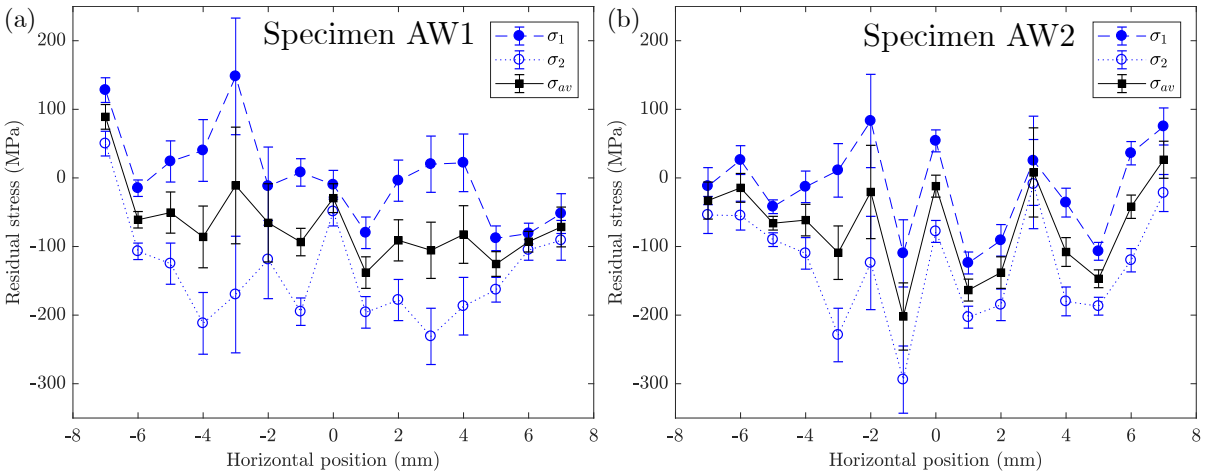

Figure 7.5 Principal stresses computed in all positions in the as-welded specimens AW1 and AW2, as well as the average of these principal stresses to be inputted into the finite element models when residual stresses are considered.

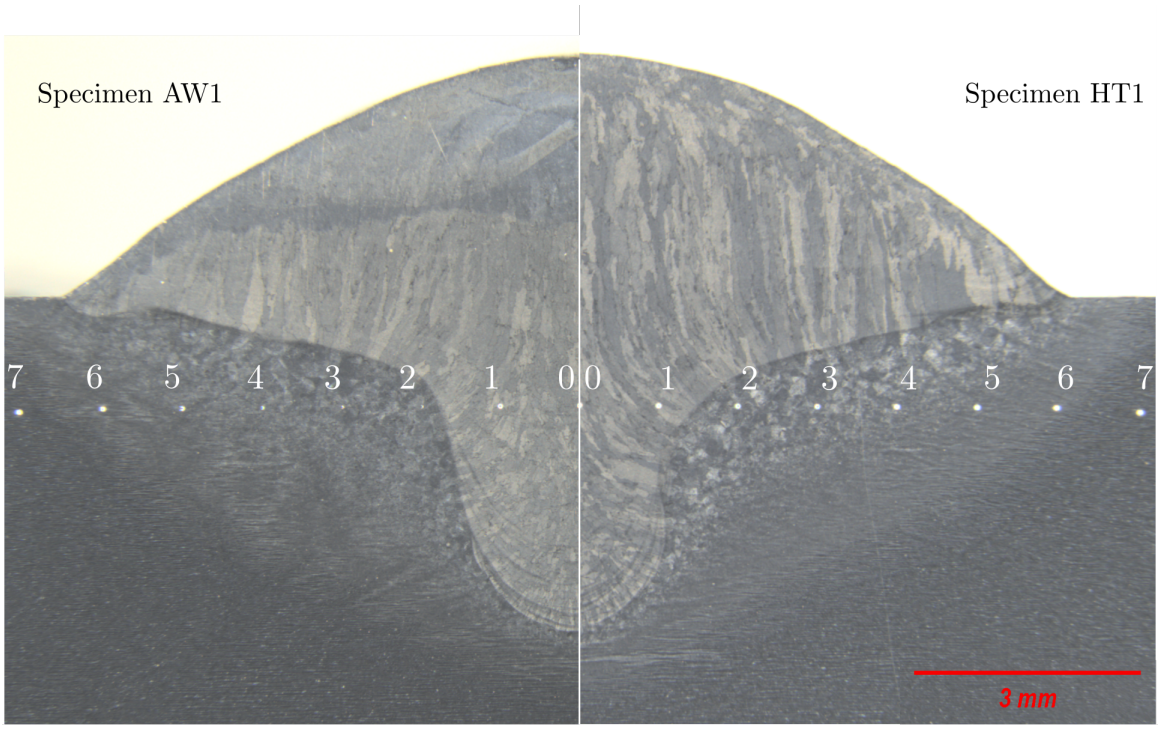

Figure 7.6 Micrograph image of half of as-welded specimen AW1 and heat treated specimen HT1 taken after indentation tests. In plane positions of residual stress measurements and indentations are indicated. It can be noticed that the as-welded specimen has an increased hardness, when compared to the heat treated specimen as indent imprints are much smaller, particularly in the case of positions 1, 2, 3 and 4.

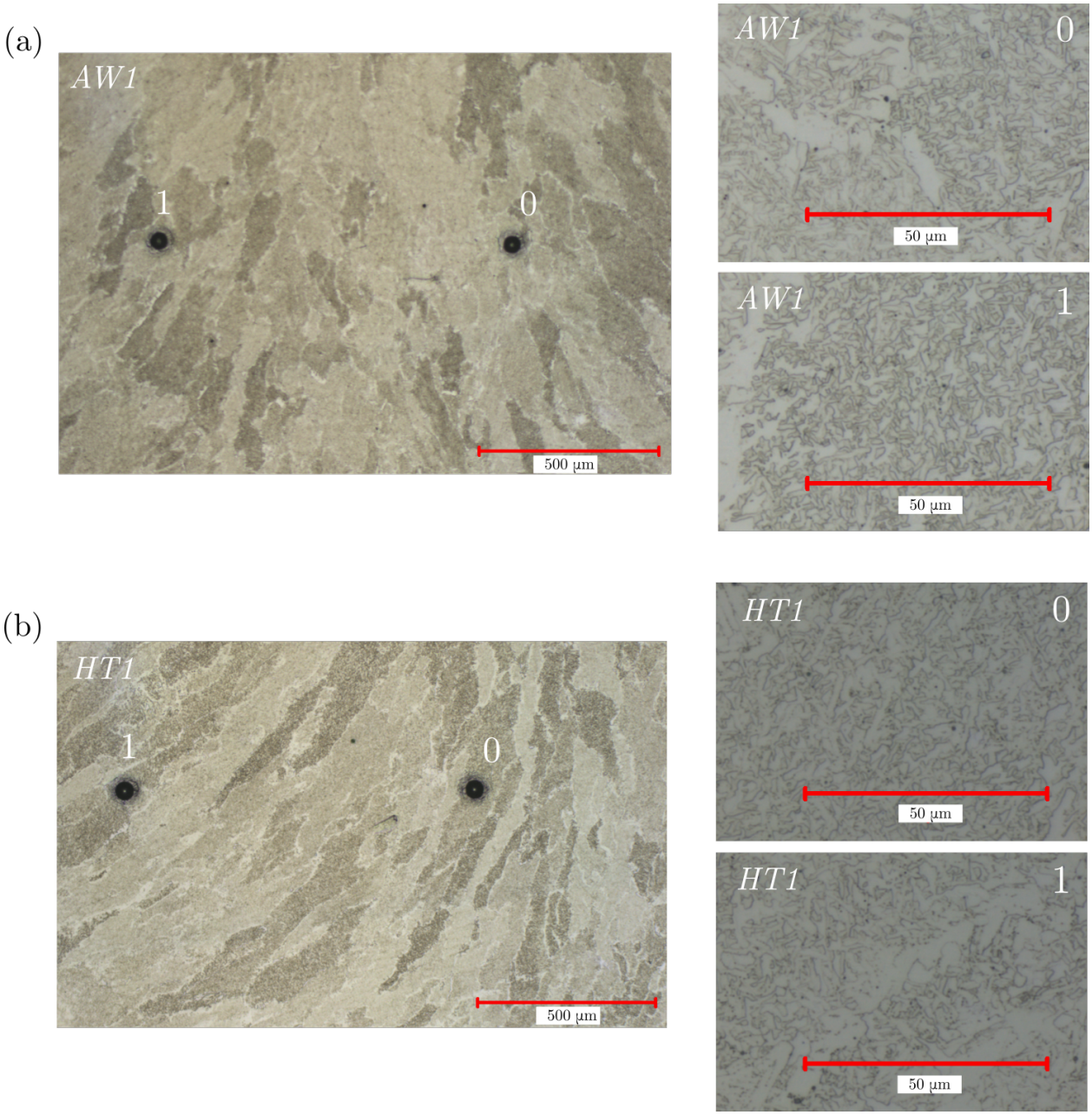

Figure 7.7 Micrograph image of indents located in positions 0 and 1: (a) in as-welded specimen AW1; and (b) heat treated specimen HT1, taken after indentation tests.

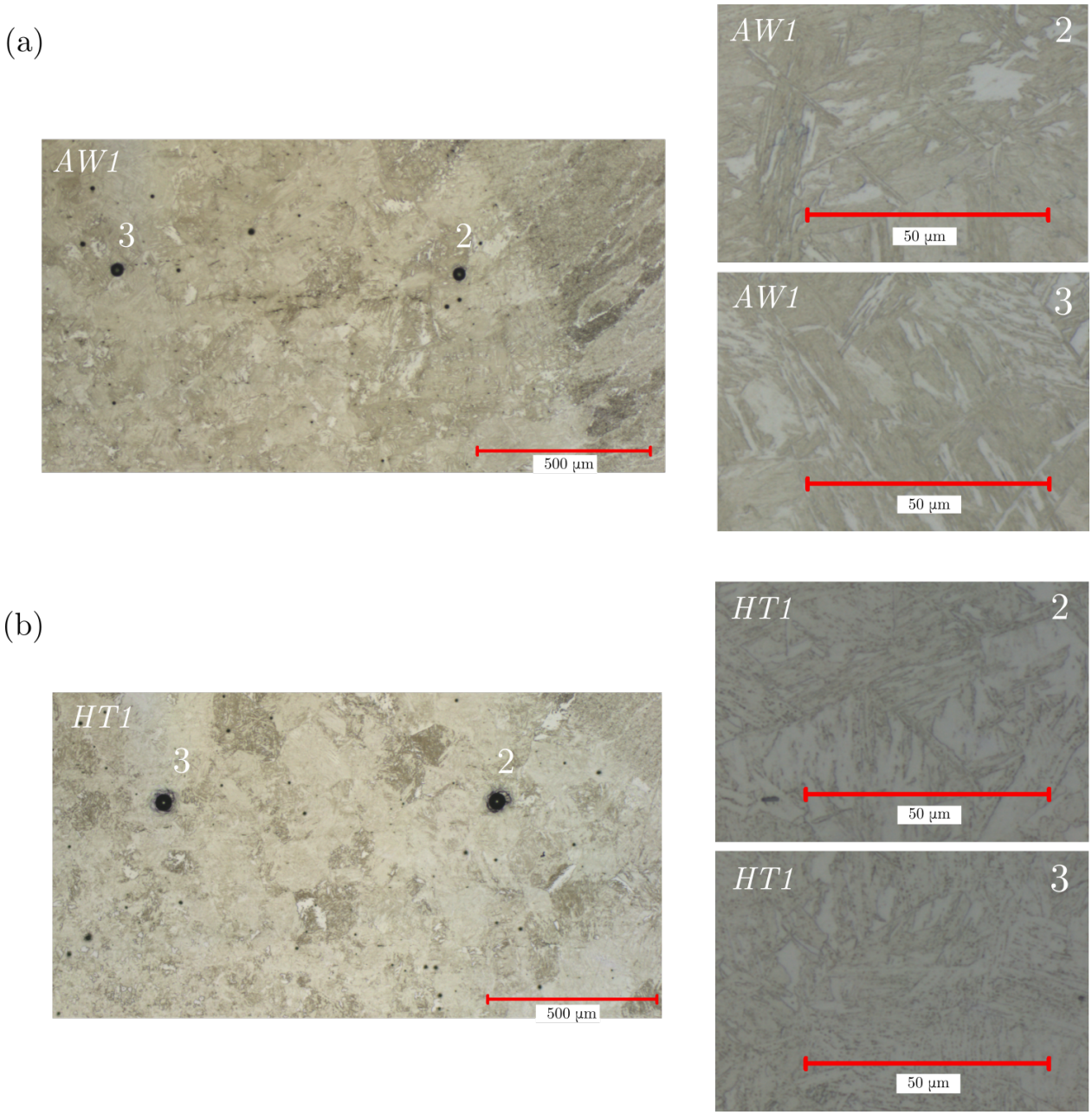

Figure 7.8 Micrograph image of indents located in positions 2 and 3: (a) in as-welded specimen AW1; and (b) heat treated specimen HT1, taken after indentation tests.

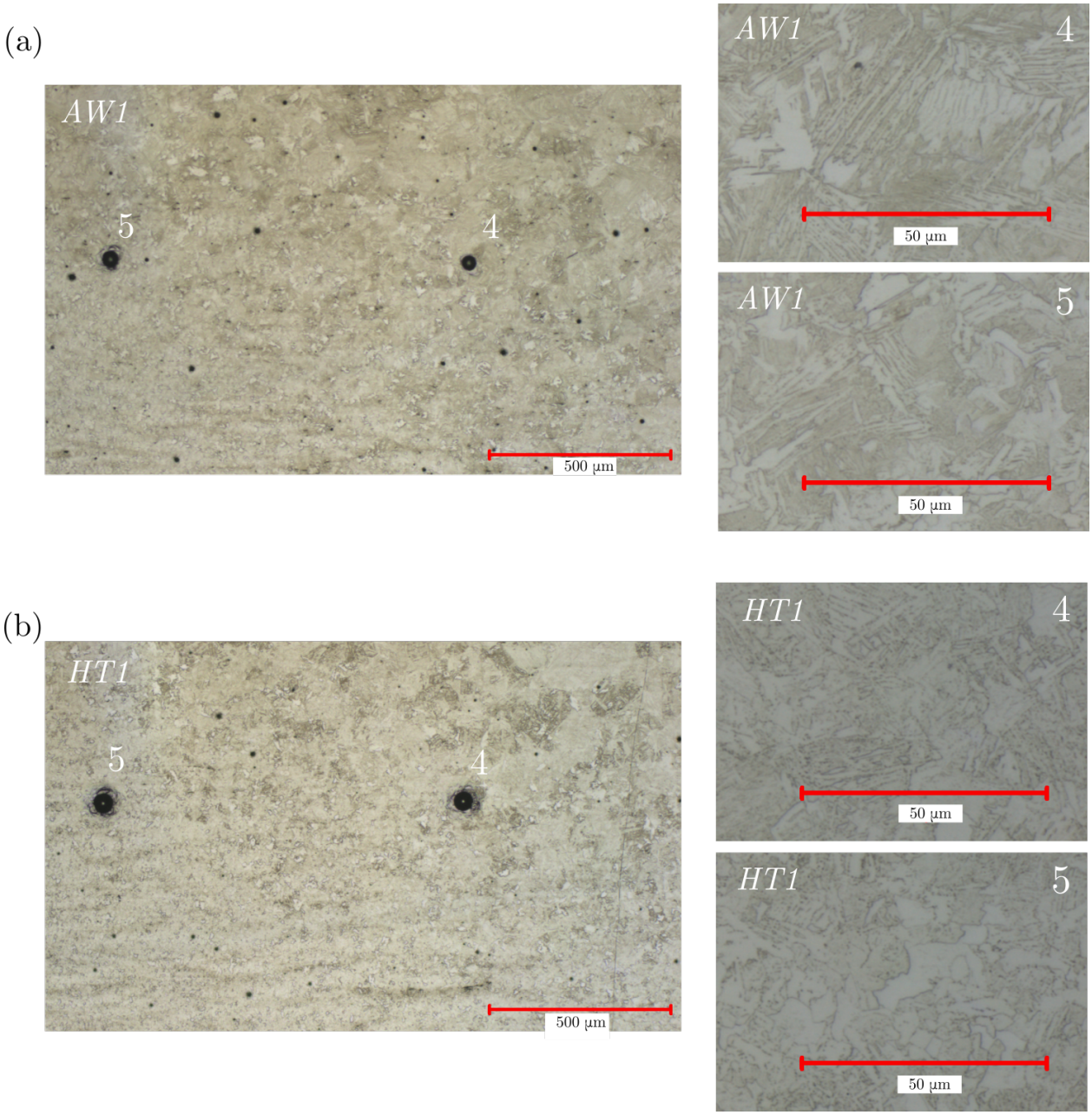

Figure 7.9 Micrograph image of indents located in positions 4 and 5: (a) in as-welded specimen AW1; and (b) heat treated specimen HT1, taken after indentation tests.

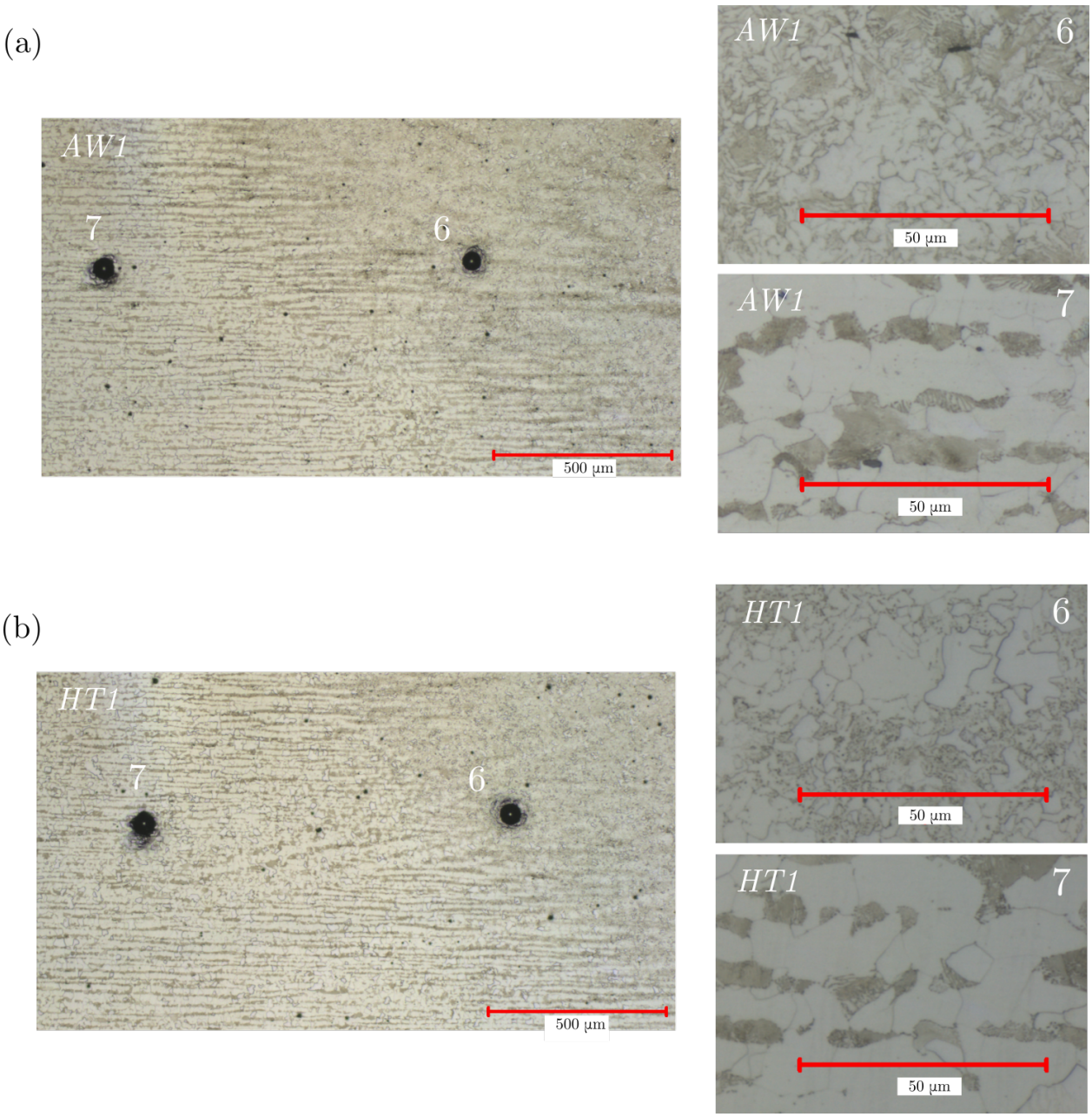

Figure 7.10 Micrograph image of indents located in positions 6 and 7: (a) in as-welded specimen AW1; and (b) heat treated specimen HT1, taken after indentation tests.

fresh martensite is estimated at 450 BHN, that of tempered martensite (371°C) at 290 BHN and that of fine pearlite at 120 BHN. For the weld metal (0.2% C), the estimated Brinell hardness of fresh martensite, tempered martensite and fine pearlite are respectively 360, 275 and 110 BHN. The computed local apparent Brinell hardness values are shown in Figure 7.11. The following paragraphs contain discussion linking the computed apparent hardness and the observed microstructures.

In the weld metal (positions 0 and 1) the microstructure is similar in both positions and states, and is identified as being mainly acicular ferrite. Since the apparent hardness values obtained in these positions are close, it indicates that the microstructure is stable in the weld metal, as shown in Figure 7.7. Also, the difference between the apparent hardness in the AW state and the hardness in the HT state is less than 26.8 BHN. A part of this difference could be caused by the relief of compressive residual stresses, which were measured to be maximal in the weld metal region (see Figure 7.4).

In the HAZ (positions 2 to 6), for both states, a gradient of microstructure can be observed. The microstructure is identified as being mainly composed of bainite in positions 2 to 4, as containing bainite and ferrite in position 5 and being mainly ferrite in position 6. The decrease of the apparent hardness values computed through the HAZ in both states makes sense with the identified microstructures, as bainite is harder than ferrite.

In the HAZ, the effect of the heat treatment is much more important, the maximum difference between the two states being 162.2 BHN at position 2. The sensitivity of indentation data to residual stress (discussed in Section 2.7.1) could not have caused such a change in the computed apparent hardness, especially since the magnitudes of the measured stresses are low, ranging from 21 to 185 MPa in position 2, considering all directions. Also, some stresses were measured to be of a tensile nature, which would contribute to lowering the hardness. It is concluded that the important softening of the material was predominantly caused by the tempering of the microstructure during the heat treatment.

In the base metal, the microstructure is a mixture of ferrite and pearlite, arranged in layers (typical band structure). The apparent hardness in the base metal is 149.4 and 143.7 BHN in the AW and HT states, respectively. The difference in apparent hardness could be attributed to the relaxing of the residual stresses. From a conversion of the average value obtained in Table 4.2, the hardness of the ASTM A516 material used in the previous chapters was 144.5 BHN. This shows that the hardness of the ASTM A516 base metal used for the weld application is similar to that of the ASTM A516 used previously.

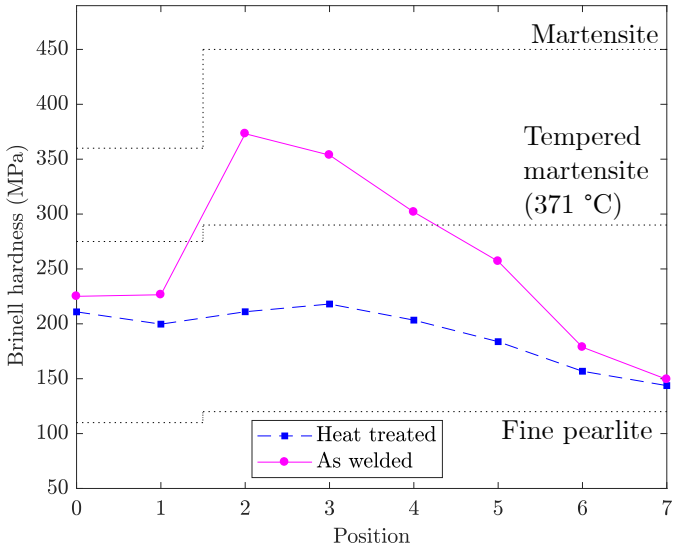

Figure 7.11 Apparent Brinell hardness as a function of position in the weld for specimens AW1 and HT1, when compared to expected values for fresh martensite, tempered martensite (371°C) and fine pearlite in the base metal and the weld metal. From these hardness values, it can be concluded that the heat treatment led to a microstructure change in the HAZ (positions 2 to 6) and not only a relaxation of the residual stresses.

7.2.3 Estimated true stress-true strain curves

This section presents the estimated true stress-true strain curves in the different positions in the weld, for both the as-welded and heat treated specimens. For the as-welded specimens, results are also presented when including the measured residual stress values and when neglecting them for comparison. Figures 7.12, 7.13, and 7.14 display the obtained tensile curves in the weld metal (positions 0 and 1), in the HAZ (positions 2 to 6) and in the base metal (position 7), respectively. To observe the variation between the positions in each studied state, Figure 7.15 illustrates the estimated yield stresses and the values of stress estimated at a fixed strain of 0.28 as a function of position for all tested conditions.

All curves shown represent the average of the estimated true stress-true strain curves obtained for symmetric positions in the two specimens in the same state. For example, the curve presented for the heat treated state in position 1 is the average of the estimated curves in positions 1 and -1 for specimens HT1 and HT2 (a total of 4 curves). However, during experiments, some indentations were inconclusive, caused by bad contact or an error from the indentation machine, and were thus not included in the analysis. A total of 8 indents on 60 were neglected in the analysis, 5 of which were located in the AW2 specimen. The variability between extracted curves between specimens as well as the number of curves used to obtain the average in each position, for each specimen is shown in Figure 7.16. The variability is

defined as the average magnitude of the relative difference between any single extracted true stress-true strain curve and the average of the extracted curves for that position. The error bars demonstrate the minimum and maximum differences between any trues stress value on an extracted curve and the corresponding averaged true stress for the same position.

From Figures 7.12 to 7.15, it is first observed that the extracted true stress-true strain curves in the heat treated specimens present lower stress values than in the as-welded specimens for all strains, and all positions within the weld. The only exception is at position 7, in the base metal, where the stresses at ε_4 are similar for all estimated curves. This trend was to be expected as the heat treatment softened the material. The effect is more pronounced in the HAZ than in the weld metal and base metal, which is in line with the microstructure study and hardness results presented in the previous section. These differences between states demonstrate that the method is capable of capturing the effect of microstructural changes in the extracted tensile curves. Also, a visible variation of the yield stress and strain hardening behaviour estimated through the positions within the specimens of the same state is observed, further supporting the capability of the method to obtain local properties in a varying microstructure.

From Figure 7.16, it can be observed that the average variability between extracted curves in each position reached a maximum of 15 %. This is explained by the fact that the positions of the measurements in each specimen were approximate as it was very difficult to indent in exactly the same in-plane location from one specimen to the next. This is supported by the fact that the lowest variability is present in the weld metal, in which the properties are stable so a slight change in positioning of the indentation would not have sampled a significant difference in properties. Also, the maximum variability is observed for positions 3 to 6 in the as-welded specimens, the region where the properties vary the most and the impact of a slight change in positioning would have the most effect on the extracted true stress-true strain curves. It is roughly estimated that the difference in location between specimens and between the symmetrical parts of the welds in the same specimen could be up to 200 µm.

Another general observation to be made from these results is that neglecting to include the residual stresses in the analysis has the effect of reducing the estimated hardening behaviour and increasing the estimated yield stress. These two effects were expected, as the measured residual stresses are in general of a compressive nature. As discussed in Section 2.7.1, a compressive stress leads to a higher maximum load in the indentation curve, and the inverse method thus finds a higher yield stress to compensate. Also, a compressive residual stress leads to an increase in pile-up height, leading to the extraction of a tensile curve with a reduced strain hardening behaviour. A quantitative comparison of results obtained when

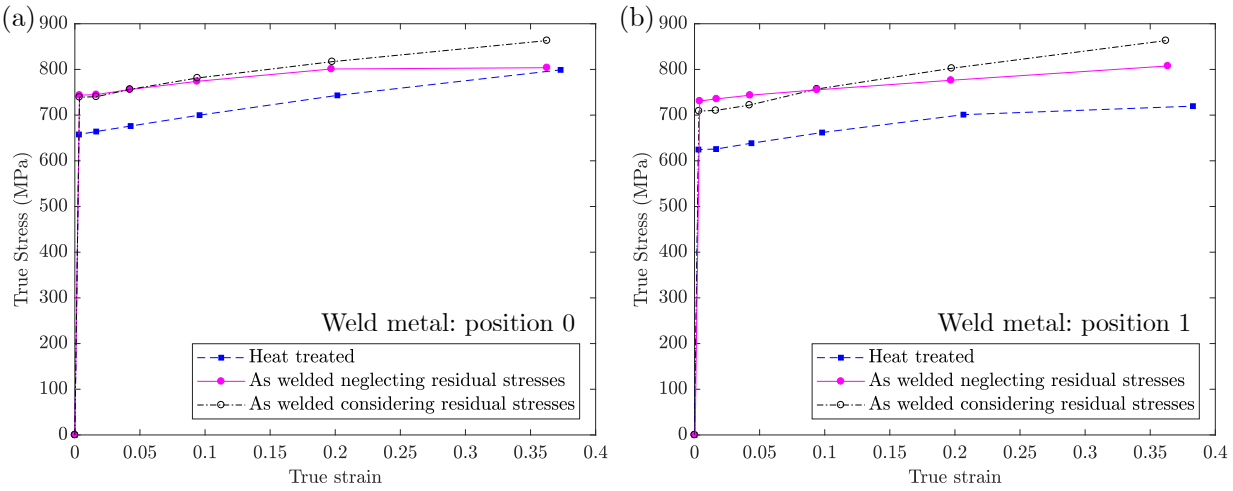

Figure 7.12 True stress-true strain curves obtained with the proposed methodology for indentations conducted in the weld metal (positions 0 and 1). The results are presented for specimens in as-welded state state and after a heat treatment. For the as-welded specimens, the method was applied including the residual stresses and neglecting them.

including and neglecting the residual stresses in as-welded specimens is presented in Table 7.2. For some positions, the errors induced on the estimated tensile curves when neglecting residual stresses can be significant (*e.g.*, an overestimation of σ_y of 20.1% in position 2, with $\sigma_{res}/\sigma_y = -0.08$). However, for other positions, in which σ_{res}/σ_y is more significant, the effect is not as pronounced (*e.g.* an overestimation of σ_y of 3.1% in position 1, with $\sigma_{res}/\sigma_y = -0.19$). The overall results demonstrate that there is no clear trend between the magnitude of the residual stress and the error induced by neglecting them in the inverse method.

A detailed analysis of the results for every position in the weld is presented in the following paragraphs. In the weld metal, Figure 7.12 shows that the estimated true stress-true strain curves have low and almost linear hardening behaviours. A slight decrease in the estimated stress values for all strains from position 0 to position 1 is also observed. The yield stress was 2% to 5% smaller in position 1 than position 0, depending on the state of the specimen. For the as-welded specimen, the effect of including the residual stress is a reduction in the estimated hardening behaviour for both positions. It is not very significant, however, the average error over the hardening region being 2.6% and 3.5% for positions 0 and 1, respectively. From Table 7.2, it can be seen that $\Delta\sigma_y$ is smallest in the weld metal, when compared to the other regions. It must be noted that the estimated yield stress is higher than expected values for the weld metal. Indeed, the nominal yield stress for WS ER70s-6 steel must be a minimum of 400 MPa per AWS 5.18 standard [13] and the extracted values in the heat

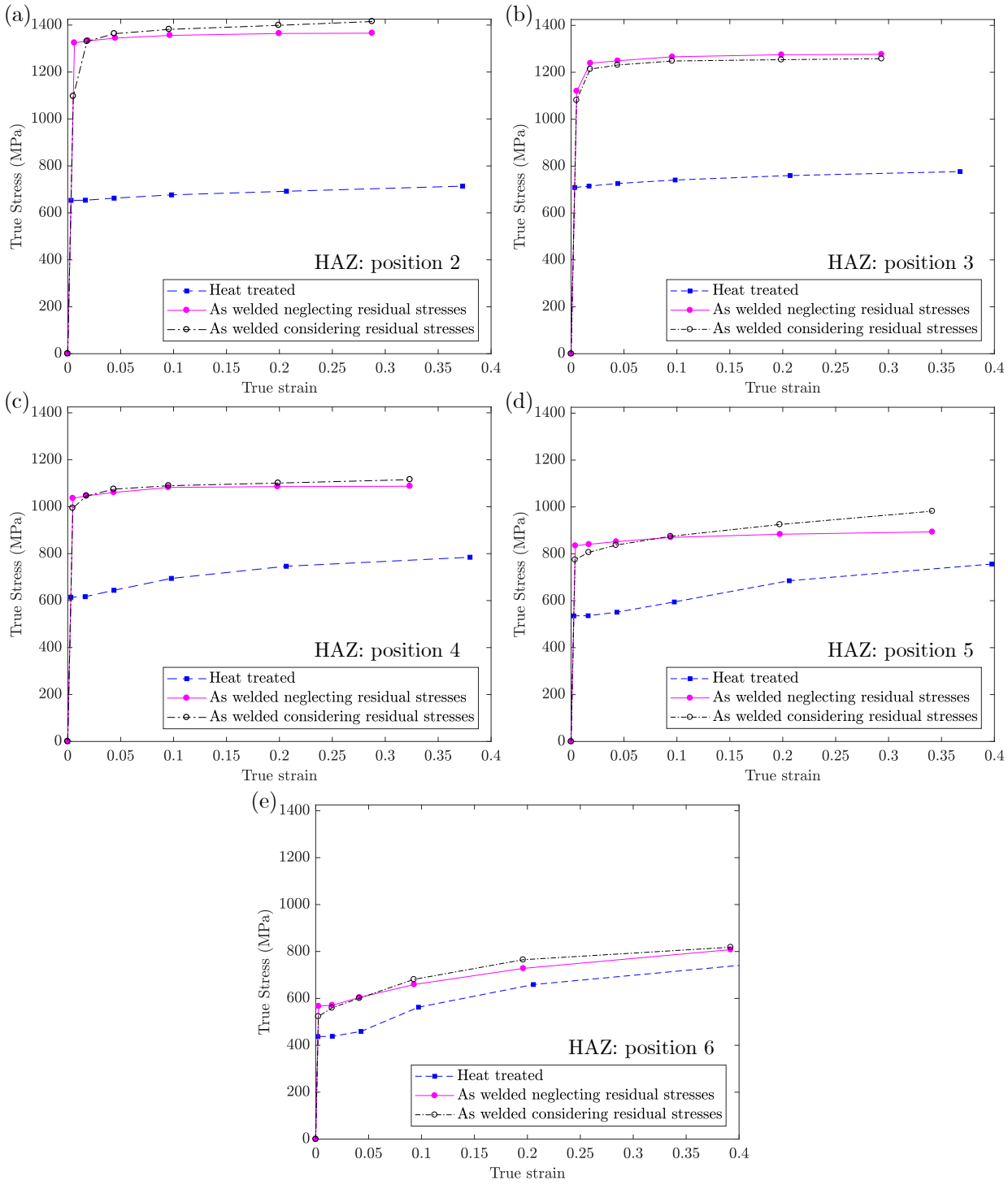

Figure 7.13 True stress-true strain curves obtained with the proposed methodology for indentations conducted in the HAZ (positions 2 to 6). The results are presented for specimens in as-welded state state and after a heat treatment. For the as-welded specimens, the method was applied including the residual stresses and neglecting them.

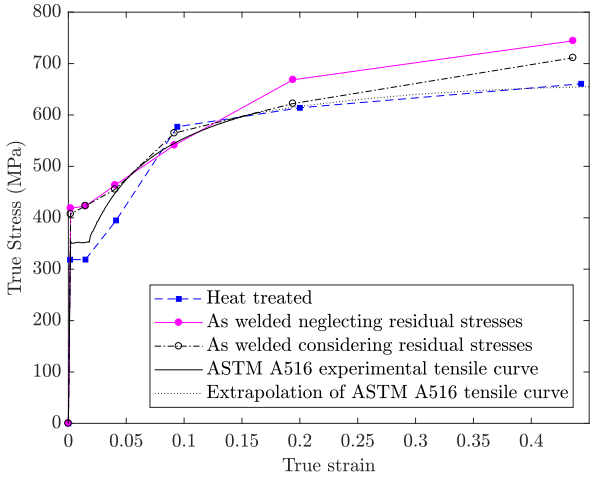

Figure 7.14 True stress-true strain curves obtained with the proposed methodology for indentations conducted in the base metal (position 7). The results are presented for specimens in as-welded state state and after a heat treatment. For the as-welded specimens, the method was applied including the residual stresses and neglecting them. The average experimental tensile curve obtained in Chapter 4 for a different batch of ASTM A516 is also shown for comparison.

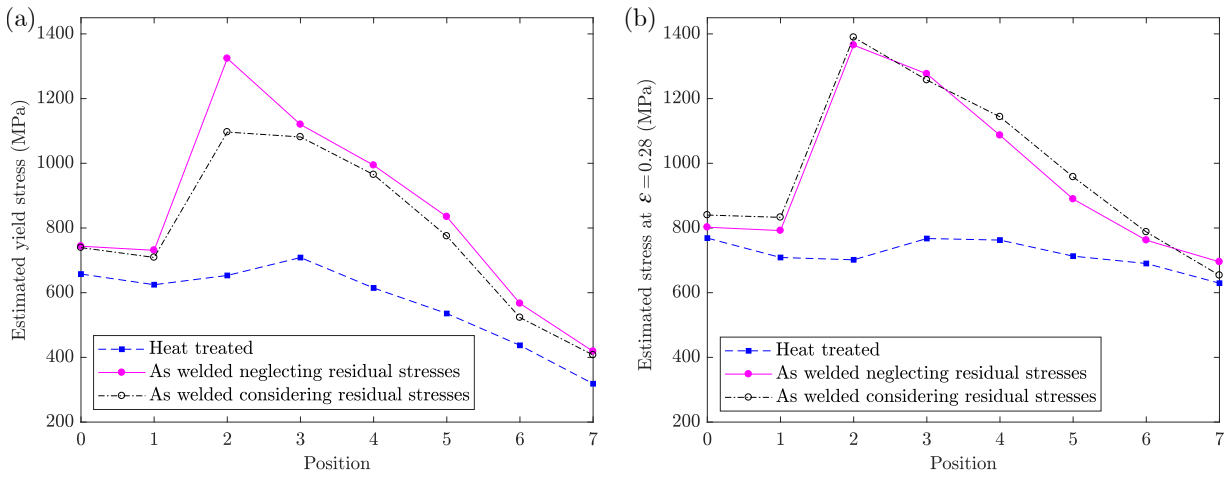

Figure 7.15 Estimated properties obtained with the proposed methodology for indentations spanning the weld metal (positions 0 and 1), the HAZ (positions 2 to 6) and the base metal (position 7): (a) yield stress; and (b) estimated stress at $\varepsilon = 0.28$. The results are presented for specimens in as-welded state and after a heat treatment. For the as-welded specimens, the method was applied including the residual stresses and neglecting them.

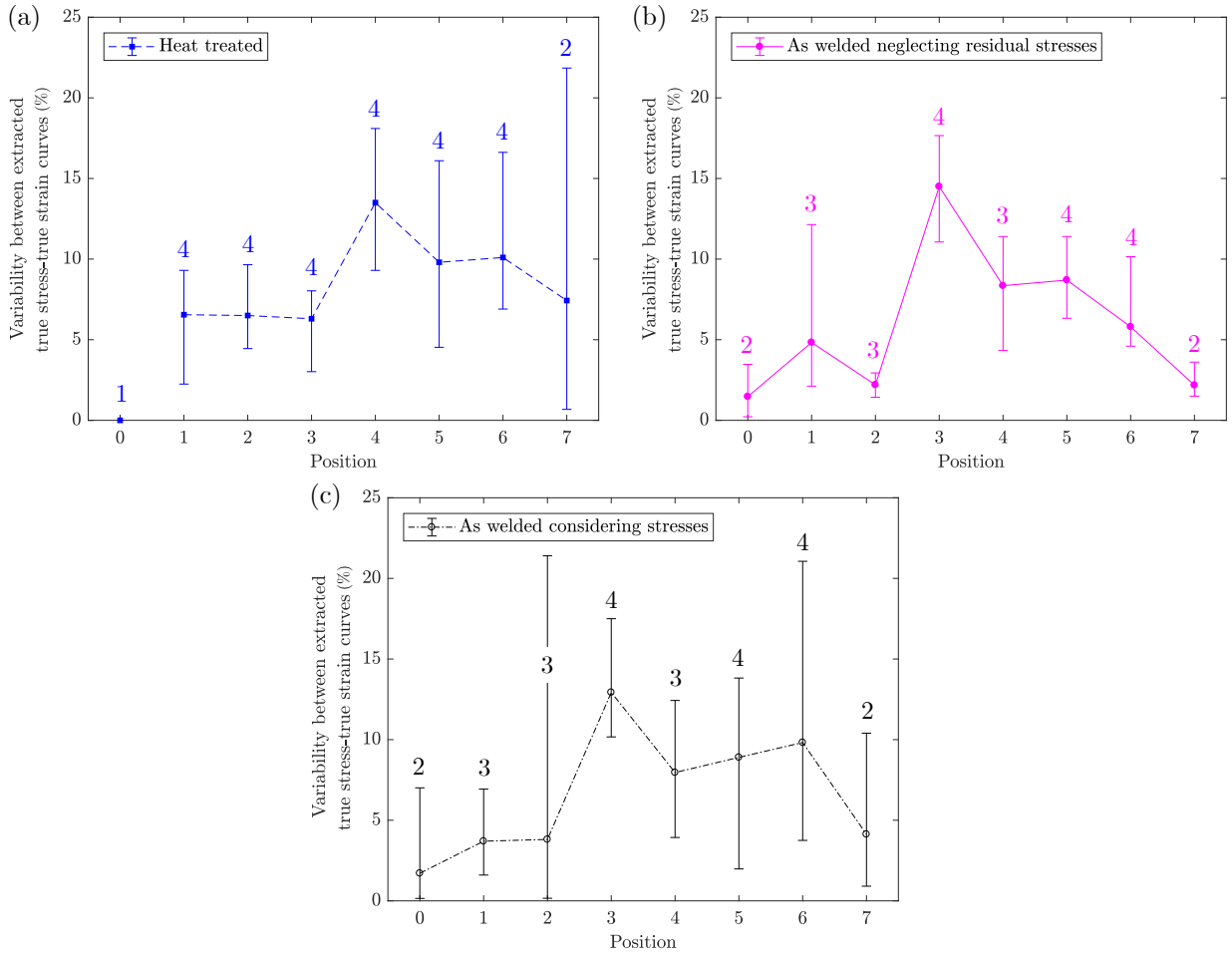

Figure 7.16 Variability between extracted true stress-true strain curves obtained with the proposed methodology for indentations spanning the weld metal (positions 0 and 1), the HAZ (positions 2 to 6) and the base metal (position 7), as well as the number of successfully extracted curves averaged for each position. The variability is defined as the average magnitude of the relative difference between any single extracted true stress-true strain curve and the average of the extracted curves for that position. The error bars demonstrate the minimum and maximum differences between any trues stress value an extracted curve and the corresponding averaged true stress for the same position.

Table 7.2 Errors induced by neglecting the presence of residual stresses on the estimated yield stress, $\Delta\sigma_y$, and overall plastic region of the tensile curve, $|\overline{\Delta\sigma_p}|$, for all positions studied in the as-welded specimens. Also shown are the average measured radial residual stress values, σ_{res}, for all positions as well as the corresponding ratio of this average residual stress to the estimated yield stress when considering the residual stresses, σ_{res}/σ_y. The residual stress values for the failed indentation tests are not included in the averages. For all positions, the yield stress is overestimated to varying degrees. No clear correlation seems to exist between the level of residual stress and the errors induced.

Position	$\Delta\sigma_y$ (%)	$\lvert\overline{\Delta\sigma_p}\rvert$ (%)	Average radial σ_{res} (MPa)	σ_{res}/σ_y
0	0.6	2.6	-20.75	-0.02
1	3.1	3.5	-131.7	-0.19
2	20.1	2.5	-98.2	-0.08
3	3.6	1.6	-54.4	-0.05
4	4.2	1.3	-92.1	-0.10
5	7.7	4.2	-97.3	-0.13
6	8.3	3.0	-52.6	-0.10
7	2.8	5.5	8.8	0.02

treated state are 657.6 MPa in position 0 and 624.7 MPa in position 1. An experimental validation of the application to a weld was not completed, but would be required in future works to better understand the differences between the extracted tensile curves and the actual local experimental tensile curves. A couple of approches could be considered for such an experimental validation. First, micro-tensile tests could be conducted in the positions where the indentation tests were conducted. Alternatively, an approach similar to that used by Kim et al. [79] could also be considered, in which a finite element model of a tensile specimen spanning the weld is developed and estimated tensile curves are included in the model at each position in the weld zone. An equivalent experimental tensile test could then be performed, using direct image correlation to measure the deformation of the different zones.

In the HAZ, Figure 7.13 shows two trends for the estimated curves for both the as-welded and heat treated states, as a function of their positions in the specimens. First, an increase in strain hardening progressively appears through position 2 to position 6. The second trend is a decrease in yield stress from position 2 through to position 6, except for position 3 in the heat treated state (see also Figure 7.15). These can be explained by the varying microstructure as discussed in Section 7.2.2. Harder constituents are present closer to the weld metal, and the metal softens as moving away from the weld metal. These varying constituents appeared during the solidification of the weld, having received various inputs of heat depending on position and having been subject to varying cooling rates. The effect is less pronounced in the heat treated specimens as the welding process which caused this hardening is partly

eradicated by the heat treatment. The yield stress values estimated in the HAZ up to position 5, inclusively, for the AW specimens are quite high, considering the microstructure is bainite or bainite and ferrite.

Another aspect to notice in the tensile curves estimated in the HAZ is the appearance of a plastic plateau, characteristic of the base metal, ASTM A516, in positions 4 to 6 in the heat treated state. In the as-welded state neglecting the residual stresses, this plateau is identified in position 6 only, and it is not at all identified when considering the residual stresses. The effect of neglecting residual stresses in the HAZ is most important in position 2, for which σ_y is overestimated by 20.1%, and in position 5, for which the average difference over the hardening region is 4.2% due to an underestimation of the hardening behaviour.

In the base metal, Figure 7.14 compares the estimated true stress-true strain curves with the experimental tensile curve obtained for the base metal, ASTM A516. This experimental tensile curve is that of a different batch of ASTM A516, as there was not sufficient material of the batch used in the weld study to conduct tensile experiments. As the hardness and compositions of both ASTM A516 batches are similar, but not exactly the same, the extracted curves in the base metal are only compared in a qualitative way with the experimental tensile curve.

It is observed that the estimated tensile curve in the heat treated state is very close to that of the ASTM A516 used in previous chapters. However, in the AW specimens, the extracted yield stress is around 30 % higher than in the HT state, both when neglecting and considering the residual stresses. However, including the residual stresses should have led to the extraction of a tensile curve closer to that obtained in the HT state. The main hypothesis which could explain this difference is that only two curves were sampled in both the as-welded and heat treated states because of experimentally unusable indentation data (see Figure 7.16). It is possible that having had all the data for this position, the averaged curves from both states would have been closer to each other.

As in position 6, a plateau is identified in the base metal for the as-welded specimen when neglecting residual stresses, while it is not identified when considering them. Neglecting residual stresses thus seems to affect the identification of a plastic plateau feature in the estimated tensile curves. Table 7.2 shows that the average difference in the hardening regions of the tensile curves estimated with and without the consideration of the residual stresses is the largest in the base metal, when compared to the other regions, *i.e.*, 5.5%. Figure 7.14 shows that this difference is mostly caused by the overestimation of the stress at ε_5. The magnitude of this effect was not expected, as the average residual stress has the lowest magnitude of all studied positions, *i.e.*, 8.8 MPa. The residual stress is also of a tensile

nature which is different than for all other positions studied. The reason for this effect is not clear. More studies should be conducted to study the effect of tensile residual stresses on the performance of the proposed inverse method.

As a whole, the effect of neglecting residual stresses when using the proposed method to characterize a weld was observed to be significant in some unpredictable cases. It is thus recommended to include the residual stresses in the analysis when applying the proposed method to a weld. To do so, the use of a non-destructive method like XRD is recommended to measure the residual stresses. Also, when characterizing a weld for an industrial application, the cross-section will most likely not be available for indentation and residual stress measurements, as this would require destroying the weld. In the cross section, it is assumed that the residual stresses are constant through the length of the weld, so the measurements were considered constant for the whole length of the specimens. If the residual stress measurements are conducted on the surface of the weld, *i.e.*, in the $X-Z$ plane in Figure 7.2, the residual stresses measured at the surface will evolve in the Y direction. Some analysis would then be required to extrapolate the stresses measured on the surface into the specimen in the Y direction, especially if a portion of the surface must be removed between the residual stress measurements and the indentation tests, as was the case in this work.

The effects of considering or neglecting residual stresses in the inverse method might be different if a hardening model was used to extract the tensile curve, as often done in the literature. Further studies could be conducted to verify if the effects are similar in these cases.

7.3 Conclusions

In this chapter, the proposed method was applied to a weld in two different states. The following conclusions were brought to light from the obtained results:

- The proposed method is capable of estimating true stress-true strain curves which vary with the local microstructure both between the as-welded and heat treated states, and between regions of specimens in the same state;
- The obtained tensile curves in the weld metal and in the heat affected zone seem to overestimate the mechanical properties. An experimental validation should be conducted in the future to better understand this overestimation.
- The variation of the yield stress and hardening behaviour of the estimated true stress-true strain curves is consistent with expectations based on microstructure observations,

the effects of heat treatment and the effects of the welding process in the various regions of the weld;

- The estimated true stress-true strain curve in the base metal region, in the heat treated state, is very close to the experimental tensile curve of ASTM A516, with an average error over the hardening region of 2.7%. A higher error is present in the as-welded state, even when considering the residual stresses;
- The residual stresses should be considered when characterizing a weld by indentation as they can, in some instances, have a significant effect on the estimated true stress-true strain curves. The residual stresses should be measured at the surface by a non destructive method, like XRD, and included in the inverse method used to estimate local tensile curves, as was done in this work.

CHAPTER 8 CONCLUSION

This work was conducted with the principal objective of developing a method for estimating local tensile curves in welded joints by instrumented indentation. The approach chosen was a finite element-based inverse method using numerical optimization. The principal novelty of the method, when compared to similar ones found in the literature, is that no hardening model is used to estimate the true stress-true strain curves from indentation.

To achieve this objective, an experimental study was first performed to investigate the influence of several experimental parameters and conditions on indentation results. The following conclusions were brought to light by this experimental study:

- Specimens should be installed on the indentation testing apparatus without the use of an adhesive since these often have very low stiffnesses (< 4 GPa). This leads to an increased and variable experimental set-up compliance which evolves with the adhesive thickness and influences the stiffness measured by indentation;
- Conventional machining causes surface hardening which have a significant effect on the indentation curves at the scale studied. A method such as EDM should be used to manufacture specimens to be tested by instrumented indentation;
- The surface preparation method can also induce surface hardening, and it is recommended to pursue polishing down to particles of a maximal size of 0.05 µm;
- Neglecting to correct for the machine compliance can lead to significant errors on the estimation of the elastic modulus;
- A method for the direct measurement of the machine compliance was developed and led to a value of $C_f = 0.299$ µm/N for the experimental set-up used in this work. This value led to satisfying estimations of the elastic modulus.

A novel methodology was then proposed and its performance was analyzed through numerical and experimental studies. It involved the development of two finite element models. The conclusions drawn from the performance studies of the method are as follows:

- The proposed method was found to be more versatile than methods using hardening models, being able to capture the shape of the tensile curves of the four studied steels. The average error over the hardening regions between the estimated and experimental

tensile curves ranged from 0.96% to 2.42%, and this error was always increased by using a hardening model;

- The OrthoMADS optimization algorithm chosen for the proposed methodology was shown to perform well for all materials, and it was demonstrated that it was capable of eluding a local minimum in the numerical application on SAE 1080 steel;
- The computation time required for the convergence of the proposed method can be substantially longer than when using a hardening model. For SAE 1080 steel, for example, using a hardening model required a time of about 2.75 hours, while the proposed method required about 25 hours;
- The study using the I-index showed that the optimal number of points to be estimated on the true stress-true strain curve is 6. It also confirmed that both the indentation curve and imprint should be used as indentation data to optimize the performance of the method;
- The proposed method was shown to perform well in the presence of experimental and modelling errors for ASTM A516 and SAE 1080 steels, the average differences between the estimated and experimental tensile curves over their hardening regions being 0.9% and 3.9%, respectively. The performance of the method was poor for AISI 304L and AISI 415 steels. It was hypothesized that scaling effects due to the smaller number of sampled grains in the indentation plastic zone for these steels or possible hardening of the alloys by phase transformations during the indentation process could explain these higher errors.

The proposed methodology was finally applied to a weld in two states to verify its ability to capture the material behaviour in the zones of a weld. The effect of residual stresses was also investigated. The conclusions of this application to welds are as follows:

- The proposed method was shown to capture changes in tensile properties through indentation tests in the base metal, HAZ and weld metal. The variations observed are aligned with expectations based on the thermal cycle involved in the welding process, as well as microstructural observations;
- The effect of residual stresses was found to be significant in some tested positions, and should not be neglected when characterizing a weld which has not been heat treated to relieve residual stresses;

- Applying a heat treatment to welded specimens to relieve residual stresses also tempers the microstructure of the specimens. Considering the residual stresses in the as-welded state thus leads to different extracted true stress-true strain curves than in the heat treated state.

Limitations and recommendations for future works

The following are limitations of the developed methodology and recommendations for future works which could provide improvements to those limitations:

- The weights for the objective and surrogate functions were set after conducting many tests. For the objective function, a study with the I-index was conducted but was inconclusive. The weight values chosen for the method were thus those observed to perform better during preliminary trials. However, no rigorous study was conducted which led to optimized weight values for performance. Such a study should be performed, using a different approach than the minimization of the I-index, to improve the convergence behaviour of the developed inverse method;

- The finite element model is not capable of capturing the material behaviour of AISI 415 and AISI 304L steels. An investigation should be performed to determine if the phase transformations or scale of indentation are the cause of this. For the scale effect, macroscopic indentation tests could be completed. For phase transformations, a material model including such effects could be incorporated and tested to verify if the indentation behaviour is then better captured;

- The computational time required for the method to converge to an estimation of a true stress-true strain curve can be up to 10 times longer than when using a hardening model. This could be reduced by the optimization of the weights, as previously mentioned. However, the method is still expected to require more computational time than popular methods. To save time, the method could be programmed in C++ language to enable the use of the parallel calculation option in NOMAD, which is not available in the version interfaced in Matlab used in this thesis;

- The study using the I-index regarding the influence of the ratio h_{max}/R found that the increase of this ratio did not lead to an increase in performance of the proposed method when using numerical indentation data. This is contrary to findings in the literature when using a pre-defined hardening model. This aspect should be further studied by performing experimental indentation tests at varying h_{max}/R ratios. The stability of

the method would be better analyzed in the presence of experimental and modelling errors, which are not present using numerical data. The effect of the ratio h_{max}/R could be more significant when using experimental data, and more reliable conclusions could be drawn with regard to the effect of this parameter on the performance of the proposed inverse method avoiding the use of a hardening model;

- The strain values at which the stress values are estimated to created points on the true stress-true strain curve are pre-defined. This can cause problems in the estimation of the length of the plastic plateau. The maximum strain value can vary based on the size of the residual imprint obtained by indentation for the studied material, but the distribution between the yield strain and this maximum strain remains the same. Some attempts were made to include the strains in the optimized variables but satisfactory tensile curves were not estimated in any of these trials. Further work could be done to improve the estimation of the length of the plastic plateau. For example, if a plateau is found, the position of the strain value which is closest to the end of the identified plateau could be optimized in a third step to the methodology;

- The effect of neglecting the presence of residual stresses when applying the inverse method to a weld was studied. However, no clear trend was found in the errors induced on the estimated tensile curves by assuming that the residual stresses are not significant. The sample studied contained almost exclusively compressive stresses and they were quite low in magnitude ($|\sigma_{res}/\sigma_y| \leq 0.21$). A complete numerical study including several magnitudes of residual stress of both compressive and tensile natures should be conducted to better understand this effect. Since the study would be numerical, the experimental errors would be eliminated, as these can be quite high in XRD measurements;

- The application to a weld did not include an experimental validation as milli-tensile tests were not conducted in the weld. Future works should include an experimental validation of the application to a weld, in which micro-tensile tests could be conducted in the positions where the indentation tests were conducted. An approach similar to that used by Kim et al. [79] could also be considered, in which a finite element model of a tensile specimen spanning the weld is developed and estimated tensile curves are included in the model at each position in the weld zone. An equivalent experimental tensile test could then be performed, using direct image correlation to measure the deformation of the different zones.

The method developed in this work demonstrates that it is possible to estimate the elasto-

plastic behaviour of a metal without assuming a hardening model. Many applications can benefit from the proposed method, especially when heterogeneous materials are present, with evolving microstructures, like in welds. The ability to obtain reliable local tensile properties in these cases can lead to increasingly precise models which can predict the behaviour of these materials when in service. This can lead to better design, increased maintenance efficiency and reduction of repair costs.

REFERENCES

[1] M. A. Abramson, C. Audet, J. E. Dennis Jr, and S. L. Digabel, "OrthoMADS: A deterministic MADS instance with orthogonal directions," *SIAM Journal on Optimization*, vol. 20, no. 2, pp. 948–966, 2009.

[2] J.-H. Ahn and D. Kwon, "Derivation of plastic stress–strain relationship from ball indentations: Examination of strain definition and pile-up effect," *Journal of Materials Research*, vol. 16, no. 11, pp. 3170–3178, 2001.

[3] S. Alarie, C. Audet, A. E. Gheribi, M. Kokkolaras, and S. Le Digabel, "Two decades of blackbox optimization applications," *EURO Journal on Computational Optimization*, vol. 9, p. 100011, 2021.

[4] ANSYS Academic Research Mechanical, Release 19.2, *Help System : Contact Technology Guide*. ANSYS, Inc.

[5] J. Antunes, J. Fernandes, L. Menezes, and B. Chaparro, "A new approach for reverse analyses in depth-sensing indentation using numerical simulation," *Acta Materialia*, vol. 55, no. 1, pp. 69–81, 2007.

[6] J. Antunes, L. Menezes, and J. Fernandes, "Three-dimensional numerical simulation of Vickers indentation tests," *International Journal of Solids and Structures*, vol. 43, no. 3-4, pp. 784–806, 2006.

[7] "Standard test method for tension testing of metallic materials," ASTM, PA, United-States, Standard, Jun. 2011.

[8] C. Audet and J. E. Dennis Jr, "Mesh adaptive direct search algorithms for constrained optimization," *SIAM Journal on optimization*, vol. 17, no. 1, pp. 188–217, 2006.

[9] C. Audet and J. E. Dennis Jr, "A progressive barrier for derivative-free nonlinear programming," *SIAM Journal on Optimization*, vol. 20, no. 1, pp. 445–472, 2009.

[10] C. Audet and W. Hare, *Derivative-Free and Blackbox Optimization*. Cham: Springer, 2017.

[11] C. Audet, S. Le Digabel, and C. Tribes, "Nomad user guide," Les Cahiers du GERAD, Montreal, Canada, Tech. Rep., 2009.

[12] C. Audet and C. Tribes, "Mesh-based Nelder-Mead algorithm for inequality constrained optimization," *Computational Optimization and Applications*, vol. 71, no. 2, pp. 331–352, 2018.

[13] "Specification for carbon steel electrodes and rods for gas shielded arc welding," American Welding Society, Miami, FL, Standard, 2021.

[14] M. Beghini, L. Bertini, and V. Fontanari, "Evaluation of the stress–strain curve of metallic materials by spherical indentation," *International Journal of Solids and Structures*, vol. 43, no. 7-8, pp. 2441–2459, 2006.

[15] M. Bocciarelli, G. Bolzon, and G. Maier, "Parameter identification in anisotropic elastoplasticity by indentation and imprint mapping," *Mechanics of Materials*, vol. 37, no. 8, pp. 855–868, 2005.

[16] M. Bocciarelli and G. Maier, "Indentation and imprint mapping method for identification of residual stresses," *Computational Materials Science*, vol. 39, no. 2, pp. 381–392, 2007.

[17] G. Bolzon, G. Maier, and M. Panico, "Material model calibration by indentation, imprint mapping and inverse analysis," *International Journal of Solids and Structures*, vol. 41, no. 11-12, pp. 2957–2975, 2004.

[18] A. J. Booker, J. E. Dennis, P. D. Frank, D. B. Serafini, V. Torczon, and M. W. Trosset, "A rigorous framework for optimization of expensive functions by surrogates," *Structural optimization*, vol. 17, no. 1, pp. 1–13, 1999.

[19] D.-A. Bouffard, "Simulation par éléments finis des contraintes résiduelles de soudage en fonction des paramètres de soudage robotisé," Ph.D. dissertation, École Polytechnique de Montréal, 2007. [Online]. Available: https://search.proquest.com/dissertations-theses/simulation-par-éléments-finis-des-contraintes/docview/304715258/se-2?accountid=40695

[20] K.-D. Bouzakis and N. Michailidis, "Coating elastic–plastic properties determined by means of nanoindentations and FEM-supported evaluation algorithms," *Thin Solid Films*, vol. 469, pp. 227–232, 2004.

[21] K.-D. Bouzakis, N. Michailidis, and G. Erkens, "Thin hard coatings stress–strain curve determination through a FEM supported evaluation of nanoindentation test results," *Surface and Coatings Technology*, vol. 142, pp. 102–109, 2001.

[22] Bouzakis, K.-D. and Michailidis, N., "An accurate and fast approach for determining materials stress–strain curves by nanoindentation and its FEM-based simulation," *Materials Characterization*, vol. 56, no. 2, pp. 147–157, 2006.

[23] N. A. Branch, G. Subhash, N. K. Arakere, and M. A. Klecka, "Material-dependent representative plastic strain for the prediction of indentation hardness," *Acta Materialia*, vol. 58, no. 19, pp. 6487–6494, 2010.

[24] J.-L. Bucaille, S. Stauss, E. Felder, and J. Michler, "Determination of plastic properties of metals by instrumented indentation using different sharp indenters," *Acta Materialia*, vol. 51, no. 6, pp. 1663–1678, 2003.

[25] V. Buljak and G. Maier, "Identification of residual stresses by instrumented elliptical indentation and inverse analysis," *Mechanics Research Communications*, vol. 41, pp. 21–29, 2012.

[26] W. Callister and D. Rethwisch, *Materials Science and Engineering.* Hoboken, NJ: Wiley, 2020.

[27] J. Campbell, R. Thompson, J. Dean, and T. Clyne, "Comparison between stress-strain plots obtained from indentation plastometry, based on residual indent profiles, and from uniaxial testing," *Acta Materialia*, vol. 168, pp. 87–99, 2019.

[28] J. Campbell, R. Thompson, J. Dean, and T. W. Clyne, "Experimental and computational issues for automated extraction of plasticity parameters from spherical indentation," *Mechanics of Materials*, vol. 124, pp. 118–131, 2018.

[29] Y. P. Cao and J. Lu, "A new method to extract the plastic properties of metal materials from an instrumented spherical indentation loading curve," *Acta Materialia*, vol. 52, no. 13, pp. 4023–4032, 2004.

[30] ——, "Size-dependent sharp indentation-II: A reverse algorithm to identify plastic properties of metallic materials," *Journal of the Mechanics and Physics of Solids*, vol. 53, no. 1, pp. 49–62, 2005.

[31] Y. P. Cao, X. Q. Qian, J. Lu, and Z. H. Yao, "An energy-based method to extract plastic properties of metal materials from conical indentation tests," *Journal of Materials Research*, vol. 20, no. 5, pp. 1194–1206, 2005.

[32] Y. Cao, X. Qian, and N. Huber, "Spherical indentation into elastoplastic materials: Indentation-response based definitions of the representative strain," *Materials Science and Engineering: A*, vol. 454, pp. 1–13, 2007.

[33] T. Capehart and Y. Cheng, "Determining constitutive models from conical indentation: Sensitivity analysis," *Journal of Materials Research*, vol. 18, no. 4, pp. 827–832, 2003.

[34] O. Casals and J. Alcalá, "The duality in mechanical property extractions from Vickers and Berkovich instrumented indentation experiments," *Acta Materialia*, vol. 53, no. 13, pp. 3545–3561, 2005.

[35] A. Chakraborty and P. Eisenlohr, "Evaluation of an inverse methodology for estimating constitutive parameters in face-centered cubic materials from single crystal indentations," *European Journal of Mechanics-A/Solids*, vol. 66, pp. 114–124, 2017.

[36] M. M. Chaudhri and Y. Y. Lim, "Nanoindentation techniques: a critical assessment of the current methods of data analysis," in *Key Engineering Materials*, vol. 345. Trans Tech Publ, 2007, pp. 1107–1114.

[37] X. Chen, N. Ogasawara, M. Zhao, and N. Chiba, "On the uniqueness of measuring elastoplastic properties from indentation: the indistinguishable mystical materials," *Journal of the Mechanics and Physics of Solids*, vol. 55, no. 8, pp. 1618–1660, 2007.

[38] X. Chen, J. Yan, and A. M. Karlsson, "On the determination of residual stress and mechanical properties by indentation," *Materials Science and Engineering: A*, vol. 416, no. 1-2, pp. 139–149, 2006.

[39] G. Cheng, X. Sun, Y. Wang, S. L. Tay, and W. Gao, "Nanoindentation study of electrodeposited Ag thin coating: An inverse calculation of anisotropic elastic-plastic properties," *Surface and Coatings Technology*, vol. 310, pp. 43–50, 2017.

[40] Y.-T. Cheng and C.-M. Cheng, "Relationships between hardness, elastic modulus, and the work of indentation," *Applied Physics Letters*, vol. 73, no. 5, pp. 614–616, 1998.

[41] ——, "Scaling approach to conical indentation in elastic-plastic solids with work hardening," *Journal of Applied Physics*, vol. 84, no. 3, pp. 1284–1291, 1998.

[42] ——, "Scaling, dimensional analysis, and indentation measurements," *Materials Science and Engineering: Reports*, vol. 44, no. 4-5, pp. 91–149, 2004.

[43] I.-S. Choi, O. Kraft, and R. Schwaiger, "Validity of the reduced modulus concept to describe indentation loading response for elastoplastic materials with sharp indenters," *Journal of Materials Research*, vol. 24, no. 3, pp. 998–1006, 2009.

[44] N. Chollacoop, M. Dao, and S. Suresh, "Depth-sensing instrumented indentation with dual sharp indenters," *Acta Materialia*, vol. 51, no. 13, pp. 3713–3729, 2003.

[45] T. W. Clyne, J. Campbell, M. Burley, and J. Dean, "Profilometry-based inverse FEM indentation plastometry (PIP)," *Advanced Engineering Materials*.

[46] J.-M. Collin, G. Mauvoisin, and P. Pilvin, "Materials characterization by instrumented indentation using two different approaches," *Materials & Design*, vol. 31, no. 1, pp. 636–640, 2010.

[47] A. R. Conn and S. Le Digabel, "Use of quadratic models with mesh-adaptive direct search for constrained black box optimization," *Optimization Methods and Software*, vol. 28, no. 1, pp. 139–158, 2013.

[48] M. Dao, N. V. Chollacoop, K. Van Vliet, T. Venkatesh, and S. Suresh, "Computational modeling of the forward and reverse problems in instrumented sharp indentation," *Acta Materialia*, vol. 49, no. 19, pp. 3899–3918, 2001.

[49] J. Dean, G. Aldrich-Smith, and T. Clyne, "Use of nanoindentation to measure residual stresses in surface layers," *Acta Materialia*, vol. 59, no. 7, pp. 2749–2761, 2011.

[50] J. Dean, J. Wheeler, and T. Clyne, "Use of quasi-static nanoindentation data to obtain stress–strain characteristics for metallic materials," *Acta Materialia*, vol. 58, no. 10, pp. 3613–3623, 2010.

[51] J. Dean and T. W. Clyne, "Extraction of plasticity parameters from a single test using a spherical indenter and FEM modelling," *Mechanics of Materials*, vol. 105, pp. 112–122, 2017.

[52] M. F. Doerner and W. D. Nix, "A method for interpreting the data from depth-sensing indentation instruments," *Journal of Materials Research*, vol. 1, no. 4, pp. 601–609, 1986.

[53] J. Dossett and G. Totten, "ASM Handbook, Volume 4A: Steel Heat Treating Fundamentals and Processes, ASM Intern," 2013.

[54] D. C. Drucker, "A definition of stable inelastic material," Brown University Providence RI, Tech. Rep., 1957.

[55] S. Dub, Y. Lim, and M. Chaudhri, "Nanohardness of high purity Cu (111) single crystals: The effect of indenter load and prior plastic sample strain," *Journal of Applied Physics*, vol. 107, no. 4, p. 043510, 2010.

[56] "Metallic materials - Instrumented indentation test for hardness and materials parameters - Part 1: Test method," British Standards Institution, London, UK, Standard, Nov. 2002.

[57] "Metallic materials - Instrumented indentation test for hardness and materials parameters - Part 2: Verification and calibration of testing machines," British Standards Institution, London, UK, Standard, Nov. 2002.

[58] A. C. Fischer-Cripps, *Nanoindentation: Anthony C. Fischer-Cripps*, 3rd ed. New York: Springer, 2011.

[59] G. Fréchette, "Étude du comportement au fluage de l'alliage 13Cr-4Ni en vue de simuler la redistribution des contraintes résiduelles lors du traitement thermique post-soudage," Master's thesis, École de Technologie Supérieure, 2018.

[60] B. Guelorget, M. François, C. Liu, and J. Lu, "Extracting the plastic properties of metal materials from microindentation tests: Experimental comparison of recently published methods," *Journal of Materials Research*, vol. 22, no. 6, pp. 1512–1519, 2007.

[61] H. Hertz, "On hardness," *Verh. Ver. Beförderung Gewerbe Fleisses*, vol. 61, p. 410, 1882, translated and re-printed in English in *Hertz's Miscellaneous Papers*, Macmillan & Co., London, 1896, Chap. 6.

[62] H. Habbab, B. Mellor, and S. Syngellakis, "Post-yield characterisation of metals with significant pile-up through spherical indentations," *Acta Materialia*, vol. 54, no. 7, pp. 1965–1973, 2006.

[63] E. Harsono, S. Swaddiwudhipong, and Z. Liu, "The effect of friction on indentation test results," *Modelling and Simulation in Materials Science and Engineering*, vol. 16, no. 6, p. 065001, 2008.

[64] E. Harsono, S. Swaddiwudhipong, Z. Liu, and L. Shen, "Numerical and experimental indentation tests considering size effects," *International Journal of Solids and Structures*, vol. 48, no. 6, pp. 972–978, 2011.

[65] C. Heinrich, A. Waas, and A. Wineman, "Determination of material properties using nanoindentation and multiple indenter tips," *International Journal of Solids and Structures*, vol. 46, no. 2, pp. 364–376, 2009.

[66] X. Hernot, C. Moussa, and O. Bartier, "Study of the concept of representative strain and constraint factor introduced by Vickers indentation," *Mechanics of Materials*, vol. 68, pp. 1–14, 2014.

[67] H. Hertz, "On the contact of elastic solids," *J. Reine Angew. Math.*, vol. 92, pp. 156–171, 1881, translated and re-printed in *Hertz's Miscellaneous Papers*, Macmillan & Co., London, 1896, Chap. 5.

[68] R. Hill, B. Storåkers, and A. Zdunek, "A theoretical study of the Brinell hardness test," *Proceedings of the Royal Society of London. A. Mathematical and Physical Sciences*, vol. 423, no. 1865, pp. 301–330, 1989.

[69] R. Hill, *The Mathematical Theory of Plasticity*. Oxford university press, 1998, vol. 11.

[70] H. C. Hyun, M. Kim, J. H. Lee, and H. Lee, "A dual conical indentation technique based on FEA solutions for property evaluation," *Mechanics of Materials*, vol. 43, no. 6, pp. 313–331, 2011.

[71] O. Iracheta, C. Bennett, and W. Sun, "Characterization of material property variation across an inertia friction welded CrMoV steel component using the inverse analysis of nanoindentation data," *International Journal of Mechanical Sciences*, vol. 107, pp. 253–263, 2016.

[72] H. J. Jeong, N. S. Lim, B. H. Lee, C. G. Park, S. Lee, S.-H. Kang, H. W. Lee, and H. S. Kim, "Local and global stress–strain behaviors of transformation-induced plasticity steel using the combined nanoindentation and finite element analysis method," *Metallurgical and Materials Transactions A*, vol. 45, no. 13, pp. 6008–6015, 2014.

[73] S. R. Kalidindi and S. Pathak, "Determination of the effective zero-point and the extraction of spherical nanoindentation stress–strain curves," *Acta Materialia*, vol. 56, no. 14, pp. 3523–3532, 2008.

[74] F. Kandil, J. Lord, A. Fry, and P. Grant, "A review of residual stress measurement methods," *A Guide to Technique Selection, NPL, Report MATC (A)*, vol. 4, 2001.

[75] J. Kang, A. Becker, and W. Sun, "A combined dimensional analysis and optimization approach for determining elastic–plastic properties from indentation tests," *The Journal of Strain Analysis for Engineering Design*, vol. 46, no. 8, pp. 749–759, 2011.

[76] ——, "Determining elastic–plastic properties from indentation data obtained from finite element simulations and experimental results," *International Journal of Mechanical Sciences*, vol. 62, no. 1, pp. 34–46, 2012.

[77] S.-K. Kang, J.-Y. Kim, I. Kang, and D. Kwon, "Effective indenter radius and frame compliance in instrumented indentation testing using a spherical indenter," *Journal of Materials Research*, vol. 24, no. 9, pp. 2965–2973, 2009.

[78] M. Khan, S. V. Hainsworth, M. Fitzpatrick, and L. Edwards, "A combined experimental and finite element approach for determining mechanical properties of aluminium alloys by nanoindentation," *Computational Materials Science*, vol. 49, no. 4, pp. 751–760, 2010.

[79] J. J. Kim, T.-H. Pham, and S.-E. Kim, "Instrumented indentation testing and FE analysis for investigation of mechanical properties in structural steel weld zone," *International Journal of Mechanical Sciences*, vol. 103, pp. 265–274, 2015.

[80] S. Le Digabel, "Algorithm 909: Nomad: Nonlinear optimization with the mads algorithm," *ACM Transactions on Mathematical Software (TOMS)*, vol. 37, no. 4, pp. 1–15, 2011.

[81] H. Lee, J. H. Lee, and G. M. Pharr, "A numerical approach to spherical indentation techniques for material property evaluation," *Journal of the Mechanics and Physics of Solids*, vol. 53, no. 9, pp. 2037–2069, 2005.

[82] J. H. Lee, T. Kim, and H. Lee, "A study on robust indentation techniques to evaluate elastic–plastic properties of metals," *International Journal of Solids and Structures*, vol. 47, no. 5, pp. 647–664, 2010.

[83] J. Lee, C. Lee, and B. Kim, "Reverse analysis of nano-indentation using different representative strains and residual indentation profiles," *Materials & Design*, vol. 30, no. 9, pp. 3395–3404, 2009.

[84] L. Li, L. Shen, G. Proust, C. K. Moy, and G. Ranzi, "Three-dimensional crystal plasticity finite element simulation of nanoindentation on aluminium alloy 2024," *Materials Science and Engineering: A*, vol. 579, pp. 41–49, 2013.

[85] Z. Liu, E. Harsono, and S. Swaddiwudhipong, "Material characterization based on instrumented and simulated indentation tests," *International Journal of Applied Mechanics*, vol. 1, no. 01, pp. 61–84, 2009.

[86] Z. Lu, Y. Feng, G. Peng, R. Yang, Y. Huan, and T. Zhang, "Estimation of surface equibiaxial residual stress by using instrumented sharp indentation," *Materials Science and Engineering: A*, vol. 614, pp. 264–272, 2014.

[87] J. Marteau, S. Bouvier, and M. Bigerelle, "Review on numerical modeling of instrumented indentation tests for elastoplastic material behavior identification," *Archives of Computational Methods in Engineering*, vol. 22, no. 4, pp. 577–593, 2015.

[88] M. Mata and J. Alcala, "The role of friction on sharp indentation," *Journal of the Mechanics and Physics of Solids*, vol. 52, no. 1, pp. 145–165, 2004.

[89] J. Matthews, "Indentation hardness and hot pressing," *Acta Metallurgica*, vol. 28, no. 3, pp. 311–318, 1980.

[90] K. McElhaney, J. J. Vlassak, and W. D. Nix, "Determination of indenter tip geometry and indentation contact area for depth-sensing indentation experiments," *Journal of Materials research*, vol. 13, no. 5, pp. 1300–1306, 1998.

[91] L. Meng, P. Breitkopf, and G. Le Quilliec, "An insight into the identifiability of material properties by instrumented indentation test using manifold approach based on P-h curve and imprint shape," *International Journal of Solids and Structures*, vol. 106, pp. 13–26, 2017.

[92] S. D. Mesarovic and N. A. Fleck, "Spherical indentation of elastic–plastic solids," in *Proceedings of the Royal Society of London A: Mathematical, Physical and Engineering Sciences*, vol. 455, no. 1987. The Royal Society, 1999, pp. 2707–2728.

[93] S. W. Moore, M. T. Manzari, and Y.-L. Shen, "Nanoindentation in elastoplastic materials: Insights from numerical simulations," *International Journal of Smart and Nano Materials*, vol. 1, no. 2, pp. 95–114, 2010.

[94] C. Moussa, O. Bartier, G. Mauvoisin, G. Delattre, and X. Hernot, "Revue bibliographique sur la caractérisation mécanique des matériaux utilisant la déformation représentative en indentation sphérique," *Matériaux & Techniques*, vol. 101, no. 3, p. 302, 2013.

[95] N. Ogasawara, N. Chiba, and X. Chen, "Measuring the plastic properties of bulk materials by single indentation test," *Scripta Materialia*, vol. 54, no. 1, pp. 65–70, 2006.

[96] W. C. Oliver and G. M. Pharr, "Measurement of hardness and elastic modulus by instrumented indentation: Advances in understanding and refinements to methodology," *Journal of Materials Research*, vol. 19, no. 1, pp. 3–20, 2004.

[97] ——, "An improved technique for determining hardness and elastic modulus using load and displacement sensing indentation experiments," *Journal of Materials Research*, vol. 7, no. 6, pp. 1564–1583, 1992.

[98] D. K. Patel and S. R. Kalidindi, "Correlation of spherical nanoindentation stress-strain curves to simple compression stress-strain curves for elastic-plastic isotropic materials using finite element models," *Acta Materialia*, vol. 112, pp. 295–302, 2016.

[99] S. Pathak and S. R. Kalidindi, "Spherical nanoindentation stress–strain curves," *Materials Science and Engineering: Reports*, vol. 91, pp. 1–36, 2015.

[100] S. Pathak, J. Michler, K. Wasmer, and S. R. Kalidindi, "Studying grain boundary regions in polycrystalline materials using spherical nano-indentation and orientation imaging microscopy," *Journal of Materials Science*, vol. 47, no. 2, pp. 815–823, 2012.

[101] S. Pathak, J. Shaffer, and S. R. Kalidindi, "Determination of an effective zero-point and extraction of indentation stress–strain curves without the continuous stiffness measurement signal," *Scripta Materialia*, vol. 60, no. 6, pp. 439–442, 2009.

[102] S. Pathak, D. Stojakovic, and S. R. Kalidindi, "Measurement of the local mechanical properties in polycrystalline samples using spherical nanoindentation and orientation imaging microscopy," *Acta Materialia*, vol. 57, no. 10, pp. 3020–3028, 2009.

[103] C. Pelletier, E. Dekkers, L. Govaert, J. Den Toonder, and H. Meijer, "The influence of indenter-surface misalignment on the results of instrumented indentation tests," *Polymer Testing*, vol. 26, no. 7, pp. 949–959, 2007.

[104] H. Pelletier, "Predictive model to estimate the stress–strain curves of bulk metals using nanoindentation," *Tribology International*, vol. 39, no. 7, pp. 593–606, 2006.

[105] E. Perdahcıoğlu and H. J. Geijselaers, "A macroscopic model to simulate the mechanically induced martensitic transformation in metastable austenitic stainless steels," *Acta Materialia*, vol. 60, no. 11, pp. 4409–4419, 2012.

[106] T.-H. Pham, J. J. Kim, and S.-E. Kim, "Estimating constitutive equation of structural steel using indentation," *International Journal of Mechanical Sciences*, vol. 90, pp. 151–161, 2015.

[107] T.-H. Pham and S.-E. Kim, "Determination of mechanical properties in SM490 steel weld zone using nanoindentation and FE analysis," *Journal of Constructional Steel Research*, vol. 114, pp. 314–324, 2015.

[108] ——, "Determination of equi-biaxial residual stress and plastic properties in structural steel using instrumented indentation," *Materials Science and Engineering: A*, vol. 688, pp. 352–363, 2017.

[109] G. Pharr, W. C. Oliver, and F. Brotzen, "On the generality of the relationship among contact stiffness, contact area, and elastic modulus during indentation," *Journal of Materials Research*, vol. 7, no. 3, pp. 613–617, 1992.

[110] S. A. R. Pulecio, M. C. M. Farias, and R. M. Souza, "Finite element and dimensional analysis algorithm for the prediction of mechanical properties of bulk materials and thin films," *Surface and Coatings Technology*, vol. 205, no. 5, pp. 1386–1392, 2010.

[111] E. Renner, A. Bourceret, Y. Gaillard, F. Amiot, P. Delobelle, and F. Richard, "Identifiability of single crystal plasticity parameters from residual topographies in Berkovich nanoindentation on FCC nickel," *Journal of the Mechanics and Physics of Solids*, vol. 138, p. 103916, 2020.

[112] F. Richard, M. Villars, and S. Thibaud, "Viscoelastic modeling and quantitative experimental characterization of normal and osteoarthritic human articular cartilage using indentation," *Journal of the Mechanical Behavior of Biomedical Materials*, vol. 24, pp. 41–52, 2013.

[113] N. Sakharova, J. Fernandes, J. Antunes, and M. Oliveira, "Comparison between Berkovich, Vickers and conical indentation tests: A three-dimensional numerical simulation study," *International Journal of Solids and Structures*, vol. 46, no. 5, pp. 1095–1104, 2009.

[114] L. Shen, Y. He, D. Liu, Q. Gong, B. Zhang, and J. Lei, "A novel method for determining surface residual stress components and their directions in spherical indentation," *Journal of Materials Research*, vol. 30, no. 8, pp. 1078–1089, 2015.

[115] S. Shim, J.-I. Jang, and G. M. Pharr, "Extraction of flow properties of single-crystal silicon carbide by nanoindentation and finite-element simulation," *Acta Materialia*, vol. 56, no. 15, pp. 3824–3832, 2008.

[116] I. N. Sneddon, "The relation between load and penetration in the axisymmetric Boussinesq problem for a punch of arbitrary profile," *International Journal of Engineering Science*, vol. 3, no. 1, pp. 47–57, 1965.

[117] G. Sun, F. Xu, G. Li, X. Huang, and Q. Li, "Determination of mechanical properties of the weld line by combining micro-indentation with inverse modeling," *Computational Materials Science*, vol. 85, pp. 347–362, 2014.

[118] S. Swaddiwudhipong, E. Harsono, J. Hua, and Z. Liu, "Reverse analysis via efficient artificial neural networks based on simulated Berkovich indentation considering effects of friction," *Engineering with Computers*, vol. 24, no. 2, pp. 127–134, 2008.

[119] S. Swaddiwudhipong, J. Hua, K. Tho, and Z. Liu, "Equivalency of Berkovich and conical load-indentation curves," *Modelling and Simulation in Materials Science and Engineering*, vol. 14, no. 1, p. 71, 2006.

[120] D. Tabor, *The Hardness of Metals*. Oxford: Clarendon Press, 1951.

[121] B. Taljat and G. Pharr, "Development of pile-up during spherical indentation of elastic–plastic solids," *International Journal of Solids and Structures*, vol. 41, no. 14, pp. 3891–3904, 2004.

[122] B. Taljat, T. Zacharia, and F. Kosel, "New analytical procedure to determine stress-strain curve from spherical indentation data," *International Journal of Solids and Structures*, vol. 35, no. 33, pp. 4411–4426, 1998.

[123] G. Turcot, D. Paquet, M. Lévesque, and S. Turenne, "A novel inverse methodology for the extraction of bulk elasto-plastic tensile properties of metals using spherical instrumented indentation," *International Journal of Solids and Structures*, vol. 236, p. 111317, 2022.

[124] E. Tyulyukovskiy and N. Huber, "Neural networks for tip correction of spherical indentation curves from bulk metals and thin metal films," *Journal of the Mechanics and Physics of Solids*, vol. 55, no. 2, pp. 391–418, 2007.

[125] C. Ullner, E. Reimann, H. Kohlhoff, and A. Subaric-Leitis, "Effect and measurement of the machine compliance in the macro range of instrumented indentation test," *Measurement*, vol. 43, no. 2, pp. 216–222, 2010.

[126] K. J. Van Vliet, L. Prchlik, and J. F. Smith, "Direct measurement of indentation frame compliance," *Journal of Materials Research*, vol. 19, no. 1, pp. 325–331, 2004.

[127] M. Wang and J. Wu, "Study on the identifiability of material properties using solely the residual imprint in instrumented indentation experiment," in *Multidisciplinary Digital Publishing Institute Proceedings*, vol. 2, no. 8, 2018, p. 443.

[128] M. Wang, J. Wu, Y. Hui, Z. Zhang, X. Zhan, and R. Guo, "Identification of elastic-plastic properties of metal materials by using the residual imprint of spherical indentation," *Materials Science and Engineering: A*, vol. 679, pp. 143–154, 2017.

[129] M. Wang, J. Wu, X. Zhan, R. Guo, Y. Hui, and H. Fan, "On the determination of the anisotropic plasticity of metal materials by using instrumented indentation," *Materials & Design*, vol. 111, pp. 98–107, 2016.

[130] A. Warren and Y. Guo, "Machined surface properties determined by nanoindentation: Experimental and FEA studies on the effects of surface integrity and tip geometry," *Surface and Coatings Technology*, vol. 201, no. 1-2, pp. 423–433, 2006.

[131] L. Xiao, D. Ye, and C. Chen, "A further study on representative models for calculating the residual stress based on the instrumented indentation technique," *Computational Materials Science*, vol. 82, pp. 476–482, 2014.

[132] Z.-H. Xu and X. Li, "Influence of equi-biaxial residual stress on unloading behaviour of nanoindentation," *Acta Materialia*, vol. 53, no. 7, pp. 1913–1919, 2005.

[133] J. Yan, X. Chen, and A. M. Karlsson, "Determining equi-biaxial residual stress and mechanical properties from the force-displacement curves of conical microindentation," *Journal of Engineering Materials and Technology*, vol. 129, no. 2, pp. 200–206, 2007.

[134] C. Ye, J. Chen, M. Xu, X. Wei, and H. Lu, "Multi-scale simulation of nanoindentation on cast inconel 718 and NbC precipitate for mechanical properties prediction," *Materials Science and Engineering: A*, vol. 662, pp. 385–394, 2016.

[135] D. Ye, F. Mi, J. Liu, Y. Xu, Y. Chen, and L. Xiao, "Use of instrumented indentation testing to study local mechanical properties of 304L SS welded joints subjected to low-cycle fatigue loadings," *Materials Science and Engineering: A*, vol. 564, pp. 76–84, 2013.

[136] M. Zhao, X. Chen, J. Yan, and A. M. Karlsson, "Determination of uniaxial residual stress and mechanical properties by instrumented indentation," *Acta Materialia*, vol. 54, no. 10, pp. 2823–2832, 2006.

[137] M. Zhao, N. Ogasawara, N. Chiba, and X. Chen, "A new approach to measure the elastic–plastic properties of bulk materials using spherical indentation," *Acta Materialia*, vol. 54, no. 1, pp. 23–32, 2006.